THE UNIVERSITY OF READING

DEPARTMENT OF CHEMISTRY

Computational Modelling of Fatty Acids at the Air-Water Interface

A Thesis Submitted in Partial Fulfilment of the Requirements for the
Degree of Doctor of Philosophy

Jana Verena Geßner

September 2017

Supervisor: Dr David Nutt

Co-Supervisor: Dr Christian Pfrang

Declaration

I confirm that this is my own work and the use of all material from other sources has been properly and fully acknowledged.

Jana Verena Geßner

Abstract

The organic fraction of aqueous atmospheric aerosols has received much recent attention due to the ability of fatty acids to partition to the air-water interface, thus altering the surface properties of the aerosol. With the complex surface films formed, there is a need for an efficient model system to understand key features. To further both our understanding of film formation processes and changes in films due to ozonolysis reactions within the atmosphere, this work employs coarse-grained molecular dynamics simulations of model surfactants at the air-water interface. Molecular dynamics simulations of surface films have not yet been widely used in atmospheric science; however, they can provide useful insight into sub-micrometre aerosols, giving a molecular level view of the structure and dynamics of the system. Thus, this work paves the way for future coarse-grained simulations in the field of atmospheric chemistry.

In the simulations in this thesis, a planar interface is assumed, mimicking a cross-section through a large aerosol with low curvature and allowing direct comparison to experimental studies on Langmuir troughs. Based on structural data derived from all-atom simulations, pressure-area isotherms were calculated from coarse-grained simulations of single component monolayers of oleic acid, stearic acid and palmitoleic acid, which were in good agreement with experimental isotherms. The phase behaviour of the main reaction products of the ozonolysis of both oleic acid and palmitoleic acid, assuming an analogue reaction pathway as for oleic acid, were determined. The simulations suggest that the only products remaining at the interface from these reactions are nonanoic acid and heptanoic acid. Pressure-area isotherms of mixed component films, which are more realistic proxies for the complex mixtures on real atmospheric aerosols, were then calculated. For systems below 10 % unsaturated material, ordered liquid-condensed phase and solid state films were formed. These may act as a transport barrier and hence supress the growth of aerosols in the atmosphere. For surface films containing more than 33 % of unsaturated material, disordered liquid-expanded films were formed. For such films, the higher the amount of unsaturated material, the higher the surface pressure of the system, and the lower the surface tension. It was shown that the ozonolysis of a surface film can lead to phase changes, hence influencing the growth potential of the aerosol, and highlighting the importance of a complete understanding of aged surface films in the atmosphere.

Acknowledgments

I would like to take this opportunity to thank the many people without this work would not have been possible. First and foremost, I would like to thank my supervisor Dr David Nutt for facilitating this research. I am immensely grateful for his valuable advice, insightful guidance and for the many thought-provoking discussions that guided me over the past four years and helped me gain new perspectives on my work. Similarly, I would like to thank my second supervisor Dr Christian Pfrang for sharing his expertise in environmental chemistry with me and giving the project direction by providing some of the experimental basis for the computational work undertaken in this thesis.

I would like to thank the UK Research Facility for granting me permission to use the Advanced Research Computing High End Resource (ARCHER) over the past year.

Furthermore, I would like to thank the past and present members of the Reading Atmospheric and Environmental Research (RACER) team, especially Prof George Marston, for always giving valuable feedback and providing a source of perspective. Thanks to Ben Thomas and Federica Sebastiani, who carried out some of the experimental work that was used as a reference for my computational work. Thanks to Sreelekha Benny for the many interesting and helpful discussions and for encouraging me to apply to ARCHER. Special thanks to Kunal Rastogi and Matt Hagreen who have been in the same research group as me since my undergraduate—for becoming good friends, always willing to help and giving their best suggestions.

I was fortunate to share the office with several other PhD students and postdoctoral researchers over the past years—I am thankful that we found a good balance between the quiet needed to concentrate and work and the tea breaks with many interesting conversations.

Last but not least I would like to thank my family and friends for their love and support. Thanks, to my mum and Burkhard for giving me the opportunity to study in the UK, for always believing in me and for finding the right words of encouragement when needed. To my dad, grandparents, sister and David who are always very happy when I manage to visit for a weekend, and who can’t wait for me to finish in the hope that I will find a job closer to home. To Sarah, for the unexpected care packages when I was writing up, which

always managed to put a smile back on my face. To Alex, who despite the bad weather moved to the UK—thanks for always believing in me, seeing the positives and for cheering me up when things don’t go according to plan.

Table of Contents

Chapter 1—Atmospheric and Computational Background 1
1.1 Introduction 1
1.2 Structure and Composition of the Atmosphere 2
1.3 Stratospheric Chemistry 4
1.4 Tropospheric Chemistry 5
1.5 Atmospheric Aerosols 6
1.6 Fatty Acids 8
1.6.1 Sources of Fatty Acids in Atmospheric Aerosols 9
1.7 Interfaces 10
1.7.1 Fatty Acid Film Formation on Atmospheric Aerosols 10
1.7.2 Dynamics of Aerosol Surfaces 11
1.7.3 Atmospheric Implications 14
1.8 Computational Modelling in Chemistry 17
1.9 Force Fields 18
1.10 All-Atom Models 24
1.11 Coarse-Grained Models 26
1.11.1 The Martini Force Field 27
1.11.1.1 Mapping 27
1.11.1.2 Bonded Interactions 28
1.11.1.3 Non-Bonded Interactions 29
1.12 Periodic Boundary Conditions 31
1.13 Energy Minimisation 33
1.14 Molecular Dynamics Computer Simulations 34
1.15 Molecular Dynamics Simulations of Lipid Monolayers 37
1.16 Pressure-Area Isotherms 38
1.17 References 43

Chapter 2—Computational Model of Oleic Acid 48
2.1 Oleic Acid Monolayer at the Air-Water Interface 48
2.2 Methodology/ Simulations 51
2.2.1 Oleic Acid 51
2.2.1.1 Coarse-Grained Mapping 51
2.2.1.2 Bonded Interactions within Oleic Acid 52

2.2.1.3 Interactions between Non-bonded Beads in the System 53
2.2.1.4 System Set Up: Algorithm for a Monolayer of Oleic Acid 54
2.2.2 Coarse-Grained Simulations 57
2.2.3 Changes to System Setup 1 58
2.2.4 Pressure-Area Isotherms of Oleic Acid at the Air-Water Interface 62
2.3 Results and Discussion 63
2.3.1 Pressure-Area Isotherm from Standard Parameters 63
2.3.2 Pressure-Area Isotherms from Reduced Bead-to-Bead Distance Parameters 66
2.3.3 Angle Analysis 72
2.4 Conclusions 78
2.5 References 79

Chapter 3—Stearic Acid Pressure-Area Isotherms 81
3.1 Stearic Acid Pressure-Area Isotherms 81
3.2 Method 83
3.2.1 Stearic Acid Mapping 83
3.2.2 CHARMM-36 Simulations of Stearic Acid 85
3.2.3 Coarse-Grained Simulations 88
3.3 Results and Discussion 89
3.3.1 Simulation Set 1 89
3.3.2 Simulation Set 2 91
3.3.3 Simulation Set 3 94
3.3.4 Simulation Set 4 96
3.4 Conclusions 106
3.5 References 107

Chapter 4—Oleic Acid and Palmitoleic Acid Ozonolysis Products 108
4.1 Monounsaturated Fatty Acids—Reactions in the Atmosphere 108
4.2 Method for All-Atom Simulations 111
4.2.1 Parameterisation of Oleic Acid Ozonolysis Products 111
4.2.2 CHARMM-36 All-Atom Simulations 112
4.3 Results and Discussion for All-Atom Simulations 113
4.3.1 Carbon-Carbon Bead Distance 113
4.3.2 Palmitoleic Acid 114
4.3.3 Nonanoic Acid 114

4.3.4 Azelaic Acid 115
4.3.5 Nonanal 116
4.3.6 9-Oxononanoic Acid 117
4.3.7 Heptanal 118
4.3.8 Heptanoic Acid 118
4.3.9 Bead-to-Bead Distance of P3 Headgroup to Chain Bead 119
4.3.10 Bead-to-Bead Distance of Na Headgroup to Chain Bead 121
4.4 Method for Coarse-Grained Simulations 122
4.4.1 Pressure-Area Isotherm of Palmitoleic Acid 122
4.4.2 Ozonolysis Products of Palmitoleic Acid and Oleic Acid 123
4.5 Results and Discussion of Coarse-Grained Simulations 124
4.5.1 Pressure-Area Isotherm of Palmitoleic Acid 124
4.5.2 Phase Behaviour of Ozonolysis Products from Coarse-Grained Simulations 130
4.5.2.1 Nonanoic Acid 130
4.5.2.2 Azelaic Acid 130
4.5.2.3 Nonanal 131
4.5.2.4 9-Oxononanoic Acid 132
4.5.2.5 Heptanal 133
4.5.2.6 Heptanoic Acid 134
4.6 Conclusions 135
4.7 References 136

Chapter 5—Mixed Component Surface Films 137
5.1 Mixed Organic Aerosols 137
5.2 Method 138
5.2.1 Composition and System Setup of Mixed Component Surface Films 138
5.2.1.1 Mixed Monolayers Containing Oleic Acid and Stearic Acid 138
5.2.1.2 Mixed Monolayers Containing Palmitoleic Acid 140
5.2.2 Pressure-Area Isotherms of Mixed Component Surface Films 141
5.3 Results and Discussion 142
5.3.1 Pressure-Area Isotherms of Mixed Monolayers Containing Oleic Acid 142
5.3.1.1 50 % Oleic Acid: 50 % Stearic Acid Mixture 142
5.3.1.2 33 % Oleic Acid: 67 % Stearic Acid Mixture 149
5.3.1.3 22 % Oleic Acid: 78 % Stearic Acid Mixture 155
5.3.1.4 10 % Oleic Acid: 90 % Stearic Acid Mixture 159
5.3.1.5 Comparison of the Simulated Mixtures 165

5.3.1.6 8 % Nonanoic Acid: 25 % Oleic Acid: 67 % Stearic Acid Mixture........................... 166
5.3.2 Pressure-Area Isotherms of Mixed Monolayers Containing Palmitoleic Acid 168
5.3.2.1 10 % Palmitoleic Acid: 90 % Stearic Acid Mixture.. 168
5.3.2.2 22 % Palmitoleic Acid: 78 % Stearic Acid Mixture.. 173
5.3.2.3 5 % Heptanoic Acid: 17 % Palmitoleic Acid: 78 % Stearic Acid Mixture................ 178
5.4 Conclusions 180
5.5 References.. 183

Chapter 6—Conclusions and Outlook 184
6.1 Conclusions and Outlook 184
6.2 References.. 190

Appendix 191
A.1 Internal Angles 191
A.2 Determining the Lowest Density Regions in the Contour Plots.................................... 193
A.3 CHARMM Parameters for Molecules Simulated in this Work 194
A.3.1 Stearic Acid.. 194
A.3.2 Azelaic Acid 197
A.3.3 Heptanal... 198
A.3.4 Heptanoic Acid 200
A.3.5 Nonanal.. 201
A.3.6 9-Oxononanoic Acid 202
A.3.7 Palmitoleic Acid.. 204
A.3.8 Nonanoic Acid 206

List of Acronyms

BAM	Brewster Angle Microscopy
CHARMM	Chemistry at Harvard Molecular Dynamics
CI	Criegee Intermediate
DPPC	Dipalmitoylphosphatidylcholine
GROMACS	Groningen Machine for Chemical Simulations
HA	Heptanoic Acid
IPCC	Intergovernmental Panel on Climate Change
NA	Nonanoic Acid
OA	Oleic Acid
POA	Palmitoleic Acid
SA	Stearic Acid
VOCs	Volatile Organic Compounds

Chapter 1

Atmospheric and Computational Background

1.1 Introduction

Atmospheric aerosols are ubiquitous in our atmosphere. They are particles which exist in solid or liquid phase suspended in air.[1] These particles are able to impact the Earth's radiation balance, which influences our climate. They have the ability to scatter as well as absorb sunlight. When acting as cloud condensation nuclei, they promote cloud formation and impact precipitation.[2] Furthermore, atmospheric aerosols can affect public health as they contribute to respiratory diseases. To fully understand the effects of these particles, detailed studies of their behaviour are necessary.[3]

A high fraction of organic material in the atmosphere is made up of fatty acids.[4] These surfactants are known to form films on the surface of aqueous aerosols, which are the focus of this work. With the wide range of components present in aerosols, there is a need for a simple model system to understand key features of these aerosols and to determine their fate once released into the atmosphere.[4] For this purpose, the oleic acid–ozone heterogeneous reaction system was chosen as the basis for this work, which has emerged as a benchmark system to study atmospheric oxidation.[4] Using computational modelling, the aim of this project is to gain further insight into the structural and dynamical properties of surfactant films. A full understanding of this oleic acid film and its oxidative degradation will help to forge a better understanding of their effects on the aerosols' properties.

This chapter will give a background regarding the Earth's atmosphere, atmospheric aerosols, their sources, size modes and distribution, and will then focus on atmospheric aerosols containing fatty acids. Research that has been conducted so far on film formation processes will be reviewed. The last part of this chapter provides details on the modelling technique used. This will give the background for the computational model for fatty acid monolayers at the air-water interface developed in this work.

This thesis focuses on single component films with results compared to experimental data where possible. Oleic acid at the air-water interface will be described in detail in Chapter 2. Chapter 3 focuses on stearic acid, the saturated analogue of oleic acid. In Chapter 4, a detailed analysis of a single component film of the shorter chain unsaturated fatty acid, palmitoleic acid, will be given and the phase behaviour of the ozonolysis products of both oleic acid and palmitoleic acid will be determined. The final chapter of this thesis investigates mixed component films, which are better proxies for the complex films formed on aerosols in the atmosphere.

1.2 Structure and Composition of the Atmosphere

The Earth's atmosphere is the layer of gases that is held in place by the gravitational pull of the Earth's body. The main gases found in the atmosphere are nitrogen, comprising 78 %, oxygen with 21 %, and argon with 0.94 % expressed as a percentage in dry air.[5] The remaining volume making up the air in our atmosphere consists of trace gases, which include a variety of chemical species such as noble gases, greenhouse gases and atmospheric oxidants.

The noble gases mentioned include krypton, helium, xenon and neon. Greenhouse gases such as carbon dioxide, methane and nitrous oxide, although only present in low concentrations, have a great impact on the Earth's climate. Their ability to absorb infrared radiation from the surface of the Earth results in a heating of the atmosphere, making them the main contributor to climate change. Ozone, nitrate radicals and hydroxyl radicals are atmospheric oxidants which are highly reactive. Their ability to react with organic compounds within the atmosphere leads to a constantly changing environment.

As shown in Figure 1, the atmosphere is divided into four main regions, distinguishable by their temperature profiles, which are known as the troposphere, stratosphere, mesosphere and thermosphere.

Closest to the Earth's surface is the troposphere. This layer is the densest, containing up to 75 % of the atmosphere's mass. Most of the water vapour in the atmosphere is found here, with concentrations varying from 0–4 % by volume.[6] The troposphere extends between 7 and 20 km from the Earth's surface; it is thinnest over the poles and thickest at the equator.[5] The troposphere is the region in which aerosols are most abundant. The temperature in the troposphere decreases as altitude increases. This leads to convection, resulting in the troposphere being well mixed ('tropos' ≡ turning).[7] The boundary above the troposphere is known as the tropopause, where a temperature inversion takes place.

The stratosphere extends from the tropopause to approximately 50 km from the Earth's surface, where its upper limit is known as the stratopause. The ozone layer, containing the highest ozone concentrations in the atmosphere, lies within the stratosphere. Stratospheric ozone is important to life on Earth as the ability of the ozone layer to absorb the UV radiation of the sun decreases the amount of short-wavelength radiation that reaches the Earth's surface, shielding us from harmful radiation. Due to the absorption of the sun's UV radiation by the ozone layer, increasing altitude causes a rise in temperature within the stratosphere. The temperature profile that is found in this layer results in stable atmospheric conditions.

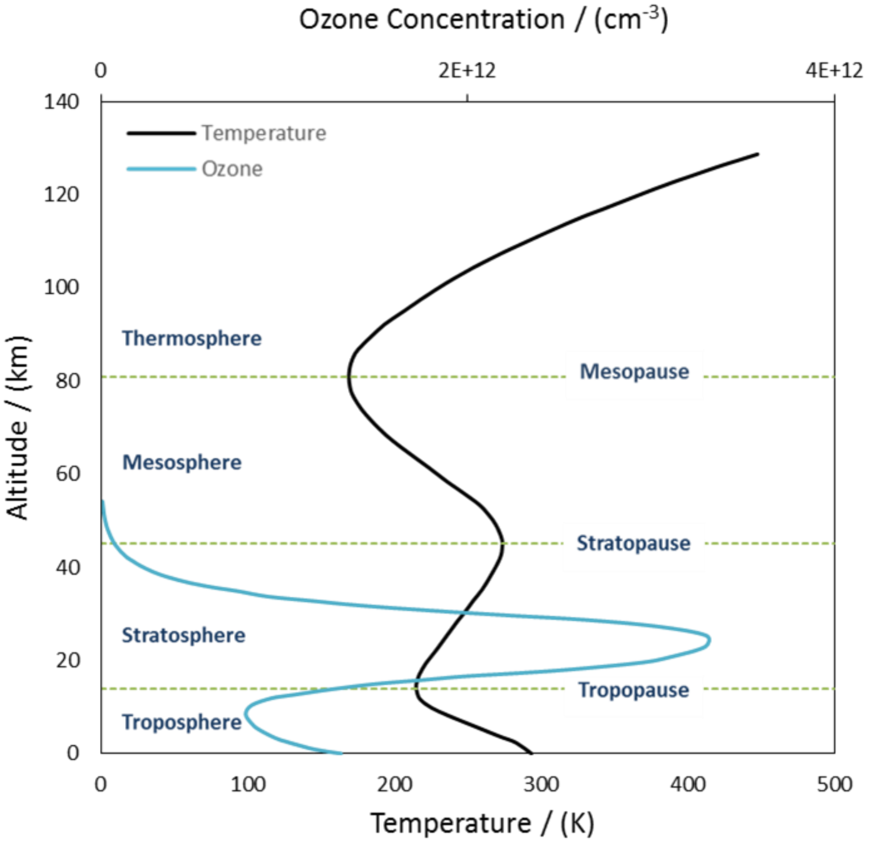

Figure 1: The Structure of the Earth's atmosphere, adapted from Watson *et al.*[8]

The layers above the troposphere include the mesosphere, thermosphere and exosphere. This upper limit of the atmosphere merges into space. We will not go into further detail regarding these layers as the most relevant layers regarding atmospheric aerosols and their reactions are the troposphere and stratosphere.

From the stratosphere, ozone is transported down into the upper troposphere by eddy diffusion,[9] where it can react with organic compounds in the atmosphere. The formation of ozone in both the stratosphere and troposphere will be discussed in more detail in the following sections.

1.3 Stratospheric Chemistry

Ozone in the stratosphere is an important component; it is able to filter the ultraviolet radiation from the sun, protecting us from harmful radiation.

In 1930, Chapman proposed a mechanism describing the ozone formation and removal processes in the stratosphere. This mechanism, known as the Chapman mechanism, consists of the following steps:[10]

$$\mathrm{O_2} + h\nu \rightarrow 2\,\mathrm{O}\cdot \tag{1}$$

$$\mathrm{O}\cdot + \mathrm{O_2} + \mathrm{M} \rightarrow \mathrm{O_3} + \mathrm{M} \tag{2}$$

$$\mathrm{O_3} + h\nu \rightarrow \mathrm{O}\cdot + \mathrm{O_2} \tag{3}$$

$$\mathrm{O}\cdot + \mathrm{O_3} \rightarrow 2\,\mathrm{O_2} \tag{4}$$

In the first reaction step (1), an oxygen molecule is photolysed to form oxygen atoms. The ultraviolet light necessary for the dissociation of the oxygen molecule needs to have a wavelength below 240 nm.[5] The product of reaction (1) is then used to produce ozone in reaction (2). The inert collision partner (M) in the mechanism is either N_2 or O_2, which are the main gases in our atmosphere. They stabilise O_3, by absorbing the energy released in the reaction. Reaction (3) shows that the photolysis of ozone leads to the formation of an oxygen atom and oxygen molecule. As reactions (1) and (4) are slower than reactions (2) and (3), reaction (3) does not necessarily lead to the removal of ozone. The oxygen atom formed by this mechanism can react again via reaction (2), forming new ozone. Therefore, mechanism (3) needs to be followed by reaction (4) to cause the destruction of ozone. A dynamic equilibrium exists between ozone being produced and destroyed through photolysis. There is more radiation at high altitude but more dioxygen at low altitude—the point at which these two limiting conditions combine to result in the maximum formation of ozone, is known as the ozone layer.

The Chapman mechanism is mainly relevant for stratospheric ozone and only influences ozone concentrations in the troposphere by the transport of ozone from the stratosphere to the troposphere.

1.4 Tropospheric Chemistry

In the troposphere itself, ozone is found naturally in very low concentrations. However, an increase in ozone in the lower troposphere over the past 100 years has mainly been attributed to pollution from human activity.[11] Unlike stratospheric ozone where its presence enables life on earth, tropospheric ozone is harmful, being toxic when inhaled.

Two main pathways for the production of ozone in the troposphere are mediated by the presence of NO and OH radicals.[12]

$$\cdot \mathrm{OH} + \mathrm{CO} \rightarrow \mathrm{CO_2} + \mathrm{H}\cdot \tag{5}$$

$$\mathrm{H} \cdot + \mathrm{O_2} + \mathrm{M} \rightarrow \mathrm{HO_2} \cdot + \mathrm{M} \tag{6}$$

$$\mathrm{HO_2} \cdot + \mathrm{NO} \cdot \rightarrow \cdot \mathrm{OH} + \cdot \mathrm{NO_2} \tag{7}$$

$$\cdot \mathrm{NO_2} + h\nu \rightarrow \mathrm{NO} \cdot + \mathrm{O} \cdot \tag{8}$$

$$\mathrm{O} \cdot + \mathrm{O_2} + \mathrm{M} \rightarrow \mathrm{O_3} + \mathrm{M} \tag{9}$$

The reaction between carbon monoxide and a hydroxyl radical produces carbon dioxide, and a H atom which rapidly reacts with oxygen to form a peroxyl radical. In the presence of $\mathrm{NO}\ \cdot$, the peroxyl radical reacts to regenerate a hydroxyl radical and $\cdot\ \mathrm{NO_2}$, according to reaction (7). The photolysis of $\cdot\ \mathrm{NO_2}$, with $\lambda < 424$ nm, leads to the generation of ozone in reaction (9).[5]

The 3 main oxidants in the troposphere are hydroxly (OH) radicals, nitrate (NO_3) radicals and O_3. They are able to oxidise volatile organic compounds (VOCs), which are carbon based trace gases in the atmosphere, to form organic aerosols. However, their production is limited, as OH radicals, produced via a photochemical reaction, are only present during the day and the nitrate radicals NO_3 are mainly present during the night time since they are photolabile. Hence, it is generally accepted that, of the three main oxidants, ozone is responsible for the largest proportion of organic aerosol in the troposphere.[13] The ozone concentration in the troposphere lies at 25–50 parts per billion (ppb), with the highest ozone concentration found in the upper stratosphere, reaching up to 10 parts per million (ppm).[14]

As mentioned earlier, atmospheric aerosols are part of the air in the Earth's atmosphere and their study is the focus of this project; hence the next section of this report will look at the sources, size and distribution of these aerosols.

1.5 Atmospheric Aerosols

Atmospheric aerosols can be divided into two categories, depending on their origin: biogenic or anthropogenic sources.[15] Deserts, volcanoes and oceans' surfaces are examples of biogenic sources causing the formation of aerosols. Anthropogenic sources on the other hand are man-made; the resulting aerosols originate from processes such as biomass burning or industrial activity.[16]

Furthermore, aerosols can be classified as being primary or secondary. Primary aerosols represent particles that are directly released into the atmosphere. Examples of these are particles emitted by abrasion, suspension and sea-spray, which are mechanical production processes, as well as particles created by soot and condensation of hot vapours from combustion processes.[17] As depicted in Figure 2, combustion processes form fine particles, with a diameter below 2.5 µm, whereas mechanical production processes form coarse particles with a diameter above 2.5 µm.

Secondary aerosols on the other hand are formed within the atmosphere itself. Here, nucleation describes molecules grouping to form clusters with diameters of approximately 1 nm. Inorganic compounds, such as sulphuric acid, and organic compounds with low volatility, formed from reactions within the atmosphere, can condense onto clusters leading to their growth. Depending on how much condensable vapour is taken up, particles belong to different size modes. The nucleation mode describes particles with diameters of 3–20 nm, with further uptake leading to particles in the Aitken mode at 20–100 nm, and the accumulation mode, describing particles with diameters in the range of 100 nm–1 µm, being formed. Further growth of the particles can be described by the coarse mode, with particle diameters reaching up to 100 µm.

The size of the aerosol is an important factor regarding its health implications. Commonly used atmospheric measurement classifications referred to when describing the health effects of atmospheric aerosols are the mass concentration of particulate matter with a diameter below 10 µm (PM_{10}) and the mass concentration of particulate matter with a diameter below 2.5 µm ($PM_{2.5}$). Both PM_{10} and $PM_{2.5}$ include particles which can enter the lungs, worsening asthma and causing respiratory symptoms.[18] The highest health risk is attributed to long term exposure to particles with $\leq PM_{2.5}$, which can cause lung cancer, cardiovascular diseases and respiratory diseases that can ultimately lead to death.[18]

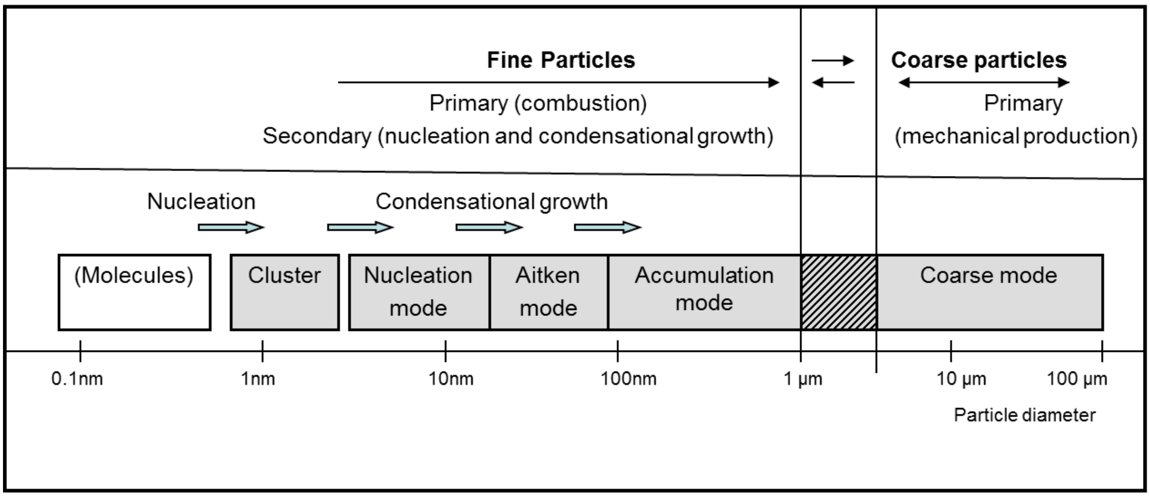

Figure 2: Atmospheric life-cycle and growth processes of atmospheric aerosols, adapted from Warnke *et al.*[17]

As described above, the size of the aerosol is determined by its formation process. This influences its growth during physical and chemical ageing and results in differences in lifetimes and deposition of the aerosols.

For fine particles in the Nucleation or Aitken mode, coagulation with other particles is the main removal process. Once particles reach the accumulation mode, the removal process is through rainout or washout. The main sink for coarse particles is through sedimentation.[17]

Atmospheric aerosols can contain inorganic as well as organic parts, with the composition and size depending largely on the source of the aerosol. The organic fraction of these aerosols often consists of fatty acids, which are the focus of this work, with details on nomenclature and categories given in the following section.

1.6 Fatty Acids

Fatty acids are carboxylic acid molecules, with the general formula R-COOH, where R is a hydrocarbon chain which can be saturated or unsaturated. Fatty acids can be categorised by their chain length—short chain fatty acids have a chain of 5 or less carbons. Fatty acids with 6–12 carbons can be classified as medium chain length. 13–21 carbon chain fatty acids are long chain fatty acids. Even longer chains are classed as very long chain fatty acids. The carboxyl group of the fatty acid is hydrophilic, whereas the hydrocarbon chain is hydrophobic; increasing chain length results in a decrease in solubility of the fatty acid in water.

To highlight the abundance of fatty acids in the troposphere, the following section will focus on fatty acid sources and fatty acid concentrations in tropospheric aerosols. In particular, the focus is set on fatty acids relevant to this project (e.g. oleic acid and stearic acid), which are depicted in Figure 3.

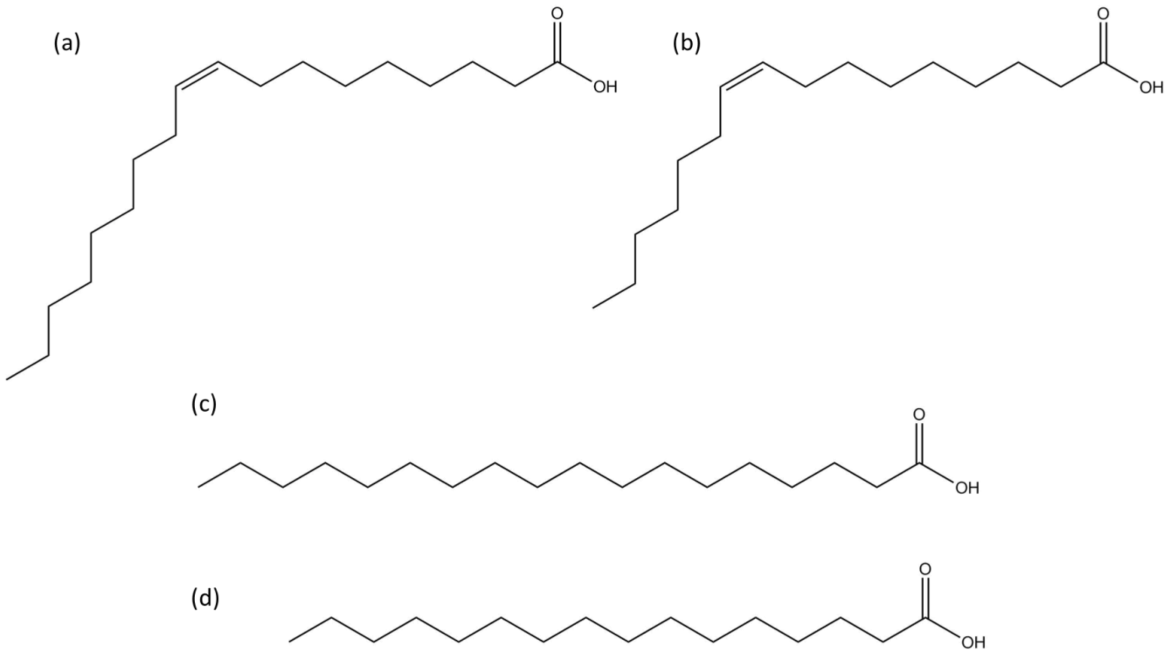

Figure 3: (a) Oleic acid ((9*Z*)-octadec-9-enoic acid), (b) palmitoleic acid ((9*Z*)-hexadec-9-enoic acid), (c) stearic acid (octadecanoic acid), and (d) palmitic acid (hexadecanoic acid).

1.6.1 Sources of Fatty Acids in Atmospheric Aerosols

As previously discussed, the organic fraction of the aerosol often consists of fatty acids, which can originate both from anthropogenic and biogenic sources.[19]

The review by Zahardis and Petrucci on the oleic acid-ozone reaction system highlights the significance of cooking emissions as a main contributor to fatty acid concentration in urban environments.[4] Recent studies show that anthropogenic aerosols from cooking sources are a significant source of fine particulate matter in the urban environment. Ots *et al*. estimate that in the UK an additional 10 % of urban $PM_{2.5}$ is attributed to cooking emissions.[20] Rogge *et al.* analyzed the chemical composition of meat cooking emissions and found palmitic, stearic and oleic acid among the prominent compounds.[21] It has been suggested that Chinese style cooking is a major source of fatty acids in the troposphere.[22-28] Wang *et al.* conducted studies on aerosols in fourteen metropolitan areas in China and calculated an annual average fatty acid concentration of 769 ng m^{-3} from their measurements.[27] The presence of unsaturated fatty acids such as oleic acid and palmitoleic acid was noted in all samples with measurements ranging from 17.4−213 ng m^{-3} in summer (seasonal average of 93.6 ng m^{-3}), and measurements in winter ranging from 76−1955 ng m^{-3} (seasonal average of 444 ng m^{-3}).[27] The lower concentration in summer was attributed to an increase in photochemical degradation of the unsaturated fatty acids.[27] Sin *et al.* report an oleic acid concentration in Hong Kong of approximately 180 ng m^{-3}.[29] They suggest evaporations of cooking oils from food outlets as a possible cause for the very high fatty acid concentration in the region.

Furthermore, enhanced fatty acid concentrations in the urban environment can be attributed to petrol and diesel emissions. 53.4 % of emissions from catalyst-equipped cars were found to contain n-alkanoic acids, including saturated fatty acids.[30] Palmitic and oleic acid respectively were the most prevalent saturated and unsaturated fatty acids.[30] Further sources of anthropogenic fatty acid emissions include biomass and coal burning.[19, 31, 32]

A major contributor to the global aerosol load is biogenic aerosol originating from a marine environment, with C12–C19 fatty acids being most prevalent.[4] These fatty acids are formed from the decomposition of organisms (e.g. phytoplankton).[33] Bubble bursting processes, due to wind and wave interaction, release aerosols from the sea into the atmosphere. Fatty acids in marine aerosols range from 1–21 ng m^{-3}; this is likely due to the presence of stearic, oleic and palmitic acid, which are the three main fatty acids reported in marine aerosols.[17] These fatty acids are represented in Figure 3.

Saturated fatty acids are commonly present at higher concentrations than unsaturated fatty acids.[34] Stearic acid was detected at 0.083 ng m^{-3} and 0.21 ng m^{-3} in studies on the Marshall Islands and North Pacific Ocean, respectively, whereas oleic acid was not detected on the Marshall Islands and was detected at much lower concentrations of 0.043 ng m^{-3} in the North Pacific Ocean.[34] Similar trends were reported for palmitoleic acid and its saturated analogue, palmitic acid.[4] This is most likely due to unsaturated fatty acids being readily oxidized within the atmosphere.

Mochida *et al.* approximate that 0.3–14 % of surface area of marine aerosols is comprised of C14–C19 saturated fatty acids.[35] Other primary biogenic sources for fatty acids include forest emissions from plants.[4]

As shown in this section, the ranges of reported fatty acid concentrations in atmospheric aerosols vary widely, accounting for the differences of aerosol composition due to the sites chosen as well as changes due to seasonal variations. This section established the abundance of fatty acids in the atmosphere—their ability to partition at the surface of water will be discussed in the following section and literature data will be reviewed.

1.7 Interfaces

An interface can be defined as the boundary between two regions with different matter or matter in different states. Examples of environmental interfaces include the surfaces of lakes, oceans and atmospheric aerosols.

1.7.1 Fatty Acid Film Formation on Atmospheric Aerosols

Fatty acids, with their hydrophilic headgroup and hydrophobic tail, are surface active, meaning they are able to partition at the air-water interface of the atmospheric aerosol. In 1999, Ellision *et al.*, who studied marine aerosols, suggested that the fatty acids encapsulating the aqueous core of the aerosol form an “inverted micelle” structure, as shown in Figure 4.[36] This process causes a change in the properties of the surface of the aerosol from being hydrophilic to hydrophobic. Gill *et al.* suggest that the film formation on the surface of the aerosol restricts particles from taking up radicals as well as stable molecules.[37,35]

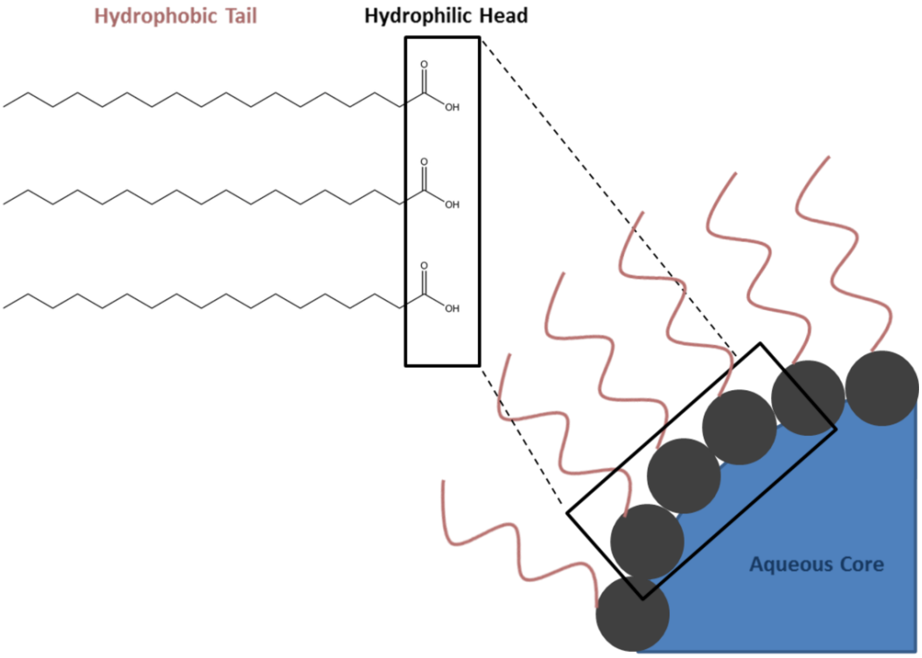

Figure 4: Model representation of a stearic acid film formation on an atmospheric aerosol.

1.7.2 Dynamics of Aerosol Surfaces

There is a difference in environment between the molecules on the surface and in the bulk of an atmospheric aerosol. This is due to molecules in the bulk experiencing equally attractive forces in all directions surrounding them, whereas surface molecules have a higher attraction towards the bulk than to the air. The net effect of this imbalance in attractive forces can be quantified as surface tension. Surface tension is generally defined as the energy needed to cause a unit increase in the interfacial area, at constant volume and temperature.[38] Polar liquids such as water have strong intermolecular interactions resulting in a high surface tension. The hydrophilic headgroup of the fatty acid dissolves in the water and stabilises the water’s surface by providing favourable interactions with the water molecules at the surface. Film formation of surfactants on atmospheric aerosols hence causes a reduction in the surface tension of the system.

An understanding of the film formation as well as the fate of these surface films in the atmosphere is important as they alter the hygroscopic and light-scattering properties of the aerosol.[36, 39] Films, consisting of a single monolayer of surfactants with a thickness of only a few nanometres, are able to lower the surface tension of the aerosol.[15] This lowering in surface tension can impact the cloud droplet formation ability of the aerosol.

Köhler theory describes the growth process of an aerosol by the uptake of water vapour above a relative humidity of 100 % (supersaturation), to form a cloud droplet.[40] The critical supersaturation of an aerosol is the minimum supersaturation required for the aerosol to act as a cloud condensation nucleus. This parameter is dependent on the composition of the aerosol. Köhler theory consists of two terms: the Kelvin term, accounting for the change in activation potential due to the surface tension and curvature of the droplet, and the Raoult term, describing the activation potential due to the solute concentration in the droplet. A higher solute concentration leads to an increase in activation potential. Furthermore, a lower surface tension, caused by the surfactants on the surface, and a larger aerosol size increase the activation potential.

When the theory was first developed, only inorganic aerosols were thought to act as cloud condensation nuclei. It has since been adapted to take the film formation of organic material that partitions to the interface into account:[15, 41]

$$\frac{P}{P_0} \cong 1 + \underbrace{\frac{2\gamma M_w}{kT\rho r}}_{\textbf{Kelvin Effect}} + \underbrace{\frac{3M_w\phi}{4\pi\rho}\left(\frac{\chi_{\mathrm{organic}}\ v_{\mathrm{organic}}\ m_{\mathrm{organic}}}{M_{\mathrm{organic}}} + \frac{v_{\mathrm{salt}}\ m_{\mathrm{salt}}}{M_{\mathrm{salt}}}\right)}_{\textbf{Raoult Effect}} \times \underbrace{\left(\frac{1}{r^3} - \frac{1}{r^3_{\mathrm{insoluble}}}\right)}_{\textbf{Insoluble Effect}} \qquad (10)$$

Here, P = vapour pressure of water over a droplet, P_0 = vapour pressure of water over a flat surface, γ = surface tension of solution; M_w = molecular weight of water; k = Boltzmann constant; T = temperature (Kelvin); ρ = solution density; Φ = solution osmotic coefficient, χ = degree of dissociation of any sparingly soluble species; v_{organic} = number of ions the organic acid dissociates into; m_{organic} = mass of organic material in solution; M_{organic} = molecular mass of organic material; v_{salt} = number of ions the salt dissociates into; m_{salt} = mass of salt in the droplet; M_{salt} = molecular mass of the salt; r = droplet radius and $r_{\mathrm{insoluble}}$ = radius of the volume of material that has not dissolved into the droplet.[15]

Studies suggest that the formation of a compressed surfactant film on the aerosol, causing a reduction in surface tension, leads to an increase in water uptake at high relative humidity. This surface tension depression causes the formation of larger droplets before the critical supersaturation is reached.[42] As the aerosol takes up water and grows, surfactant molecules on the surface move further apart from one another. At the critical supersaturation, an extended film exists, which no longer causes a surface tension depression—here, the surface tension is equal to that of water.[42] In 2005, Ervens *et al.* modelled surface tension effects of organic films on aerosol surfaces and reported an increase in activated cloud droplets with a lowering of surface tension.[43] This agrees with the recent study of Ovadenevaite *et al.*, who state that the changes in surface tension due to the growth process of the aerosols result in a reduction in the critical supersaturation, hence leading to an increase in cloud condensation nuclei.[44]

King *et al.* showed in 2009 that the ozonolysis of an oleic acid monolayer on a droplet with an initial diameter of 0.1 µm, assuming the formation of a nonanoic acid surface film, causes a decrease in the critical supersaturation relative to a particle without an organic surface layer.[15] This highlights the importance of a full understanding of changes to surface films due to reactions in the atmosphere, as this will ultimately affect the ability of the aerosol to become a cloud droplet. Köhler curves, illustrating the Köhler equation, which describe changes to the water uptake and activation potential of the aerosol by the partitioning of organic material to the surface of the aerosol, are shown in Figure 5.

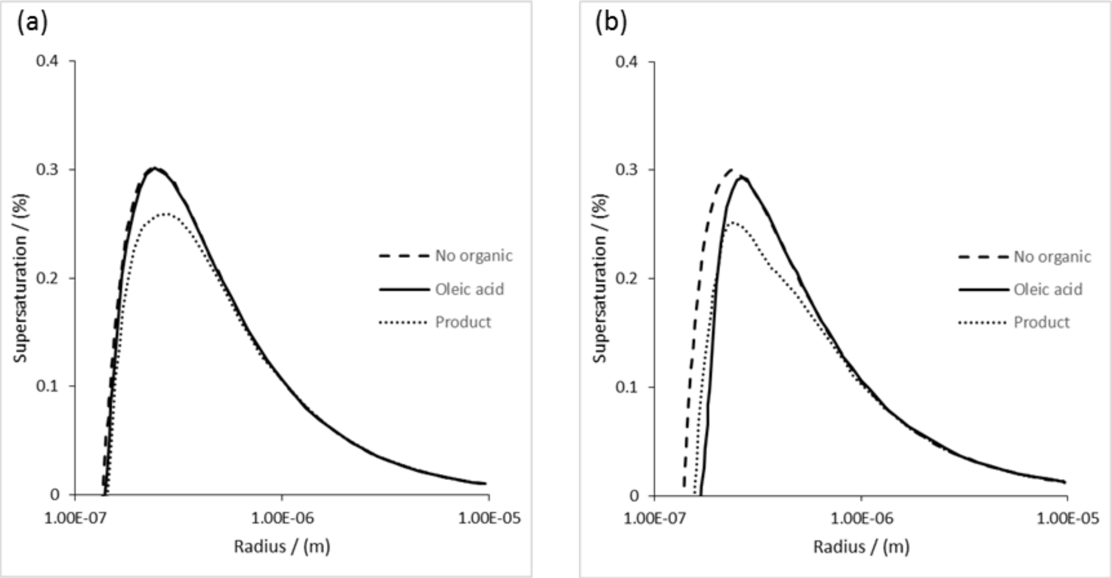

Figure 5: Köhler curves for three aerosols containing NaCl solution and no organic (dashed line), NaCl solution and oleic acid (solid line) and NaCl solution with azelaic acid (nonanedioic acid) and nonanoic acid (dotted line). An initial radius of 0.1 µm is assumed, with the aerosol containing 0.56 mol dm^3 [NaCl] and (a) an equivalent of one monolayer and (b) an equivalent of three monolayers of oleic acid. Graphs are adapted from King *et al.*[15]

As highlighted in this section, surfactant films can alter the aerosols' growth, lifetime and potential to act as cloud condensation nuclei, which ultimately affects the aerosols' impact on our climate. However, the effects of these films are still not well understood. More studies are needed to gain a better understanding of the film formation process and the fate of these organic films in the atmosphere, which will be further investigated in this report.

1.7.3 Atmospheric Implications

The Earth can be approximated as a black-body radiator, meaning it takes up and subsequently re-emits radiation. Solar radiation ($\lambda \geq 310$ nm) is taken up by the Earth's surface. The re-emitted outgoing infrared radiation is susceptible to being absorbed by greenhouse gases. This is important as it ensures that the average temperature on Earth remains high enough to support life. However, chemical changes in the atmosphere can greatly influence our climate. A significant increase in anthropogenic emissions, largely due to economic and population growth, has led to a rise in CO_2, CH_4, and N_2O levels, increasing the uptake of energy by our climate system, affecting global temperatures.[3] The latest Climate Change Synthesis Report by the Intergovernmental Panel on Climate Change (IPCC) states a total rise of 0.78 °C in global temperatures between the average temperature of the period 1850–1900 and the average temperature of the period 2003–2012.[3]

Both anthropogenic and natural emissions have the ability to alter the Earth's energy budget and hence are driving forces of climate change. To quantify these effects, the concept of radiative forcing is used, which accounts for changes to the Earth's energy budget, usually expressed in W m^{-2}. Processes with positive radiative forcing values account for an increase in surface temperatures, whereas negative radiative forcing values are indicative of processes causing a decrease in surface temperatures.

Natural forcings, caused by volcanic aerosols and changes in solar irradiance, cause an overall increase in surface temperatures. Volcanic aerosols that reach the stratosphere are able to influence temperatures even years after a major volcanic eruption.[3] However, in the wider context, natural forcings have a comparatively small effect on the overall radiative forcing budget, as highlighted in Figure 6.

The power per area for the total anthropogenic forcings (including well-mixed greenhouse gases and other anthropogenic forcings, such as short lived gases, aerosols and land use changes) has increased by 2.3 W m^{-2} in 2011 relative to 1750, as shown in Figure 6, accounting for the increase in surface temperatures.

The radiative forcing of greenhouse gases, which over the period 1750–2011 is estimated at approximately 2.8 W m^{-2}, results in an increase in surface temperatures.

What makes the study of atmospheric aerosols most relevant are their implications for climate change. The estimate of aerosol radiative forcing lies at -0.9 W m^{-2}. Hence, aerosols have a cooling effect associated with them, enabling them to counteract radiative forcing from greenhouse gases.

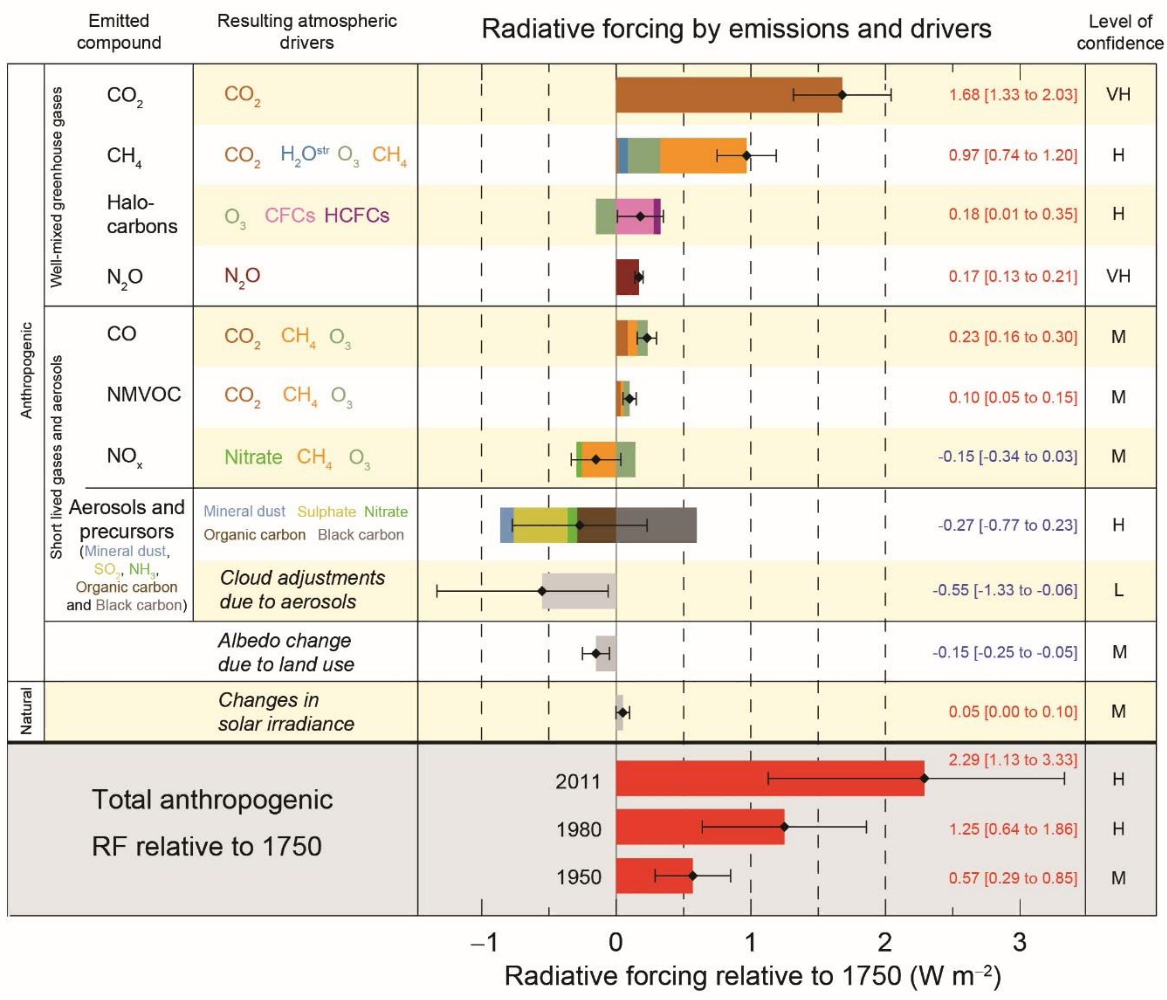

Figure 6: Estimates of radiative forcing in 2011 relative to 1750 for the main drivers of climate change. Black diamonds show the estimate of net radiative forcing with corresponding uncertainty intervals. Numerical values for each category are stated on the right hand side. Confidence levels in net forcing are stated (VH – very high, H – high, M – medium, L – low, VL – very low). Graphic reproduced from IPCC (2013).[45]

As stated in the latest IPCC report, even though estimates on radiative forcing from aerosols have improved, they remain the largest uncertainty in the total radiative forcing estimate to date.[3] Further research needs to be conducted on aerosols in order to reduce uncertainty regarding their radiative forcing contribution, allowing for more accurate climate change predictions.

As the background, purpose and importance of developing models of fatty acids at the air-water interface have been identified, the next part of this chapter will focus on the introduction to the molecular dynamics computer simulation method chosen.

1.8 Computational Modelling in Chemistry

Computational modelling is of growing importance in the chemical research community. As a powerful tool to study processes at the molecular level, it is often easier, quicker and cheaper than experimental studies. Further benefits include there being no significant health or environmental risk associated with computational modelling. Complementary to experiments, computational modelling can allow atomic level insight into experimental studies. Nevertheless, computational modelling is still largely dependent on experimental studies when it comes to the validation of the model, which is a key part of the modelling process.

A model, which is a simplified version of reality that allows calculations and predictions to be made, requires two key parts: a representation of the system and a set of rules governing the system. In chemistry, the two main types of models are based on quantum mechanics or on classical mechanics. Quantum mechanics is applied to small systems and takes into account the electronic structure. Classical mechanics on the other hand, which is used in this work, can be applied to much larger systems and ignores the electronic structure.

In classical mechanics the system is represented by balls connected by springs, governed by a set of rules. These rules are defined by Newton’s equations of motion, which we shall discuss in more detail later on. The representation of the system can either describe all atoms individually or group a number of atoms or molecules into a single interaction site (bead)—an approach described as coarse-grained modelling.

In molecular dynamics simulations, force fields provide a way of calculating the energy of the system as a function of the coordinates. Usually based on pairwise forces between the interaction sites, the molecular dynamics technique allows the time evolution of a system of interacting particles to be computed.[46] The molecular dynamics package GROMACS (GROningen MAchine for Chemical Simulation) was chosen to perform simulations within this project.[47] In molecular dynamics simulations, GROMACS does not have a force field of its own but is compatible with several force fields such as CHARMM[48], GROMOS[49], AMBER[50], OPLS[51] and MARTINI.[47] We shall discuss the general form of a force field in the following section which applies both to all-atom and coarse-grained models, with details of the models used in this work given in the sections thereafter.

1.9 Force Fields

The potential function gives the total potential energy of the system. Typically, it is a summation of several terms including intramolecular terms, such as bonds, angles, dihedrals and improper dihedrals as well as intermolecular terms including van der Waals and electrostatic interactions. An example of such a function for a force field is given by:[52]

$$V(\mathbf{r}_N) = E_{\text{bonds}} + E_{\text{angles}} + E_{\text{dihedrals}} + E_{\text{improper dihedrals}} + E_{\text{vdw}} + E_{\text{elec}} \qquad (11)$$

The function $V(\mathbf{r}_N)$ above defines the total potential energy of a system containing N interaction sites at positions $\mathbf{r}$. The energy terms in this function will be discussed in turn in the following sections, starting with the intramolecular terms. Terms will be described in reference to atoms; however, it should be noted that the same principles apply for coarse-grained beads.

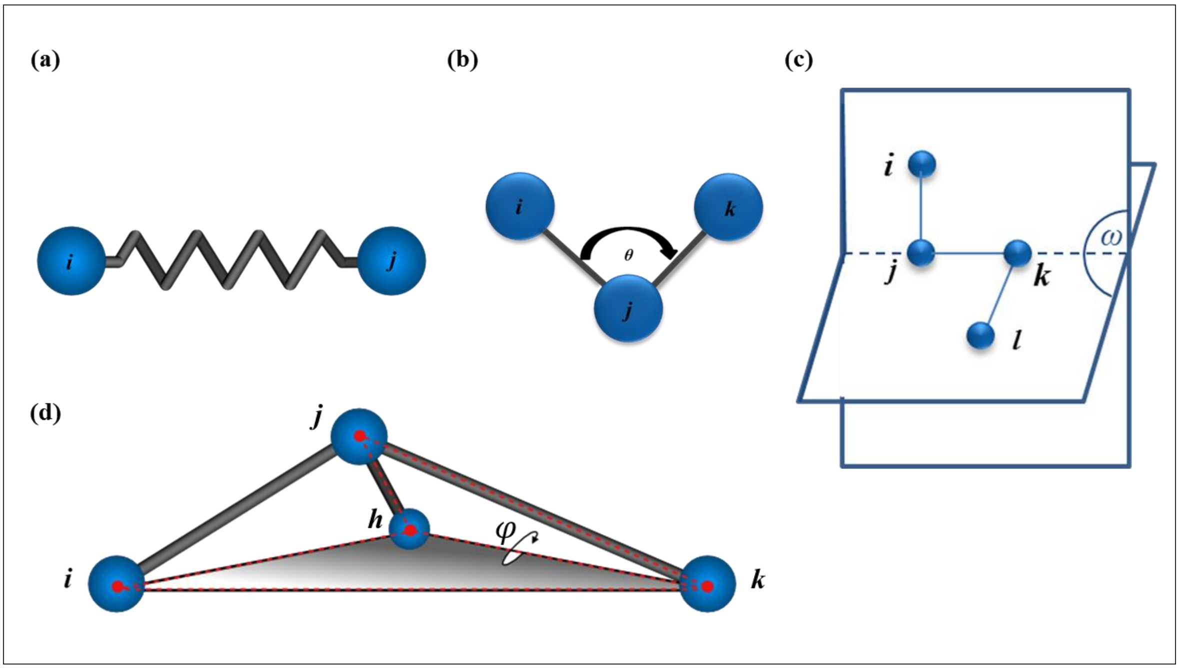

Figure 7: Intramolecular interactions in molecules:
(a) bonds, (b) angles, (c) dihedrals and (d) improper dihedrals.

Atoms are represented as a point mass, and hence the electronic structure is not taken into account. Bonds between atoms *i* and *j*, depicted in Figure 7 (a), are commonly connected by a harmonic spring, which has a force constant k_i. The first term in the potential energy function describing the energy of the bond can then be written as:[52]

$$E_{\text{bonds}} = \sum_{\text{bonds},i} k_i \ (l_i - l_{0,i})^2 \tag{12}$$

This specifies a harmonic potential. It shows that the deviation in the bond length l_i from the equilibrium bond length $l_{0,i}$ results in an increased energy. Hence, two parameters are needed to define the energy of a bond, which are the force constant k_i and the equilibrium bond length, $l_{0,i}$.

Bonds in reality are not harmonic. The potential energy associated with stretching a bond has a Morse potential shape. The harmonic approximation is a good approximation around the minimum. However, with a harmonic potential, stretching a bond causes an increase in energy—the potential energy does not level off, and hence it is impossible to break a bond. This is possibly the most significant restriction of a force field approach as it is not possible to study bond making or bond breaking processes.

Each bond has its own force constants and equilibrium bond length. Hence, to distinguish between different bonds, the concept of atom types is used. An atom type is a label for an atom corresponding to a certain environment. These are specific to each force field and will be discussed in detail later on in the chapter.

As represented in Figure 7 (b), the angle potential describes, with a harmonic potential, the potential energy of angle deformation between 3 atoms *i, j, k*. The energy term describing the angle potential can hence be written as:[52]

$$E_{\text{angles}} = \sum_{\text{angles},i} k_i \,(\theta_i - \theta_{0,i})^2 \tag{13}$$

Here, k_i represents the force constant for angle deformation, θ_i, the actual angle and $\theta_{0,i}$ is the equilibrium angle.

The third term in the potential energy function describes dihedral angles, also known as torsions. These dihedral angles are between 4 atoms that are connected. Hence, as represented in Figure 7 (c), if atoms *i, j* and *k* are in one plane and atoms *j, k* and *l* are in another plane, then a torsion angle can be defined between the two planes. The energy is typically represented by a periodic cosine potential. The energy of dihedrals gives the energy change that is produced by the rotation about a bond between four bonded atoms and can hence be written as:[52]

$$E_{\text{dihedrals}} = \sum_{\text{dihedrals},i} V_n[1 + \cos(n\omega - \gamma)] \tag{14}$$

In the equation above, V_n represents the force constant for the rotation; *n* is the multiplicity, which shows how many minima there are when the dihedral angle is rotated through 360°; ω is the actual dihedral angle and γ represents the phase angle, which is a phase difference expressed as an angle for a full cycle (360 degrees).

Within the CHARMM force field the potential can be described as a sum of cosine potentials, providing additional flexibility, as shown in Figure 8.

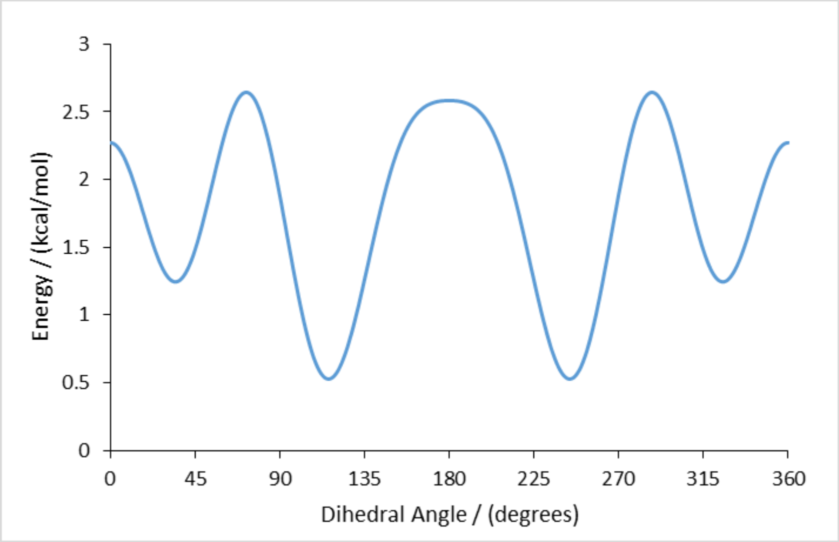

Figure 8: Variation in energy for a dihedral potential with four cosine terms.

The fourth term in the potential energy function describes improper dihedrals as illustrated in Figure 7 (d). Improper dihedrals are used to maintain the planarity or chirality between a central atom bonded to three other atoms.

$$E_{\text{impropers}} = \sum_{\text{impropers},i} k_{\text{imp}}\ (\varphi_i - \varphi_{0,i})^2 \tag{15}$$

Here, k_{imp} represents the improper dihedral angle force constant, φ_i, the actual angle, which corresponds to the deviation from planarity and $\varphi_{0,i}$ is the equilibrium angle.

The final part of the potential energy equation describes the non-bonded interactions, which are for interactions between non-bonded atoms, and commonly for all atoms *i* and *j* that have a minimum separation of 3 bonds between them (1–4 interactions). Interactions between atoms separated by fewer bonds (1–2 and 1–3 interactions) would, due to the small distance between the atom pairs, result in strongly repulsive or strongly attractive potentials and are hence excluded. Furthermore, these interactions are considered to be already correctly described by the intramolecular terms.

Coulomb potentials are used to describe electrostatic interactions.

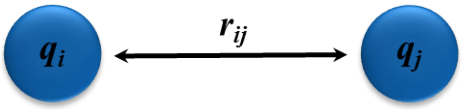

Figure 9: Coulomb interactions between charges, q_i and q_j, at a distance r_{ij}.

Hence, as can be seen in Figure 9, two particles with charges q_i and q_j at a distance r_{ij} have an energy of:[52]

$$E_{\text{elec}} = \frac{q_i q_j}{4\pi\epsilon_0\epsilon_r r_{ij}} \tag{16}$$

$4\pi\epsilon_0$ is a constant, which can be set to 1 when working in atomic units. The actual charges are parameters and depend on the atomic environment. ϵ_r is the dielectric constant, which is a measure of solvent polarity and accounts for the difference in behaviour between two ions in a solvent compared to a vacuum.

A Lennard-Jones potential is used to describe van der Waals interactions.[52]

$$E_{\text{vdw}} = 4\varepsilon_{ij}\left[\left(\frac{\sigma_{ij}}{r_{ij}}\right)^{12} - \left(\frac{\sigma_{ij}}{r_{ij}}\right)^{6}\right] \tag{17}$$

The long range attractive component in the Lennard-Jones 12–6 potential is represented by the r^{-6} term, and the short range repulsion by r^{-12}.

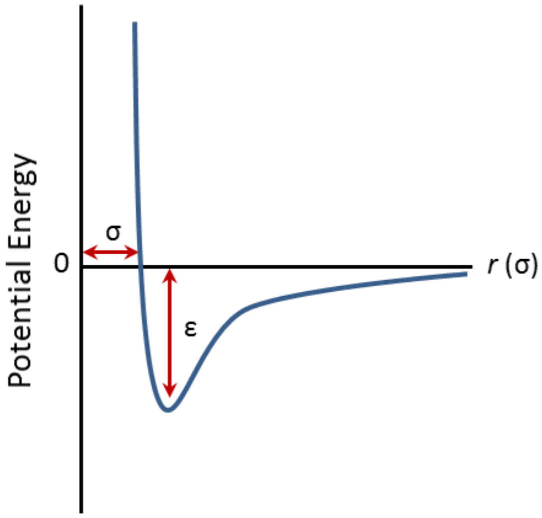

Figure 10: Lennard Jones Potential, adapted from A. R. Leach.[52]

The Lennard-Jones well-depth, ε_{ij}, represents the interaction strength and is defined by the maximum attractive interaction of the particles *i* and *j*. σ_{ij} is the collision diameter, which can be described as the distance at which the energy is equal to 0. σ has dimensions of distance and ε has dimensions of energy.

To generate pair parameters, the following combining rules are applied:

$$\varepsilon_{ij} = \sqrt{(\varepsilon_i \varepsilon_j)} \tag{18}$$

$$\sigma_{ij} = \frac{\sigma_i + \sigma_j}{2} \tag{19}$$

To calculate the total potential energy, the sum of all interactions for *N* atoms can be written as:[52]

$$\begin{aligned} V(\boldsymbol{r}_N) = & \sum_{\text{bonds}} k_i \, (l_i - l_{0,i})^2 + \sum_{\text{angles}} k_i \, (\theta_i - \theta_{0,i})^2 \\ & + \sum_{\text{dihedrals}} V_n [1 + \cos(n\omega - \gamma)] + \sum_{\text{impropers}} k_{\text{imp}} \, (\varphi_i - \varphi_{0,i})^2 \\ & + \sum_{i=1}^{N} \sum_{j=i+1}^{N} \left(4\varepsilon_{ij} \left[\left(\frac{\sigma_{ij}}{r_{ij}} \right)^{12} - \left(\frac{\sigma_{ij}}{r_{ij}} \right)^{6} \right] + \frac{q_i q_j}{4\pi\epsilon_0 \epsilon_r r_{ij}} \right) \end{aligned} \tag{20}$$

Computationally, this is a task of order N^2. Hence, the time to calculate the total potential energy of the system scales as N^2. In order to reduce computational time, non-bonded terms are often truncated.[52] For any atoms that are at a distance *r*, which is greater than a cut-off distance r_{cut}, the interaction energy will be set to 0; hence interactions beyond this point will not be considered. There are three ways to do so, including the use of truncation, shift cut-offs and switch cut-offs.[53] When using truncation, the total energy curve will follow its normal path until the energy will be set to 0 abruptly at the set cut-off distance. When a switch option is chosen the energy gets smoothly truncated over a set range of distances.[53] The shift cut-off on the other hand has an effect over a whole range of distances. These options are represented in Figure 11.

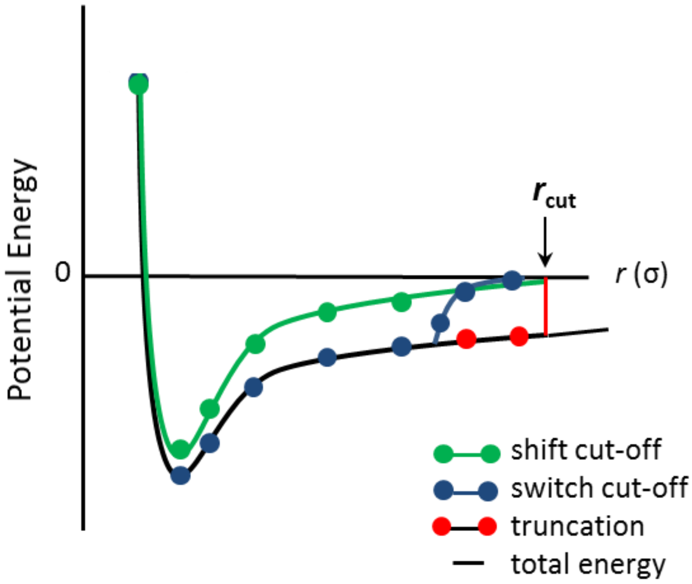

Figure 11: Truncations in the Lennard-Jones Potential.

1.10 All-Atom Models

The CHARMM (Chemistry at HARvard Molecular Mechanics) force field has been developed since the late 1960s and was implemented in GROMACS in 2009.[48] This project uses the CHARMM-36 force field with the GROMACS-5 simulation software. Within CHARMM-36 all atoms are taken into account.

The potential energy function in CHARMM has the form:[54]

$$\begin{aligned} V(\boldsymbol{r}_N) = \sum_{\text{bonds}} k_i\ (l_i - l_{0,i})^2 + \sum_{\text{UB}} k_{\text{UB}}\ (b_{1-3} - b_{0,1-3})^2 + \sum_{\text{angles}} k_i\,(\theta_i - \theta_{0,i})^2 \\ + \sum_{\text{torsions}} V_n[1 + \cos(n\omega - \gamma)] + \sum_{\text{impropers}} k_{\text{imp}}\ (\varphi_i - \varphi_{0,i})^2 \\ + \sum_{i=1}^{N} \sum_{j=i+1}^{N} \left(\varepsilon_{ij} \left[\left(\frac{\sigma_{ij}}{r_{ij}} \right)^{12} - \left(\frac{\sigma_{ij}}{r_{ij}} \right)^{6} \right] + \frac{q_i q_j}{\epsilon_1 r_{ij}} \right) \end{aligned} \tag{21}$$

As well as the terms previously described in section 1.9, the CHARMM force field has the Urey-Bradley angle term as an additional term. The Urey-Bradley angle term is a harmonic term that applies to atoms that are separated by two bonds (1–3 interactions). It is based on the distance between the two terminal atoms in an angle, where k_{UB} is the Urey-Bradley force constant, $b_{0,1-3}$ is the equilibrium distance between the two atoms, and b_{1-3} is the actual distance.

The atom types used in this project are shown in Figure 12, with atom types for molecules with aldehyde groups represented in (a) and atom types for the carboxylic acids represented in (b). The TIP3P model is used to represent water, which is a rigid water monomer with three interaction sites.[55]

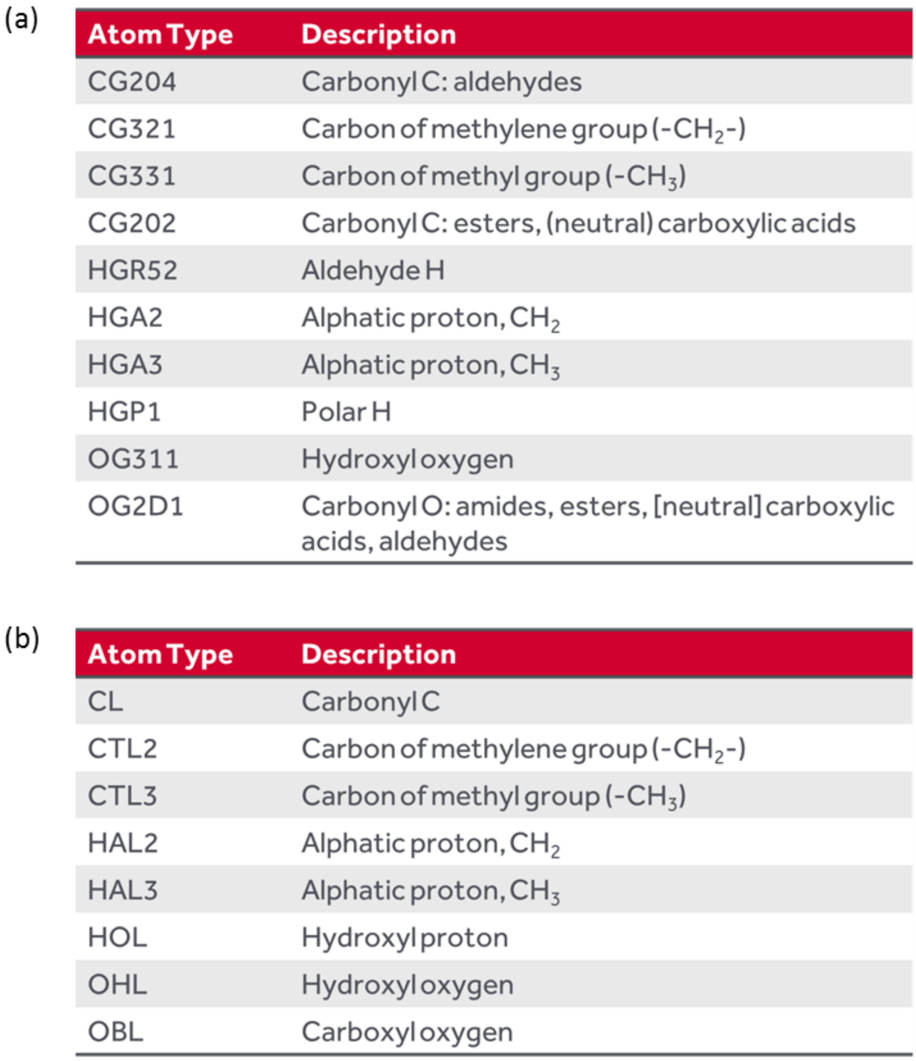

(a)

Atom Type	Description
CG204	Carbonyl C: aldehydes
CG321	Carbon of methylene group (-CH_2-)
CG331	Carbon of methyl group (-CH_3)
CG202	Carbonyl C: esters, (neutral) carboxylic acids
HGR52	Aldehyde H
HGA2	Alphatic proton, CH_2
HGA3	Alphatic proton, CH_3
HGP1	Polar H
OG311	Hydroxyl oxygen
OG2D1	Carbonyl O: amides, esters, [neutral] carboxylic acids, aldehydes

(b)

Atom Type	Description
CL	Carbonyl C
CTL2	Carbon of methylene group (-CH_2-)
CTL3	Carbon of methyl group (-CH_3)
HAL2	Alphatic proton, CH_2
HAL3	Alphatic proton, CH_3
HOL	Hydroxyl proton
OHL	Hydroxyl oxygen
OBL	Carboxyl oxygen

Figure 12: Atom types used in this project (a) atom types for aldehydes using the CHARMM-36 general force field[56] (b) atom types for fatty acids using the CHARMM-36 lipid force field.[57]

For each atomic centre, the electrostatic interactions are represented by partial point charges. Charges in each group must add up to 0. For example, in a CH_2 group the carbon has a charge of -0.18 and the two associated hydrogens have charges of +0.09, where for a CH_3 group the carbon has a charge of -0.27 with the three associated hydrogens having charges of +0.09.

CHARMM simulations in this work were used to gain structural insight into the lipid molecules in order to optimise the bonded interactions for a coarse-grained model. Hence, the next section of this report will give a general overview of the coarse-grained approach and will then focus on the Martini force field, which is used for coarse-grained simulations in this work.

1.11 Coarse-Grained Models

Coarse-grained models replace atomistic details by the use of lower resolution beads. Hence, complex systems are simplified by grouping atoms or whole molecules into single interaction sites.[58] In comparison to all-atom models, this enables simulation of larger scale molecular systems, overcoming the time as well as length scale limitations of all-atom models.[46] It has to be noted that the energy landscapes of coarse-grained particles are smoother than is the case for atomistic representations, hence dynamics are faster, resulting in the actual time sampled being 3–6 times longer than the set simulation time.[59] Simulation times reported in this project will state the set simulation time and not the actual time.

There are two common methods in developing coarse-grained force fields, which are bottom-up and top-down approaches. The bottom-up approach is structure based and uses reference atomistic simulations to determine bonded and non-bonded interactions.[46] Top-down approaches on the other hand are thermodynamics based. This means that the model is developed based on bulk experimental data of thermodynamic properties such as the free energies of hydration, vaporization and partitioning between water and organic phases.[46] In comparison, bottom-up approaches are better at representing the fine details of interaction, whereas top-down approaches are designed for a wider range of applications, without having to reparametrise the model for each molecule, making it easily transferable. For this project, the Martini force field was chosen, which was originally developed from all-atom simulations. However, the main validation is based on the calibration of the beads against experimental thermodynamic data—hence, using a top-down approach.[60] This force field will be explained in more detail in the next section.

1.11.1 The Martini Force Field

The Martini force field is a coarse-grained model for molecular simulations. The first version, published in 2004, was developed for lipid simulations and was then extended to include a protein and peptide version of the force field in 2007.[61,59] In the last 10 years, the applications of the Martini force field have increased dramatically, reflecting the flexibility and good transferability of the force field. Applications today that are of interest for this project include the self-assembly of surfactants as well as compression and expansion of monolayers.[62] The philosophy of the Martini model is not to capture every detail of an atomistic simulation; however, it was developed taking detailed atomistic models into account. An increased applicability and transferability is achieved in the developed model by using simple modular building blocks with only a few parameters and standard interaction potentials needed. It is a simple model—easy to use and allowing rapid computations, yet flexible enough to allow simulations of a variety of molecular systems.[62] The original model was developed for use with the GROMACS software.[59]

1.11.1.1 Mapping

The standard Martini model was chosen for this project. In this model, a 4-to-1 mapping is used, meaning that a single coarse-grained bead represents approximately 4 heavy atoms including their associated hydrogens.[61,59,62] The different beads are labelled according to the following system: polar sites (P), apolar sites (C), nonpolar sites (N) and charged sites (Q).[59] Polar sites are representative of hydrophilic neutral sites. Apolar sites are used for hydrophobic groups of atoms. Nonpolar sites are mixed groups of atoms, which are partly polar and partly apolar. Charged sites are associated with ionised groups. Only fully charged groups are included in this category. These four main categories are subdivided further to allow a more precise description of the physical properties of each interaction site. When choosing a subtype, a letter needs to be allocated to each bead that has the main category N or Q and a number to each bead in categories P and C. Letters indicate the hydrogen-bonding capabilities, where d stands for donor, a for acceptor, da is used when both are present and zero if neither is applicable.[59] Numbers on the other hand denote the degree of polarity. This is done on a scale from 1–5, where 1 indicates a low and 5 a high polarity.[59] There are 18 bead types in total. In this standard model, 4 water molecules are represented by one interaction site—a P4 bead. Examples of these categories are presented in Table 1 below.

Q			P		
subtype	building block	examples	subtype	building block	examples
da	H_3N^+-C_2-OH	ethanolamine	5	H_2N-C_2=O	acetamide
d	H_3N^+-C_3	1-propylamine	4	HOH (x 4)	water
	Na^+OH	sodium		HO-C_2-OH	ethanediol
a	PO_4^-	phosphate	3	HO-C_2=O	acetic acid
	Cl^-OH	chloride		C-NH-C=O	methylformamide
0	C_3N^+	choline	2	C_2-OH	ethanol
			1	C_3-OH	1-propanol
					2-propanol

N			C		
subtype	building block	examples	subtype	building block	examples
da	C_4-OH	1-butanol	5	C_3SH	1-propanethiol
d	H_2N-C_3	1-propylamine		C-S-C_2	methyl ethyl sulfide
a	C_3=O	2-propanone	4	C_2=C_2	2-butyne
	C-NO_2	nitormethane		C=C-C=C	1,3-butadiene
	C_3=N	proprionitrile		C-X_4	chloroform
	C-O-C=O	methylformate	3	C_2=C_2	2-butene
	C_2HC=O	propanal		C_3-X	1-chloropropane
0	C-O-C_2	methoxyethane	2	C_3	propane
			1	C_4	butane
					isopropane

Table 1: Examples of coarse-grained Martini bead types and bead mapping, adapted from Marrink *et al*.[59]

1.11.1.2 Bonded Interactions

Bonded interactions in the Martini force field are represented by a weak harmonic potential (see section 1.9).[59] The default value for the equilibrium bead-to-bead distance is $l_{0,l}$ = 0.47 nm with a default force constant of k_l = 1250 kJ mol^{-1} nm^{-2}. It has to be noted that the default values are not fixed values and can be adapted by the user.

To describe chain stiffness, angles are represented by a harmonic potential.[59] However, this is subtly different to the previous equation for the angle potential in section 1.9 as the Martini force field uses the cosine type to represent the harmonic potential.[59]

$$E_{\mathrm{angles}} = \sum_{\mathrm{angles},i} \frac{k_i}{2}\left[\cos(\theta_i) - \cos(\theta_{0,i})\right]^2 \tag{22}$$

Less energy is required for a deviation from the equilibrium angle than for an equivalent percentile change from the equilibrium bead-to-bead distance. This is reflected in the value of the force constant which is much lower for angles than for bonds. In aliphatic chains, the default force constant for angles is k_i = 25 kJ mol^{-1}. The default equilibrium bond angle in this case is $\theta_{0,i}$ = 180°.[59] Trans-unsaturated bonds are also modelled with a bond angle of $\theta_{0,i}$ = 180°; however, the force constant is changed to k_i = 45 kJ mol^{-1}.[59] In simulations of systems with cis-unsaturated bonds, the force constant is the same as for trans-unsaturated bonds. However, the equilibrium angle is reduced to $\theta_{0,i}$= 120°.[59] This will be needed to model the unsaturated double bond in oleic acid.

The potential energy for dihedral angles is determined as previously described in section 1.9. However, the primary use for dihedral potentials within the Martini force field is to impose secondary structure on peptide backbones and hence will not be discussed in further detail.[63]

1.11.1.3 Non-Bonded Interactions

A Lennard-Jones 12–6 potential that was described in section 1.9 is used to describe the non-bonded interactions in this force field.[59,62] The Lennard-Jones parameters in the Martini force field are as follows: the Lennard-Jones default collision diameter is set to σ = 0.47 nm. Values for the strength of interaction, ε_{ij}, vary from 2.0 kJ mol^{-1} representing interactions between polar and apolar groups to 5.6 kJ mol^{-1}, when strongly polar groups are present.[59] The interaction matrix for the Martini force field, represented in Table 2, is divided into 10 strength levels. This matrix will be used in this project to determine the interaction strength between beads in the simulated systems.

		Q				P					N				C				
	sub	da	d	a	0	5	4	3	2	1	da	d	a	0	5	4	3	2	1
Q	da	O	O	O	II	O	O	O	I	I	I	I	I	IV	V	VI	VII	IX	IX
	d	O	I	O	II	O	O	O	I	I	I	III	I	IV	V	VI	VII	IX	IX
	a	O	O	I	II	O	O	O	I	I	I	I	III	IV	V	VI	VII	IX	IX
	0	II	II	II	IV	I	O	I	II	III	III	III	III	IV	V	VI	VII	IX	IX
P	5	O	O	O	I	O	O	O	O	O	I	I	I	IV	V	VI	VI	VII	VIII
	4	O	O	O	O	O	I	I	II	II	III	III	III	IV	V	VI	VI	VII	VIII
	3	O	O	O	I	O	I	I	II	II	II	II	II	IV	IV	V	V	VI	VII
	2	I	I	I	II	O	II	II	II	II	II	II	II	III	IV	IV	V	VI	VII
	1	I	I	I	III	O	II	II	II	II	II	II	II	III	IV	IV	IV	V	VI
N	da	I	I	I	III	I	III	II	II	II	II	II	II	IV	IV	V	VI	VI	VI
	d	I	III	I	III	I	III	II	II	II	II	III	II	IV	IV	V	VI	VI	VI
	a	I	I	III	III	I	III	II	II	II	II	II	III	IV	IV	V	VI	VI	VI
	0	IV	IV	IV	IV	IV	IV	IV	III	III	IV	IV	IV	IV	IV	IV	IV	V	VI
C	5	V	V	V	V	V	V	IV	IV	IV	IV	IV	IV	IV	IV	IV	IV	V	V
	4	VI	VI	VI	VI	VI	VI	V	IV	IV	V	V	V	IV	IV	IV	IV	V	V
	3	VII	VII	VII	VII	VI	VI	V	V	IV	VI	VI	VI	IV	IV	IV	IV	IV	IV
	2	IX	IX	IX	IX	VII	VII	VI	VI	V	VI	VI	VI	V	V	V	IV	IV	IV
	1	IX	IX	IX	IX	VIII	VIII	VII	VII	VI	VI	VI	VI	VI	V	V	IV	IV	IV

Table 2: Default interaction matrix for non-bonded interactions between beads, adapted from Marrink *et al.*[59] Interaction levels; O = 5.6 kJ mol^{-1} (supra attractive). I = 5.0 kJ mol^{-1} (attractive). II = 4.5 kJ mol^{-1} (almost attractive). III = 4.0 kJ mol^{-1} (semi attractive). IV = 3.5 kJ mol^{-1} (intermediate). V = 3.1 kJ mol^{-1} (almost intermediate). VI = 2.7 kJ mol^{-1} (semi repulsive). VII = 2.3 kJ mol^{-1} (almost repulsive). VIII = 2.0 kJ mol^{-1} (repulsive). IX = 2.0 kJ mol^{-1} (super repulsive).

In this project, switch cut-offs are used for van der Waals interactions, as described in section 1.9. A switch is applied in the range of 0.9 nm to $r_{\mathrm{cut}} = 1.2$ nm for the Lennard-Jones potential.[59]

Charged beads of type Q have a full charge q_i associated with them. These interact with a Coulombic potential energy function as shown previously in section 1.9, equation (16).[59] A shift cut-off is used in this case between 0–1.2 nm. The relative dielectric constant $\varepsilon_r = 15$.[59]

On its own, the use of cut-offs is not very efficient in reducing the time to compute the non-bonded interactions as this would result in the need to calculate all distances between all pairs of beads in the system in order to find out if they are in the cut-off range, and hence if their interaction energy needs to be calculated. The calculations of all the distances is computationally expensive.[52] It is known that the beads' neighbours do not change significantly over 10–20 molecular dynamics steps.[52, 59] Hence, to solve the problem of having to calculate all distances between beads in the system, neighbour lists can be used that store all beads within a certain range. The neighbour list cut-off is set to 1.4 nm, which is the default Martini distance.[59] This distance is slightly larger than the cut-off distance for non-bonded interactions which is set to 1.2 nm, hence the neighbour list includes all beads in the non-bonded cut-off range as well as the ones that are in close proximity, which results in an improvement in the energy conservation. The neighbour list is updated every 10 steps during each simulation in this project, which is the recommended value in the Martini force field.

1.12 Periodic Boundary Conditions

In order to simulate a system of *N*-beads, an initial configuration has to be determined. To do so beads are placed into a box. Several box shapes can be applied, including a cube, rectangular or hexagonal prism. [52] In this project, a rectangular box will be used.
The problem with simulating a relatively small number of particles in a box is that this causes unphysical boundaries of the system and the surrounding vacuum. To avoid this, periodic boundary conditions can be applied to the box.[52]

As can be seen in Figure 13, the use of these periodic boundaries results in the box being surrounded by translated copies of itself.[53] For clarity, this is shown in two dimensions; however it has to be noted that in calculations the box is surrounded in three dimensions by translated copies. Hence, the molecules simulated experience forces as if they were in an infinitely large system.

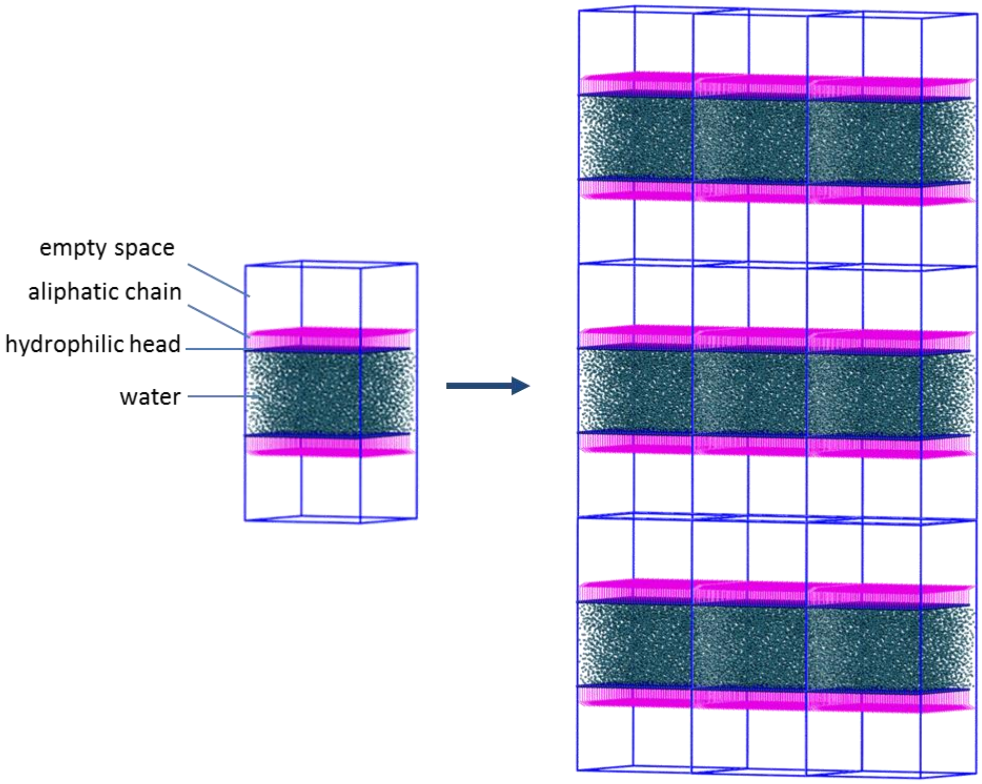

Figure 13: Schematic representation of periodic boundary conditions in two dimensions. The primary box is surrounded by replicas of itself.

After the application of periodic boundary conditions, the concept of a minimum image is used, which means that only interactions with the nearest image are computed. A spherical truncation, as previously discussed in section 1.9, is employed. As shown in Figure 14, this means that only interactions between sites that are separated by a distance smaller than the cut-off distance are calculated. The cut-off distance cannot be greater than half the box length. This is to avoid the interaction of a particle and more than one image.

Due to the periodic boundary conditions, molecules that move out of the box on one side, as indicated by the arrows in Figure 14, will reappear on the other side of the box. This means that the number of molecules within the box remains constant throughout the simulation.

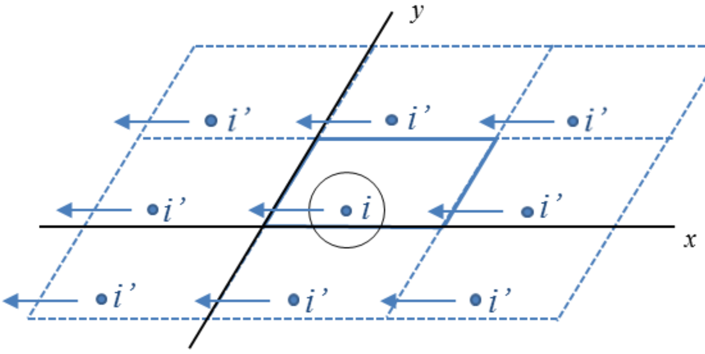

Figure 14: Top view representation of periodic boundary conditions in two dimensions, adapted from the GROMACS user manual.[53] As shown for the reference molecule *i,* interactions are only calculated for molecules within the cut-off distance, indicated by the circle. Arrows indicate the movement of molecules.

1.13 Energy Minimisation

The potential energy function of a molecular system is generally a complex surface. The deepest point on the potential energy surface is known as the global minimum.[52, 53] A large number of local minima may also be present on this surface. At a minimum, the first derivative of the energy function is zero with respect to the coordinates and all second derivatives are positive.[53] When a starting configuration is provided, most energy minimisation algorithms go downhill on the energy surface in order to find the nearest local minimum. In this work, the energy minimisations performed make use of the steepest descent algorithm. For any point on the surface, it calculates the gradient and moves it one step downhill in the direction of the largest gradient.[53] This gradually moves the bead positions, where the starting points for each step are the bead coordinates obtained in the previous step.

Performing an energy minimisation ensures a relaxed structure, avoiding steric clashes and inappropriate geometries. Hence, in this project, before the start of each molecular dynamics simulation an energy minimisation will be performed in order to avoid unphysical interactions.

1.14 Molecular Dynamics Computer Simulations

Taking the negative derivative of the potential function $V(\boldsymbol{r}_N)$ allows the determination of the force on each atom.[53]

$$F_i = -\frac{\partial V}{\partial r_i} \tag{23}$$

Newton’s second law, also known as the equation of motion, which states that force is equal to mass times acceleration, is solved within molecular dynamics simulations for each of the atoms in the system.[53]

$$m_i \frac{\partial^2 r_i}{\partial t^2} = F_i , i = 1 \ldots N \tag{24}$$

The calculation of the force with Newton’s equation of motion leads to the determination of the new coordinates of the atoms a short time later. Small time steps are adopted to solve these equations simultaneously. For example, integration time steps for simulations with the Martini force field should be between 20 fs and 40 fs, which is the range of time steps that was used for the parameterisation of the Martini force field. [59]

There are several methods that allow the numerical integration of the equations of motion. In this project the leap-frog algorithm is used, which is the default algorithm of GROMACS. This algorithm makes use of equations (25) and (26) to determine positions and velocities.[52]

$$\mathbf{r}(t + \delta t) = \mathbf{r}(t) + \delta t \mathbf{v}\left(t + \frac{1}{2}\delta t\right) \tag{25}$$

$$\mathbf{v}\left(t + \frac{1}{2}\delta t\right) = \mathbf{v}\left(t - \frac{1}{2}\delta t\right) + \delta t \mathbf{a}(t) \tag{26}$$

In the equations above, **v** is the velocity; **a** is the acceleration, which is the second derivative of the positions with respect to time and **r** is the atomic position. As can be seen in equation (26), velocities are calculated every half time step and acceleration at every full time step. Hence, the velocities leap over the positions to give their new values and vice versa.

The general molecular dynamics scheme applies 4 steps, where steps 2–4 are repeated for the set number of time steps.[53] The scheme includes the following steps:

1. The initial coordinates of all atoms and their velocities need to be determined. These, in addition to the run parameters and force field parameters, are used as inputs.
2. Forces on each atom in the system are calculated.
3. New positions of the atoms in the system are calculated.
4. The data is recorded at the desired time interval (e.g. every 30 ps).

Initial velocities can be generated by the program at a given temperature with a Maxwell-Boltzmann velocity distribution, using a random number seed:[53]

$$p(v_i) = \sqrt{\frac{m_i}{2\pi kT}} \exp\left(-\frac{m_i v_i^2}{2kT}\right) \tag{27}$$

Where v_i is the initial velocity, $p(v_i)$ is the probability that an atom has an initial velocity of v_i, k is the Boltzmann constant, T is the temperature, m_i is the mass of the atom.

Changing the random number seed results in different initial velocities. Therefore, different simulations can be performed from the same starting structure. This means that by running simulations with the same starting structure but different random number seed the 95 % confidence interval can be determined for each simulation set.

Temperatures as well as pressures can be kept constant in the system. There are several different temperature and pressure coupling schemes implemented in GROMACS. Details of the coupling schemes used in this project are described in the following.

In order to maintain temperatures, the Berendsen temperature coupling is used for coarse-grained simulations in this project.[53] This is the common temperature coupling scheme used in Martini simulations.[64] It is a weak-coupling algorithm with an external 'heat bath' being used at a given temperature T_0. Deviations from temperature T_0 within the system will be corrected by transferring energy between the bath and the system, using the following equation:[53]

$$\frac{\mathrm{d}T}{\mathrm{d}t} = \frac{T_0 - T}{\tau} \tag{28}$$

T_0 is the given temperature; T is the actual temperature and τ is a time constant.

A problem with the Berendsen thermostat is that one species may be heated disproportionately with respect to the others. To avoid this problem, the temperature of individual groups is coupled separately.[53]

Temperatures in the all-atom simulations in this project are kept constant using the velocity-rescaling temperature coupling, which is a modified Berendsen thermostat.[53]

The Berendsen barostat is the pressure coupling algorithm used for coarse-grained simulations in this project. This is the common pressure coupling scheme used in Martini simulations.[64] It allows pressures to be controlled in a similar fashion as the temperature control described previously, this time using a ‘pressure bath’.[53]

By adjusting the dimensions of the simulation box during the simulation time, the system is maintained at a chosen pressure. The coordinates and box vectors are scaled every n_{PC} steps, using a scaling matrix μ. The pressure, P, is adjusted towards the reference pressure P_0, where τ_p is a time constant:[53, 65]

$$\frac{\mathrm{d}P}{\mathrm{d}t} = \frac{P_0 - P}{\tau_p} \tag{29}$$

The scaling matrix, μ, is determined according to:[53, 65]

$$\mu_{ij} = 1 - \frac{n_{PC}\delta t}{3\tau_p}\beta_{ij}[P_{0ij} - P_{ij}(t)] \tag{30}$$

β is a diagonal matrix, which is the isothermal compressibility of the system and does not affect the average pressure of the system. Hence, it is sufficient to estimate the value of β.

All-atom simulations in this project use Parrinello-Rahmen pressure coupling, where the box vectors follow their own equation of motion, with vectors being able to change over time.[53]

In the pressure settings, the coupling constant and compressibilities need to be determined for the system. These will be specified for each simulation in this project separately.

Two different methods that were applied in this project to run simulations are:

1. NPT Ensemble

In this ensemble number of particles, pressure and temperature are kept constant. Semi-isotropic pressure coupling is used, which means that the *z*-direction of the box can be scaled independently from the isotropically scaled *x*/*y*-directions, hence making this the ideal coupling method for systems with interfaces. Furthermore, components of the compressibility can be set to 0 in order to allow scaling in only *x*/*y* or *z*.[53]

2. NVT Ensemble

Simulations were performed in the NVT ensemble, also known as the canonical ensemble. This ensemble describes a system where number of particles, volume and temperature are kept constant during the simulation.[53]

1.15 Molecular Dynamics Simulations of Lipid Monolayers

Several simulations on lipid monolayers (all-atom and coarse-grained) have been reported in the literature, with applications in various fields including biology and atmospheric chemistry.[33, 66-80] Many studies focus on dipalmitoylphosphatidylcholine (DPPC) monolayers, which are of interest when studying lung surfactants.[66-69, 72, 73, 76, 78-80] As this is a well-studied system, reported simulations in the literature on pressure-area isotherms of this compound will be used as a basis for the chosen simulation method in this thesis.

Simulations reported in the literature have allowed molecular level insight into several processes—work that is of relevance for this thesis includes the study of the phase behaviour of monolayers under compression/decompression,[66, 68, 76, 78] monolayer collapse at high surface pressures,[69] and the incorporation of various molecules into a monolayer.[33, 76, 77, 80] To date, most simulations focus on single component surface layers—Habartová *et al.* note that simulations of multicomponent monolayers are still scarce.[33] This thesis will use pressure-area isotherms from single component monolayers as a basis for comparison between simulations and experimental data, with further details given in the following section, and then move on to study mixed multicomponent monolayers of atmospheric relevance.

1.16 Pressure-Area Isotherms

As previously mentioned, an important step in the development of a computational model is the validation of the simulated data by comparison to experimental data. Measuring the surface pressure of a surfactant monolayer with respect to the surface area of water available per molecule is the most useful experimental tool for determining properties of a monolayer. Hence, pressure-area isotherms for several compounds will be simulated in this work and compared to experimental isotherms reported in the literature, allowing the validation of the developed model.

The majority of experimental isotherms are produced using a Langmuir trough filled with water. The surfactant, dissolved in hexane or methanol, is spread on the water surface where the organic solvent evaporates. The isotherm is then generated by compressing the monolayer with movable barriers, recording the surface area and resulting surface pressure throughout the process.[81-83]

A further method described in the literature involves spreading the monolayer on an aqueous pendant drop, created at the tip of a stainless steel capillary.[84] The use of a surface tensiometer allows the surface tension and the droplet volume, from which its surface area is derived, to be determined. In this method, the area per molecule can be altered by withdrawing or adding water to the droplet using an automated micro syringe, allowing calculation of both the area per molecule and surface pressure.

The possible phase behaviour of a fatty acid monolayer at the air-water interface under compression is illustrated on the left hand side in Figure 15. At (A), molecules are far apart from one another; they do not interact with each other and hence behave as a two-dimensional gas. Under compression, with a decrease in water surface area available per molecule, molecules move closer together and start to interact with one another (B)—here the monolayer is in a liquid-expanded phase. This results in a decrease in the surface tension of the system and in an increase in the surface pressure. The molecules might order and orient under compression, resulting in the formation of a liquid-condensed phase, as illustrated in Figure 15 (C). Once the equilibrium spreading pressure is reached, (D), molecules cannot move any closer together. This results in a breakdown of the system, with materials being lost from the surface, forming three-dimensional structures such as micelles—this is known as the film collapse region (E).

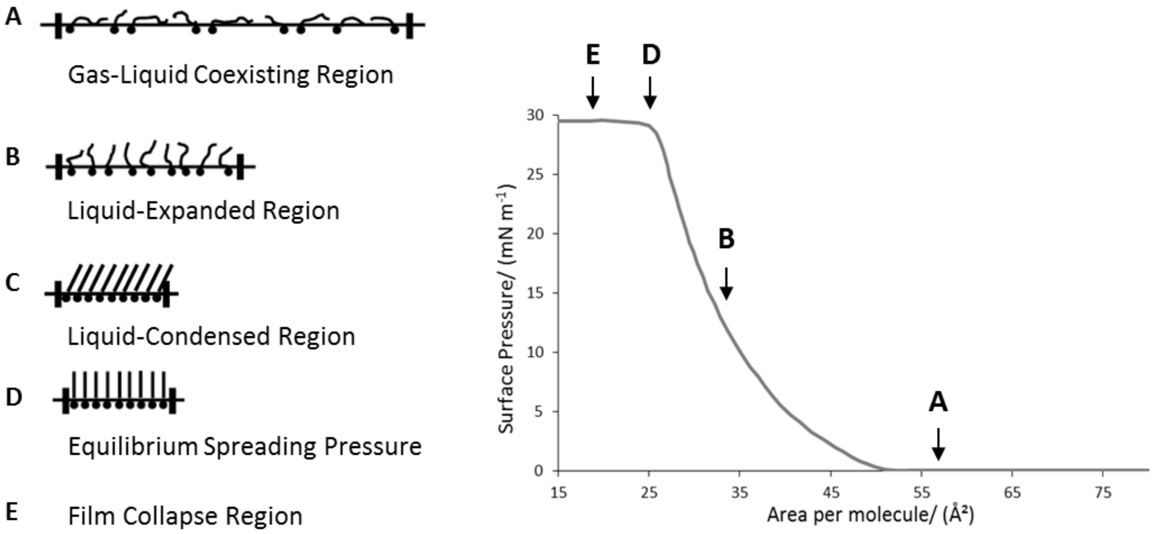

Figure 15: Possible phase behaviour of a fatty acid monolayer at the air-water interface under compression. Pressure-area isotherm of an oleic acid monolayer at the air-water interface, adapted from Voss et al., with phase behaviour indicated.[81]

Each surfactant has a distinct pressure-area profile and hence is a good basis for the validation of the model developed in this work. An experimental isotherm from the literature for a monolayer of oleic acid at the air-water interface is illustrated in Figure 15, with the phase behaviour indicated. Oleic acid does not form a liquid-condensed phase with molecules staying disordered throughout. In a similar way to the isotherm shown in Figure 15, the phase behaviour of the monolayers simulated in this work will be indicated for each pressure-area isotherm.

In order to produce a pressure-area isotherm from simulations, the surface tension of the monolayer at the vacuum-water interface needs to be determined. The surface tension, γ_m, in the monolayers is obtained from the production run for each of the generated starting structures. The surface tension of the monolayer, γ_m, at a certain area per fatty acid, $A_{\text{fatty acid}}$, can be calculated from the difference of the normal pressure, P_N, and lateral pressure, P_L, in the box, where L_z is the box length in the *z*-direction. P_L is determined by taking the mean of the pressures in the *x* and *y* directions, P_{xx} and P_{yy}.[68]

$$P_L = \frac{(P_{xx} + P_{yy})}{2} \tag{31}$$

$$\gamma_m(A_{\text{fatty acid}}) = (P_N - P_L) \times \frac{L_z}{2} \tag{32}$$

Equations (31) and (32) need to be solved for monolayers of several dimensions, each using a specific area of water surface available per molecule, which is calculated by multiplying the *x* box length by the *y* box length, divided by the number of molecules in the monolayer. This results in a point on the tension-area isotherm. Once the tension-area isotherm is obtained, this can be used to calculate points on the pressure-area isotherm by applying equation (33).[68]

$$\Pi\big(A_{\text{fatty acid}}\big) = \gamma_{vw} - \gamma_m(A_{\text{fatty acid}}) \tag{33}$$

$\Pi\big(A_{\text{fatty acid}}\big)$ is the surface pressure at a certain area per molecule, γ_{vw} is the surface tension of the vacuum-water interface and $\gamma_m(A_{\text{fatty acid}})$ is the previously determined point from the tension area isotherm.

Coarse-grained models typically underestimate the surface tension of the vacuum-water interface in comparison to experimental data.[59] This is due to the limited fluid range resulting from the use of a Lennard-Jones 12–6 potential.[59] This results in the coarse-grained condensed phase being less stable than it should be. Calculated interfacial tensions for the vacuum-water interface lie at 45 mN m^{-1} for small systems (400 coarse-grained water beads) and at 30 mN m^{-1} for large systems (1600 coarse-grained water beads).[59] In comparison, the interfacial tension for the air-water interface from experiments is 73 mN m^{-1}.[59] To account and compensate for this difference, Baoukina *et al.* introduce the adjustable parameter $\gamma_{vw}*$, the effective surface tension of the vacuum-water interface.[68] $\gamma_{vw}*$, which applies for the whole isotherm, enables the comparison of experimental and simulated pressure-area isotherms.

The point on the pressure-area isotherm from simulations in this work is therefore calculated by:[68]

$$\Pi^{corr}\left(A_{\text{fatty acid}}\right) = \gamma_{vw^*} - \gamma_m(A_{\text{fatty acid}}) \tag{34}$$

Baoukina *et al.* use different effective surface tensions depending on the system size. They apply a correction factor of 47 mN m^{-1} to a small system, containing 128 DPPC molecules, and 55 mN m^{-1} to a large system, containing 8192 DPPC molecules.[68] DPPC shows a liquid-expanded liquid-condensed coexisting region at 310 K, forming a constant-pressure plateau in the isotherm. Boukina *et al.* obtained their effective surface tension by fitting the pressure-plateau of their simulated isotherm to the one of the experimental isotherms.[68] Details about the effective surface tension used for simulations in this work will be specified for each isotherm separately.

In the review article by Marrink and Tieleman, the authors state that good agreement between the Martini force field and experimental data can be obtained with the standard Martini water model when it comes to the study of properties of lipid monolayers in the liquid phases.[62] Furthermore, the model is suitable to study the collapse of monolayers at high surface pressures. However, difficulties are reported when it comes to the reproducibility of the pressure-area isotherm in the low surface pressure region (liquid expanded—gas coexisting region).[62, 79] Here, an artificial stabilisation of pores that form within the monolayer is reported, which is caused by the surface tension of the vacuum-water interface in the standard Martini water model being too low.[79, 80] Miguel *et al.* recently achieved improvements to the pressure-area isotherm of three lipids in the low surface pressure region by using and modifying the Big Multi-pole Water model (BMW-Martini force field) and by optimising the lipid geometries.[85] Work carried out in this thesis, however, will use with the standard Martini water model as a basis, as previous simulations show that pressure-area isotherms produced in this way give a good approximation of the equilibrium spreading pressure, which will be used as a basis for comparison.

Duncan *et al.* compare experimental and simulated pressure-area isotherms of DPPC monolayers with the standard Martini water model and note that these are in rough agreement.[66] A steeper slope of the isotherm in comparison to experimental data is reported.[66] This might be due to the finite size effect, where the use of periodic boundary conditions enhance the symmetry of the simulation system and prevent undulations.[66]

However, in general there are usually larger variations reported between experimental isotherms than between simulated isotherms—this may be due to the experimental setup. Leakage, resulting in the loss of material from the surface, and a possible disorder of molecules near the walls of the Langmuir trough can affect the calculated area per molecule and hence result in shifts of the pressure-area isotherm.[66]

With the reported variations in pressure-area isotherms, the most significant part of the isotherm, which will be used in this thesis as a point of comparison, is the monolayer's equilibrium spreading pressure and the observed phase behaviour of the monolayer. These features show good agreement between reported experimental and simulated pressure-area isotherms, and hence are a good basis for comparison.

1.17 References

1. U. Pöschl, *Angew. Chem. Int. Ed,*, 2005, **44**, 7520-7540.
2. Z. Li, F. Niu, J. Fan, Y. Liu, D. Rosenfeld and Y. Ding, *Nature Geosci*, 2011, **4**, 888-894.
3. IPCC, 2014: *Climate Change 2014: Synthesis Report. Contribution of Working Groups I, II and III to the Fifth Assessment Report of the Intergovernmental Panel on Climate Change* [Core Writing Team, R.K. Pachauri and L.A. Meyer (eds.)]. IPCC, Geneva, Switzerland, 151 pp., Geneva.
4. J. Zahardis and G. A. Petrucci, *Atmos. Chem. Phys.*, 2007, **7**, 1237-1274.
5. R. A. Bailey, H. M. Clark, J. P. Ferris, S. Krause and R. L. Strong, *Chemistry of the Environment*, eds. R. A. Bailey, H. M. Clark, J. P. Ferris, S. Krause and R. L. Strong, Academic Press, San Diego, 2002, pp. 1-835.
6. S. Solomon, K. H. Rosenlof, R. W. Portmann, J. S. Daniel, S. M. Davis, T. J. Sanford and G.-K. Plattner, *Science*, 2010, **327**, 1219-1223.
7. A. D. Del Genio, *Encyclopedia of Planetary Science*, Springer Netherlands, Dordrecht, 1997, pp. 841-842.
8. R. T. Watson, M. A. Geller, R. S. Stolarski and R. F. Hampson, *NASA Reference Publication 1162* 1986, 20.
9. R. Atkinson and J. Arey, *Atmos. Environ.*, 2003, **37**, 197-219.
10. R. M. Velasco, F. J. Uribe and E. Pérez-Chavela, *J. Math. Chem.*, 2008, **44**, 529-539.
11. W. J. Collins, R. G. Derwent, B. Garnier, C. E. Johnson, M. G. Sanderson and D. S. Stevenson, *J. Geophys. Res. Atmos.*, 2003, **108**.
12. W. R. Stockwell, C. V. Lawson, E. Saunders and W. S. Goliff, *Atmosphere*, 2011, **3**, 1-32.
13. T. Hoffmann, J. R. Odum, F. Bowman, D. Collins, D. Klockow, R. C. Flagan and J. H. Seinfeld, *J. Atmos. Chem.*, 1997, **26**, 189-222.
14. R. Vingarzan, *Atmos. Environ.*, 2004, **38**, 3431-3442.
15. M. D. King, A. R. Rennie, K. C. Thompson, F. N. Fisher, C. C. Dong, R. K. Thomas, C. Pfrang and A. V. Hughes, *Phys. Chem. Chem. Phys.*, 2009, **11**, 7699-7707.
16. U. Baltensperger and S. Nyeki, *Physical and Chemical Properties of Aerosols*, ed. I. Colbeck, Blackie Academic & Professional, London, 1998, 7, pp. 280-329.
17. T. Hoffmann and J. Warnke, *Volatile Organic Compounds in the Atmosphere*, ed. R. Koppmann, Blackwell Publishing Ltd., Oxford, 2007, 9, pp. 342-388.
18. World Health Organization, (2013), *Health effects of particulate matter*, http://www.euro.who.int/__data/assets/pdf_file/0006/189051/Health-effects-of-particulate-matter-final-Eng.pdf, [June 2017]

19. O. Vesna, S. Sjogren, E. Weingartner, V. Samburova, M. Kalberer, H. W. Gäggeler and M. Ammann, *Atmos. Chem. Phys.*, 2008, **8**, 4683-4690.
20. R. Ots, M. Vieno, J. D. Allan, S. Reis, E. Nemitz, D. E. Young, H. Coe, C. Di Marco, A. Detournay, I. A. Mackenzie, D. C. Green and M. R. Heal, *Atmos. Chem. Phys.*, 2016, **16**, 13773-13789.
21. W. F. Rogge, L. M. Hildemann, M. A. Mazurek, G. R. Cass and B. R. T. Simoneit, *Environ. Sci. Technol.*, 1991, **25**, 1112-1125.
22. J. Feng, M. Hu, C. K. Chan, P. S. Lau, M. Fang, L. He and X. Tang, *Atmos. Environ.*, 2006, **40**, 3983-3994.
23. Z. G. Guo, L. F. Sheng, J. L. Feng and M. Fang, *Atmos. Environ.*, 2003, **37**, 1825-1834.
24. L.-Y. He, M. Hu, X.-F. Huang, B.-D. Yu, Y.-H. Zhang and D.-Q. Liu, *Atmos. Environ.*, 2004, **38**, 6557-6564.
25. X. Hou, G. Zhuang, Y. Sun and Z. An, *Atmos. Environ.*, 2006, **40**, 3251-3262.
26. X.-F. Huang, L.-Y. He, M. Hu and Y.-H. Zhang, *Atmos. Environ.*, 2006, **40**, 2449-2458.
27. G. Wang, K. Kawamura, S. Lee, K. Ho and J. Cao, *Environ. Sci. Technol.*, 2006, **40**, 4619-4625.
28. Y. Zhao, M. Hu, S. Slanina and Y. Zhang, *Environ. Sci. Technol.*, 2007, **41**, 99-105.
29. D. W. Sin, W. H. Fung, Y. Y. Choi, C. H. Lam, P. K. Louie, J. C. Chow and J. G. Watson, *J. Air Waste Manag. Assoc.*, 2005, **55**, 291-301.
30. W. F. Rogge, L. M. Hildemann, M. A. Mazurek, G. R. Cass and B. R. T. Simoneit, *Environ. Sci. Technol.*, 1993, **27**, 636-651.
31. D. R. Oros and B. R. T. Simoneit, *Appl. Geochem.*, 2001, **16**, 1513-1544.
32. W. F. Rogge, M. A. Mazurek, L. M. Hildemann, G. R. Cass and B. R. T. Simoneit, *Atmos. Environ. A-Gen.*, 1993, **27**, 1309-1330.
33. A. Habartová, M. Roeselová and L. Cwiklik, *Langmuir*, 2015, **31**, 11508-11515.
34. K. Kawamura and R. B. Gagosian, *Nature*, 1987, **325**, 330-332.
35. M. Mochida, Y. Kitamori and K. Kawamura, *J. Geophys. Res.*, 2002, **107**, 1-10.
36. G. Ellison, A. Tuck and V. Vaida, *J. Geophys. Res.*, 1999, **104**, 11633-11641.
37. A. Tabazadeh, *Atmos. Environ.*, 2005, **39**, 5472-5480.
38. D. J. Donaldson and V. Vaida, *Chem. Rev.*, 2006, **106**, 1445-1461.
39. C. R. Ruehl and K. R. Wilson, *J. Phys. Chem. A*, 2014, **118**, 3952-3966.
40. H. Kohler, *J. Chem. Soc. Faraday Trans.*, 1936, **32**, 1152-1161.
41. M. L. Shulman, M. C. Jacobson, R. J. Carlson, R. E. Synovec and T. E. Young, *Geophys. Res. Let.*, 1996, **23**, 277-280.
42. C. R. Ruehl, J. F. Davies and K. R. Wilson, *Science*, 2016, **351**, 1447-1450.

43. B. Ervens, G. Feingold and S. M. Kreidenweis, *J. Geophys. Res. Atmos.*, 2005, **110**, D18211.

44. J. Ovadnevaite, A. Zuend, A. Laaksonen, K. J. Sanchez, G. Roberts, D. Ceburnis, S. Decesari, M. Rinaldi, N. Hodas, M. C. Facchini, J. H. Seinfeld and C. O' Dowd, *Nature*, 2017, **546**, 637-641.

45. IPCC, 2013: Summary for Policymakers. In: *Climate Change 2013: The Physical Science Basis. Contribution of Working Group I to the Fifth Assessment Report of the Intergovernmental Panel on Climate Change* [Stocker,T.F., D. Qin, G.-K. Plattner, M. Tignor, S.K. Allen, J. Boschung, A. Nauels, Y. Xia, V. Bex and P.M. Midgley (eds.)]. Cambridge University Press, Cambridge, United Kingdom and New York, NY, USA.

46. H. I. Ingólfsson, C. A. Lopez, J. J. Uusitalo, D. H. de Jong, S. M. Gopal, X. Periole and S. J. Marrink, *Comput. Mol. Sci.*, 2014, **4**, 225-248.

47. D. Van Der Spoel, E. Lindahl, B. Hess, G. Groenhof, A. E. Mark and H. J. C. Berendsen, *J. Comput. Chem.*, 2005, **26**, 1701-1718.

48. P. Bjelkmar, P. Larsson, M. A. Cuendet, B. Hess and E. Lindahl, *J. Chem. Theory Comp.*, 2010, **6**, 459-466.

49. C. Oostenbrink, A. Villa, A. E. Mark and W. F. Van Gunsteren, *J. Comput. Chem.*, 2004, **25**, 1656-1676.

50. J. W. Ponder and D. A. Case, *Adv. Protein Chem.*, 2003, **66**, 27-85.

51. W. L. Jorgensen and J. Tirado-Rives, *J. Am. Chem. Soc.*, 1988, **110**, 1657-1666.

52. R. L. Leach, *Molecular Modelling: Principles and Applications*, Pearson Education Limited, Essex, 2001, pp. 1-784.

53. D. v. d. Spoel, E. Lindahl, B. Hess and t. G. d. team,(2013), *GROMACS User Manual version 4.6.5*, www.gromacs.org, [August 2016]

54. A. D. MacKerell, D. Bashford, M. Bellott, R. L. Dunbrack, J. D. Evanseck, M. J. Field, S. Fischer, J. Gao, H. Guo, S. Ha, D. Joseph-McCarthy, L. Kuchnir, K. Kuczera, F. T. K. Lau, C. Mattos, S. Michnick, T. Ngo, D. T. Nguyen, B. Prodhom, W. E. Reiher, B. Roux, M. Schlenkrich, J. C. Smith, R. Stote, J. Straub, M. Watanabe, J. Wiórkiewicz-Kuczera, D. Yin and M. Karplus, *J. Phys. Chem. B*, 1998, **102**, 3586-3616.

55. W. L. Jorgensen, J. Chandrasekhar, J. D. Madura, R. W. Impey and M. L. Klein, *J. Chem. Phys.*, 1983, **79**, 926-935.

56. K. Vanommeslaeghe, E. Hatcher, C. Acharya, S. Kundu, S. Zhong, J. Shim, E. Darian, O. Guvench, P. Lopes, I. Vorobyov and A. D. MacKerell, *J. Comput. Chem.*, 2010, **31**, 671-690.

57. J. B. Klauda, R. M. Venable, J. A. Freites, J. W. O'Connor, D. J. Tobias, C. Mondragon-Ramirez, I. Vorobyov, A. D. MacKerell and R. W. Pastor, *J. Phys. Chem. B*, 2010, **114**, 7830-7843.

58. M. G. Saunders and G. A. Voth, *Annu. Rev. Biophys.*, 2013, **42**, 73-93.

59. S. J. Marrink, H. J. Risselada, S. Yefimov, D. P. Tieleman and A. H. de Vries, *J. Phys. Chem. B*, 2007, **111**, 7812-7824.

60. J. J. Uusitalo, H. I. Ingólfsson, P. Akhshi, D. P. Tieleman and S. J. Marrink, *J. Chem. Theory Comp.*, 2015, **11**, 3932-3945.

61. S. J. Marrink, A. H. de Vries and A. E. Mark, *J. Phys. Chem. B*, 2004, **108**, 750-760.

62. S. J. Marrink and D. P. Tieleman, *Chem. Soc. Rev.*, 2013, **42**, 6801-6822.

63. L. Monticelli, S. K. Kandasamy, X. Periole, R. G. Larson, D. P. Tieleman and S.-J. Marrink, *J. Chem. Theory Comp.*, 2008, **4**, 819-834.

64. D. H. de Jong, S. Baoukina, H. I. Ingólfsson and S. J. Marrink, *Comput. Phys. Commun.*, 2016, **199**, 1-7.

65. H. J. C. Berendsen, J. P. M. Postma, W. F. van Gunsteren, A. DiNola and J. R. Haak, *J. Chem. Phys.*, 1984, **81**, 3684.

66. S. L. Duncan and R. G. Larson, *Biophys. J.*, 2008, **94**, 2965-2986.

67. S. L. Duncan, I. S. Dalal and R. G. Larson, *Biochim. Biophys. Acta Biomembr.*, 2011, **1808**, 2450-2465.

68. S. Baoukina, L. Monticelli, S. J. Marrink and D. P. Tieleman, *Langmuir*, 2007, **23**, 12617-12623.

69. S. Baoukina, L. Monticelli, H. J. Risselada, S. J. Marrink and D. P. Tieleman, *Proc. Natl. Acad. Sci. U.S.A.*, 2008, **105**, 10803-10808.

70. W. Lin, A. J. Clark and F. Paesani, *Langmuir*, 2015, **31**, 2147-2156.

71. H. Lee, S. K. Kandasamy and R. G. Larson, *Biophys. J.*, 2005, **89**, 3807-3821.

72. S. Baoukina, S. J. Marrink and D. P. Tieleman, *Faraday Discuss.*, 2010, **144**, 393-409.

73. S. L. Duncan and R. G. Larson, *Biochim. Biophys. Acta Biomembr.*, 2010, **1798**, 1632-1650.

74. P. Kulovesi, J. Telenius, A. Koivuniemi, G. Brezesinski, A. Rantamäki, T. Viitala, E. Puukilainen, M. Ritala, S. K. Wiedmer, I. Vattulainen and J. M. Holopainen, *Biophys. J.*, 2010, **99**, 2559-2567.

75. J. Telenius, A. Koivuniemi, P. Kulovesi, J. M. Holopainen and I. Vattulainen, *Langmuir*, 2012, **28**, 17092-17100.

76. B. Liu, M. I. Hoopes and M. Karttunen, *J. Phys. Chem. B*, 2014, **118**, 11723-11737.

77. E. C. Griffith, T. R. C. Guizado, A. S. Pimentel, G. S. Tyndall and V. Vaida, *J. Phys. Chem. C*, 2013, **117**, 22341-22350.

78. M. Javanainen, A. Lamberg, L. Cwiklik, I. Vattulainen and O. H. S. Ollila, *Langmuir*, 2017.

79. S. Baoukina and D. P. Tieleman, *Biochim. Biophys. Acta Biomembr.*, 2016, **1858**, 2431-2440.

80. A. a. F. Eftaiha, S. N. Wanasundara, M. F. Paige and R. K. Bowles, *J. Phys. Chem. B*, 2016, **120**, 7641-7651.
81. L. F. Voss, M. F. Bazerbashi, C. P. Beekman, C. M. Hadad and H. C. Allen, *J. Geophys. Res.*, 2007, **112**.
82. C. Pfrang, F. Sebastiani, C. O. M. Lucas, M. D. King, I. D. Hoare, D. Chang and R. A. Campbell, *Phys. Chem. Chem. Phys.*, 2014, **16**, 13220-13228.
83. J. Kleber, K. Laß and G. Friedrichs, *J. Phys. Chem. A*, 2013, **117**, 7863-7875.
84. E. Gonzalez-Labrada, R. Schmidt and C. E. DeWolf, *Phys. Chem. Chem. Phys.*, 2007, **9**, 5814-5821.
85. V. Miguel, M. A. Perillo and M. A. Villarreal, *Biochim. Biophys. Acta Biomembr.*, 2016, **1858**, 2903-2910.

Chapter 2

Computational Model of Oleic Acid

2.1 Oleic Acid Monolayer at the Air-Water Interface

This chapter focuses on oleic acid, also known as cis-9-octadecenoic acid, which is an 18-carbon monounsaturated fatty acid. As established in Chapter 1, both anthropogenic and biogenic sources release oleic acid into the atmosphere—with the most significant oleic acid emissions coming from cooking sources and from the ocean's surface.

By generating pressure-area isotherms from simulations and comparing to experimental isotherms reported in the literature, the model of oleic acid at the air-water interface developed in this project will be validated. In the literature, several pressure-area isotherms for systems of oleic acid at the air-water interface have been obtained from experiments, as shown in Figure 16.

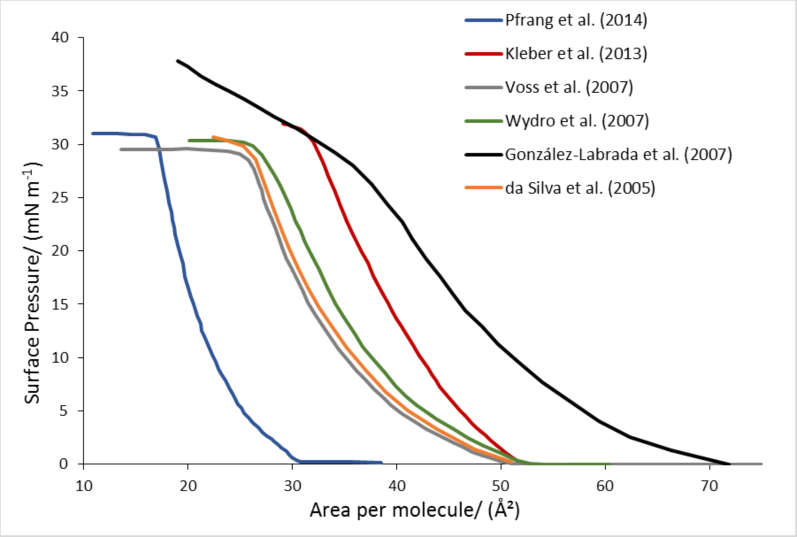

Figure 16: Pressure-area isotherms reported in the literature for oleic acid monolayers at the air-water interface.[1-6]

The isotherms by Kleber *et al.*, Wydro *et al.*, da Silva *et al.*, Voss *et al.* and Pfrang *et al.* were generated by the use of a Langmuir trough, whereas the isotherm by González-Labrada *et al.* was generated by spreading the monolayer on a droplet.[1-6]

The isotherms reported by Kleber *et al.*, Wydro *et al.*, da Silva *et al.* and Voss *et al.*, as shown in Figure 16, all show the same starting point.[2-5] The isotherm reported by Pfrang *et al.* is shifted to lower areas per molecule.[1]

Voss *et al.* determined their pressure-area isotherm at room temperature and atmospheric pressure using a Langmuir trough.[3] At large areas above 51 Å^2 molecule^{-1}, the molecules in the monolayer are widely spaced; the monolayer exists as a two-dimensional gas and molecules do not interact with one another. Hence, surface pressures are low.[3] When compressed laterally, the monolayer undergoes a phase transition to the liquid phase. The molecules start to interact with one another, causing an increase in surface pressure, as can be seen for monolayers in the range of 28–51 Å^2 molecule^{-1}, until the equilibrium spreading pressure is reached.[3] The equilibrium spreading pressure is the point at which the monolayer cannot be compressed any further without causing the monolayer to collapse into three-dimensional structures such as micelles. A plateau in the pressure-area isotherms obtained from experiments can be seen, which is known as the film collapse region. Once the film collapse region is reached, material is lost from the surface under compression. This results in an inaccurate estimation of the water surface available per molecule, meaning data sampled in this region can be disregarded as it does not represent the system accurately.

The pressure-area isotherm of Pfrang *et al.* represented in Figure 16 shows the same regions as the one reported by Voss *et al.* and both isotherms reach a maximum surface pressure at approximately 30 mN m^{-1}. However, the isotherm by Pfrang *et al.* is shifted to lower areas per molecule. Here, the monolayer with an area per molecule above the phase transition at ca. 31 Å^2 is in a gas-liquid coexisting region. Monolayers with areas per molecule in the range of ca. 18–31 Å^2 are part of the liquid phase and monolayers below approximately 18 Å^2 per molecule are in the film-collapse region.[1]

The isotherm by Kleber *et al.* shows two distinct points: At an area per molecule of 52.5 Å^2 there is a phase transition from gas to liquid phase, and at 32 Å^2 per molecule, after which the monolayer starts to collapse.[4] Here, the pressure lies at approximately 30 mN m^{-1}. Kleber *et al.* acknowledge that results that they obtained at the beginning were often not reproducible and point out substantial deviation in literature data regarding both the lift-off point, when surface pressures start to increase, and the collapse pressure.[4] They conclude that in their work isotherms with lift-off points that were shifted to lower areas per molecule were attributed to an overestimation of surface concentrations due to a loss of material from the surface through oxidation by ambient oxidisers.[4]

The isotherm by González-Labrada *et al.* produced by a different method is shifted to a slightly higher area per molecule.[6] They state that at a surface pressure of 30 mN m^{-1} the isotherm collapses, which is in good agreement with the other reported isotherms.[6] Data at lower areas per molecule, after this point, can be disregarded.

Simulations in this work will be compared to isotherms produced with the Langmuir trough method as the set-up is comparable to the simulation set-up used. By comparing all 5 pressure-area isotherms of oleic acid at the air-water interface produced in this way, it can be concluded that, even though reported areas of water surface available per molecule differ between isotherms, the obtained range of surface pressures is similar in all 5 experiments. The most significant point on the isotherm is the equilibrium spreading pressure which, for all 5 isotherms, lies between 29.0–32.0 mN m^{-1}.

Brewster Angle Microscopy (BAM) is an experimental technique that gives insight into the structure and morphology of surface films at an air-water interface. This can be used to establish whether the film is isotropic or not, and hence can be used to determine phase changes in the isotherm. This technique results in images in the micrometre range, showing different phases. In the literature, Sebastiani produced several BAM images from experiments for a range of fatty acids at an air-water interface.[7, 8] Images produced from simulations in this work, although not directly comparable to BAM images due to size differences, will be analysed to provide complementary information. From BAM images, the intensity of the signal can allow the tilt angle of molecules to be determined. This analysis was not carried out in Sebastiani's work, but simulations in this work will be further analysed to determine tilt angles of the molecules in the monolayer, giving further insight into the structure of the monolayer.

2.2 Methodology/ Simulations

2.2.1 Oleic Acid

2.2.1.1 Coarse-Grained Mapping

The chemical structure of oleic acid was mapped to the coarse-grained representation by using the general Martini force field mapping. Decisions regarding the bead types were made in accordance with Table 1, depicted in section 1.11.1.1 of the introduction, as well as by comparison to existing mappings of other molecules. As depicted in Figure 17, the oleic acid molecule was broken down into six coarse-grained sites. The hydrophobic tail, which represents 16 methyl/methylene groups, was modelled using four C2 and one C3 beads. The C3 bead represents the 2-butene unit in the hydrophobic chain. As all other carbons in the chain should be chemically equivalent, four C2 units were chosen to represent the rest of the carbon chain, as depicted in Figure 17. The hydrophilic headgroup bead was chosen by comparing to available literature data of other molecules comprised of a carboxyl headgroup and carbon chain. Therefore, a P3 bead was used to represent the headgroup.[9]

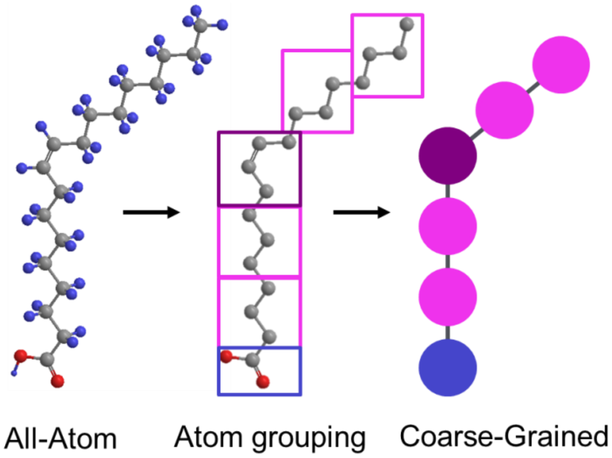

Figure 17: All-atom (left image) in comparison to coarse-grained (right image) mapping. Central image: Representation of the grouping for the coarse-grained beads in an oleic acid molecule. Five beads representing the hydrophobic oleic acid chain (pink, dark pink) and one bead representing the hydrophilic oleic acid headgroup (blue).

After the atom-to-bead mapping was chosen more details about the bonded interactions between beads are described in the next section.

2.2.1.2 Bonded Interactions within Oleic Acid

As depicted in Table 3, the standard Martini bead-to-bead distance of 0.47 nm between bonded beads (i, j) and the standard force constant of 1250 kJ mol^{-1} nm^{-2} were used for all bonded beads within the model.[10] The beads are numbered as follows: 1 = P3, 2 = C2, 3 = C2, 4 = C3, 5 = C2 and 6 = C2. This numbering will be used in Table 3, Table 4 and Table 6.

i	j	Length (nm)	Force constant (kJ mol^{-1} nm^{-2})
1	2	0.47	1250
2	3	0.47	1250
3	4	0.47	1250
4	5	0.47	1250
5	6	0.47	1250

Table 3: Bead-to-bead distance and force constants between bonded beads in each oleic acid molecule.

In agreement with the default values for cis-bonds in the Martini force field, as shown in Table 4, a smaller equilibrium bond angle was used to model the unsaturated cis-bond in the oleic acid chain and the force constant was set to 45 kJ mol^{-1}.[10] All other equilibrium bond angles were set to 180°, in accordance with the standard Martini force field parameters for chain-like molecules.[10]

i	j	k	Angle (degrees)	Force constant (kJ mol^{-1} nm^{-2})
1	2	3	180	25
2	3	4	180	25
3	4	5	120	45
4	5	6	180	25

Table 4: Angles and force constants between bonded beads in each oleic acid molecule.

After the bonded interactions and beads have been determined for the oleic acid molecules in the system, the non-bonded interactions in the system will be discussed in the following section.

2.2.1.3 Interactions between Non-bonded Beads in the System

The default interaction matrix for non-bonded interactions in the system is taken from Marrink *et al.* and this general matrix is depicted in the introduction in section 1.11.1.3.[11] A matrix for the beads in the system that will be modelled in this project is shown in Table 5. This matrix is used to determine the interaction strength between the beads in the model. The initial model includes water beads as well as the oleic acid beads, which were described in section 2.2.1.1. Four water molecules are modelled by a single P4 bead.

Bead Type		**P**	**P**	**C**	**C**
	sub	4	3	3	2
P	4	I	I	VI	VII
P	3	I	I	V	V
C	3	VI	V	IV	IV
C	2	VII	VI	IV	IV

Table 5: Interaction matrix for the non-bonded interactions between the beads in the simulated system.[10] Interaction levels are distinguished as followed; O = 5.6 kJ mol^{-1} (supra attractive). I = 5.0 kJ mol^{-1} (attractive). II = 4.5 kJ mol^{-1} (almost attractive). III = 4.0 kJ mol^{-1} (semi attractive). IV = 3.5 kJ mol^{-1} (intermediate). V = 3.1 kJ mol^{-1} (almost intermediate). VI = 2.7 kJ mol^{-1} (semi repulsive). VII = 2.3 kJ mol^{-1} (almost repulsive). VIII = 2.0 kJ mol^{-1} (repulsive). IX = 2.0 kJ mol^{-1} (super repulsive).

From the interaction matrix, it can be seen that the interaction of two P4 water beads is attractive with a strength of 5.0 kJ mol^{-1}. P3 headgroup beads experience the same level of attractive interaction between themselves. P3 beads and water beads have an interaction strength of 5.0 kJ mol^{-1} between one another. It is reasonable that these beads have a similar strength as the aim of the project is to create a monolayer on the water's surface. The hydrophobic tails of the oleic acid molecules present in the system experience "intermediate" levels of interaction between the beads, C2–C2, C3–C3 and C3–C2. The interaction between the C3 chain bead and the P3 headgroup bead is defined as "almost intermediate", with the interaction strength being slightly lower than that for the "intermediate" interactions. The interaction strength is 3.1 kJ mol^{-1}. Water beads show a "semi-repulsive" interaction with the C3 bead in the oleic acid chain. The C2 beads of the oleic acid chains and the oleic acid headgroups also show a semi-repulsive interaction. "Almost repulsive" interactions are experienced between the water and the C2 beads of the chain, describing the hydrophobic character of the chain.

2.2.1.4 System Set Up: Algorithm for a Monolayer of Oleic Acid

In the following, the initial setup (setup 1) of the oleic acid system at the vacuum-water interface will be described. This initial setup is revised later, with details of changes to the setup given later on in this chapter.

Setup 1: a box of length 12 nm × 12 nm × 24 nm, with the *z*-axis reaching from −12 nm to +12 nm and the *x* and *y*-axes from 0 nm to +12 nm was constructed, as shown in Figure 18 (a). The *x*- and *y*-dimension of the box were chosen based on the spacing between molecules in the monolayer. This initial set up, places molecules 0.52 nm apart from one another. Non-bonded beads are further apart than bonded beads, which have a bead-to-bead distance of 0.47 nm. Hence, this spacing should result in a close packed structure. This is just an initial set up, as in the NPT simulations, the spacing between the molecules will be able to change, as box dimensions are scaled.

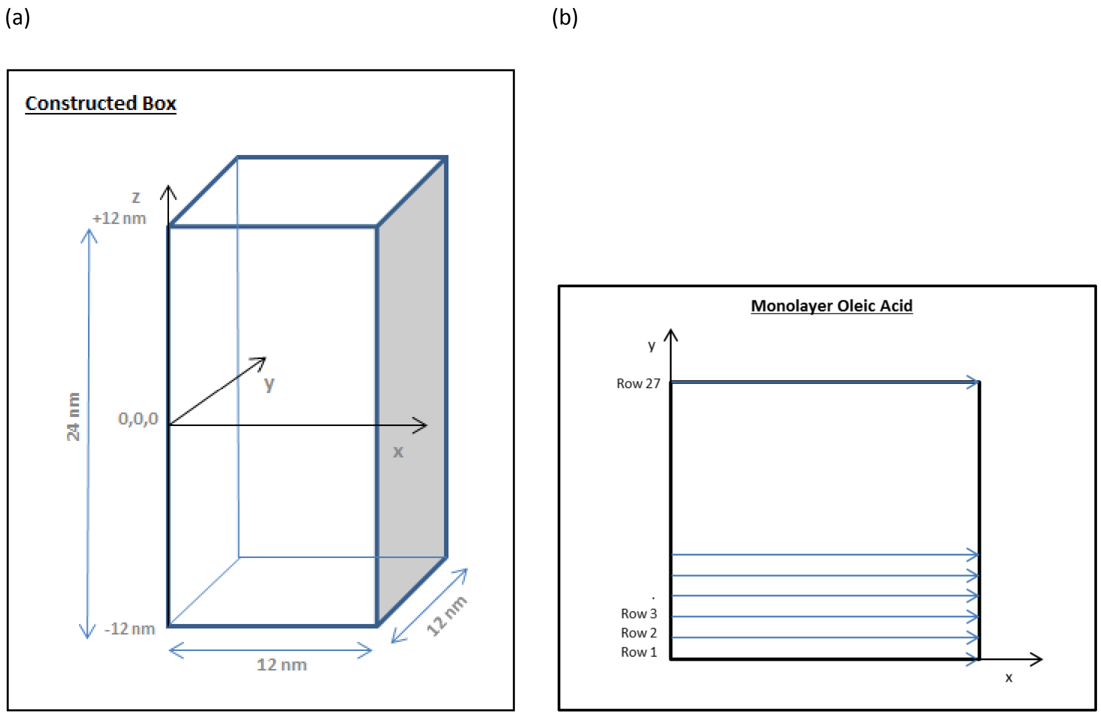

Figure 18: (a) Representation of the constructed box. (b) Representation of box filling to obtain a monolayer.

Each oleic acid molecule that was placed in the box was modelled using 6 beads, as described in section 2.2.1.1. All bead-to-bead distances between the centres of the beads were set to 0.47 nm with bond angles of 180°, and with the bond angle between C2-C3-C2 beads being reduced to 120°.

The first oleic acid molecule was placed in the box so that the centre of mass of the P3 head bead lies at (0, 0, 4), with the following two C2 beads and a C3 bead all aligned along the positive *z*-axis. At an angle of 120° in the *xz*-plane the position of the next C2 bead is followed by another C2 bead. Positions for these beads are as presented in Table 6.

Bead Number	Bead	x (nm)	y (nm)	z (nm)
1	COO	0	0	4.000
2	B1	0	0	4.470
3	B2	0	0	4.940
4	B3	0	0	5.410
5	B4	0.407	0	5.645
6	B5	0.814	0	5.880

Table 6: Coordinates of a single oleic acid molecule in a three-dimensional space. COO represents the headgroup bead. B1, B2, B4 and B5 represent the C2 beads in the chain and B3 is the C3 bead of the chain.

A further 22 oleic acid molecules were placed in the box in the same way, shifting them 0.52 nm in the positive *x*-direction each time. When the box boundary was reached, the next bead was placed 0.52 nm in the *y*-direction from the 1st bead. The second row was filled in the *x*-direction in the same way as the first row, as shown in Figure 18 (b). The process was repeated, adding a further 22 rows in the same fashion to give a square lattice with a total of 23 × 23 rows, making the monolayer consist of 529 oleic acid molecules. Due to the periodic boundary conditions of the box explained in the introduction in section 1.12, the box will be surrounded by copies of itself. Hence, to avoid the presence of an air-water interface along the positive *z*-axis, two oleic acid monolayers need to be modelled. A mirror image of the first monolayer was created using the $z = 0$ plane as a mirror plane, resulting in the headgroups of the two monolayers facing one another. This is represented in Figure 19.

Air in the model is approximated as a vacuum, which is a common approximation in simulations of interfaces.[12] It is suggested that this is a reasonable approximation as, with the small system size and time scales used in simulations, the number of gas molecules interacting with the surface would be expected to be rather small and hence may be disregarded.[13]

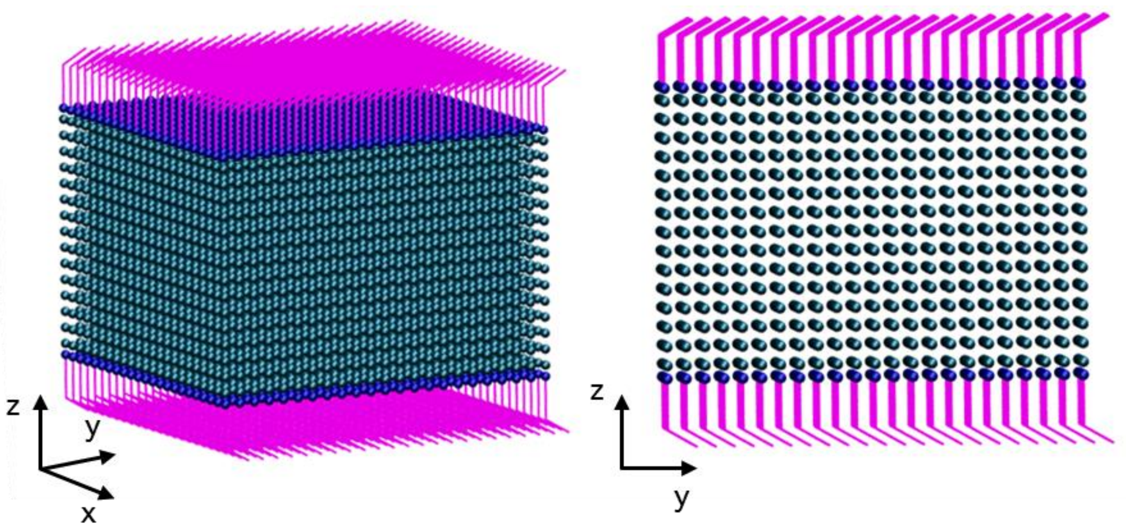

Figure 19: Oleic acid monolayers separated by water beads. Teal beads represent the water beads in the system. Blue beads are representative of the oleic acid headgroup beads and the magenta represent the hydrophobic chain.

The oleic acid headgroups were separated by a space of approximately 7.50 nm × 12.00 nm × 12.00 nm. This space was filled with P4 water beads. The centre of mass of the first water bead was placed at (0, 0, 0.52). A further 22 water beads were added to the system, shifting them 0.52 nm in the positive *x*-direction until the box boundary was reached. The next bead was placed 0.52 nm in the *y*-direction from the 1st water bead. The second row in the *x*-direction was filled in the same way as the first row. This was repeated, adding a further 22 rows in the same fashion, to give a total of 23 x 23 rows containing 529 coarse-grained water beads. After filling the first layer, another water bead was added at (0, 0, 1.04) and the layer was filled in the same way as the first one. This procedure was carried out for another 5 layers, shifting them 0.52 nm in the positive *z*-direction each time. Once the space in the positive *z*-direction was filled up to the monolayer, the *z* = 0 plane was used to create a mirror image of the first 7 layers of the water beads to give a total of 14 layers of coarse-grained water beads in the space between the monolayers. A final water layer was added with the centre of mass of the first water bead placed at (0, 0, 0), and the layer with *z* = 0 was filled according to the same procedure as before.

Every 3rd water bead that was added to the system was shifted by +0.2 nm along a random axis—*x*, *y* or *z*—in order to disrupt the lattice and hence avoid freezing of the water. A total of 7935 coarse-grained water beads were added to the system. Now that the system has been set up containing water beads as well as the oleic acid beads, the next section of this report will give details on the parameters used to set up all coarse-grained simulations in this chapter.

2.2.2 Coarse-Grained Simulations

The standard coarse-grained particle definitions of the Martini force field for biomolecular simulations were used, and initial positions of each bead were determined.[9, 10] All calculations in this chapter were run using the GROMACS (4.0.7) simulation software in combination with the coarse-grained Martini force field.[14] The initial run parameter file was taken from an on-line tutorial[15] and adapted to fit the system, specifying the simulation parameters including neighbour list update frequency, time steps, as well as the switch function.

For simulations in this chapter, a time step of 40 fs is used. The neighbour list is updated every 10 steps, with the neighbour list cut-off set to 1.4 nm. The default values of the Martini force field for cut-offs used in this project mean that van der Waals interactions are shifted in the range of 0.9–1.2 nm and electrostatic interactions are shifted between 0–1.2 nm.[10] Hence, only interactions within the cut-off range of 1.2 nm are calculated.

In order to maintain temperature, the Berendsen temperature coupling is used, where water beads and oleic acid beads are coupled separately. The model is designed for use at near ambient conditions. Hence, temperatures for simulations in this project are kept to 298 K or 300 K, and will be specified on a case by case basis. Pressure settings were adapted from Baoukina *et al*.[16] The coupling constants for temperatures are set to 1 ps. Berendsen pressure coupling is used to maintain pressures. The pressure coupling constants are set to 4 ps. Semi-isotropic pressure coupling is used, unless stated otherwise, with compressibilities in the *x*/*y* dimensions of the box set to 5×10^{-5} bar^{-1} and to 0 bar^{-1} in the *z*-dimension.

2.2.3 Changes to System Setup 1

A 15 ns NPT simulation with semi-isotropic pressure coupling was set up. The temperature of the bath was set to 298 K. The box was set up using system setup 1, described in section 2.2.1.4, containing two monolayers with 529 oleic acids in each layer and 7935 water beads between the layers. This initial model (setup 1) modelled the water in the system by using P4 water beads. To disrupt the lattice when placing the water beads in the simulation box every third water bead was displaced by 0.2 nm. However, as shown in Figure 20, the displacement did not prevent the water from freezing.

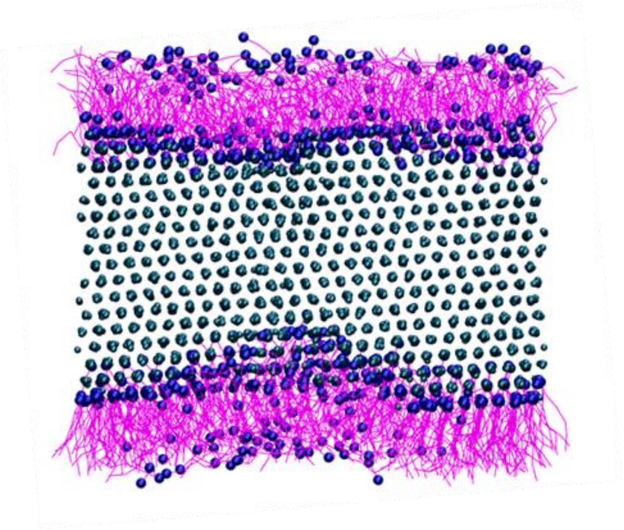

Figure 20: Ordered water lattice showing the freezing of water beads in the system.

The water froze at 298 K due to the limitations of the Martini model. This is a known problem in simulations with the Martini model. The freezing temperature of the modelled P4 water beads compared to that of real water is too high. This can cause the modelled water to freeze between 280 K and 300 K, which is dependent on the chosen simulation parameters.[10, 17] Freezing driven by the presence of nucleation sites such as solid surfaces and bilayer systems is rapid and irreversible.[18] In order to model water that behaves more realistically with respect to real water, antifreeze beads, denoted BP4, can be introduced to the system.[10] The Lennard-Jones parameter, σ, indicating the closest distance between two particles is increased for the interaction between BP4 and P4 to σ = 0.57 nm.[10] Hence, BP4 beads are bigger in size, preventing the formation of a water lattice. Furthermore, phase separation of water beads with antifreeze beads is avoided by setting the interaction between them to "supra attractive" with an interaction strength, ε, of

5.6 kJ mol^{-1}. In the literature it is proposed that exchanging approximately 10 % of the P4 beads by BP4 beads is sufficient in order to prevent the freezing of the water beads in the system.[10] Nevertheless, the introduction of antifreeze beads affects the self-diffusion constant as well as the density. At a mole fraction of $n_{AF} = 0.1$, both decrease by ca. 10 %, due to both increased size and interaction strength of the antifreeze particles.[10] However, as tested by Marrink *et al.* on DPPC bilayer systems, properties such as area per lipid, lateral self-diffusion constant and the transition temperatures for gel phase formation are not affected. Due to the findings presented above, antifreeze beads were introduced to the system. The interaction strength between the antifreeze beads, BP4, and other beads in the system is as follows: BP4–BP4 bead interactions and BP4–P3 bead interactions of oleic acid molecules with antifreeze beads are “attractive” with an interaction strength, ε, of 5.0 kJ mol^{-1}. The BP4–C3 interaction of the oleic acid chain with antifreeze beads is “semi-repulsive” at 2.7 kJ mol^{-1}. An “almost repulsive” interaction, with an interaction strength of 2.3 kJ mol^{-1}, is present for BP4–C2 bead interactions of the oleic acid chain and antifreeze beads.

Setup 2: to avoid water freezing in the system, changes were made to its initial setup. The oleic acid molecules in the system are set up in the same way as previously described in setup 1. However, instead of inserting rows of water into the box, a pre-equilibrated water box was inserted between the two oleic acid monolayers. The generation of this water box is described in the following:

A box of dimensions 12.7 nm × 12.7 nm × 12.7 nm, containing only water was generated. The box was filled with 7935 beads, of which 7213 were water beads and 722 were antifreeze beads. An energy minimisation was performed to relax the system, followed by a simulation for 27 ns in the NPT ensemble, hence keeping the number of particles, pressure and temperature constant. This was done to ensure an equilibrium spacing between the water beads in the system. The box was scaled isotropically, allowing changes to the box size in all dimensions. Compressibilities and pressures in all dimensions were set to 5×10^{-5} bar^{-1} and 1 bar respectively. The box size decreased during the simulation to reach a final box size of 10.15 nm × 10.15 nm × 10.15 nm. As shown in Figure 21, the chosen run time is sufficient, as the box size stabilises after 15 ns. The final box volume = 1045.67 nm^3. The system has a total of 7935 beads, including 7213 water beads and 728 antifreeze beads, making the average volume per solvent bead 0.1318 nm^3.

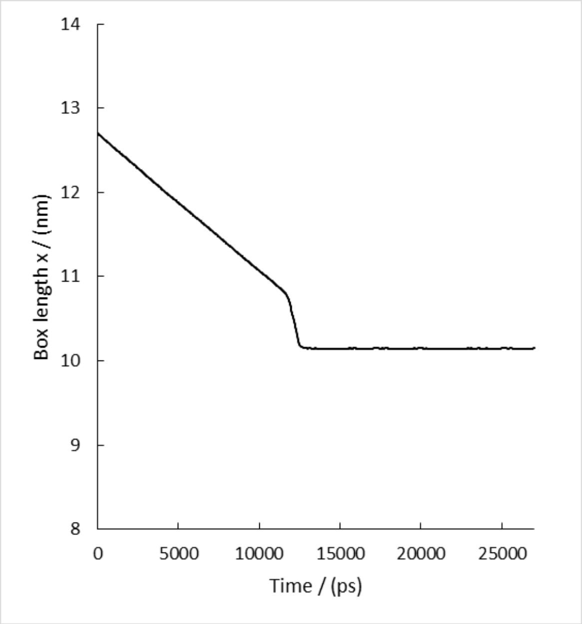

Figure 21: Change in box length *x*-dimension over the set simulation time.

In the updated algorithm, the thickness of the water layer in the box will be determined by the *z*-displacement of the oleic acid monolayer and hence will be set to:

$$\text{water thickness} = (2 \times z \text{ displacement of monolayer}) - 0.47 \text{ nm} \tag{35}$$

A slab of this thickness was cut out of the previously simulated NPT run of water, in order to generate the new coordinates of the water beads. To ensure that enough water beads were present in the system, periodic images of the simulated water box were produced. To ensure that a 10 % fraction of antifreeze beads was maintained in the cut-out slab of water beads, the algorithm was adapted to check and replace water beads with antifreeze beads or vice versa where necessary. The way oleic acid molecules are set up in the system remains the same as described in the initial setup (section 2.2.1.4).

The final composition of the system included: 7447 water beads, 828 antifreeze beads and 882 oleic acids, as shown in Figure 22. The *z*-dimension of the box was increased to 42 nm, increasing the space occupied by vacuum and ensuring that the monolayers do not interact with one another. This spacing should be sufficient, as only interactions within the cut-off distance of 1.2 nm are calculated.

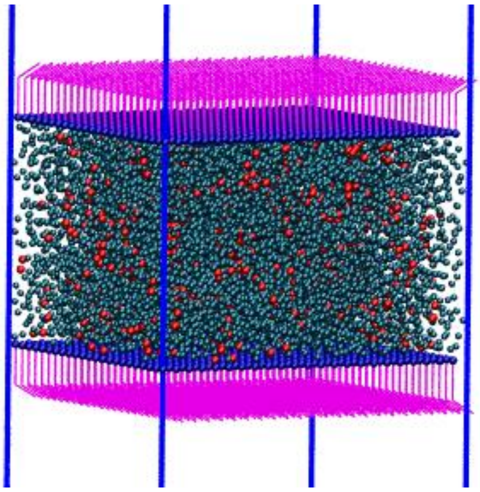

Figure 22: System Setup 2: A water slab is cut out of a pre-equilibrated water box and inserted between the two monolayers. Approximately 10 % of water beads are replaced by antifreeze beads. Oleic acid chain (magenta), oleic acid headgroup (blue), water beads (teal), antifreeze beads (red).

Setup 3: in order to allow the generation of monolayers at a low area per molecule, the algorithm was further modified to allow a hexagonally close packed setup, as shown in Figure 23 (b).

From this point onwards, Setup 2 (Figure 23 (a)) will be used to generate monolayers at high areas per molecule, and Setup 3 (Figure 23 (b)) will be used to generate close packed structures. Water is described in the same way in Setups 2 and 3. Both setups use a *z*-box dimension of 42 nm.

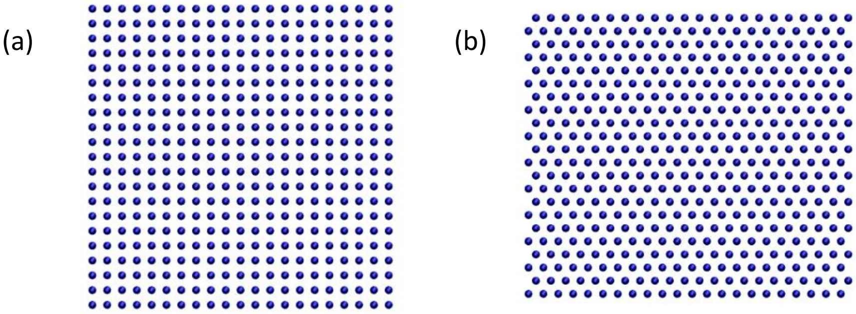

Figure 23: Top layer view of the COO beads in (a) Setup 2 and (b) Setup 3.

Pressure-area isotherms will be produced from simulations in this work. The chosen system set up, assuming a planar interface, resembles the system set up used to produce pressure-area isotherms in experiments, where a planar interface on a Langmuir trough is expanded or compressed, thus allowing direct comparison between experiments and simulations. The system size differs between experiments with interfacial areas in the cm^2 range and simulations with interfacial areas in the nm^2 range.

Simulations mimic a cross-section through an atmospheric aerosol. Assuming a fine particle with a diameter below 2.5 µm, as is expected to be produced from cooking emissions, results in a cross-section curvature of less than 1°, for the range of surface areas studied in this work. This makes the assumption of a flat interface in simulations a realistic basis to study surface films on fine particles. Details of the run parameters and resulting pressure-area isotherm for oleic acid at the air-water interface will be given in the following sections.

2.2.4 Pressure-Area Isotherms of Oleic Acid at the Air-Water Interface

In order to assess the agreement with experimental data, several pressure-area isotherms were produced for oleic acid from simulations, following the method described in the literature by Baoukina *et al.*[16] An initial structure was compressed or expanded in the lateral dimensions, without altering the box length in the normal direction. The number of beads, pressure and temperature was kept constant in the box. Semi-isotropic pressure coupling was applied to the system, with pressures controlled by a Berendsen pressure bath. A coupling time constant of 4 ps with a compressibility of 5×10^{-5} bar^{-1} in the *x*/*y* dimensions of the box was used. A lateral pressure, of +60 bar or −60 bar, was applied to the system for 100 ns, with positive pressures causing a decrease in water surface area available per molecule and negative pressures causing an increase in the interfacial area of the system.

Taking snapshots during the compression run allows the generation of several new starting structures, each at a different surface area per molecule. As shown in Figure 24, each starting structure is simulated for 1000 ns (200 ns equilibration and 800 ns production time), keeping the number of beads, box volume and temperature constant (NVT ensemble). Only the data generated from the production run was used for data analysis. In both NVT and NPT ensemble calculations, temperature was controlled separately for oleic acid, water and antifreeze beads with a Berendsen heat bath and a coupling constant of 1 ps at 300 K.

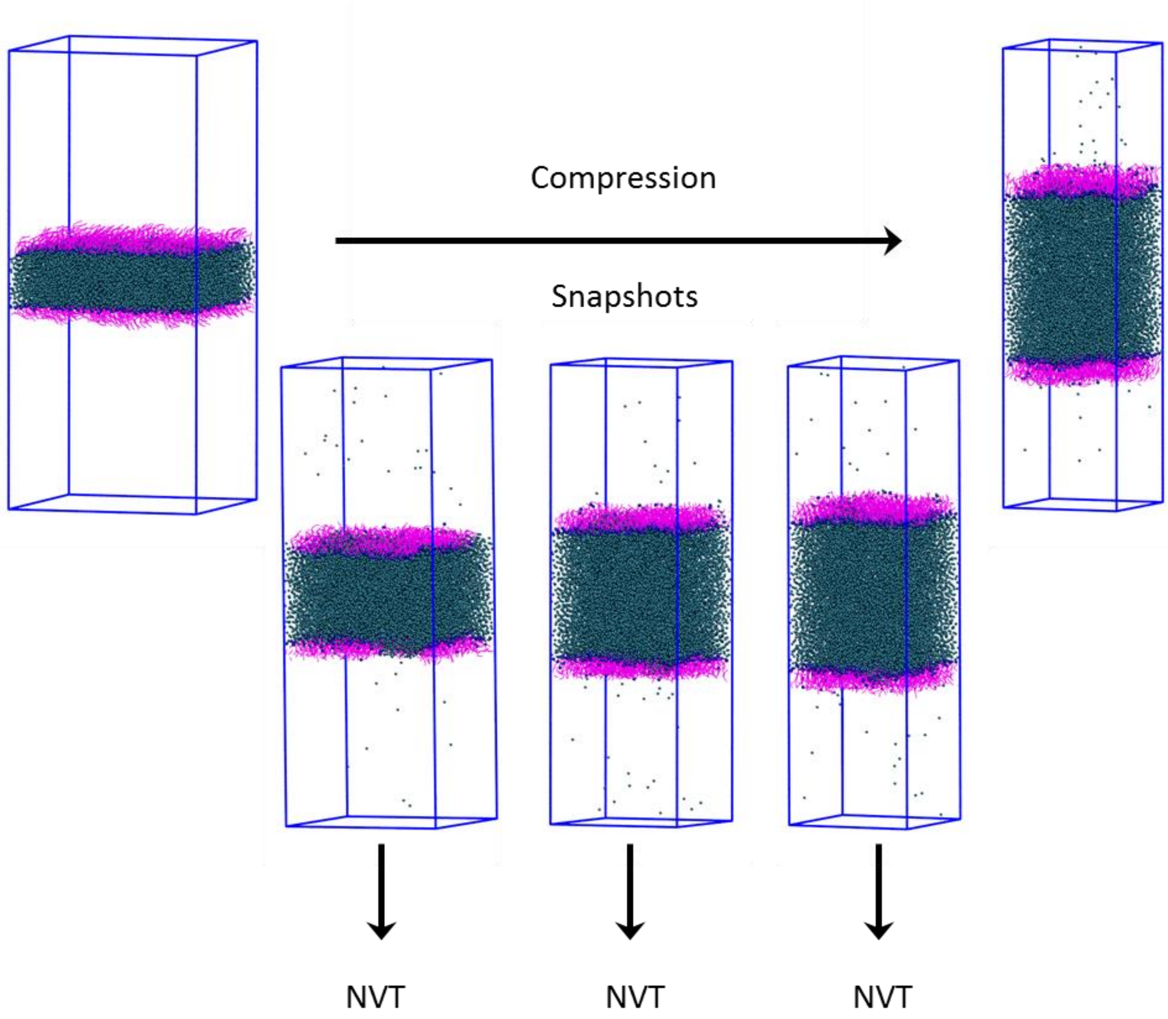

Figure 24: Compression run in the NPT ensemble, keeping the number of beads, pressure and temperature constant. The box is able to vary size only in the *x*/*y* dimensions. This is done to create monolayers at a range of areas per molecule. This is followed by a 1000 ns simulation in the NVT ensemble. Oleic acid chain (magenta), oleic acid headgroup (blue), water (teal).

2.3 Results and Discussion

Several simulations were performed to produce pressure-area isotherms for oleic acid at the vacuum-water interface. In the following, each simulated pressure-area isotherm will be discussed in turn and compared to experimental data.

2.3.1 Pressure-Area Isotherm from Standard Parameters

To obtain the first pressure-area isotherm, the standard Martini force field parameters were used. A box of size 18 nm × 18 nm × 42 nm was created using setup method 2, containing 882 oleic acid molecules (441 in each monolayer), 12852 water beads and 1300 antifreeze beads. This large interfacial area was chosen, in order to generate an expanded starting structure, with molecules far apart from one another. Using the NPT ensemble with semi-isotropic pressure coupling, this initial structure was compressed laterally. Seventeen snapshots were taken from the compression run, generating monolayers with areas per molecule in the range of 29.74–39.28 Å^2. The decision about the effective surface tension was based on the system size, with 882 oleic acid molecules, the system size can be considered to be small.[16] Hence, the effective surface tension, γ_{vw^*}, was adopted from the simulations of Baoukina *et al.* and was set to 47 mN m^{-1}, allowing the surface pressure at each area per molecule to be calculated as described in the introduction in section 1.16.[16]

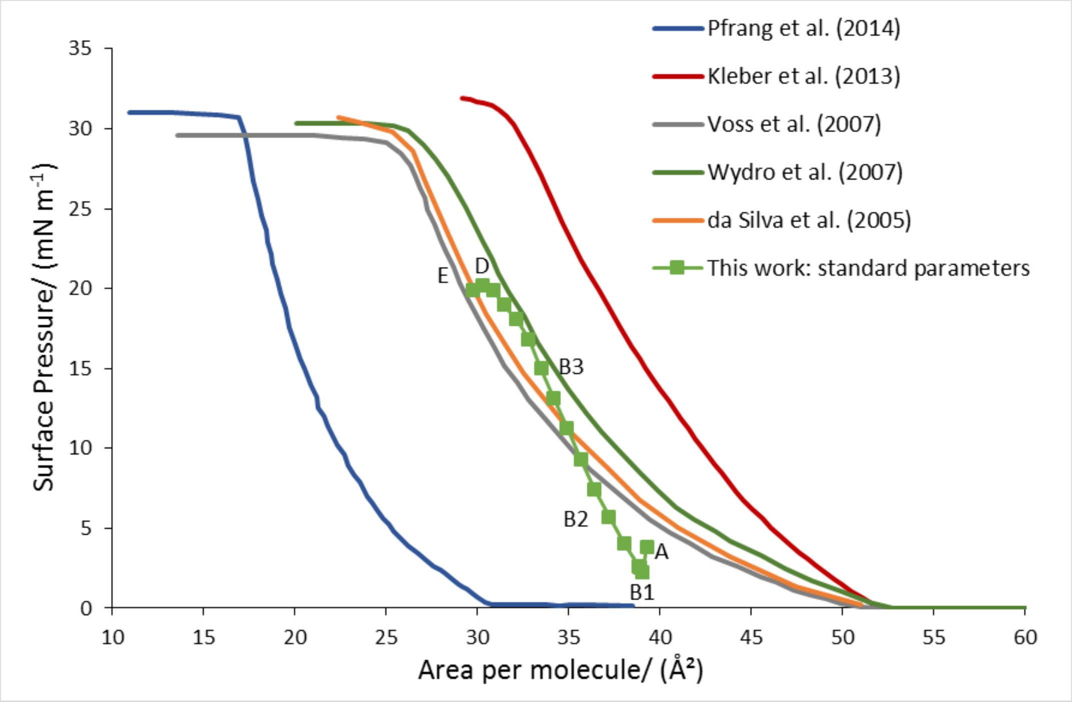

Figure 25: Pressure-area isotherm for oleic acid at the air-water interface from simulations in comparison to experimental isotherms reported in the literature.[1-5] Standard parameters; bead-to-bead distances and force constants used: P3-C2 = 0.47 nm, fc = 1250 kJ mol^{-1} nm^{-2}; C2-C2 = 0.47 nm, fc = 1250 kJ mol^{-1} nm^{-2}. Phase behaviour of simulated isotherm indicated: (A) gas-liquid coexisting region, (B1, B2 and B3) liquid-expanded region, (D) equilibrium spreading pressure and (E) film collapse region.

As presented in Figure 25, the first pressure-area isotherm simulated with the standard Martini force field parameters shows that, upon compression, the molecules in the monolayer move closer together. As shown in the images produced at several points along the pressure-area isotherm in Figure 26, there is no clear ordering within the oleic acid chains. As the water surface area decreases and surface pressure consequently increases, the chains of the molecules stay disordered.

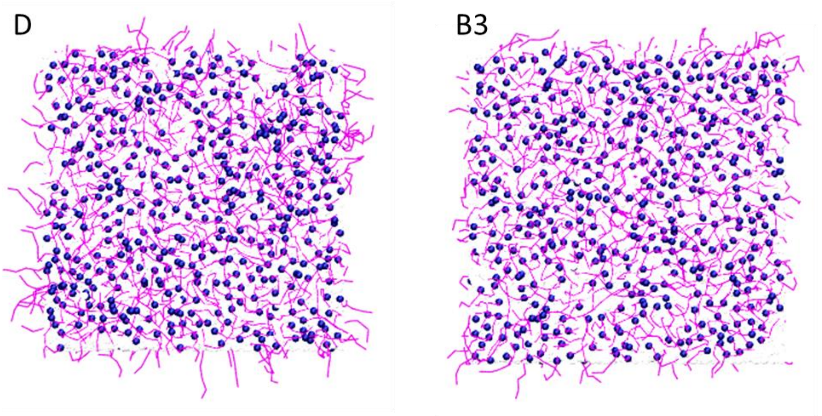

Area per molecule = 30.28 Å^2
Surface pressure = 20.18 mN m^{-1}

33.48 Å^2
15.01 mN m^{-1}

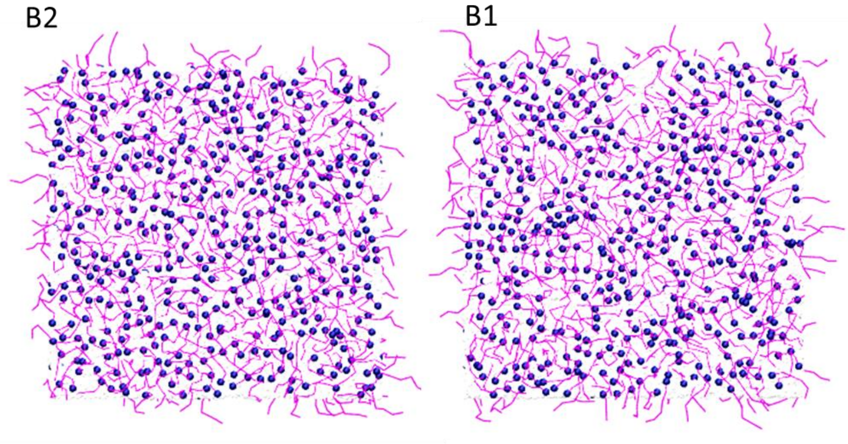

Area per molecule = 37.20 Å^2
Surface pressure = 5.71 mN m^{-1}

39.05 Å^2
2.27 mN m^{-1}

Figure 26: Top view of the upper oleic acid monolayer, using the standard parameters, at several points along the pressure-area isotherm (B1, B2, B3, D—points indicated on isotherm in Figure 25). Oleic acid chains stay disordered under compression. Oleic acid headgroup: purple, oleic acid chain: magenta.

As the system is dynamic, oleic acid molecules move constantly within the layer—occasionally molecules get squeezed out of the layer and will move back into the layer at a different point where more space is available. However, with decreasing area of the water surface, more molecules squeeze out of the layer, as shown in Figure 27. Due to the restricted space they are not able to move back into the layer. Consequently, the system collapses and surface pressures start to decrease. In comparison with experimental isotherms the simulated system using the standard parameters collapses a lot earlier than expected from literature data. In the following sections, the parameters will be tuned in order to obtain closer agreement.

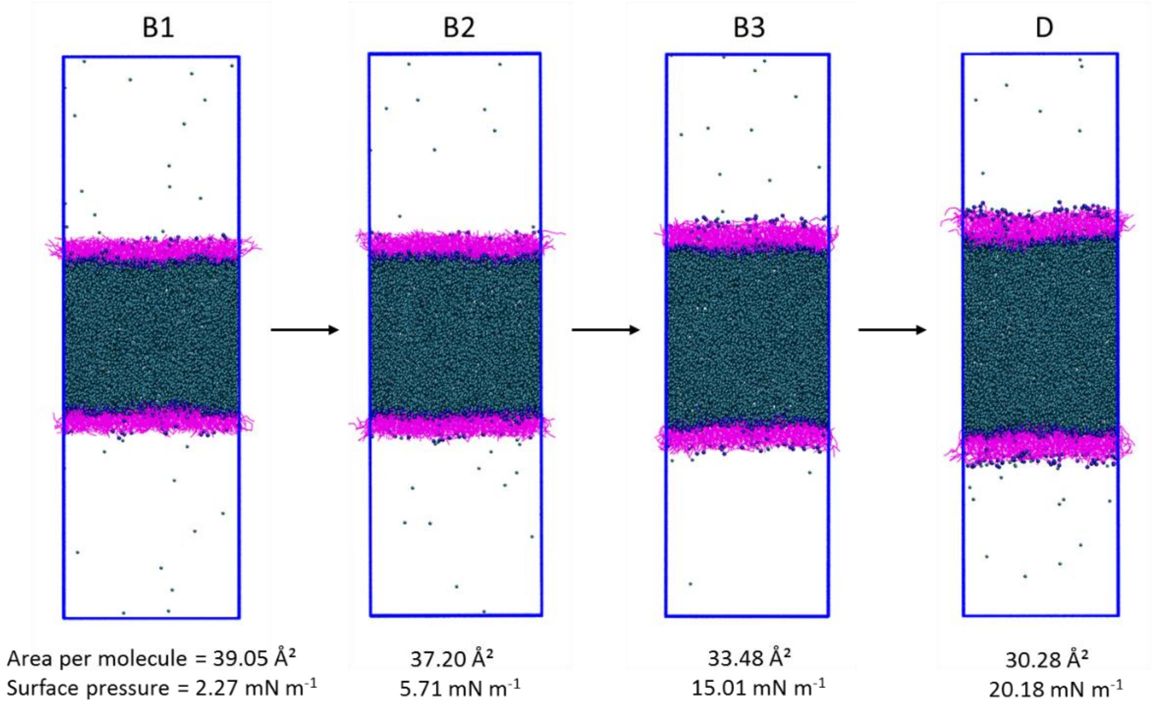

Figure 27: Comparison of oleic acid monolayers from low to high surface pressures at several points along the pressure-area isotherm (B1, B2, B3, D—points indicated on isotherm in Figure 25). Under compression more oleic acid molecules squeeze out of the layer, indicating a collapse of the system.
Oleic acid headgroup: purple, oleic acid chain: magenta, water: teal.

2.3.2 Pressure-Area Isotherms from Reduced Bead-to-Bead Distance Parameters

The second isotherm simulated in this work uses the same system set up as for the first pressure-area isotherm; however, the Martini default bead-to-bead distance was shortened from 0.47 nm to 0.32 nm between the oleic acid carboxyl headgroup bead and chain. This is in agreement with literature data for molecules containing a carboxyl group and carbon chain.[19] Furthermore, the force constant for the bond was increased to 7500 kJ mol^{-1} nm^{-2}. With the reduced bead-to-bead distance setup, eighteen monolayers with interfacial areas in the range of 28.71–38.88 Å^2 per molecule were generated.

The effective surface tension, γ_{vw^*}, is a vertical "tuning" parameter. As shown in Figure 28, when applying the previously used correction factor of 47 mN m^{-1} to the new isotherm, negative surface pressures are observed at some areas per molecule. This is not observed in experimental isotherms and hence the correction factor was adjusted to shift the isotherm so that the lowest point in the isotherm lies at a surface pressure of

0 mN m^{-1}. The correction factor for the systems with 'reduced bead-to-bead distance' was set to 49 mN m^{-1}.

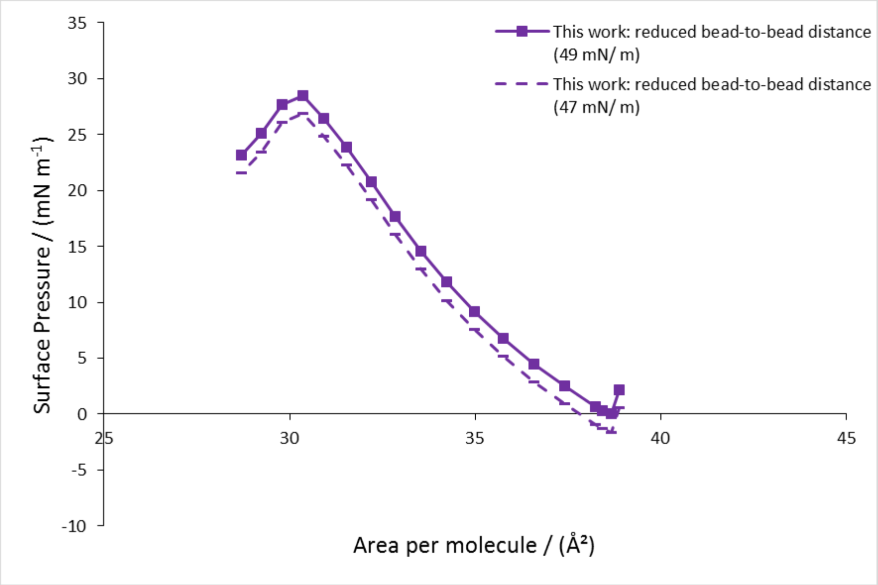

Figure 28: Fitting of the calculated pressure-area isotherm of oleic acid at the vacuum-water interface by the use of the effective surface tension, γ_{vw^*}, correction factor.

For the second isotherm, the bead-to-bead distance between the oleic acid P3 headgroup bead and the first bead of the chain (C2 bead), was reduced and the corresponding force constant was increased. This results in a reduced freedom of movement of the headgroup to the chain beads of the oleic acid molecules. As shown in Figure 29, the range in obtained surface pressures increases, indicating that the oleic acid molecules, with the new set of parameters, are able to pack more closely.

The highest obtained surface pressure for the second isotherm is 28.51 mN m^{-1}. This is slightly lower than but close to the expected equilibrium spreading pressures reported from experiments, which lie in the range of 29.0–32.0 mN m^{-1} as shown in Figure 29.

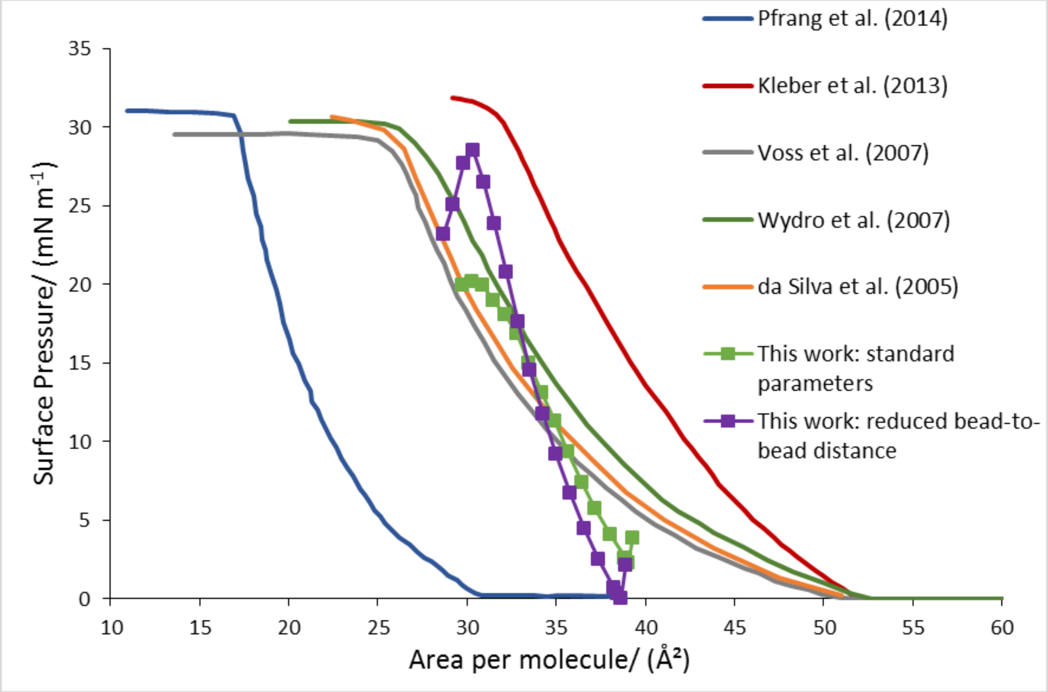

Figure 29: Pressure-area isotherm for oleic acid at the air-water interface with reduced bead-to-bead distance from simulations in comparison to previously generated isotherm with standard parameters and to experimental isotherms reported in the literature.[1-5] The following parameters were used for the isotherm with reduced bead-to-bead distance: P3-C2 = 0.32 nm, fc = 7500 kJ mol^{-1} nm^{-2}; C2-C2 = 0.47 nm, fc = 1250 kJ mol^{-1} nm^{-2}. Initial structures for the isotherm were generated from a compression run.

With the same parameters for the oleic acid molecules as used in the previous isotherm, the following isotherm was generated by expanding a surface film from a hexagonally close packed structure. To stabilise the close-packed structure, position restraints were initially applied to the carboxyl headgroup bead for each oleic acid molecule in the system, restricting their movement in the *x*/*y* directions. These restraints were slowly released after each 100 ns simulation time in steps of 200 kJ mol^{-1} nm^{-2} from 1000 kJ mol^{-1} nm^{-2} to 0 kJ mol^{-1} nm^{-2}, ensuring that a relaxed and stable structure is obtained.

In this setup it is possible to observe an equilibrium spreading pressure of 31 mN m^{-1}, as shown in Figure 30. This is in agreement with experimental isotherms.

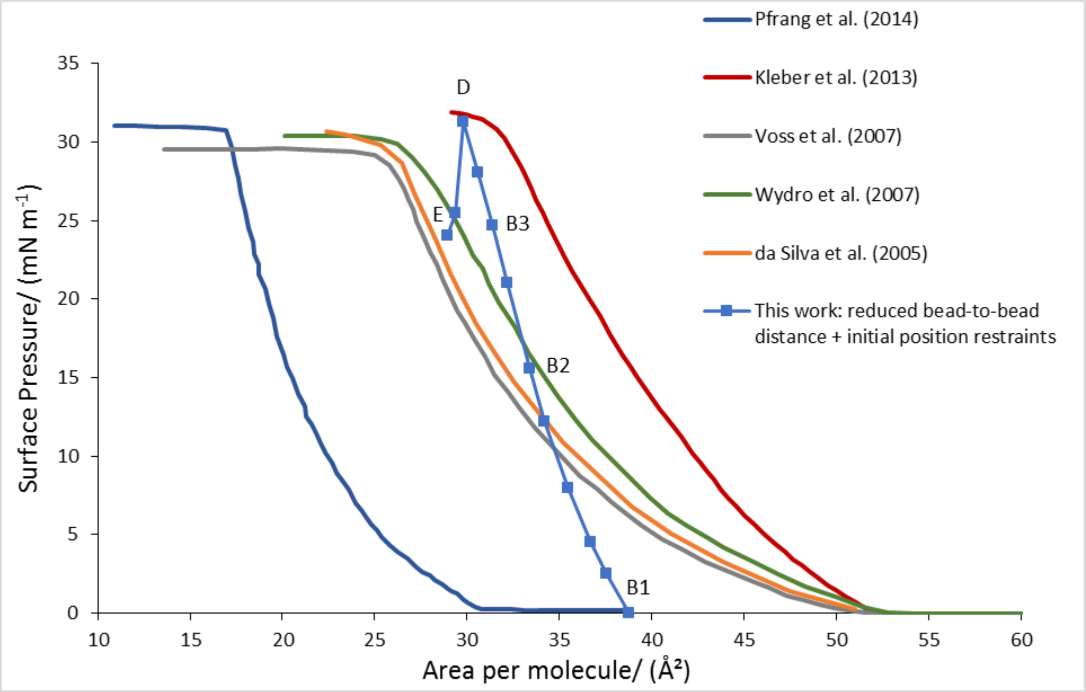

Figure 30: Pressure-area isotherm for oleic acid at the air-water interface from simulations in comparison to experimental isotherms reported in the literature.[1-5] The following parameters were used: P3-C2 = 0.32 nm, fc = 7500 kJ mol^{-1} nm^{-2}; C2-C2 = 0.47 nm, fc = 1250 kJ mol^{-1} nm^{-2}. Initial structures were produced from an expansion run from a hexagonally close packed structure, enabling the equilibrium surface pressure to be reached. Phase behaviour of simulated isotherm indicated: (B1, B2 and B3) liquid-expanded region, (D) equilibrium spreading pressure and (E) film collapse region.

Three repeats of calculations were performed whilst changing the random seed, as described in Chapter 1 in section 1.14, allowing determination of the 95 % confidence interval as shown in Figure 31. The error bar for the equilibrium spreading pressure, the highest point on the isotherm, is much larger than for the lower surface pressures, explaining the deviation in previously obtained measurements. The equilibrium spreading pressure is 28.48 ± 3.02 mN m^{-1}, which is in good agreement with experimental data.

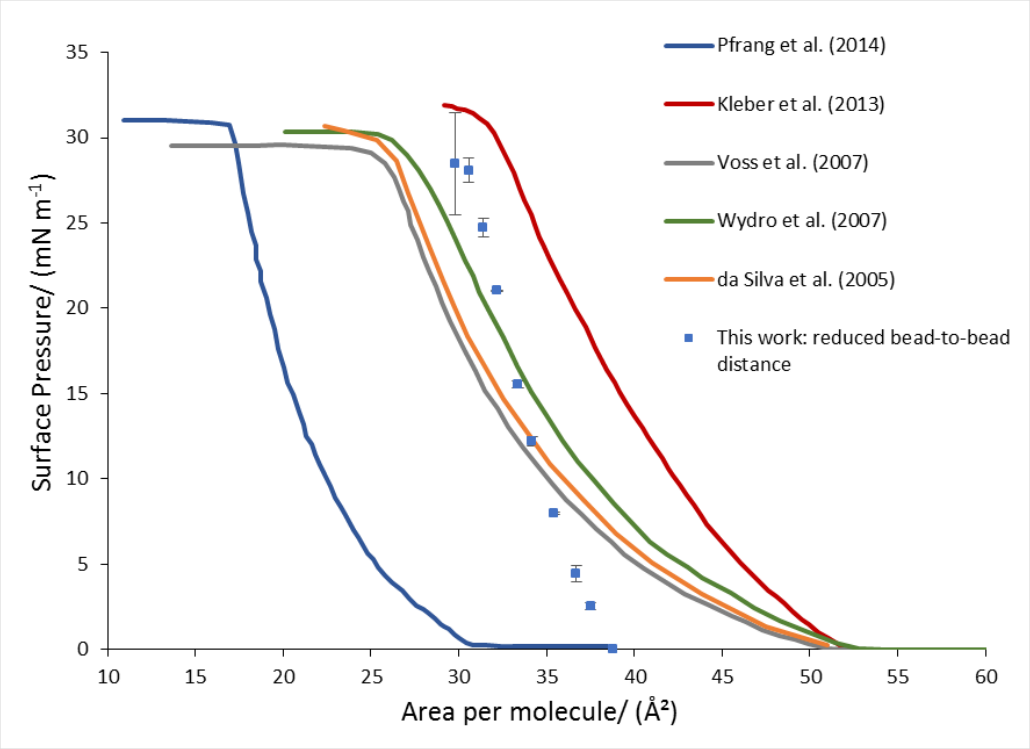

Figure 31: Pressure-area isotherm for oleic acid at the air-water interface compared to literature data.[1-5] Mean surface pressures, with 95 % confidence intervals shown. Errors at phase transitions are comparatively high, explaining deviations in simulations.

There is no observable phase change for oleic acid surface films with increasing surface pressures. Oleic acid chains stay disordered throughout, as shown in Figure 32, indicating that the surface film remains in the liquid-expanded phase. This agrees with the findings of experimental studies.[1-6]

The BAM image obtained by Sebastiani, for an oleic acid monolayer at low surface pressure (3 mN m^{-1}), shows an isotropic surface—the layer is in a liquid-expanded phase.[7] At the highest obtained surface pressure, the monolayer starts to collapse—with white spots on the BAM images being indicative of bulk liquid droplets forming on the surface. On a molecular scale, this can be observed in the simulations in this work by an increase in oleic acid molecules that squeeze out of the layer, as shown in Figure 33.

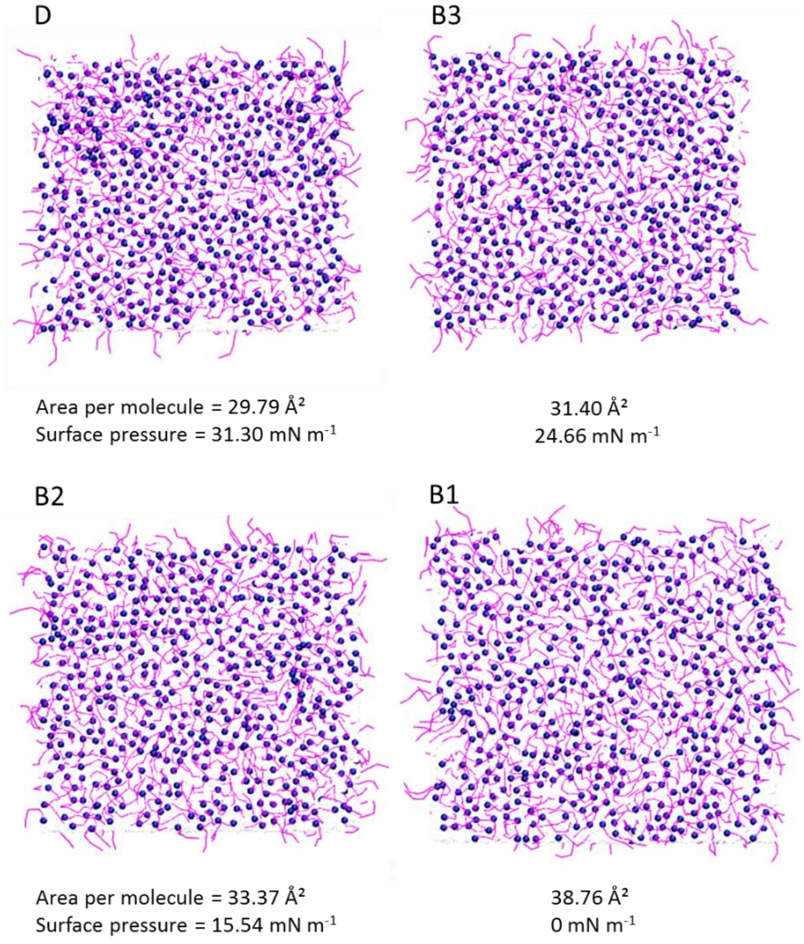

Figure 32: Top view of the upper oleic acid monolayer, using the reduced bead-to-bead distance parameters, at several points along the pressure-area isotherm (D, B3, B2, B1—points indicated on isotherm in Figure 30). Final images of the 1000 ns NVT run from initial structures generated from the hexagonally close packed starting structure. Oleic acid chains stay disordered under compression. Oleic acid headgroup: purple, oleic acid chain: magenta.

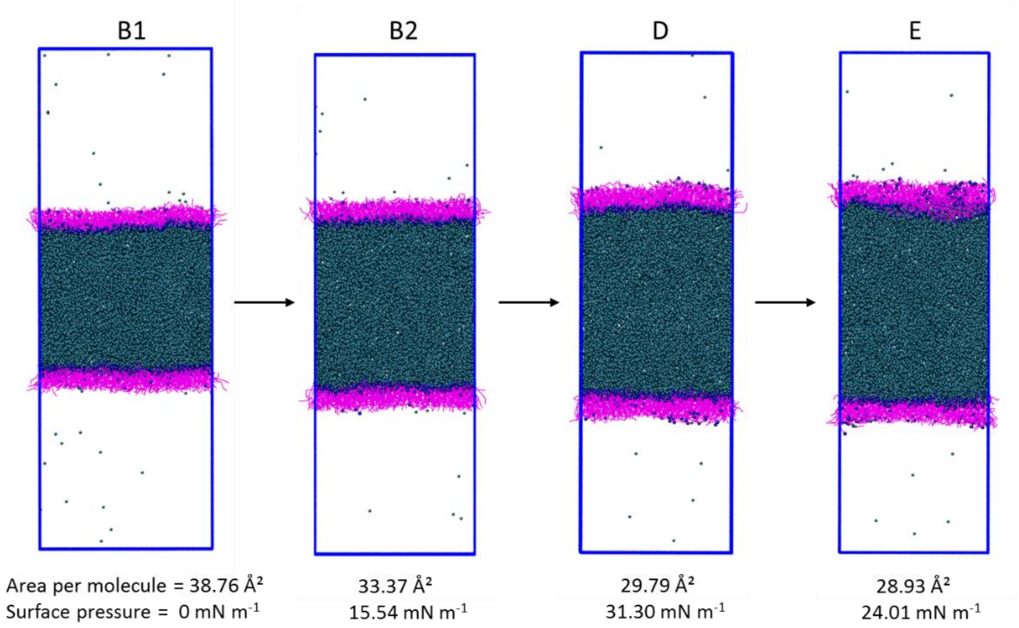

Figure 33: Comparison of oleic acid monolayers from low to high surface pressures at several points along the pressure-area isotherm (B1, B2, D, E—points indicated on isotherm in Figure 30). Oleic acid molecules turn in and out of the layers throughout simulations. Once the equilibrium surface pressure (D) is reached the layer starts to buckle, squeezing oleic acid molecules out of the layer, causing the monolayer to collapse (E). A reduction in surface pressures is observed. Oleic acid headgroup: purple, oleic acid chain: magenta, water: teal.

2.3.3 Angle Analysis

The monolayers were further analysed by looking at the internal angles of the molecules, in order to give insight into the packing of the molecules and structure of the monolayer. Angle (α) represents the tilting of the molecules in the monolayer with respect to the *z*-axis, and angle (θ), represents the angle between the oleic acid headgroup bead, cis-double bond bead and last bead of the chain, as shown in Figure 34. For details on the algorithm please see appendix A.1.

Analysis was performed for each of the three isotherms at three different points along each isotherm: one at or close to a surface pressure of 0 mN m^{-1}, one in the middle of each isotherm at a surface pressure of ca. 15 mN m^{-1} and one towards the highest point on each isotherm.

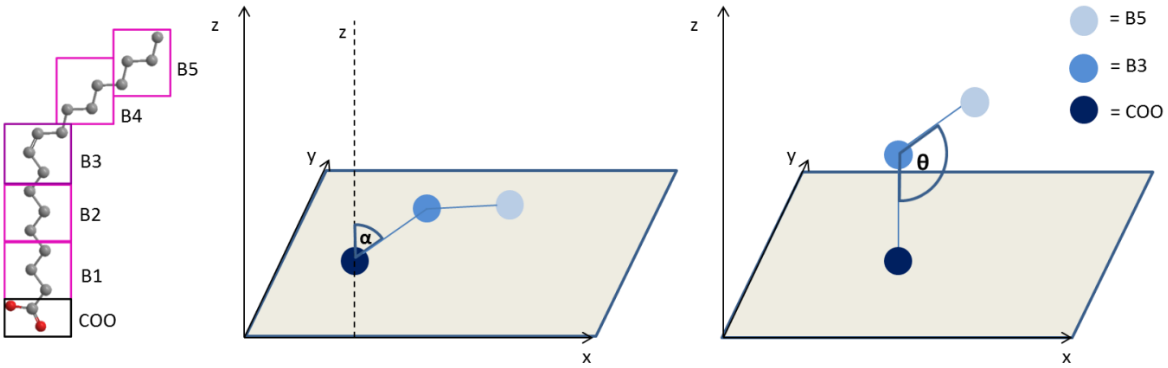

Figure 34: Representation of angles (α) and (θ) of an oleic acid molecule.

As represented in Figure 35, angle (α) shows the general trend that the more compressed the monolayers get, the smaller the tilting of the molecules. At a surface pressure of 0 mN m^{-1}, tilting of 30°–31° is observed. Once the monolayers are compressed, angle (α) gets reduced to 21° for the reduced bead-to-bead distance and initial position restraints with reduced bead-to-bead distance simulations and to 25° for simulations with standard parameters. This is due to the monolayers with standard parameters not packing as closely as the reduced bead-to-bead distance simulations and thus only reaching surface pressures of 19 mN m^{-1}.

In the graphs of the angle distribution of angle (θ) represented in Figure 35 it can be seen that, for all isotherms at high surface areas of water available per headgroup and low surface pressures, the peaks are, as expected, close to the equilibrium angle of 120°. When the systems are compressed, a decrease in area per molecule results in an increase in angle (θ). The largest angle (θ) is observed for the reduced bead-to-bead distance simulation with $\theta = 131°$ at a surface pressure of 29 mN m^{-1}.

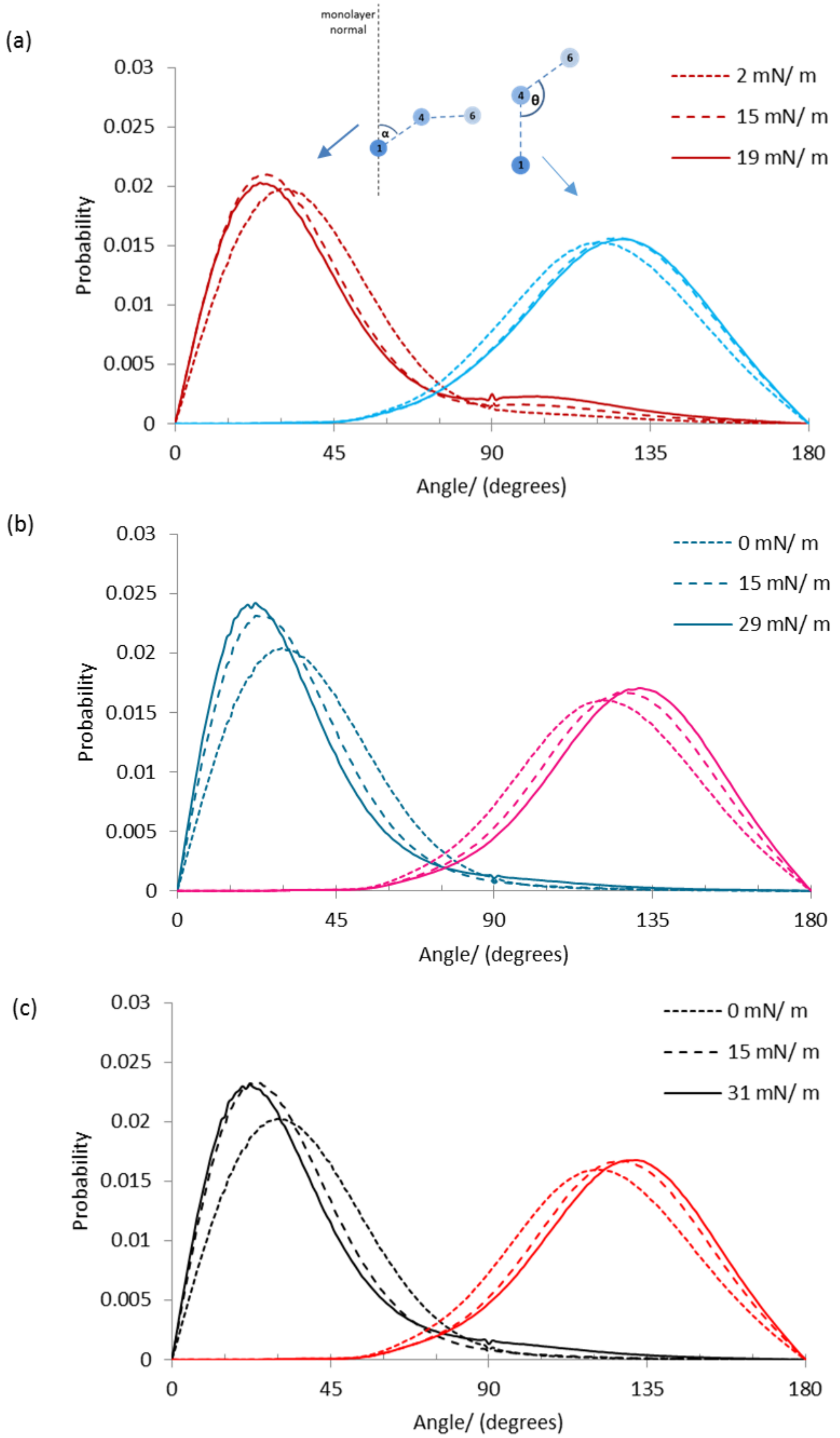

Figure 35: Angle distributions of angle (α) and (θ) for 3 surface pressures in each isotherm: (a) standard parameters (b) reduced bead-to-bead distance (c) reduced bead-to-bead distance + initial position restraints.

These observations allow conclusions to be drawn on the monolayer thickness. By reducing the area per molecule, the molecules become oriented in a way so as to increase their packing ability. Increasing the packing density of the molecules causes them to align straighter with respect to the *z*-axis. This suggests that the higher the packing density in the monolayer, the thicker the monolayer.

As the surface pressure increases the number of molecules where angle (α) is greater than 90° increases. This is most likely due to molecules moving out of the layer and changing orientation, as illustrated in Figure 36. Further analysis was performed on the system with a reduced bead-to-bead distance, which as shown previously gave the best agreement with experimental data. By correlating angle (α) for each molecule with the respective *z*-coordinate of the molecules headgroup, contour plots were produced, as shown in Figure 37. The contour plots show both the top monolayer and the bottom monolayer. In the plots, each monolayer shows two distinct regions—the highest density regions indicating the molecules within the layer and the second regions at higher angles indicating the molecules that have moved out of the layer. The contour plots in Figure 37 show that, under compression, more molecules move out of the layer.

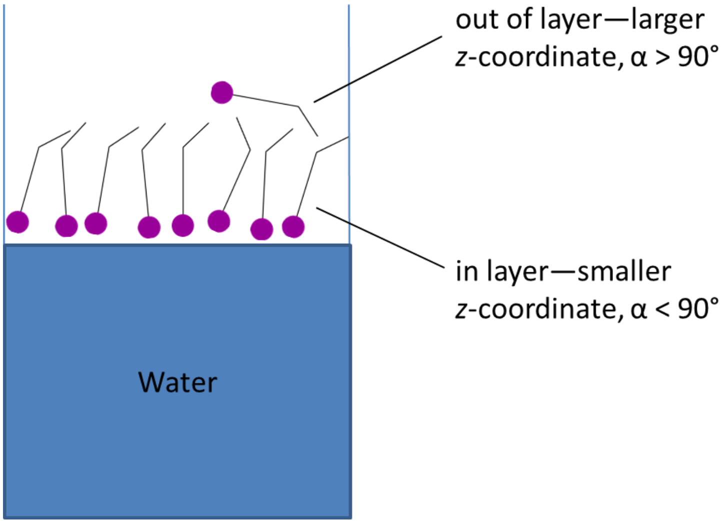

Figure 36: Illustration of top monolayer in the simulation box, with molecules referred to as 'in the monolayer' and molecules referred to as 'out of the monolayer' shown.

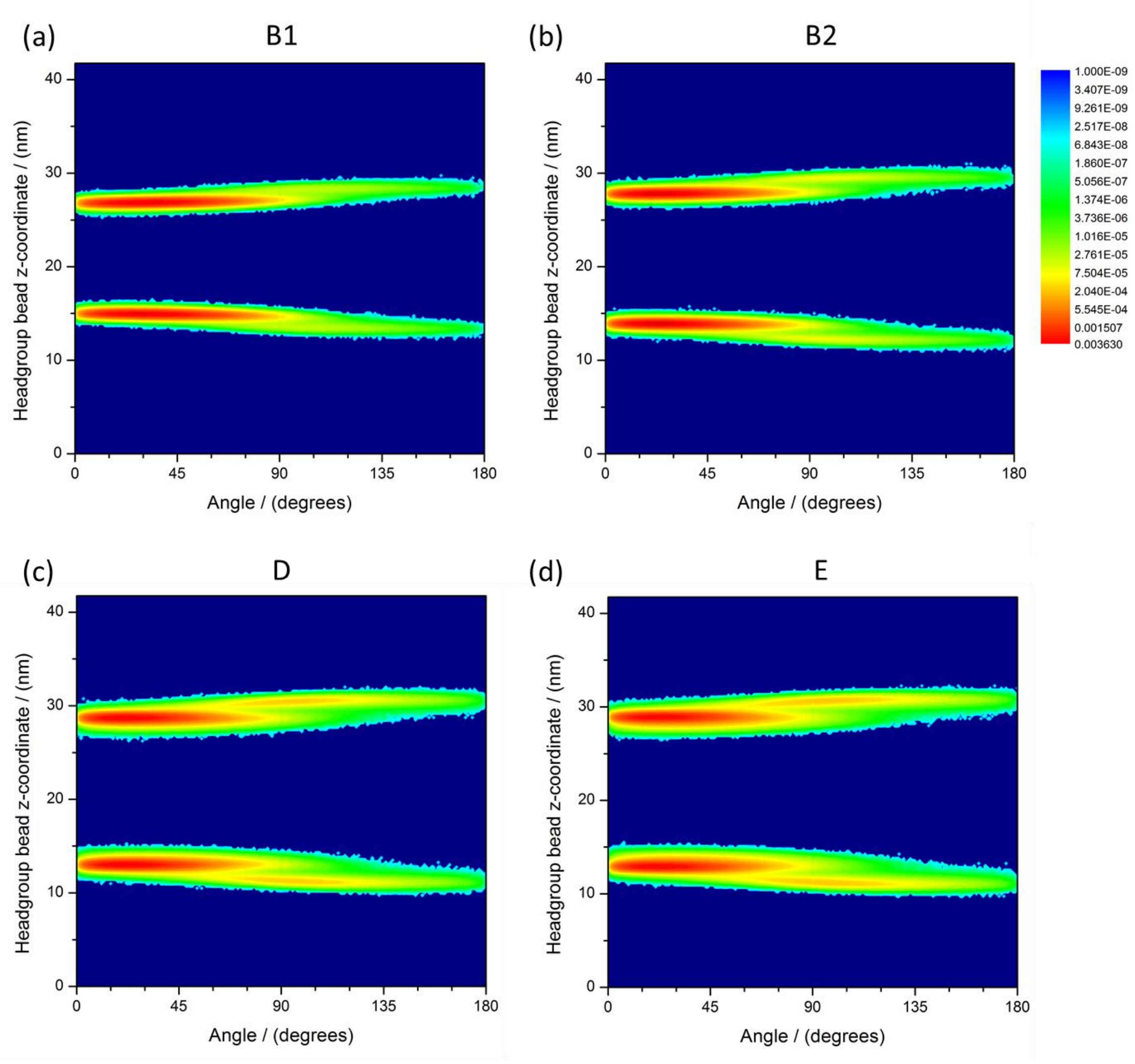

Figure 37: Contour plots showing the probability of finding the headgroup of a molecule at a certain *z*-coordinate with respect to the molecules angle (α) for two systems where monolayers in (a) (B1) have an area per molecule of 38.76 Å^2 and a surface pressure of 0 mN m^{-1}, monolayers in (b) (B2) have an area per molecule of 33.37 Å^2 and a surface pressure of 15.54 mN m^{-1}, monolayers in (c) (D) have an area per molecule of 29.79 Å^2 and a surface pressure of 31.30 mN m^{-1}, and monolayers in (d) (E) have an area per molecule of 29.37 Å^2 and a surface pressure of 25.49 mN m^{-1}. Points B1, B2, D and E are indicated on pressure-area isotherm in Figure 30.

Determining the lowest density regions in the contour plots between the two regions in each monolayer, as illustrated in appendix A.2, allowed for the approximation of the percentage of molecules that move out of the layer for each monolayer during the production time. As shown in Figure 38, the general trend shows that the lower the area per molecule and the higher the surface pressure, the more molecules move out of the layer.

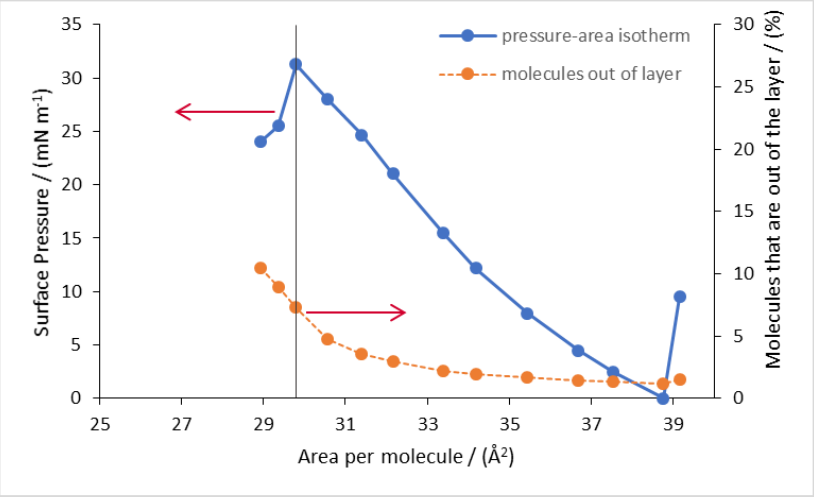

Figure 38: Pressure-area isotherm of oleic acid and percentage of oleic acid molecules that are out of the layer during the production time, based on calculations from the contour plots, against the area per molecule. Vertical line indicates the percentage of molecules that move out of the layer at the equilibrium spreading pressure (area per molecule of 29.79 Å^2 and a surface pressure of 31.30 mN m^{-1}). Arrows indicate relevant axes.

Until a surface pressure of 15 mN m^{-1} is reached, less than 2 % of molecules move out of the layer. After this point the percentage of molecules that move out of the layer increases—at the equilibrium spreading pressure, 7.3 % of molecules are not in the normal monolayer position. Further compression results in a drop in surface pressures; this is due to a further increase in molecules that move out of the layer. The area per molecule refers to the available area per fatty acid molecule in the monolayer; however, if a significant proportion of these molecules move out of the layer, less molecules are in the normal monolayer position explaining the reduction in surface pressure—at this point the monolayer has collapsed.

The break-down of the monolayer in simulations at high surface pressures agrees well with experimental data—BAM images produced by Sebastiani show a homogenous surface layer at a low surface pressure, whereas at the equilibrium spreading pressure, bright white spots appear, indicating the collapse of the system.[7] This can be correlated to simulation data, with a significantly higher percentage of molecules moving out of the layer at the highest surface pressure.

2.4 Conclusions

The results presented in this chapter show that using default Martini parameters for oleic acid does not give a good agreement with experimental data. However, increasing the force constant and decreasing the bead-to-bead distance between the headgroup and chain allowed experimental results to be reproduced. It is now important to see whether the parameters developed for oleic acid can be directly applied to other fatty acid molecules, or if further work is needed to optimise these.

Analysis of oleic acid monolayers at several points along the isotherm allowed for insight into the structure of the surface film. A decrease in the surface area per molecule and consequent increase in surface pressures caused the molecules to align straighter with respect to the *z*-axis. This implies that an increase in the film packing density results in an increase in film thickness.

Further analysis of the monolayers, over the production time, allowed molecules that are inside the layer and have the typical monolayer configuration to be distinguished from molecules that have moved out of the layer. This was done by calculating the tilt of the molecules with respect to the *z*-axis and considering the position of the molecules' headgroup. It was shown that the smaller the area per molecule, the more oleic acid molecules move out of the layer.

2.5 References

1. C. Pfrang, F. Sebastiani, C. O. M. Lucas, M. D. King, I. D. Hoare, D. Chang and R. A. Campbell, *Phys. Chem. Chem. Phys.*, 2014, **16**, 13220-13228.
2. A. M. Gonçalves da Silva and R. I. S. Romão, *Chem. Phys. Lipids*, 2005, **137**, 62-76.
3. L. F. Voss, M. F. Bazerbashi, C. P. Beekman, C. M. Hadad and H. C. Allen, *J. Geophys. Res.*, 2007, **112**.
4. J. Kleber, K. Laß and G. Friedrichs, *J. Phys. Chem. A*, 2013, **117**, 7863-7875.
5. P. Wydro, B. Krajewska and K. Hąc-Wydro, *Biomacromolecules*, 2007, **8**, 2611-2617.
6. E. Gonzalez-Labrada, R. Schmidt and C. E. DeWolf, *Phys. Chem. Chem. Phys.*, 2007, **9**, 5814-5821.
7. F. Sebastiani, *Neutron Reflectometry and Ellipsometry Applied to Atmospheric Night-time Oxidation*, University of Reading Ph.D., 2014.
8. M. W. A. Skoda, B. Thomas, M. Hagreen, F. Sebastiani and C. Pfrang, *RSC Adv.*, 2017, **7**, 34208-34214.
9. L. Monticelli, S. K. Kandasamy, X. Periole, R. G. Larson, D. P. Tieleman and S.-J. Marrink,(2008), *The MARTINI Forcefield: Extension to Peptides and Proteins*, http://md.chem.rug.nl/cgmartini/images/parameters/ITP/martini_v2.1_aminoacids.itp, [August 2014]
10. S. J. Marrink, H. J. Risselada, S. Yefimov, D. P. Tieleman and A. H. de Vries, *J. Phys. Chem. B*, 2007, **111**, 7812-7824.
11. M. G. Saunders and G. A. Voth, *Annu. Rev. Biophys.*, 2013, **42**, 73-93.
12. T. Jue, S. H. Risbud, M. L. Longo and R. Faller, *Biomembrane Frontiers: Nanostructures, Models, and the Design of Life*, Humana Press, 2009.
13. K. Bernardino and A. F. de Moura, *Langmuir*, 2015, **31**, 10995-11004.
14. D. v. d. Spoel, E. Lindahl, B. Hess and t. G. d. team,(2013), *GROMACS User Manual version 4.6.5*, www.gromacs.org, [August 2016]
15. J. Lemkul,(2008), *Gromacs Tutorial: Lysozyme in Water*, www.bevanlab.biochem.vt.edu/Pages/Personal/justin/gmx-tutorials/lysozyme, [March 2014]
16. S. Baoukina, L. Monticelli, S. J. Marrink and D. P. Tieleman, *Langmuir*, 2007, **23**, 12617-12623.
17. S. J. Marrink and D. P. Tieleman, *Chem. Soc. Rev.*, 2013, **42**, 6801-6822.

18. S. J. Marrink, H. J. Risselada, S. Yefimov, D. P. Tieleman and A. H. d. Vries,(2007), *The MARTINI forcefield: coarse grained model for biomolecular simulations*, http://md.chem.rug.nl/cgmartini/images/parameters/ITP/martini_v2.0.itp, [August 2014]

19. L. Monticelli, S. K. Kandasamy, X. Periole, R. G. Larson, D. P. Tieleman and S.-J. Marrink, *J. Chem. Theory Comp.*, 2008, **4**, 819-834.

Chapter 3

Stearic Acid Pressure-Area Isotherms

3.1 Stearic Acid Pressure-Area Isotherms

This chapter summarises the results for stearic acid pressure-area isotherms produced from simulations with differing sets of parameters. Stearic acid, also known as octadecanoic acid, is a saturated 18-carbon chain acid. It is one of the main fatty acids reported in marine aerosols, and is one of the prominent fatty acids emitted through meat cooking processes. It has low solubility in water and a low vapour pressure making it, with its long carbon chain, a good surfactant.[1]

In the literature, several pressure-area isotherms for stearic acid at the air-water interface are reported. In this introduction we will discuss a selected range of experimentally determined isotherms, shown in Figure 39.

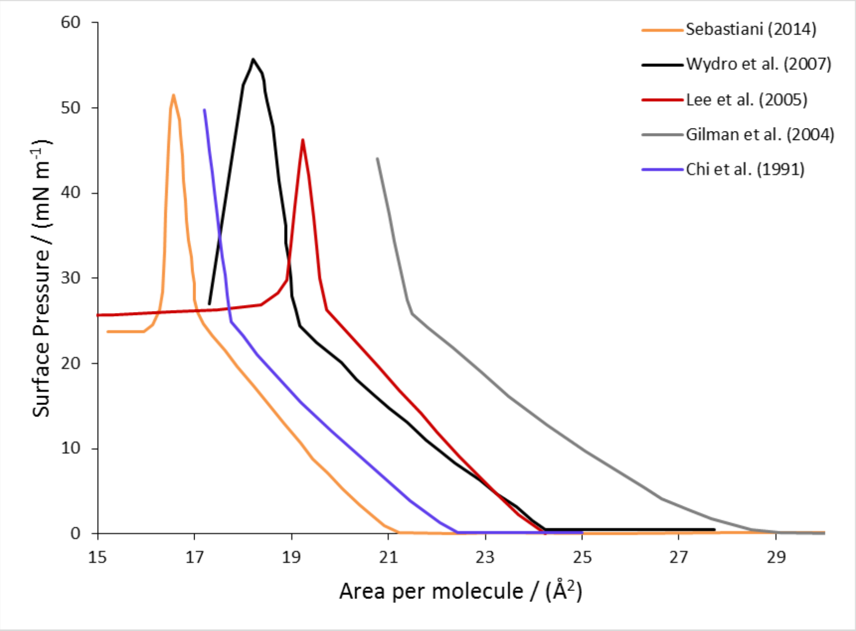

Figure 39: Experimental pressure-area isotherms for stearic acid at the air-water interface.[1-5]

Gilman *et al.* state that below a surface pressure of 1 mN m^{-1}, stearic acid molecules form an expanded phase.[1] Compression leads to the alignment of the molecules' chains, forming an ordered stable film.[1]

The phase transition point for the pressure area isotherm by Lee *et al.* lies at 27 mN m^{-1} with the collapse pressure at 47 mN m^{-1}.[4] Wydro *et al.* report a phase transition from the liquid-condensed to the solid state at 25 mN m^{-1}. The equilibrium spreading pressure lies in this case at a surface pressure of 55 mN m^{-1}.[3]

Gericke *et al.* measured pressure-area isotherms of stearic acid both on a pure water subphase (pH 6), and on a subphase at pH 2 by adding 1 M HCl solution to the subphase, and found that the order of the stearic acid chains in the monolayers is comparable between the subphases.[6] Both isotherms have a phase transition from the liquid-condensed to the solid phase. At both pH 6 and pH 2, the phase transition point occurs at an area per molecule of 19.9 $Å^2$ and a surface pressure of 25.8 ± 0.4 mN m^{-1} for pH 6 and 26.0 ± 0.2 mN m^{-1} for pH 2.

Commonly, stearic acid isotherms show two distinct regions: condensed liquid phase and solid state. This phase behaviour is represented on the molecular level by an increase in ordering of the fatty acid carbon chains under compression of the monolayer. All isotherms reported for stearic acid, represented in Figure 39, show a change in gradient as the phase changes, with the hydrophobic chains of the molecules aligning.

The equilibrium spreading pressures, at which point the monolayers of stearic acid are in a solid state, lie between 42–55 mN m^{-1} for the reported isotherms. Further compression results in a collapse of the monolayer, represented by a sharp decrease in surface pressures.

Possible reasons for variations in reported equilibrium spreading pressures, position and gradient of the experimental isotherms are due to differences in compression rate, geometry of experimental set-up and type of apparatus, experimental artifacts such as leakage, spreading solvent used, and pH of subphase.

The phase behaviour of stearic acid, reflected in the isotherms, differs from the previously discussed behaviour of oleic acid. Due to the saturated linear carbon chain, stearic acid is able to pack more closely and hence phase changes are clearly observed.

3.2 Method

3.2.1 Stearic Acid Mapping

Stearic acid, $C_{18}H_{36}O_2$, has the same chain length as oleic acid, albeit with two more hydrogen atoms, making it a saturated fatty acid. The coarse-grained mapping for this molecule was altered during the course of the project to reach a good agreement with experimental data and will be discussed in the following paragraph.

There are many possible ways to map stearic acid, two of which are shown in Figure 40. The headgroup in both cases is represented by a P3 bead, in accordance with the previously mapped oleic acid. This is followed by 4 × C1 beads or 5 × C2 beads, respectively.

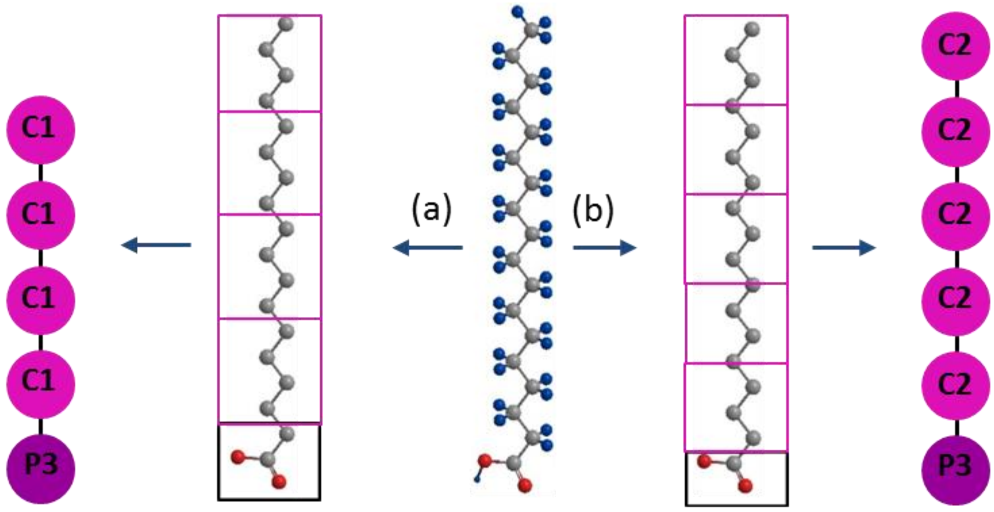

Figure 40: All-atom (centre image) in comparison to coarse-grained mapping. (a) Four C1 beads representing the hydrophobic stearic acid chain (pink) (b) Five C2 beads representing the hydrophobic stearic acid chain (pink). In both cases (a) and (b) a P3 bead represents the hydrophilic stearic acid headgroup (purple).

Systems were set up using both mapping (a) and (b), with details of all 4 systems given in Table 7.

Simulation Set	Stearic Acid Parameters	Bead-to-Bead Distance (nm)	Force Constant (kJ mol^{-1} nm^{-2})	Comments
1	P3-C2 C2-C2	0.47 0.47	1250 1250	Standard bead-to-bead distance and standard force constant
2	P3-C2 C2-C2	0.32 0.47	7500 1250	Reduced bead-to-bead distance and increased force constant
3	P3-C1 C1-C1	0.32 0.47	7500 1250	Reduced bead-to-bead distance and increased force constant Change to C1 beads in chain
4	P3-C1 C1-C1	0.44 0.47	2550 1250	Headgroup-Chain distance and force constant fitted to all atom simulations

Table 7: Summary of stearic acid mapping in all four simulation sets.

Each mapping and the corresponding results will be discussed in turn in the following paragraphs.

Simulation Set 1: the first isotherm uses the standard Martini bead-to-bead distances (0.47 nm) and force constants (1250 kJ mol^{-1} nm^{-2}) for all bonded beads in the system. The bead types are based on the previously discussed oleic acid mapping (Chapter 2, section 2.3.2). A P3 bead representing the hydrophilic headgroup and 5 C2 beads representing the hydrophobic chain are used.

Simulation Set 2: for the second isotherm, the bead-to-bead distances and force constants of stearic acid were based on the final parameterisation of oleic acid, with the chosen parameters represented in Table 7. The headgroup bead is represented by a P3 bead, and the distance between this bead and the first bead of the carbon chain was reduced from the standard Martini bead-to-bead distance of 0.47 nm to 0.32 nm. The force constant was increased to 7500 kJ mol^{-1} nm^{-2}. The carbon chain is mapped to 5 C2 beads and the standard Martini bond length (0.47 nm) and force constant of 1250 kJ mol^{-1} nm^{-2} are used here.

Simulation Set 3: the chain length of stearic acid makes it feasible to use two different mappings when it comes to its carbon chain. The previous two simulation sets use 5 C2 beads to represent the carbon chain. However, even though both descriptions are feasible, the typical Martini bead mapping incorporates 4 heavy atoms per interaction site. As this description conforms more rigidly to the Martini bead description, and is less computationally expensive due to the decrease in the number of interaction sites, the new mapping was adopted. Hence, for the following simulation sets, the hydrophilic headgroup of stearic acid is represented by one P3 bead, and the carbon chain by 4 C1 beads. Simulation Set 3 uses the same parameters for bead distances and force constants as in Simulation Set 2.

Simulation Set 4: in the case of a headgroup bead, containing fewer than 4 heavy atoms bonded to a chain bead, it is advisable to tune the parameters for both the bead distance and force constant to obtain an accurate representation of the underlying chemical structure. For bonded beads in the Martini force field, the standard equilibrium bead distance is 0.47 nm with a force constant of 1250 kJ mol^{-1} nm^{-2}.[7] In the literature it is suggested that the bead-to-bead distance between an acid headgroup and carbon chain is better represented by a shorter bond length (0.32 nm) and higher force constant (7500 kJ mol^{-1} nm^{-2}).[8] As previously shown in Chapter 2, this was tested in simulations of pressure-area isotherms for oleic acid and proved to provide a good agreement with experimental data for the system. However, as will be seen later, stearic acid isotherms produced with these parameters did not provide an accurate description of the molecule, with monolayers being somewhat too stable.

In order to obtain a better description of the underlying chemical structure, comparison of molecules simulated with all-atom models provide a particularly useful tool to optimise the bonded parameters in the coarse-grained model. Optimisation of the bonded parameters for stearic acid within the Martini force field was achieved by performing all-atom simulations using the CHARMM-36 force field and the GROMACS-5 simulation software. Details of parameters for Simulation Set 4, based on CHARMM-36 all-atom simulations, are given in the following section.

3.2.2 CHARMM-36 Simulations of Stearic Acid

Simulations were set up in a box of dimensions 5.5 nm × 4.8 nm × 42 nm. Two monolayers were set up, with 81 molecules in each layer, corresponding to an area per molecule of 33 Å^2 /molecule. This area per molecule was chosen so that molecules are in the liquid-expanded phase and have enough space to move without being restrained. The space between the molecules' headgroups was filled with TIP3P water molecules. Air in the model is approximated as a vacuum.

For all CHARMM simulations in this work a 2 fs time step was used. Fast smooth Particle-Mesh Ewald was used for long-range electrostatics.[9] The cut-off range for short-range electrostatics was set to 1.2 nm. A switch cut-off was applied between 1.0–1.2 nm for van der Waals interactions. All bonds with hydrogen atoms were constrained. Simulations were performed in the NVT ensemble for 4 ns (1 ns equilibration time and 3 ns production time). Only the production time was used for analysis. Temperature was controlled separately for each fatty acid and water molecule with a Velocity-rescale heat bath and a coupling time constant of 0.1 ps at 300 K.

From the CHARMM force field simulations, the centre of mass of the groups of atoms describing the equivalent coarse-grained headgroup bead and the first bead of the carbon chain in the stearic acid molecules were determined. These were based on mapping scheme (a) in Figure 40, assuming 4 atoms per bead. Determining the position of the centre of mass allowed the distribution of distances between the bead sites to be determined from CHARMM-36 simulations. The distribution was then normalised and fitted to a harmonic potential, with a force constant, k_r, and bead-to-bead equilibrium distance, r_e, as variables:

$$\ln(\text{Probability}) = \frac{-k_r(r - r_e)^2}{k_B T} \tag{36}$$

Data derived from CHARMM-36 simulations with the corresponding fit to a harmonic potential are shown in Figure 41.

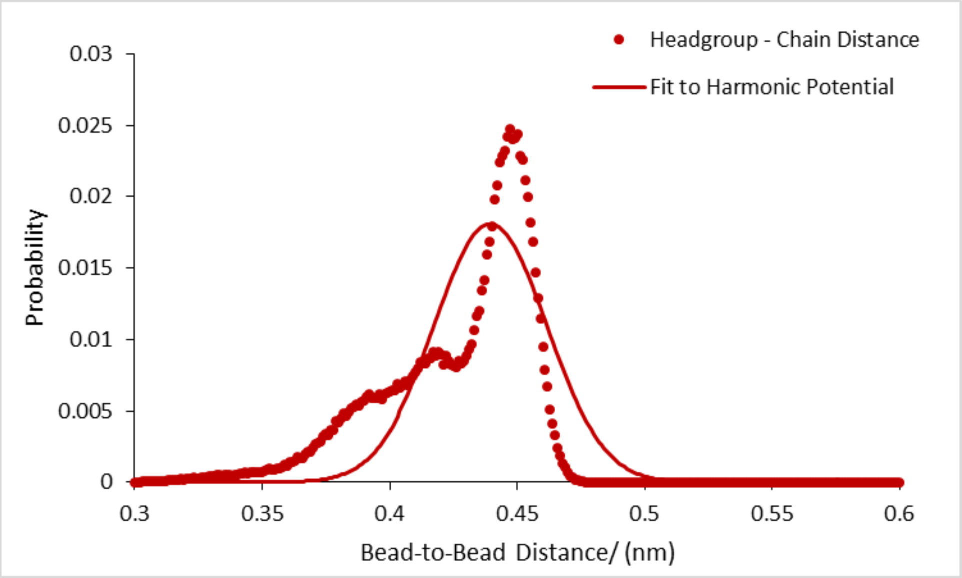

Figure 41: Bead-to-bead distance between (B1–B2) the stearic acid headgroup bead (P3) and the first bead of the carbon chain (C1) from CHARMM-36 simulations. Harmonic potential, using both the bead distance and force constant as variables.

For Simulation Set 4, the parameters for the equilibrium distance and force constant for the bond between the headgroup and the first bead of the chain were adapted from CHARMM-36 simulations. Values have been rounded to the nearest 50, as appears to have been the approach used by Marrink *et al.*[7]

A known limitation of coarse-grained models is, that the reduction in degrees of freedom by the use of beads, does not allow the same chain flexibility as found in all-atom simulations. Hence, a fit of the data to a harmonic curve, as shown in Figure 41, does not perfectly describe the all-atom distribution. This is a known limitation of coarse-grained models, as the coarse-grained philosophy is to give good approximations of the system, using less detail than the reference model.

The remaining beads in the carbon chain of stearic acid are parameterised according to the standard Martini mapping, with parameters summarised in Table 8. This is in accordance with the previously mapped oleic acid, where only the headgroup to chain distance and force constant were altered.

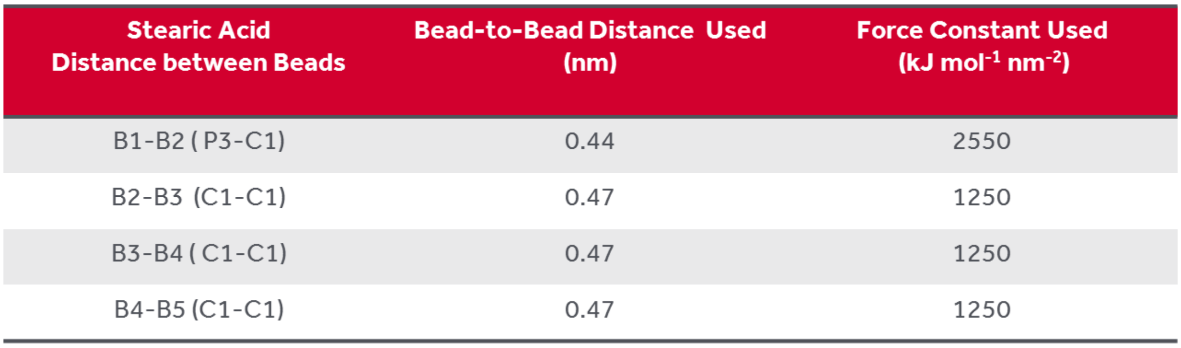

Stearic Acid Distance between Beads	Bead-to-Bead Distance Used (nm)	Force Constant Used (kJ mol^{-1} nm^{-2})
B1-B2 (P3-C1)	0.44	2550
B2-B3 (C1-C1)	0.47	1250
B3-B4 (C1-C1)	0.47	1250
B4-B5 (C1-C1)	0.47	1250

Table 8: Bead-to-bead distances and force constants for stearic acid in simulation set 4.

3.2.3 Coarse-Grained Simulations

All coarse-grained simulations in this chapter were run using the GROMACS (4.6.5) simulation software in combination with the Martini force field. Simulations were performed as described in section 2.2.4 in Chapter 2.

3.3 Results and Discussion

3.3.1 Simulation Set 1

To obtain the first pressure-area isotherm, the standard Martini force field parameters were used. A box of size 11.3 nm × 9.8 nm × 42 nm was created, containing 968 stearic acid molecules (484 in each monolayer), 11850 water beads and 1208 antifreeze beads. Initially, the stearic acid molecules in the monolayers are hexagonally close packed. Using the NPT ensemble, this initial structure was expanded laterally. Snapshots to be used as starting structures were taken from the expansion runs.

An isotherm was produced for stearic acid at the air-water interface, as shown in Figure 42. The correction factor was set to 91 mN m^{-1} to shift the lowest point on the isotherm to a surface pressure of 0 mN m^{-1}.

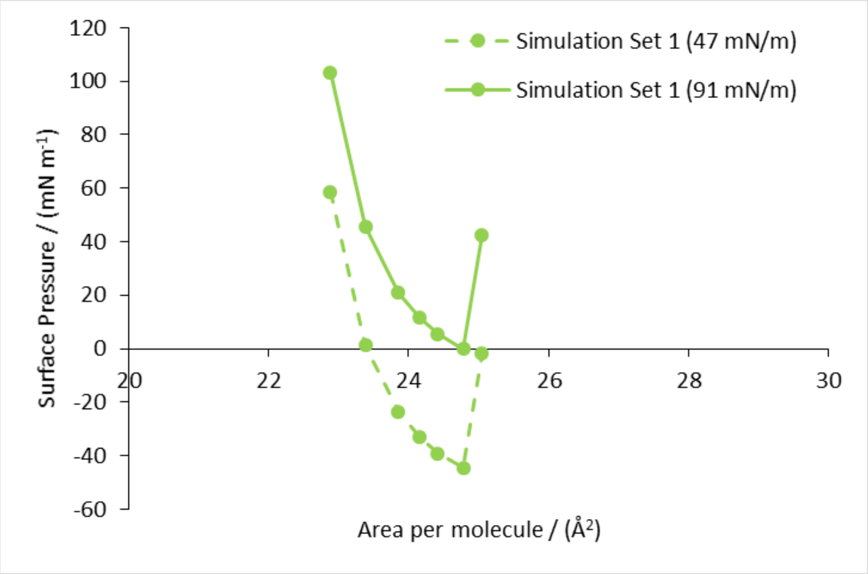

Figure 42: Correction factor, $\gamma_{vw}*$, for the stearic acid isotherm produced from standard Martini parameters.

Surface pressures increase once the stearic acid chains start to order, as shown in Figure 44. However, in comparison to experimental data (Figure 43), the range of surface pressures obtained for the stearic acid monolayers is too wide. At a surface pressure of 103 mN m^{-1}, as shown in Figure 45, stearic acid molecules are well-ordered. There are no molecules that are not in the typical monolayer configuration, indicating a stable layer.

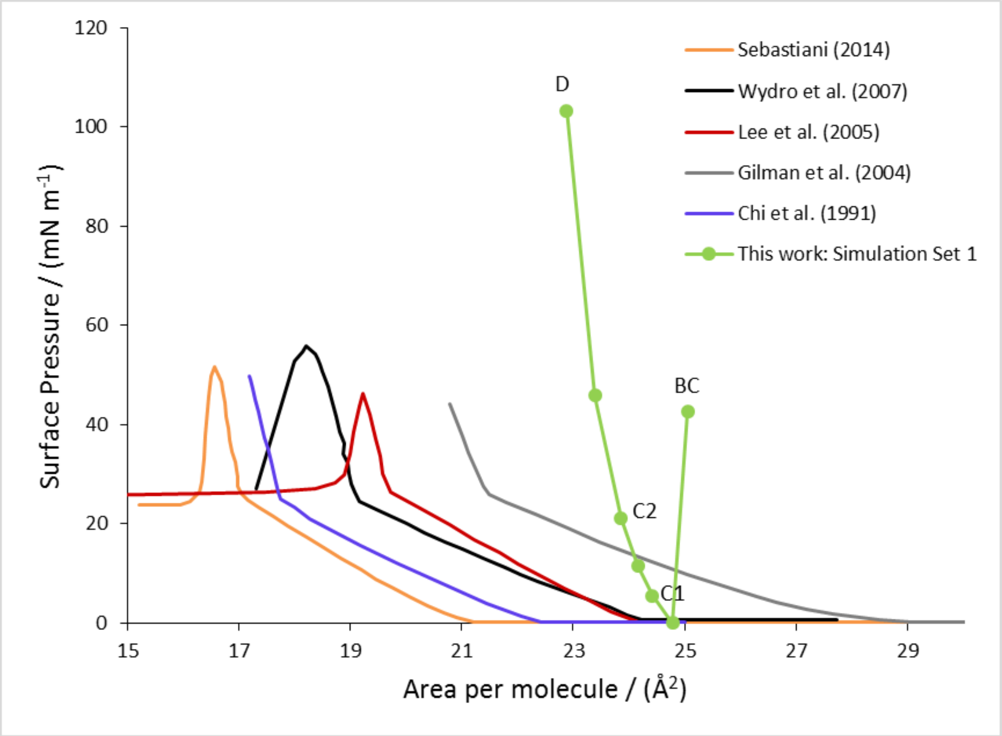

Figure 43: Pressure-area isotherm for stearic acid at the air-water interface from simulations in comparison to experimental isotherms reported in the literature.[1, 3-6] Simulation Set 1: Stearic acid represented by P3, C2, C2, C2, C2, C2. Bead distances and force constants used; P3-C2: $r_e = 0.47$ nm, $k_e = 1250$ kJ mol^{-1} nm^{-2}; C2-C2: $r_e = 0.47$ nm, $k_e = 1250$ kJ mol^{-1} nm^{-2}. Phase behaviour of simulated isotherm indicated: (BC) liquid-expanded liquid-condensed coexisting region, (C1 and C2) liquid-condensed region and (D) equilibrium spreading pressure.

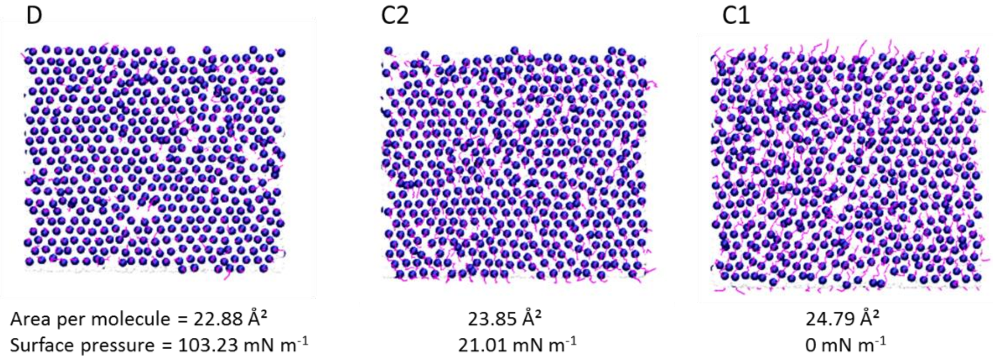

Area per molecule = 22.88 Å²
Surface pressure = 103.23 mN m^{-1}

23.85 Å²
21.01 mN m^{-1}

24.79 Å²
0 mN m^{-1}

Figure 44: Top layer view of the stearic acid monolayers at several points along the pressure-area isotherm of simulation set 1 (D, C2, C1—points indicated on isotherm in Figure 43). An increase in ordering of the stearic acid chains causes an increase in surface pressures. Stearic acid headgroup: purple, stearic acid chain: magenta.

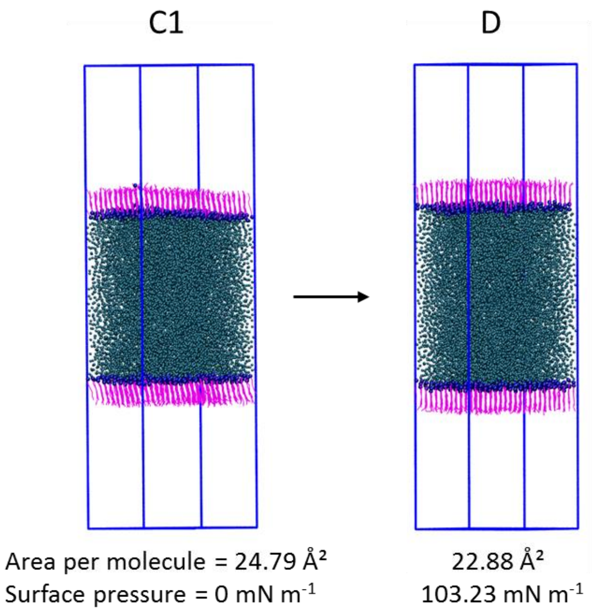

Figure 45: Comparison between stearic acid monolayers at the lowest and highest surface pressure in the pressure-area isotherm (C1, D—points indicated on isotherm in Figure 43). Stearic acid headgroup: purple, stearic acid chain: magenta, water: teal.

For both oleic acid, as shown in the previous chapter, and stearic acid, as shown in this section, the standard Martini force field parameters do not give an accurate representation of the system compared to experimental data. Hence, the next section will adapt reduced bead-to-bead distance and increased force constant parameters, previously used for oleic acid, for the stearic acid molecules in the system.

3.3.2 Simulation Set 2

The second isotherm simulated in this work uses the same bead definitions as for the first pressure-area isotherm; however, the Martini default bead-to-bead distance was reduced from 0.47 nm to 0.32 nm between the stearic acid carboxyl headgroup beads and chains. Furthermore, the force constant for the bond was increased to 7500 kJ mol^{-1} nm^{-2}. A box of size 18 nm × 18 nm × 42 nm was created, containing 882 stearic acids (441 in each monolayer), 12852 water beads and 1300 antifreeze beads. This results in an area per molecule of 73 Å^2 for the stearic acids in the monolayers, meaning molecules are in the two-dimensional gas phase, which is similar to the starting set ups used in experiments. This initial structure was compressed laterally. The correction factor, $\gamma_{vw}*$, was set to 67 mN m^{-1}, shifting the lowest point on the isotherm to a surface pressure of 0 mN m^{-1}, as shown in Figure 46.

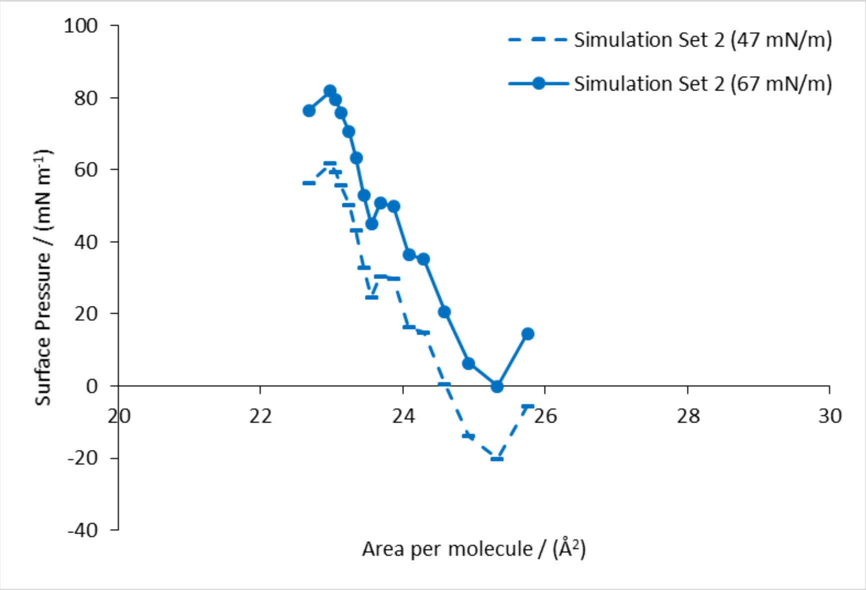

Figure 46: Correction factor, $\gamma_{vw}*$, for simulation set 2.

Surface pressures start to increase once most of the stearic acid chains become aligned. From the lowest surface pressure to the highest surface pressure, an increase in chain ordering is observed, as shown in Figure 48 and Figure 49, indicating a shift from the liquid-expanded to the liquid-condensed phase.

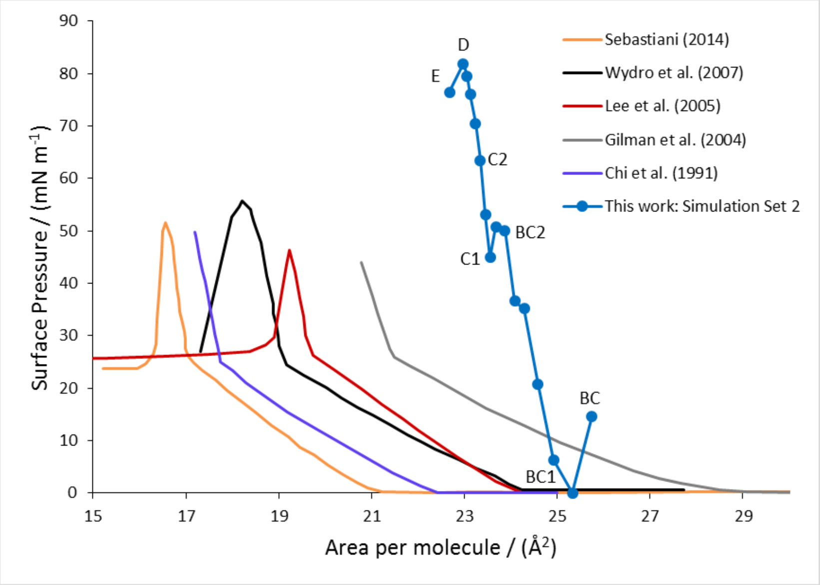

Figure 47: Pressure-area isotherm for stearic acid at the air-water interface from simulations in comparison to experimental isotherms reported in the literature.[1, 3-6] Simulation set 2: Stearic acid represented by P3, C2, C2, C2, C2, C2. Bead-to-bead distances and force constants used; P3-C2: r_e = 0.32 nm, k_r = 7500 kJ mol^{-1} nm^{-2}; C2-C2: r_e = 0.47 nm, k_r = 1250 kJ mol^{-1} nm^{-2}. Phase behaviour of simulated isotherm indicated: (BC, BC1 and BC2) liquid-expanded liquid-condensed coexisting region, (C1 and C2) liquid-condensed region, (D) equilibrium spreading pressure and (E) film collapse region.

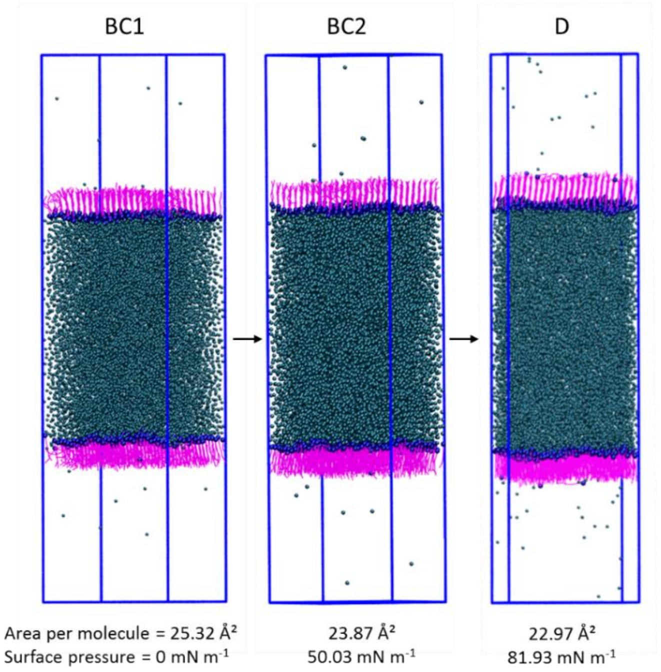

Figure 48: Side view of the simulation box, showing that monolayers stay in an ordered state under compression, without the system breaking down.
Snapshots BC1, BC2 and D are indicated on isotherm in Figure 47.

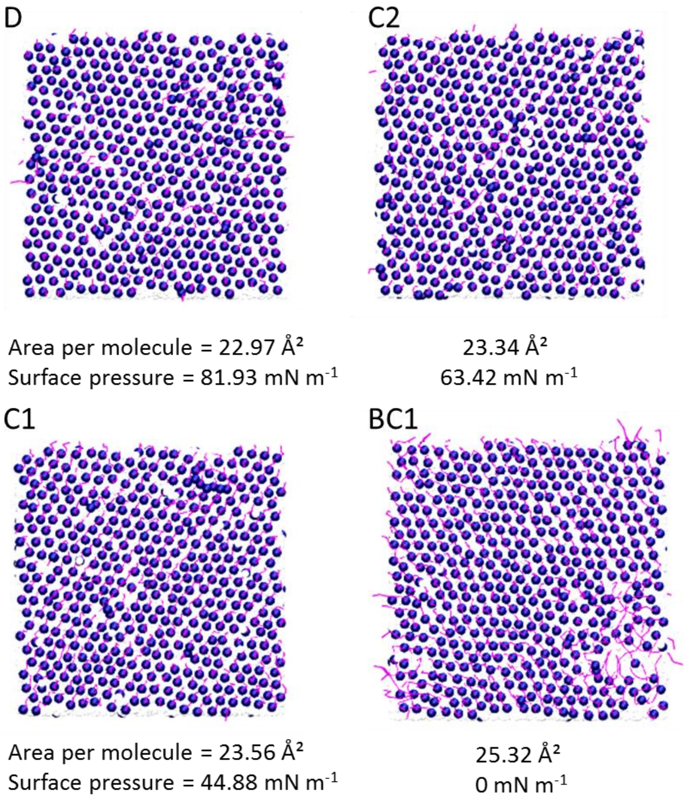

Figure 49: Top layer view of the stearic acid monolayers at several points along the pressure-area isotherm of simulation set 2 (D, C2, C1, BC1—points indicated on isotherm in Figure 47). An increase in ordering of the stearic acid chains causes an increase in surface pressures.
Stearic acid headgroup: purple, stearic acid chain: magenta.

The equilibrium spreading pressure, as for the previous isotherm, exceeds the surface pressures reported in the literature (Figure 47). At this point, monolayers are still in an ordered state as shown in Figure 48, indicating that the monolayers are too stable.

Simulation sets 1 and 2 both produce isotherms that are too stable—the monolayers do not break down, as expected from experimental data, and can be compressed to much higher surface pressures. To test whether this is due to the chosen parameterisation of the molecule, which was based on the previously used parameterisation of oleic acid, the mapping of stearic acid is altered for the next simulation set to better agree with the typical Martini mapping of four heavy atoms per interaction site.

3.3.3 Simulation Set 3

This setup uses the same parameters as described for simulation set 2, with the only difference being the chain description of the stearic acid molecules, which is represented by 4 × C1 beads instead of 5 × C2 beads. The isotherm produced is shown in Figure 50. The correction factor was set to 57 mN m^{-1} to shift the lowest point on the isotherm to a surface pressure of 0 mN m^{-1}.

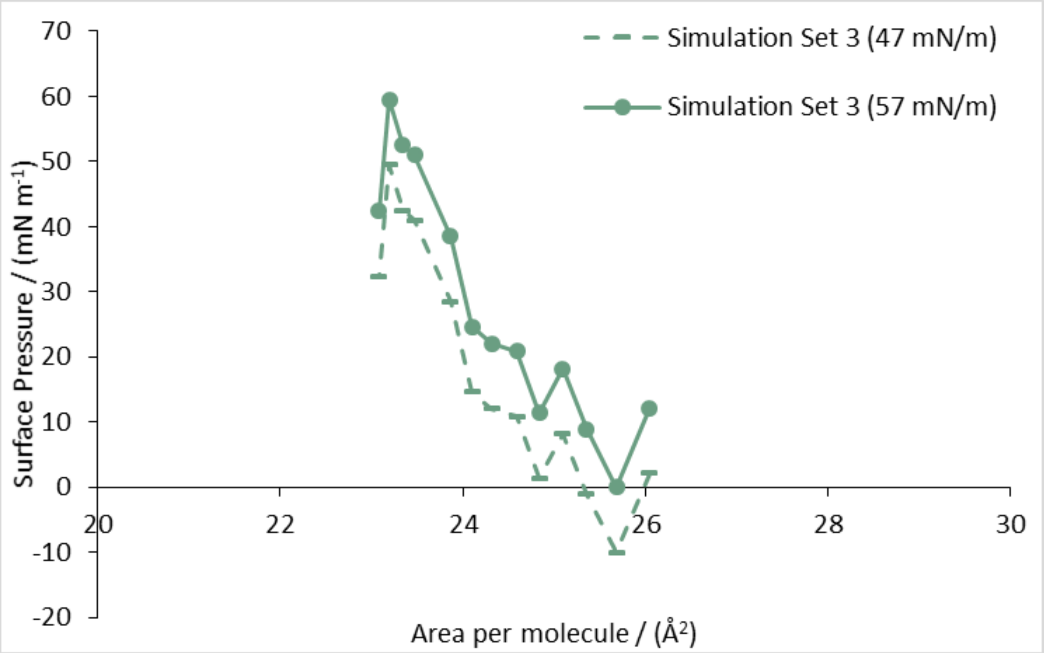

Figure 50: Correction factor, $\gamma_{vw}*$, for simulation set 2.

Surface pressures start to increase once most of the stearic acid chains are aligned. At the lowest surface pressure, some chains are disordered, under compression all stearic acid chains order indicating a change from the liquid-expanded liquid-condensed coexisting region to a purely liquid-condensed region, as shown in Figure 52 and Figure 53.

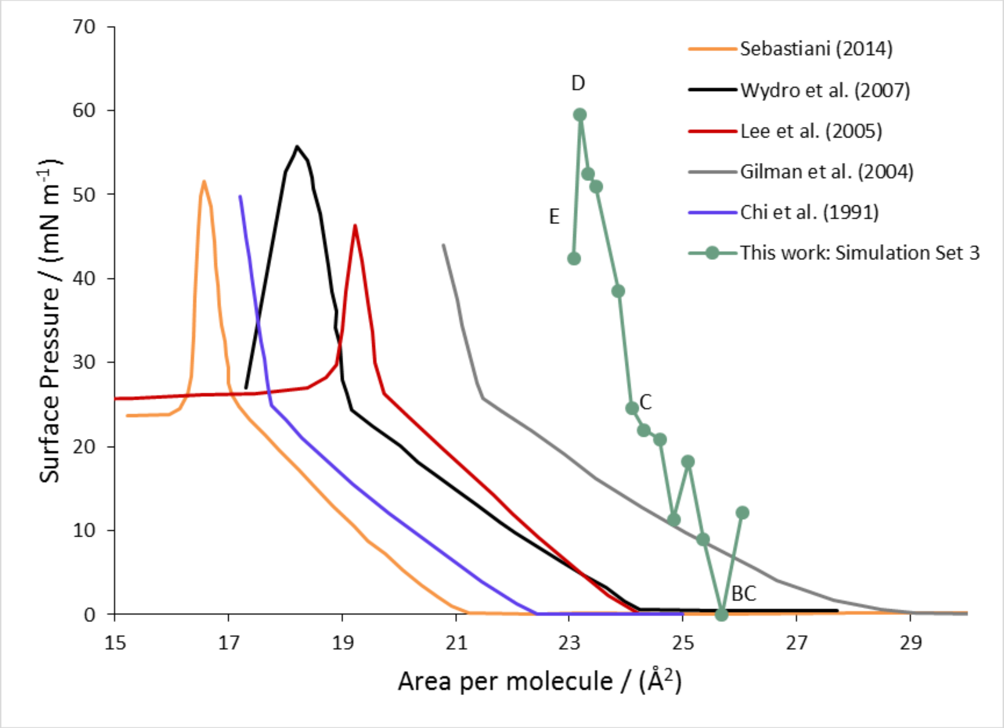

Figure 51: Pressure-area isotherm for stearic acid at the air-water interface from simulations in comparison to experimental isotherms reported in the literature.[1, 3-6] Simulation set 3: stearic acid represented by P3, C1, C1, C1, C1. Bead-to-bead distances and force constants used; P3-C2: r_e = 0.44 nm, k_r = 2250 kJ mol^{-1} nm^{-2}; C2-C2: r_e = 0.47 nm, k_r = 1250 kJ mol^{-1} nm^{-2}. Phase behaviour of simulated isotherm indicated: (BC) liquid-expanded liquid-condensed coexisting region, (C) liquid-condensed region, (D) equilibrium spreading pressure and (E) film collapse region.

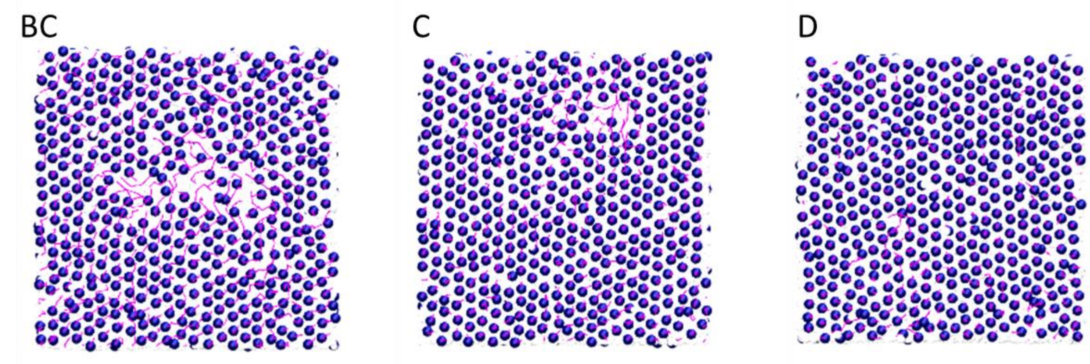

Area per molecule = 25.69 Å^2
Surface pressure = 0 mN m^{-1}

24.10 Å^2
24.62 mN m^{-1}

23.19 Å^2
59.51 mN m^{-1}

Figure 52: Top layer view of the stearic acid monolayers at several points along the pressure-area isotherm of simulation set 3 (BC, C, D—points indicated on isotherm in Figure 51). Stearic acids order under compression. Stearic acid headgroup: purple, stearic acid chain: magenta.

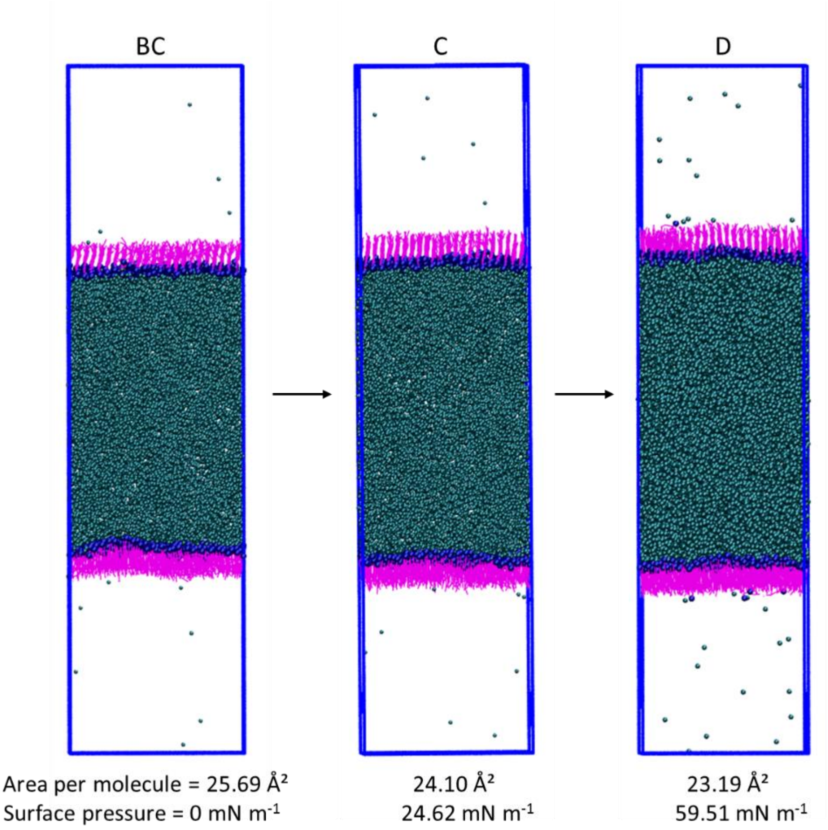

Figure 53: Side view of the simulation box, showing the ordering of the stearic acid molecules in the top layer under compression (BC, C, D—points indicated on isotherm in Figure 51). Stearic acid headgroup: purple, stearic acid chain: magenta, water: teal.

This simulation set only slightly overestimates the range of surface pressures, with the equilibrium surface pressure at 59 mN m^{-1}—showing that a better agreement with experimental data can be obtained by the use of the typical Martini bead mapping of four heavy atoms per bead. To further optimise the mapping of stearic acid, CHARMM-36 all-atom simulations were used to calculate the bead-to-bead distance between the headgroup bead and first bead of the chain of the stearic acid molecules. Resulting isotherms will be described in the following section.

3.3.4 Simulation Set 4

For this simulation set, the parameters from the CHARMM-36 simulations were adapted for the bead-to-bead distance and force constant between the stearic acid headgroup and chain. A box of size 18 nm × 18 nm × 42 nm was created, containing 882 stearic acids (441 in each monolayer), 12852 water beads and 1300 antifreeze beads. This initial structure was compressed laterally. Snapshots taken during the compression run were set up in the NVT ensemble for 1000 ns, each producing a point on the pressure-area isotherm, as shown in Figure 54 below.

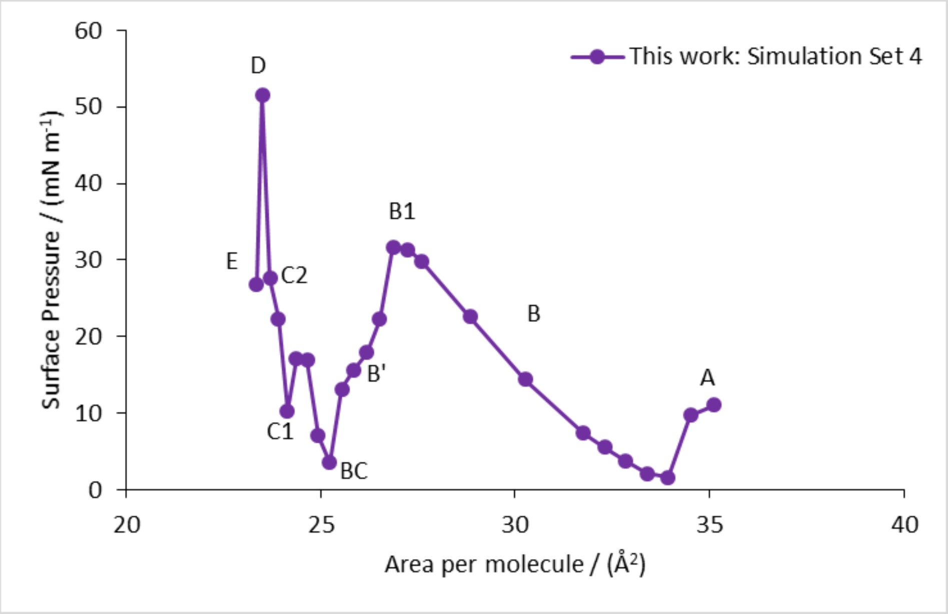

Figure 54: Pressure-area isotherm for stearic acid at the air-water interface from simulations. (A) gas-liquid coexisting region, (B and B1) liquid-expanded phase, (B’) rearrangement, (BC) liquid-condensed liquid-expanded coexisting region (C1 and C2) liquid-condensed phase and (D) equilibrium spreading pressure, (E) film collapse region.

The pressure-area isotherm shows several regions, each will be discussed in the following:

(B) Pressure starts to rise at an area per molecule of 33.93 Å^2 until a surface pressure of 31 mN m^{-1} is reached. In this region, molecules are disordered, indicating a liquid-expanded phase. Here, the decrease in area per molecule causes an increase in molecules that change orientation, as shown in Figure 55. This is similar to the previously discussed isotherm of oleic acid.

(B’) After this point, the molecules in the monolayer rearrange rapidly, causing a decrease in surface pressures. Only once molecules start to order do the surface pressures increase again.

(BC) A phase change from the liquid-expanded to the liquid-condensed phase is observed, with areas where chains of the stearic acid molecules are disordered and areas where chains are ordered, as shown in Figure 56. At an area of 23.70 Å^2/ molecule (C2), a sharp increase in surface pressures is observed. The number of molecules that move out of the layer decreases to 0.53 %. Here, molecules are in a solid state. The equilibrium spreading pressure (D) in the simulated isotherm lies at 51 mN m^{-1}. After this point, an increase in molecules that move out of the layer causes a decrease in surface pressures, as shown in Figure 55, indicating the collapse of the film.

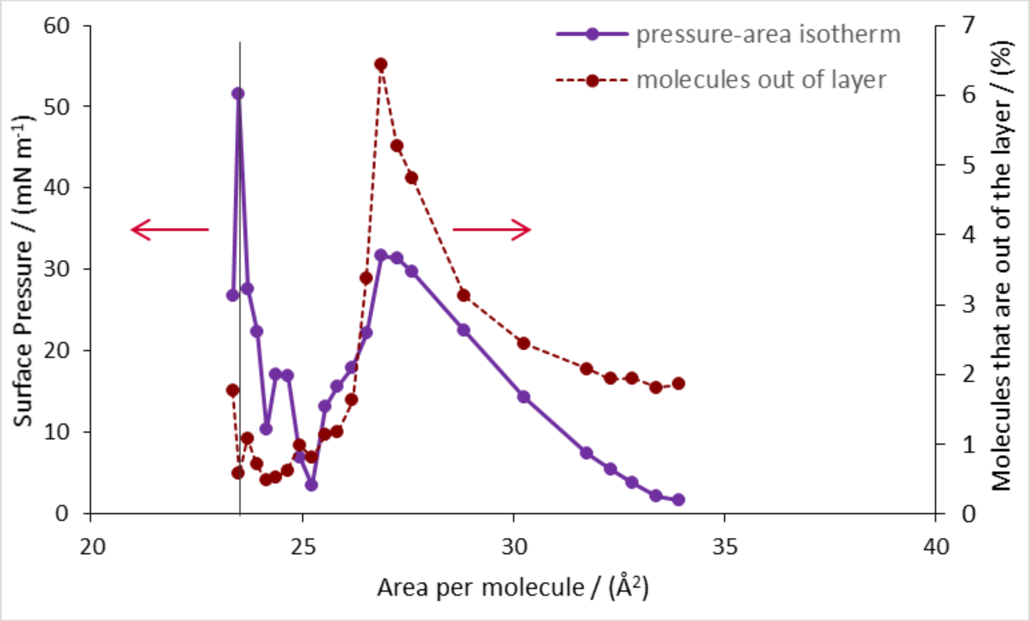

Figure 55: Pressure-area isotherm of stearic acid and percentage of stearic acid molecules that are out of the layer during the production time, based on calculations from the contour plots (Figure 64), against the area per molecule. Vertical line indicates the percentage of molecules that move out of the layer at the equilibrium spreading pressure (area per molecule of 23.51 Å^2 and a surface pressure of 51 mN m^{-1}). Arrows indicate relevant axes.

In simulations, stearic acid shows a liquid-expanded phase which then rearranges to form a liquid-condensed phase and solid state, as shown in Figure 57. This differs from the previously discussed oleic acid isotherm, which stays in the liquid-expanded phase until the monolayer collapses. In experimental isotherms, only the liquid-condensed state and solid phase are observed for stearic acid on a pure water subphase. Chi *et al.*, reported in addition to a solid state and liquid-condensed phase, a liquid-expanded to liquid-condensed phase transition for stearic acid on an aqueous subphase containing poly(ethyleneimine) (2.13×10^{-3} M PEI$_{1800}$).[5] The existence of a liquid-expanded to liquid-condensed phase on a pure water subphase seems to be an artefact of the model. However, as both the liquid-expanded and liquid-condensed phase are clearly separable in simulations, the presence of a liquid-expanded phase can be neglected without affection other regions of the isotherm.

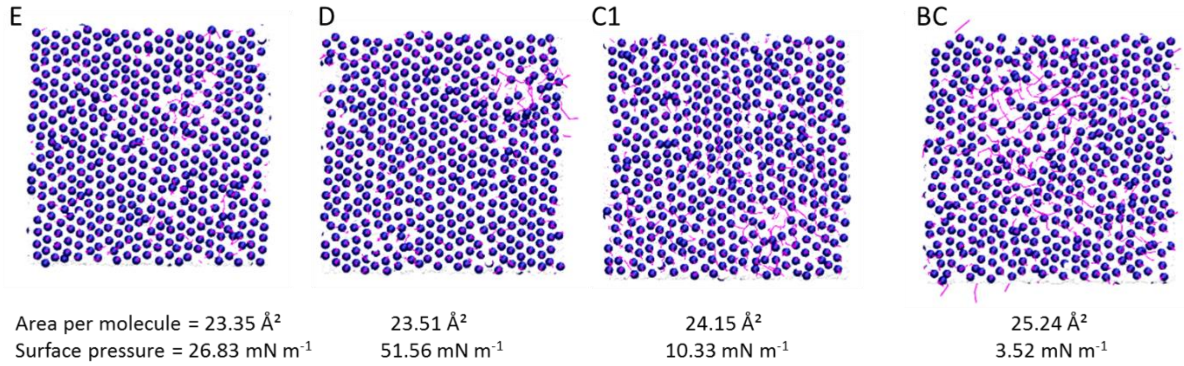

Figure 56: Top layer view of the stearic acid monolayers at several points along the pressure-area isotherm of simulation set 4 (E, D, C1, BC—points indicated on isotherm in Figure 54). Stearic acid orders under compression. A change from liquid-expanded to liquid-condensed phase is observed. Stearic acid headgroup: purple, stearic acid chain: magenta.

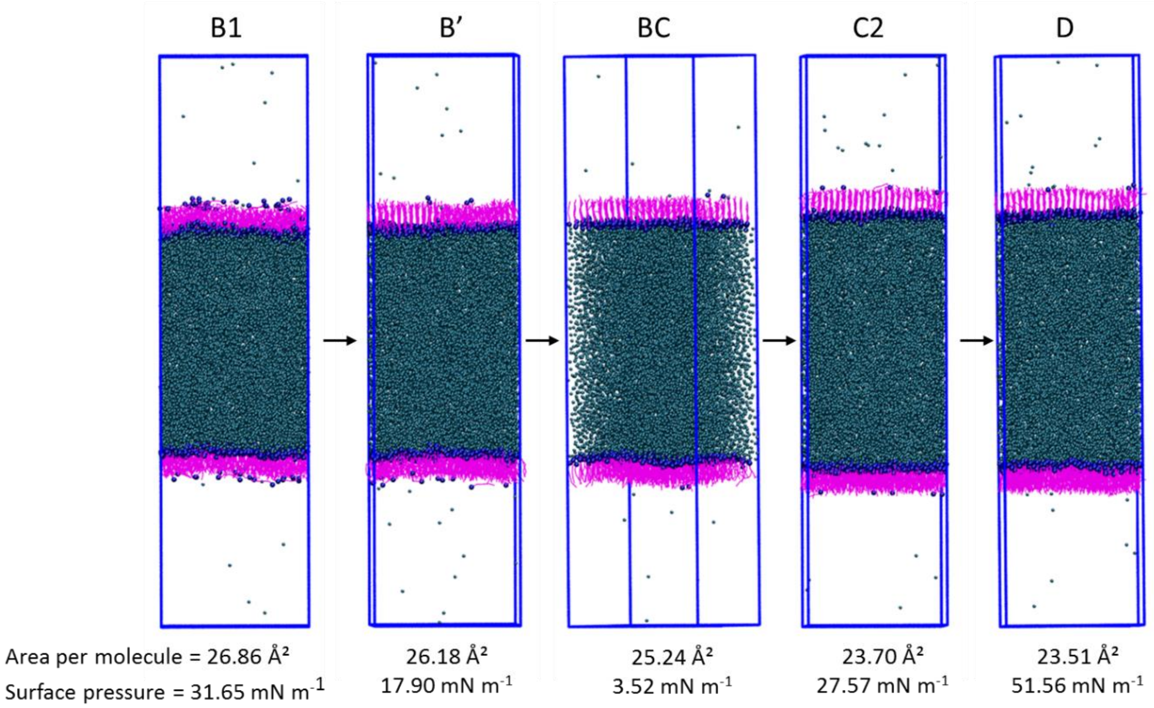

Figure 57: Side view of the simulation box showing the rearrangement of the top monolayer under compression (B1, B', BC, C2, D—points indicated on isotherm in Figure 54). Surface pressures decrease when the monolayer rearranges from the liquid-expanded to a liquid-condensed phase. Only once molecules are in an ordered state do surface pressures increase again. Monolayers move from a liquid-condensed to solid state, indicated by a sharp increase in surface pressures. Stearic acid headgroup: purple, stearic acid chain: magenta, water: teal.

The equilibrium spreading pressure in the simulated isotherm lies at 51 mN m^{-1} and hence is in good agreement with the aforementioned experimental data, shown in Figure 58, which lie between 42–55 mN m^{-1}, giving the best agreement out of the four simulated isotherms in this work.

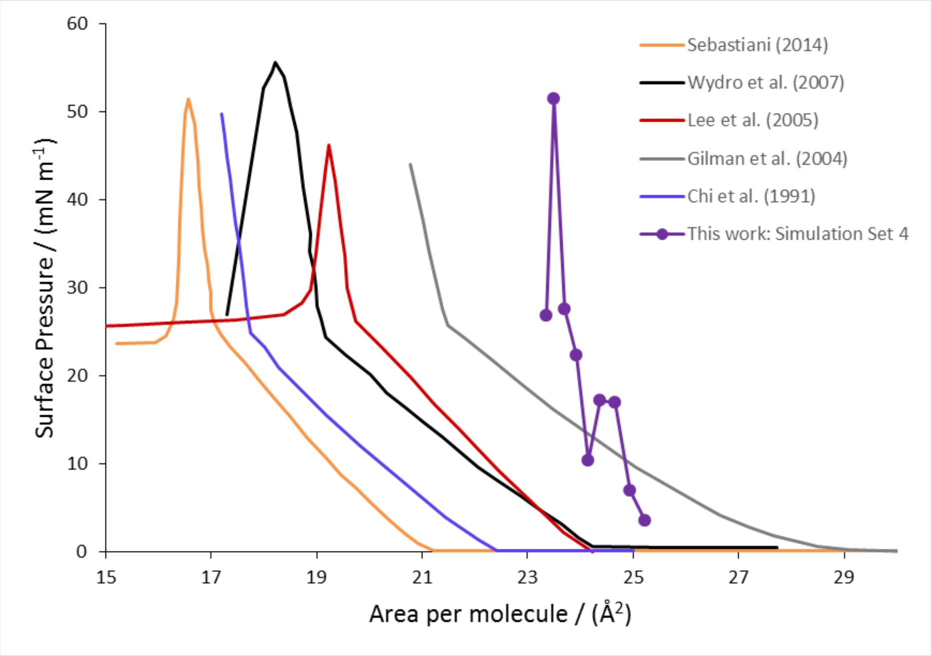

Figure 58: Pressure-area isotherm for stearic acid at the air-water interface from simulations in comparison to experimental isotherms reported in the literature.[1, 3-6] Simulation Set 4: stearic acid represented by P3, C1, C1, C1, C1. Bead-to-bead distances and force constants used; P3-C2; r_e = 0.44 nm, k_r = 2250 kJ mol^{-1} nm^{-2}; C2-C2: r_e = 0.47 nm, k_r = 1250 kJ mol^{-1} nm^{-2}

As previously discussed, a higher uncertainty in measurements is expected at points which lie at phase transitions. In the above simulation set, an increase in surface pressures is observed, followed by a drop in surface pressures at 24.15 Å^2/ molecule. When comparing to experimental data by Donaldson *et al.,* 'kinks' in the isotherm can be seen at phase transitions.[10] Both expanded liquid and condensed liquid phases coexist in the region where the increase in surface pressures occurs, as shown in the images in Figure 56. Repeats of the simulations with different random seeds allows for calculation of the 95 % confidence for each of the points on the isotherm. Figure 59 shows the confidence intervals for the whole isotherm, and Figure 60 focuses on the liquid-condensed and solid phases relevant to this project.

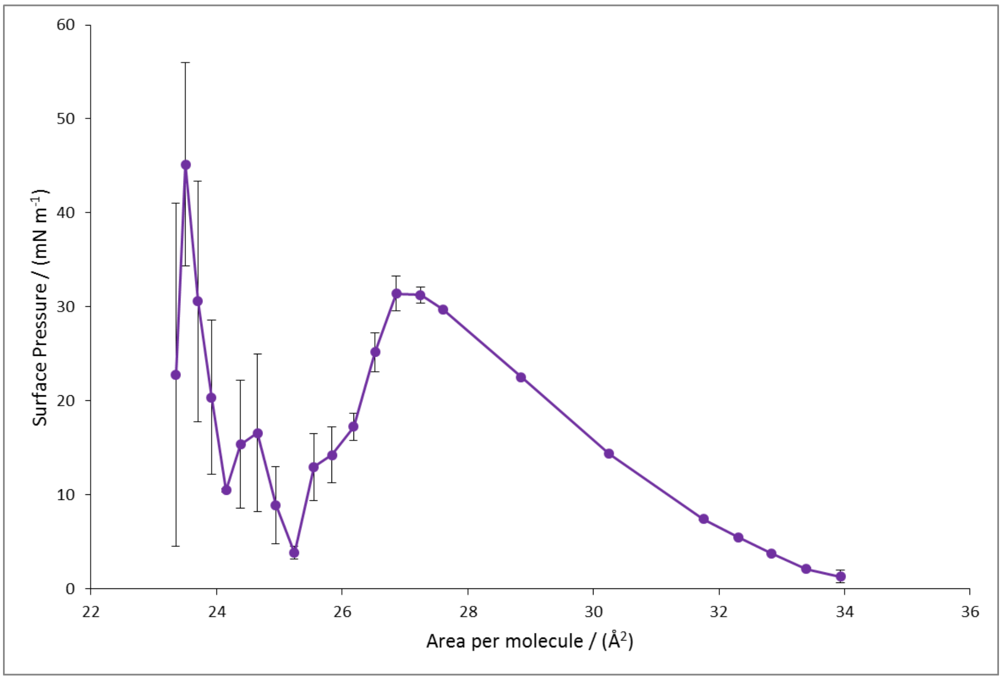

Figure 59: Pressure-area isotherm for stearic acid at the air-water interface from simulations. Mean surface pressures, with 95 % confidence intervals shown.

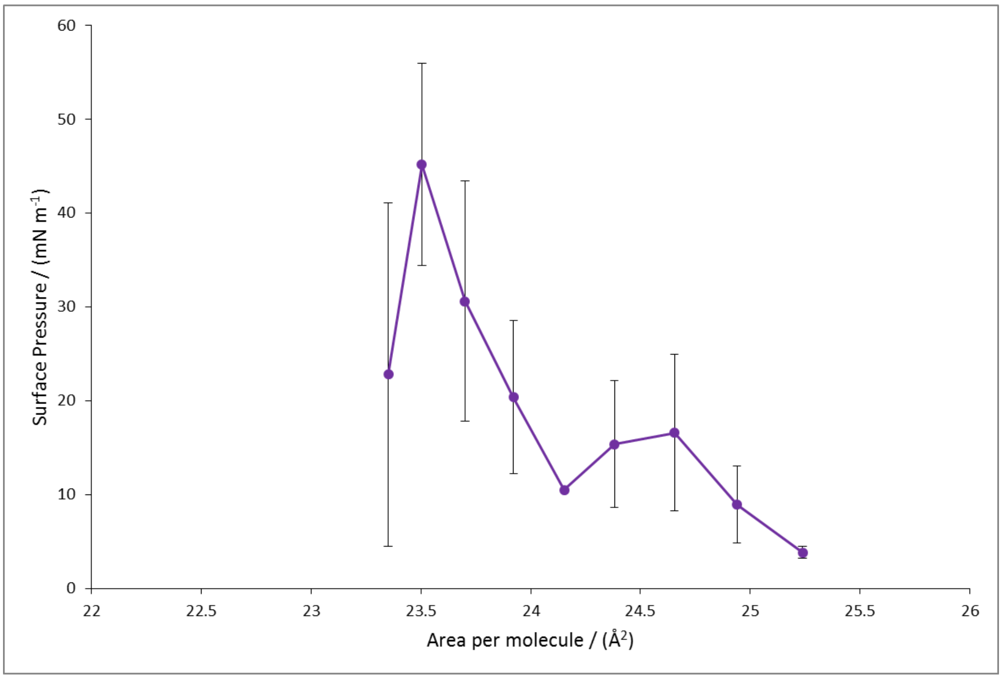

Figure 60: Pressure-area isotherm for liquid-condensed and solid phases expanded from Figure 59. Mean surface pressures, with 95 % confidence intervals shown.

Error bars for the close-packed structures are much higher than for the expanded phase. When looking at the data points of the repeats, as shown in Figure 61, it becomes clear why this is the case—for each area per molecule there are two distinct surface pressures. For the highest point on the isotherm at an area per molecule of 23.51 Å^2/ molecule, simulations either have a surface pressure of 51 mN m^{-1} or 39 mN m^{-1}, which suggests that there are two separate phases.

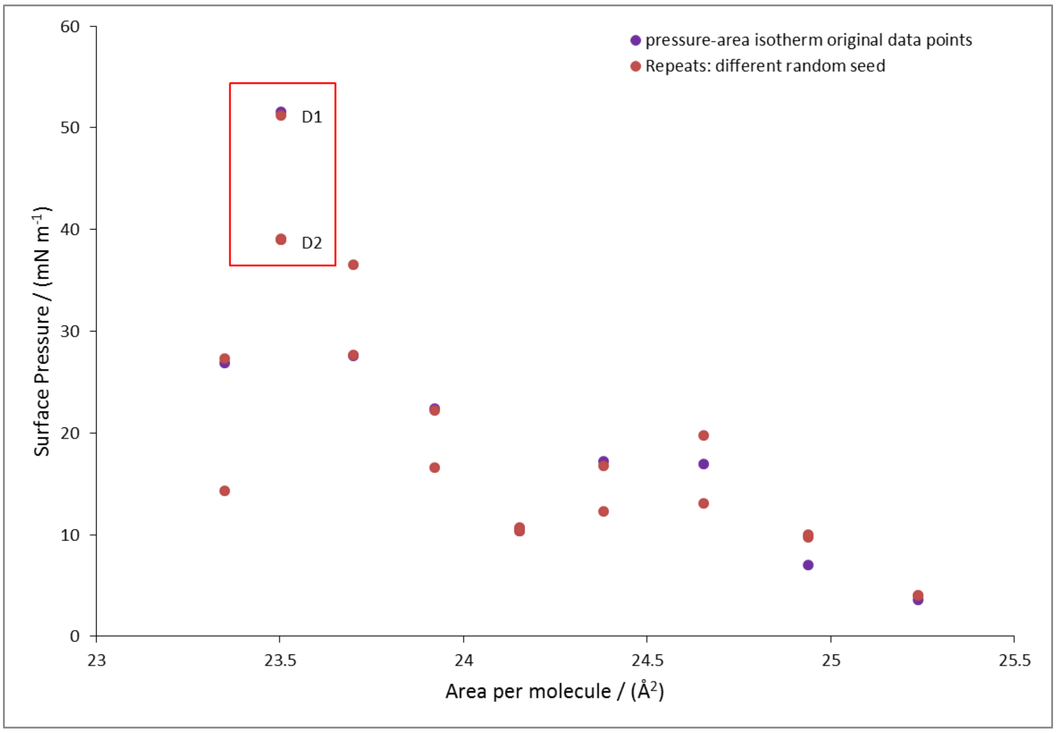

Figure 61: Three simulations with changing random number for each area per molecule on the stearic acid pressure-area isotherm. The box highlights systems with surface pressures of 51 mN m^{-1} (D1) and 39 mN m^{-1} (D2).

Monolayers with surface pressures of 51 mN m^{-1} and 39 mN m^{-1} were further analysed, correlating the angle of the molecules with respect to the *z*-axis, as shown in Figure 62, and the *z*-coordinate of the headgroup bead of stearic acid. The produced contour plots are shown in Figure 63 (a) and (b) for systems with a surface pressure of 51 mN m^{-1} and in Figure 63 (c) and (d) for systems with a surface pressure of 39 mN m^{-1}.

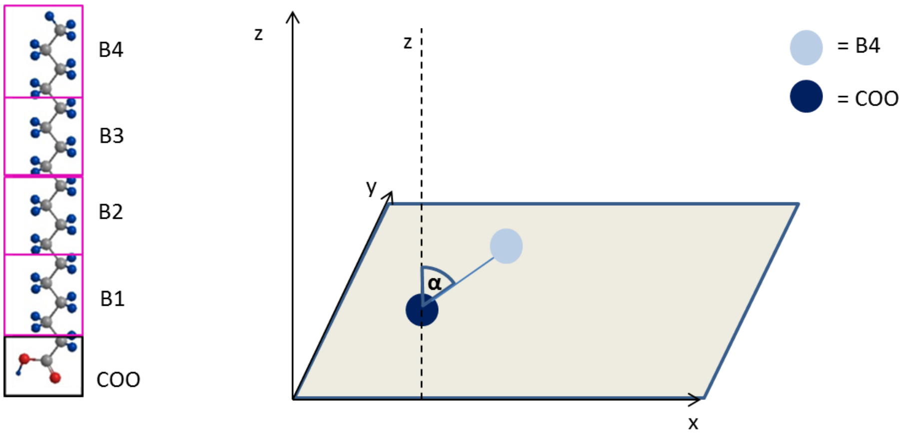

Figure 62: Representation of angle (α).

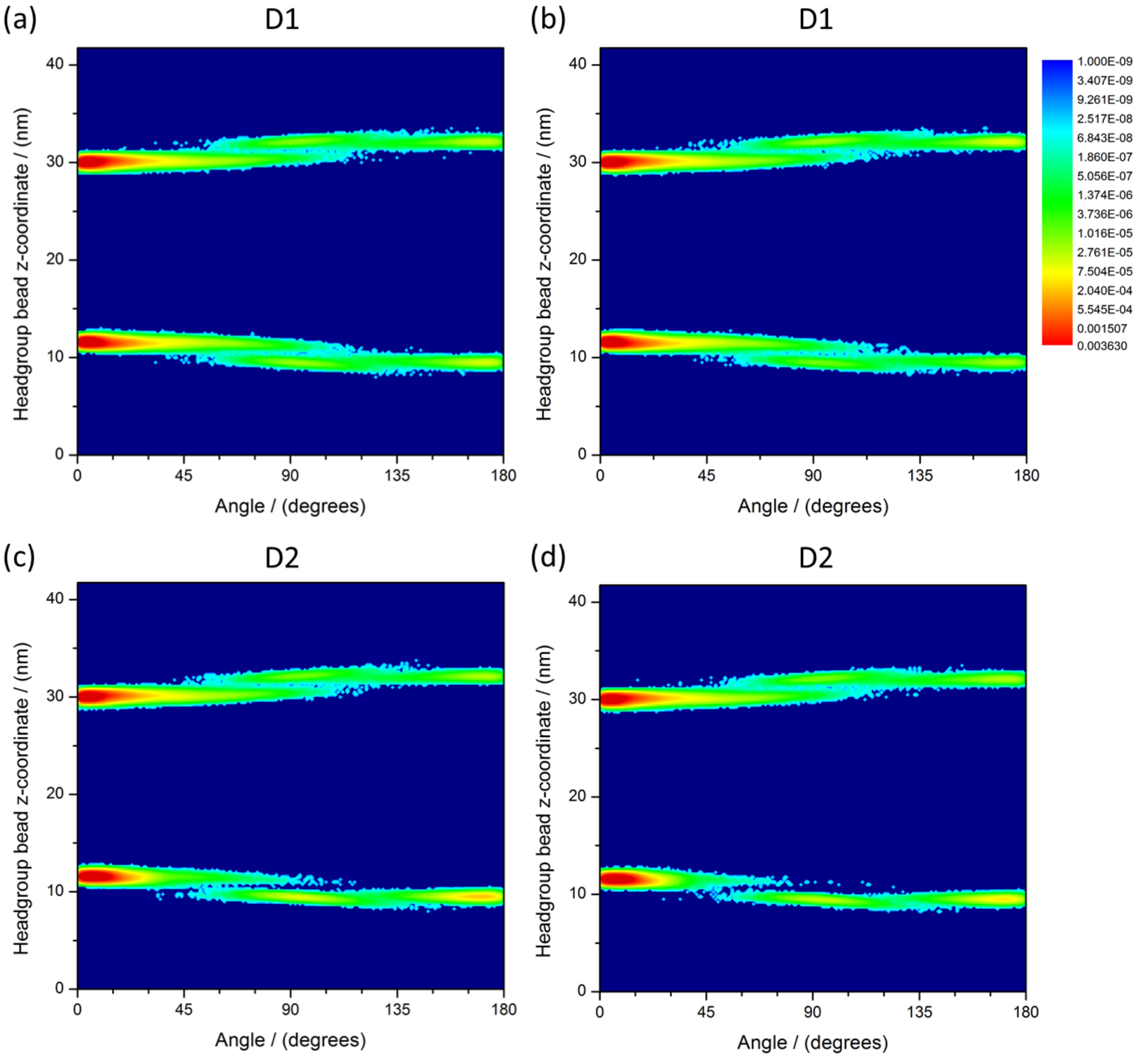

Figure 63: Contour plots showing the probability of finding the headgroup of a molecule at a certain *z*-coordinate with respect to the angle (α) for systems produced from simulations with different random seeds, where (a) and (b) (D1) have an area per molecule of 23.51 Å^2/ molecule and a surface pressure of 51 mN m^{-1}, and monolayers in (c) and (d) (D2) have an area per molecule of 23.51 Å^2/ molecule and a surface pressure of 39 mN m^{-1}. Points D1 and D2 are indicated on the pressure-area isotherm in Figure 61.

As shown in the contour plots for the four simulations at an area per molecule of 23.51 Å^2/ molecule, for the systems with a surface pressure of 51 mN m^{-1} both the top and bottom monolayer are similar, whereas for the systems with surface pressures of 39 mN m^{-1} the top monolayer differs from the bottom monolayer, where more molecules are not in the normal monolayer position. To quantify this, the lowest density regions in the contour plots between the two regions in each monolayer were determined, which allowed to make an approximation of the percentage of molecules that move out of the layer for each monolayer during the production time, as shown in Table 9.

Simulation	Original run 51 mN/m	Repeat 1 51 mN/m	Repeat 2 39 mN/m	Repeat 3 39 mN/m
% Out of Layer	0.57	0.58	1.32	0.85
% Out of Top	0.76	0.52	0.39	0.43
% Out of Bottom	0.38	0.63	2.25	1.27

Table 9: Calculated percentage of molecules that move out of the layer for the original run and the three repeats of the simulation.

In all four simulations, a low percentage of molecules change orientation in the top monolayer. This is the expected behaviour as the monolayer for stearic acid at the equilibrium spreading pressure is in the solid state, meaning the molecules are close packed, and hence the surface pressure in the system is high. However, the bottom monolayer differs between the four systems. In the systems with a surface pressure of 51 mN m^{-1}, the percentages of molecules that move out of the top layer are low, at 0.38 % and 0.63 %—here, the top and bottom monolayer show a similar behaviour. For the systems with surface pressure of 39 mN m^{-1}, the percentage of molecules that move out of the layer is, at 2.25 % and 1.27 %, much higher than the percentage in the top layers, which lie respectively at 0.29 % and 0.43 %. This suggests that not all monolayers reach a solid state. As this is the closest packed structure in the isotherm, an early collapse of the system will cause a reduction in surface pressures. As experimental data suggest that a solid state is formed it can be assumed that this is thermodynamically the most stable phase, and hence comparison to simulation systems where top and bottom layer show the same behaviour and are in the solid state, are a more realistic basis for comparison. Here, surface pressures agree well with experimental isotherms.

Two expansion runs, with a lateral pressure of −30 bar, were set up: one from a simulation system with a surface pressure of 51 mN m^{-1} and one from a simulation system with a surface pressure of 39 mN m^{-1}. Snapshots taken during the expansion were set up for 1000 ns in the NVT ensemble. Only the last 800 ns were used for analysis, with each of the simulations resulting in a point on the pressure area isotherms. The resulting expansion isotherms are shown in Figure 64, alongside the compression isotherm and repeats.

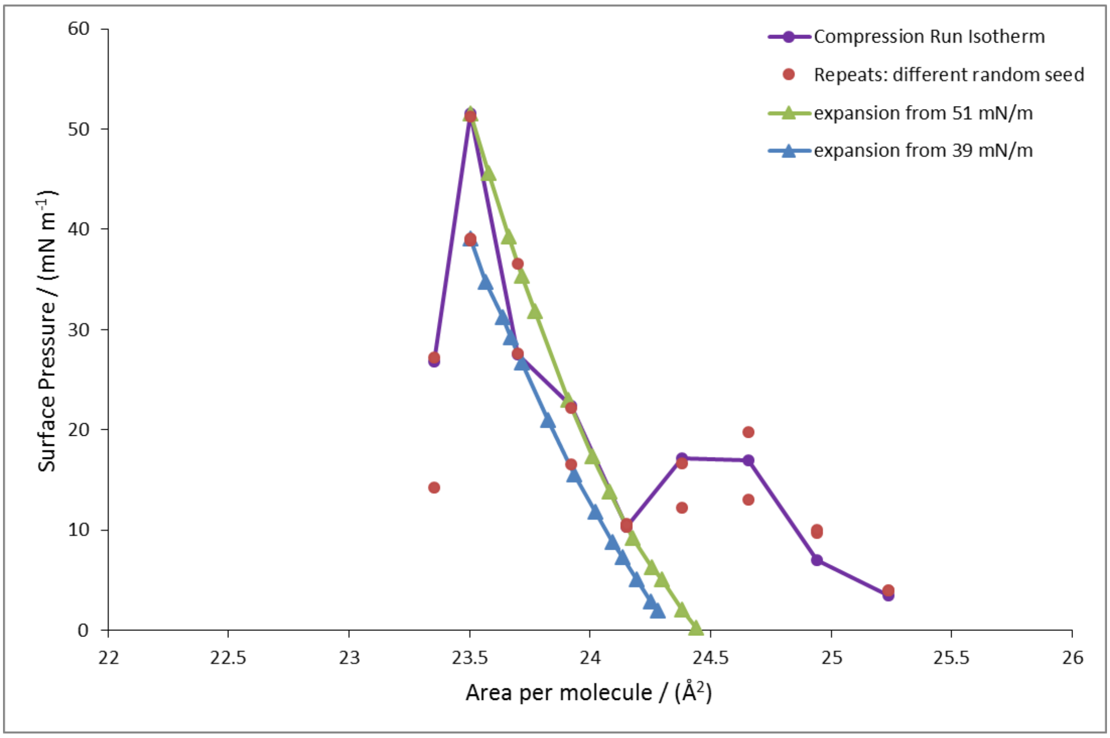

Figure 64: Expansion run isotherms starting from systems with a surface pressure of 51 mN m^{-1} (green) and 39 mN m^{-1} (blue), alongside the original compression run (purple) and repeats (red).

Points generated from the two expansion isotherms show a clear difference—the isotherms starting from the system at 39 mN m^{-1} are shifted to lower surface pressures. This is due to the increase in molecules that change orientation in one of the monolayers, resulting in a lower surface pressure in the system. The expansion run shows that the repeats of the original system lie either on the line of the 51 mN m^{-1} expansion run or the 39 mN m^{-1} expansion run, explaining the large error bars in this region, which were shown in Figure 60.

3.4 Conclusions

Simulations in this chapter showed that, for stearic acid, similarly to oleic acid, the use of the standard Martini force field parameters does not give an accurate description of the molecule. Simulations using a shorter bead-to-bead distance and higher force constant for the headgroup bead to the first bead of the chain, with two different molecule mappings showed that, where possible, the use of the standard Martini mapping of four heavy atoms per beads is favourable, giving a better description of the molecule.

As the distance between the headgroup bead and the first bead of the chain seems to be a critical parameter, the parameters of the molecule were further optimised by back-mapping its structure to all-atom simulations. This approach allows a more systematic way of determining the distance and force constants for each molecule individually, and will be used in future parameterisations. The obtained range of surface pressures for stearic acid with this new set of parameters showed a good agreement with experimental data.

The simulation setup used requires two separate monolayers to be simulated in each system in order to avoid vacuum-water interfaces. Simulations of stearic acid showed that care needs to be taken when analysing the resulting monolayers. Several structures showed differences between the top and the bottom monolayers—meaning the simulation system does not always show the same phase behaviour, resulting in too low a value for surface pressure. Repeats of the simulation points with changing random seeds showed that it is possible to obtain systems where both monolayers are in the same phase. As experimental monolayers at the equilibrium spreading pressure are in the solid state, we assume that this is thermodynamically the most stable. Comparison to simulations where both monolayers in the system are in the solid state show a good agreement with experimental surface pressures.

3.5 References

1. J. B. Gilman, T. L. Eliason, A. Fast and V. Vaida, *J. Colloid Interf. Sci.*, 2004, **280**, 234-243.
2. F. Sebastiani, *Neutron Reflectometry and Ellipsometry Applied to Atmospheric Night-time Oxidation*, University of Reading Ph.D., 2014.
3. P. Wydro, B. Krajewska and K. Hąc-Wydro, *Biomacromolecules*, 2007, **8**, 2611-2617.
4. Y.-L. Lee, Y.-C. Yang and Y.-J. Shen, *J. Phys. Chem. B*, 2005, **109**, 4662-4667.
5. L. F. Chi, R. R. Johnston and H. Ringsdorf, *Langmuir*, 1991, **7**, 2323-2329.
6. A. Gericke and H. Huehnerfuss, *J. Phys. Chem.*, 1993, **97**, 12899-12908.
7. S. J. Marrink, H. J. Risselada, S. Yefimov, D. P. Tieleman and A. H. d. Vries,(2007), *The MARTINI forcefield: coarse grained model for biomolecular simulations*, http://md.chem.rug.nl/cgmartini/images/parameters/ITP/martini_v2.0.itp, [August 2014]
8. L. Monticelli, S. K. Kandasamy, X. Periole, R. G. Larson, D. P. Tieleman and S.-J. Marrink, *J. Chem. Theory Comp.*, 2008, **4**, 819-834.
9. U. Essmann, L. Perera, M. L. Berkowitz, T. Darden, H. Lee and L. G. Pedersen, *J. Chem. Phys.*, 1995, **103**, 8577-8593.
10. D. J. Donaldson and V. Vaida, *Chem. Rev.*, 2006, **106**, 1445-1461.

Chapter 4

Oleic Acid and Palmitoleic Acid Ozonolysis Products

4.1 Monounsaturated Fatty Acids—Reactions in the Atmosphere

The oleic acid/ozone reaction system has emerged as a benchmark for the study of atmospheric oxidation of organic compounds.[1-4] However, the fate of oleic acid surface films in the atmosphere is still poorly understood. It is vital to gain a better understanding of the changes to the aerosol droplets' composition and the changes to the surface film after ozonolysis as this will determine the growth of the aerosol droplets and ultimately determine their lifetimes in the atmosphere, as it changes the terms in the Köhler theory as explained in Chapter 1 section 1.7.2.

As it is not possible to study bond making or bond breaking processes within the computational model used, we rely on literature data regarding reaction products of the ozonolysis of oleic acid. The most commonly reported products in the literature for the ozonolysis of oleic acid are nonanal, azelaic acid, nonanoic acid and 9-oxononanoic acid.[3, 5] A possible reaction scheme for the formation of these products is shown in Figure 65.

The reaction scheme is divided into two reaction pathways. From the primary ozonide, one pathway results in the formation of nonanal and a Criegee intermediate (CI1) with a terminal carboxylic acid group. The other pathway leads to 9-oxononanoic acid being formed as well as a Criegee intermediate (CI2) with an alkyl end group. The rearrangement of CI1 then leads to the formation of azelaic acid and the rearrangement of CI2 to the formation of nonanoic acid.

In addition to the reaction pathway described above, there are several other reactions reported in the literature for the CIs (CI1 and CI2). The recombination of CI1 and nonanal forms secondary ozonides or polymeric ozonides.[3] Hydroperoxides are formed when Criegee intermediates react with solvents.[3] Furthermore, CIs can react with other CIs to form peroxides or polymeric peroxides.[3] The solvolysis of these peroxidic products also leads to the formation of nonanoic acid and azelaic acid.[3]

This chapter will focus on the most commonly reported products (nonanal, 9-oxononanoic acid, azelaic acid and nonanoic acid) and aim to determine whether they stay at the surface of the water, diffuse into the water or evaporate from the surface. This is particularly interesting for 9-oxononanoic acid which is not readily commercially available.

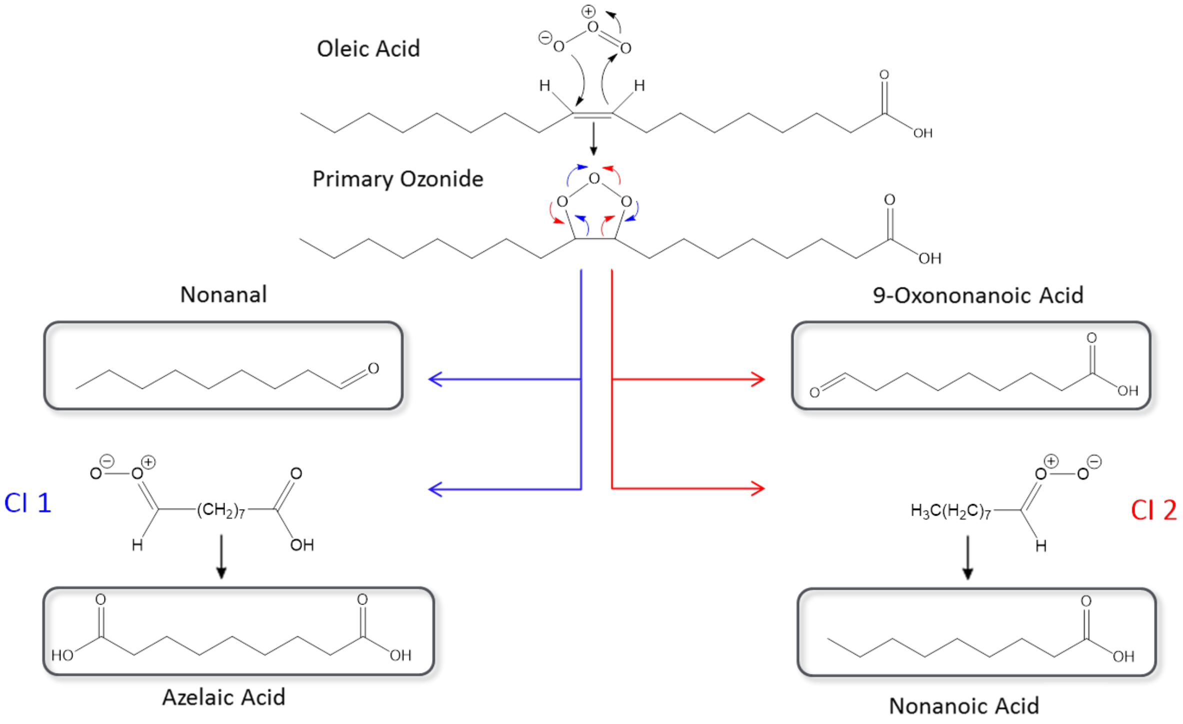

Figure 65: Ozonolysis of oleic acid, reproduced from Pfrang *et al.*[1]

Further to the ozonolysis of oleic acid, this chapter focuses on palmitoleic acid, the C16 analogue of oleic acid. Alongside oleic acid, palmitoleic acid is the most prevalent unsaturated fatty acid in animal fats and vegetable oils;[6] however, a lot less research has been conducted on this compound to date.

Assuming a similar reaction pathway as for the ozonolysis of oleic acid, the primary ozonide would lead to the formation of heptanal, 9-oxononanoic acid and two CIs, where CI1 leads to the formation of azelaic acid and CI2 leads to the formation of heptanoic acid as shown in Figure 66.

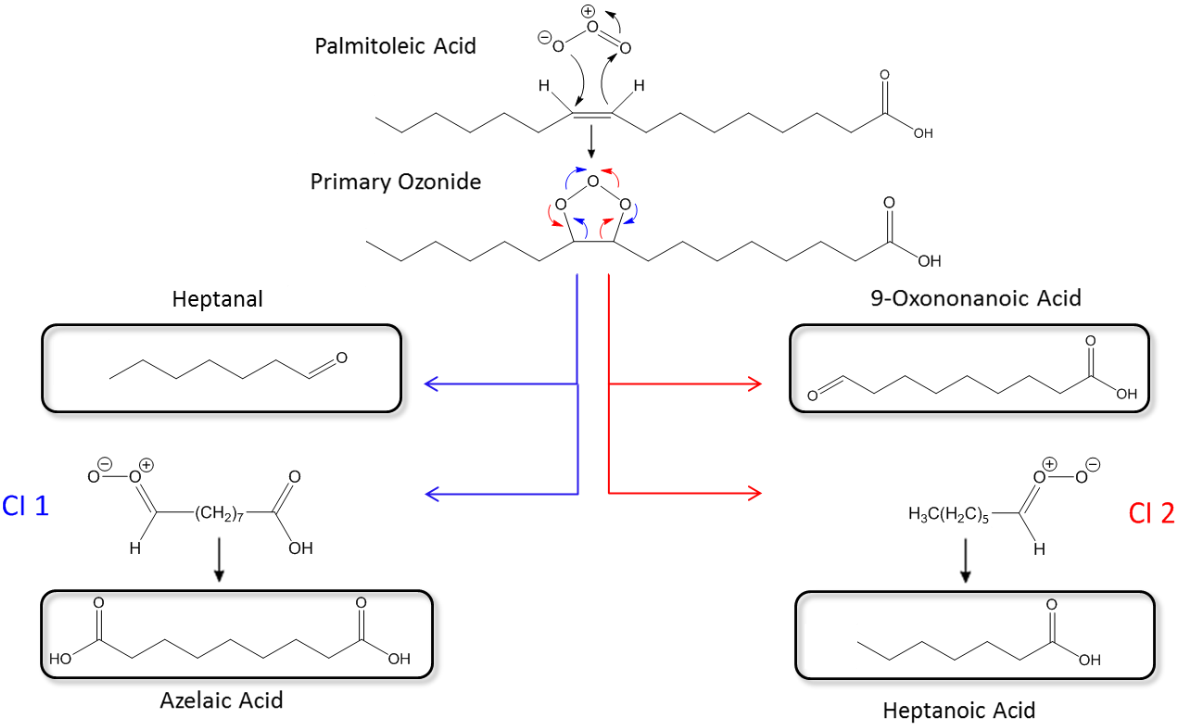

Figure 66: Ozonolysis of palmitoleic acid, based on oleic acid mechanism.

In this chapter, a pressure-area isotherm for palmitoleic acid was produced from simulations and will be compared to experimental data. Furthermore, simulations of the ozonolysis products of both oleic acid and palmitoleic acid (nonanoic acid, nonanal, azelaic acid, 9-oxononanoic acid, heptanal and heptanoic acid) will allow for the determination of which compounds are surface active. These will then be used in future simulations to model the aging of surface films.

4.2 Method for All-Atom Simulations

4.2.1 Parameterisation of Oleic Acid Ozonolysis Products

As previously discussed, the Martini force field uses a building block approach where 4 heavy atoms are typically mapped to a single interaction site. As this mapping is not feasible for all molecules, and with the mapping not being restricted to integer numbers of atoms, some interaction sites may correspond to a slightly larger or smaller number of atoms. However, sometimes more significant deviations from the ideal mapping may be unavoidable, having for example 2 adjacent beads containing each only 3 heavy atoms. This issue can be addressed in two ways: by adjusting the bead assignment, or by adjusting the bead-to-bead distance and force constants within the molecule.

For carbon chains, the solution to the problem, provided by the authors of the Martini force field, allows two different bead types to be chosen to represent three carbons and four carbons respectively without the need to reparametrise the distance between adjacent carbon beads.[7] This method was applied in Chapter 2 and Chapter 3 for the carbon chains of oleic acid and stearic acid.

For headgroup to chain distances and force constants, comparison to the structural details of all-atom simulations, as shown in Chapter 3, provides a good basis for parameterisation. For molecules where there are no pre-existing data, the structural comparison of molecules simulated with all-atom models is a particularly useful tool in optimising the bonded parameters in the coarse-grained model.[7]

In order to determine the bonded parameters for palmitoleic acid and for the ozonolysis products of both palmitoleic and oleic acid within the Martini force field, all-atom simulations were performed using the CHARMM-36 force field and the GROMACS-5 simulation software, following the same method as described in section 3.2.2 in Chapter 3. By calculating the centre of mass of the atoms corresponding to each bead in the coarse-grained simulation, the probability of a molecule having a certain bead-to-bead distance was determined for the simulated molecules.

4.2.2 CHARMM-36 All-Atom Simulations

Parameters for each molecule simulated in this chapter are represented in the appendix A.3. Following the same method as described for the all-atom simulations of stearic acid, simulations were set up in boxes of dimensions 5.5 nm × 4.8 nm × 42.0 nm. This results in a surface area per molecule of 33 Å^2, meaning surface active molecules will be in a disordered liquid-expanded phase. Other molecules may diffuse into the water or into the vacuum. As the system set up resembles the setup used in coarse-grained simulations later on, this should give a reasonable approximations of the distances between groups of atoms within a molecule.

Two monolayers were set up facing one another with 81 molecules in each layer. The space between the molecules' headgroups was filled with TIP3P water molecules, by cutting a slab out of a pre-equilibrated water box. Therefore, the number of water molecules may differ slightly between simulation systems. Air in the model is approximated as a vacuum. Using a 2 fs time step, simulations were performed at 300 K in the NVT ensemble for 4 ns (1 ns equilibration time and 3 ns production time). Only the production time was used for analysis.

Simulation	Number of Acids/ Aldehydes	Water Molecules
1	162 palmitoleic acid	7126
2	162 nonanoic acid	7120
3	162 azelaic acid	7106
4	162 nonanal	7059
5	162 9-oxononaoic acid	7127
6	162 heptanal	7081
7	162 heptanoic acid	7135

Table 10: Simulation set up for palmitoleic acid, nonanaoic acid, azelaic acid, nonanal, 9-oxononanoic acid, heptanal and heptanoic acid.

4.3 Results and Discussion for All-Atom Simulations

4.3.1 Carbon-Carbon Bead Distance

As previously mentioned, the ideal Martini mapping uses a 4–1 approach. When measuring the distance between the centres of masses of two 4 carbon sites, we therefore expect the equilibrium bead distance to lie at the standard Martini bead-to-bead distance of 0.47 nm. To validate our approach with the CHARMM force field we measured the distance between the centre of mass of the 4 carbons and determined the best fit within a harmonic potential using both the bead distance and force constant as variables. As shown in Figure 67, the bead-to-bead distance obtained from simulations lies as expected at 0.47 nm. The simulated force constant was 1397 kJ mol^{-1} nm^{-2}, slightly higher than the standard Martini force constant of 1250 kJ mol^{-1} nm^{-2}. This lower value used as the standard Martini force constant allows a deviation from the equilibrium bead-to-bead distance of around 15 %, which is consistent with allowing a deviation from the 4 atoms per bead mapping. As shown in Figure 67, a good agreement with the Martini force field parameters was obtained, giving confidence in the approach used.

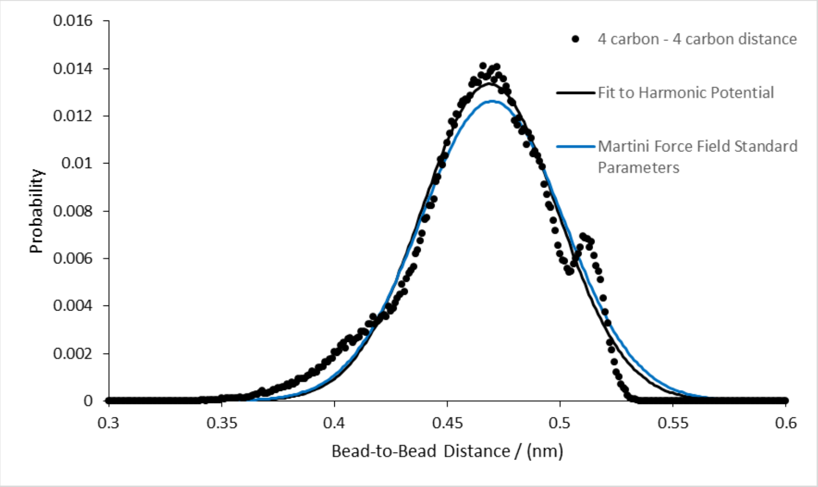

Figure 67: Bead-to-bead distance data, each bead containing 4 carbon atoms and fit to harmonic potential, in comparison to the harmonic potential used in the Martini force field, with a bead-to-bead distance of 0.47 nm and force constant of 1250 kJ mol^{-1} nm^{-2}.

4.3.2 Palmitoleic Acid

Palmitoleic acid, $C_{16}H_{30}O_2$, has a similar structure to oleic acid with its chain being only 2 carbons shorter. The molecule is split into 5 sites in the chosen coarse-grained representation. In accordance with oleic acid, the hydrophilic headgroup of palmitoleic acid consists of 3 heavy atoms and is represented by a P3 bead as shown in Figure 68 (a). The chain of palmitoleic acid is made up of the following beads: C1, C1, C3, C1. This makes the chain of palmitoleic acid one bead shorter than that of oleic acid. To account for the deviation of only 2 carbons between oleic acid and palmitoleic acid, the bead type was adjusted from C2 to C1. The cis-double bond in the chain of palmitoleic acid is mapped onto a C3 bead containing 4 heavy atoms.

As shown in Figure 68 (b), the equilibrium bead-to-bead distance for palmitoleic acid obtained by fitting the data from all-atom simulation to a harmonic potential lies at 0.35 nm. The corresponding force constant is found to be 6106 kJ mol^{-1} nm^{-2}.

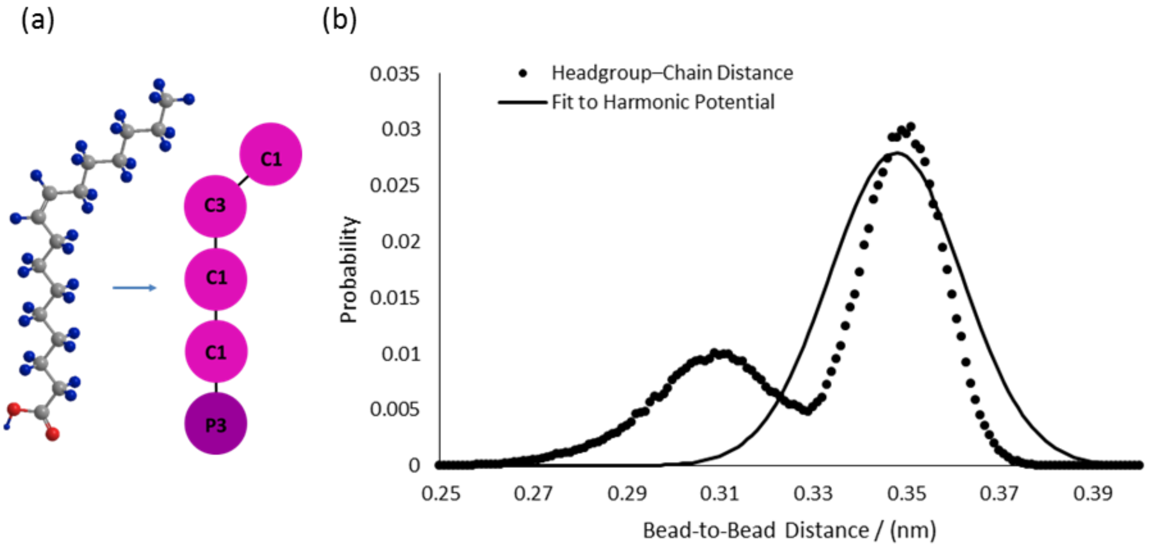

Figure 68: (a) All-atom to coarse-grained mapping of a palmitoleic acid molecule (b) Distances between centre of mass of the palmitoleic acid carboxyl headgroup bead and first bead of the carbon chain, from CHARMM all-atom simulations.

4.3.3 Nonanoic Acid

Similarly to oleic acid, the carboxyl group, mapped by a P3 bead, contains 3 heavy atoms, as shown in Figure 69 (a). The saturated chain of nonanoic acid can be mapped to the ideal mapping of 4 heavy atoms per bead. Therefore, the assignment of beads agrees best with using the standard C1 bead type, representing four carbons. Due to the headgroup and chain containing one bead more than for oleic acid, the bead-to-bead distance between the headgroup and chain was determined using all-atom simulations.

As shown in Figure 69 (b), the headgroup to chain distance is higher than that for oleic acid due to the additional carbon bead, changing from C2 in oleic acid to a C1 bead in nonanoic acid. The equilibrium bead-to-bead distance lies at 0.35 nm with a force constant of 3012 kJ mol^{-1} nm^{-2}.

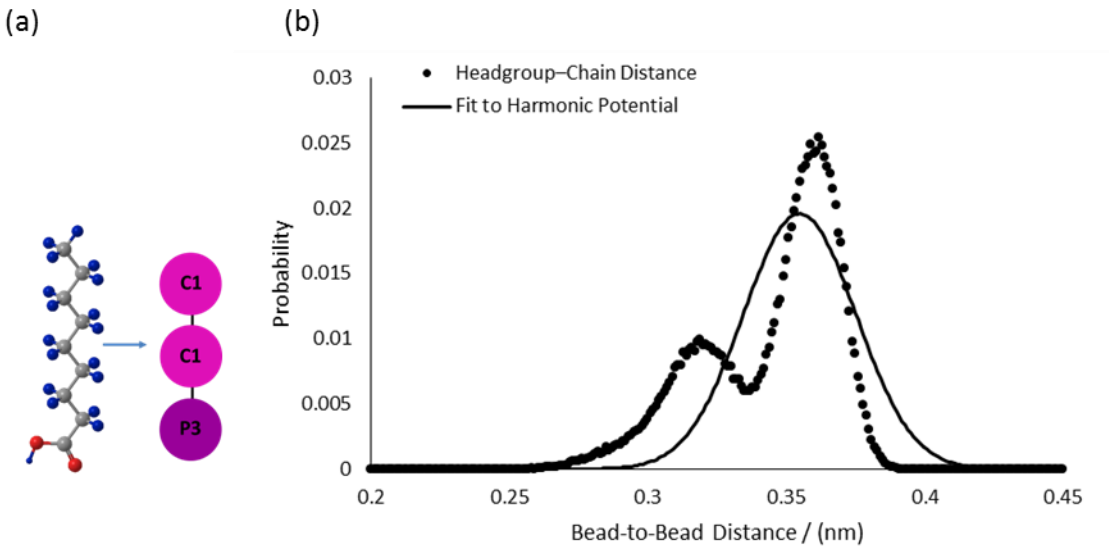

Figure 69: (a) All-atom to coarse-grained mapping of a nonanoic acid molecule (b)Distances between centre of mass of the nonanoic acid carboxyl headgroup bead and first bead of the carbon chain (4 carbons), from CHARMM all-atom simulations.

4.3.4 Azelaic Acid

Azelaic acid has a carboxyl group at either end of the chain, each being mapped to P3 beads in accordance with oleic acid and nonanoic acid. The carbon chain between them contains 7 carbons: 3.5 carbons per bead. Therefore, two C2 beads were chosen.

As expected, both sides of the chain behave similarly in the all-atom simulations showing the same peaks. The equilibrium distance between beads, lies at 0.32 nm with a force constant of 1720 kJ mol^{-1} nm^{-2}.

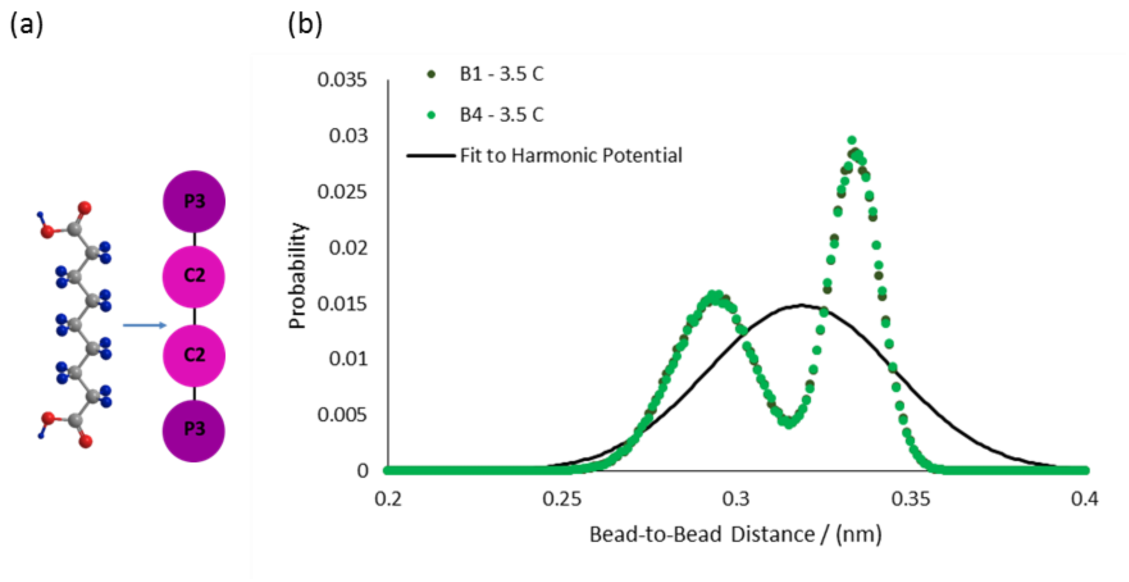

Figure 70: (a) All-atom to coarse-grained mapping of an azelaic acid molecule (b) Distances between centre of mass of the azelaic acid carboxyl groups (B1 and B4) bead and the respective next carbon chain bead (3.5 carbons), from CHARMM all-atom simulations.

4.3.5 Nonanal

For nonanal, the aldehyde group is represented by a Na bead, containing 4 heavy atoms. The remaining 6 carbons were mapped to two C2 beads, each containing 3 carbons. As shown in Figure 71, the equilibrium bead-to-bead distance between the aldehyde group and chain bead lies at 0.38 nm, with a force constant of 1224 kJ mol^{-1} nm^{-2}.

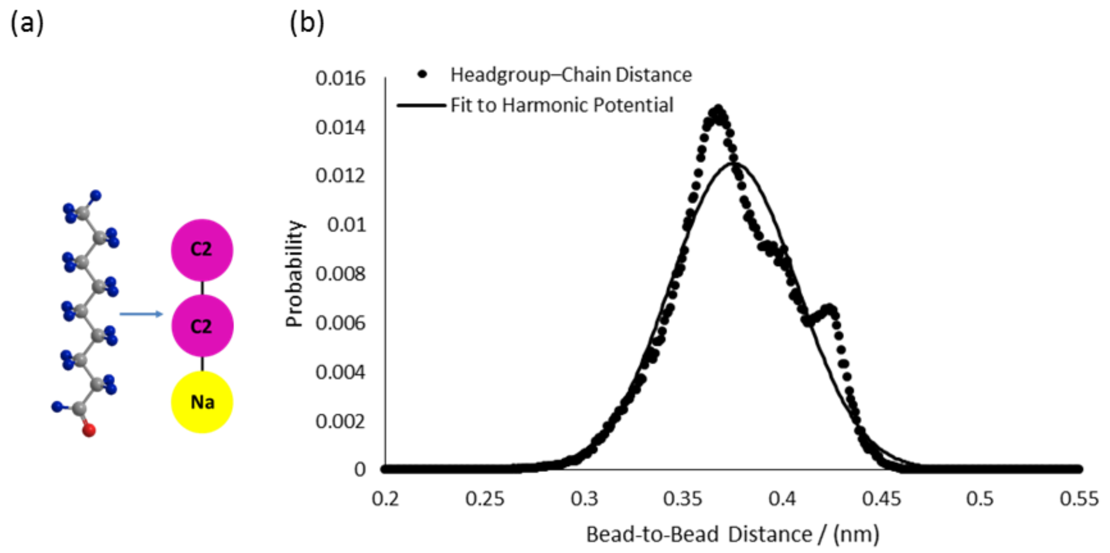

Figure 71: (a) All-atom to coarse-grained mapping of nonanal (b) Distances between centre of mass of the nonanal aldehyde group bead and the first bead in the carbon chain (3 carbons), from CHARMM all-atom simulations.

4.3.6 9-Oxononanoic Acid

9-oxononanoic acid allows the ideal Martini mapping of 4 heavy atoms per bead to be employed. A mapping of 4 heavy atoms for each the carboxyl group and aldehyde group was chosen. This leaves 4 carbon atoms, which can be mapped onto a C1 bead. This results in a mapping of P3, C1, Na. Bead-to-bead distances and force constants were calculated from all-atom simulations. The obtained results for the distance between aldehyde group and carbon bead and the distance between the carboxyl group and carbon bead are represented in Figure 72. The P3–C1 equilibrium bead distance lies at 0.38 nm with a force constant of 1520 kJ mol^{-1} nm^{-2}. For the aldehyde bead bonded to the carbon bead, an equilibrium distance of 0.43 nm with a force constant of 972 kJ mol^{-1} nm^{-2} was determined.

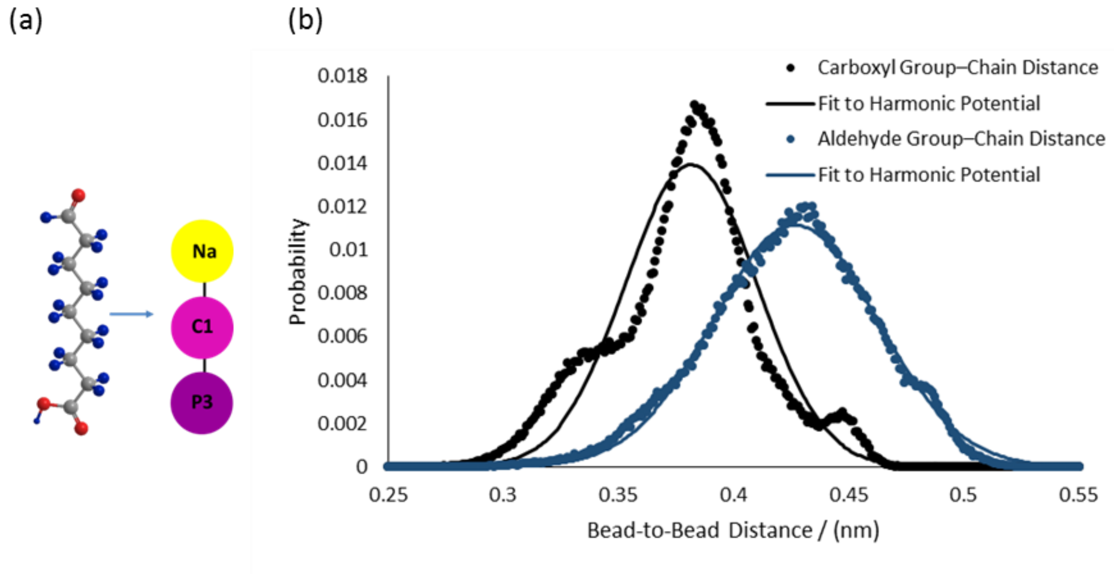

Figure 72: (a) All-atom to coarse-grained mapping for 9-oxononanoic acid (b) Distances between centre of mass of the 9-oxononanoic acid carboxyl headgroup bead and carbon bead, and distances between centre of mass of the aldehyde group bead and carbon bead, from CHARMM all-atom simulations.

4.3.7 Heptanal

Heptanal, $C_7H_{14}O$, is only two carbons shorter than nonanal, which is mapped by a Na bead followed by two C2 beads. To account for the shorter chain length, heptanal is mapped by a Na bead followed by a C1 bead. The equilibrium bead-to-bead distance and corresponding force constants were obtained from all-atom simulation and lie at 0.43 nm and 1001 kJ mol^{-1} nm^{-2} respectively, as shown in Figure 73.

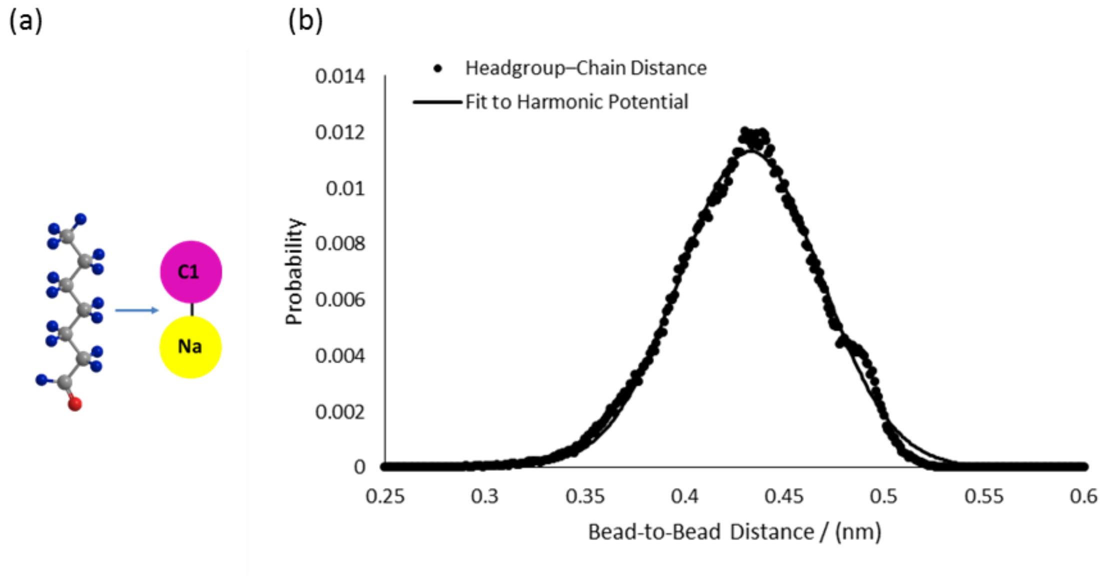

Figure 73: (a) All-atom to coarse-grained mapping of heptanal (b) Distances between centre of mass of the heptanal aldehyde headgroup bead and carbon chain bead, from CHARMM all-atom simulations.

4.3.8 Heptanoic Acid

Another product formed from the ozonolysis of palmitoleic acid is heptanoic acid, $C_7H_{14}O_2$. Heptanoic acid's mapping is based on nonanoic acid. Nonanoic acid consists of a P3 bead followed by two C1 beads. To account for the difference of two carbons between nonanoic acid and heptanoic acid, the chain of heptanoic acid is mapped onto C2 beads. Hence, the final mapping for heptanoic acid contains one P3 headgroup bead and two C2 beads. The equilibrium bead-to-bead distance between the headgroup bead and first bead of the chain obtained from all-atom simulations, as shown in Figure 74, lies at 0.31 nm. The corresponding force constant is 10436 kJ mol^{-1} nm^{-2}.

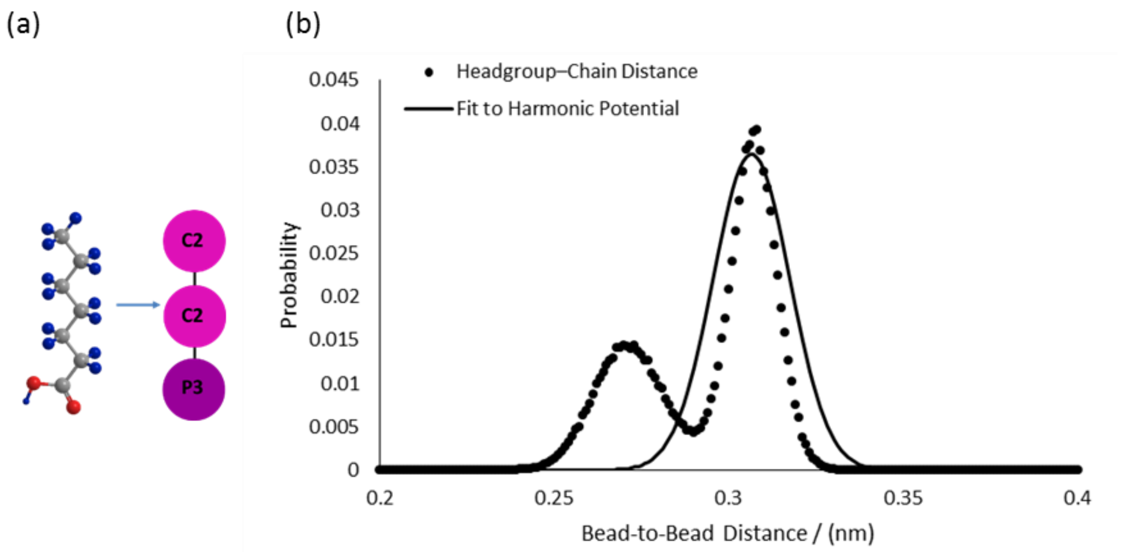

Figure 74: (a) All-atom to coarse-grained mapping of heptanoic acid (b) Distances between centre of mass of the heptanoic acid carboxyl headgroup bead and carbon chain bead, from CHARMM all-atom simulations.

4.3.9 Bead-to-Bead Distance of P3 Headgroup to Chain Bead

Figure 75 shows the data for the bead-to-bead distances between the headgroup bead and chain bead calculated from all-atom simulations and their corresponding fit to a harmonic potential for the carboxylic acid molecules parameterised in this chapter. The carbon number of the first chain bead is given in the legend.

As expected, the number of carbons associated with the beads in the chain determines the distance between the centres of mass of the corresponding beads. Heptanoic acid's P3 headgroup is bonded to a bead with only three carbons. This limits the movement of the chain, resulting in the beads in the coarse-grained representation having a rigid bond with a high force constant. Monticelli *et al.*, who parameterised proteins using the Martini force field, use bond constraints for all molecules that have a force constant higher than 7500 kJ mol^{-1} nm^{-2}.[8] As the force constant for heptanoic acid lies at 10436 kJ mol^{-1} nm^{-2}, this approach was adapted, constraining the bead-to-bead distance to 0.31 nm.

With the exception of azelaic acid, the general trend shows that the larger the number of heavy atoms per bead, the larger the bead-to-bead distance and the lower the associated force constant, accounting for the higher range of possible bead distances due to an increase in chain length. Azelaic acid differs from the other carboxylic acids parameterised here, having a carboxyl group at either end of the chain with two C2 beads in the middle. Each C2 bead contains 3.5 carbons, placing azelaic acid between heptanoic acid and palmitoleic acid based on its parameterisation. However, the force constant for the bead-to-bead distance between the carboxyl headgroup beads and chain beads is 1720 kJ mol^{-1} nm^{-2}, which is lower than suggested by the trend.

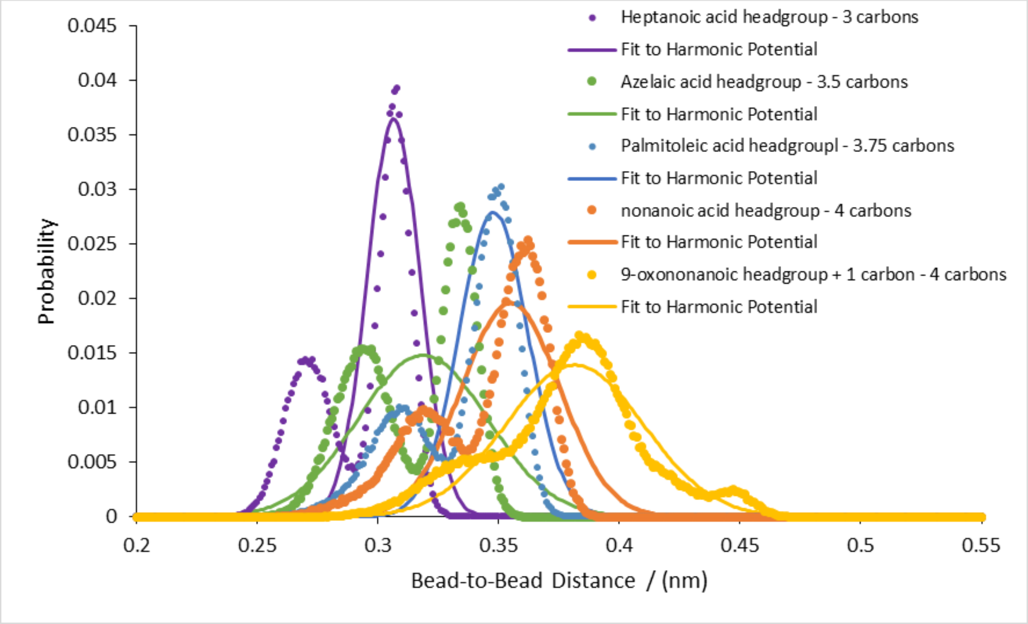

Figure 75: Carboxyl group to carbon bead distance for palmitoleic acid and for the ozonolysis products of both palmitoleic and oleic acid, with varying number of atoms per bead, indicated in the legend.

The equilibrium bead-to-bead distances and force constants obtained from calculations based on all-atom simulations for the carboxylic acids parameterised in this chapter are summarised in Table 11. The bead-to-bead distance for heptanoic acid was constrained to represent the rigidity of the bond. For the other carboxylic acid molecules, force constant values have been rounded to the nearest 50 kJ mol^{-1} nm^{-2} as appears to have been the approach used by Marrink *et al.*[9]

Molecule	Fitted Bead-to-Bead Distance (nm)	Fitted Force Constant (kJ mol^{-1} nm^{-2})	Force Constant Used (kJ mol^{-1} nm^{-2})
heptanoic acid	0.31	10436	Constraint
azelaic acid	0.32	1720	1700
palmitoleic acid	0.35	6106	6100
nonanoic acid	0.35	3012	3000
9-oxononanoic acid	0.38	1520	1500

Table 11: Bead-to-bead distances between the carboxyl bead and first bead of the chain for heptanoic acid, azelaic acid, palmitoleic acid, nonanoic acid and 9-oxononanoic acid determined from fitting to CHARMM all-atom simulations.

4.3.10 Bead-to-Bead Distance of Na Headgroup to Chain Bead

The data obtained for the distance between the aldehyde group bead and adjacent carbon bead, and the fits to harmonic potentials for nonanal, heptanal and 9-oxononanoic acid are shown in Figure 76. For all three molecules, the Na bead corresponds to 4 heavy atoms. The next bead of the molecule contains 4 carbons in the case of 9-oxononanoic acid and heptanal, and 3 carbons in the case of nonanal.

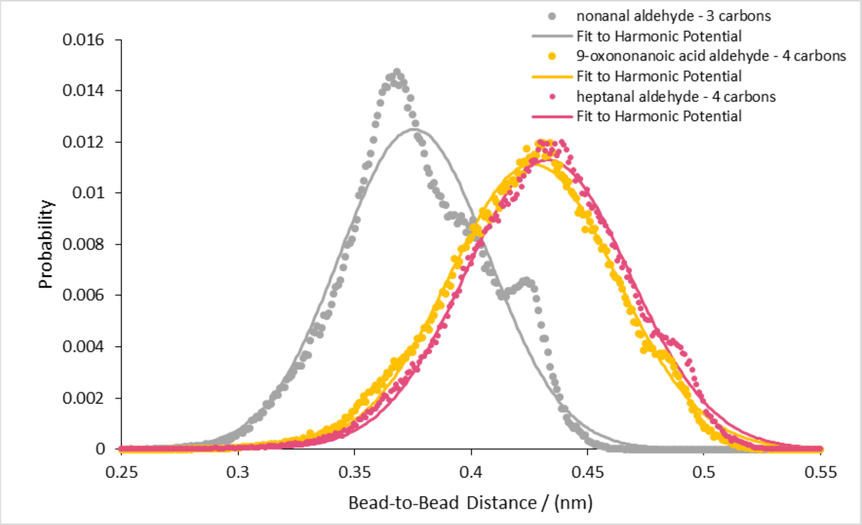

Figure 76: Comparison of bead-to-bead distances between the aldehyde group and first bead of the chain for 9-oxononanoic acid, heptanal and nonanal. The same number of atoms are mapped by the aldehyde beads. The mapping of the first bead of the carbon chain differs, however, with 4 carbons for 9-oxononanoic acid and heptanal and 3 carbons for nonanal.

The results obtained from all-atom simulations for the bead-to-bead distance and force constants are summarised in Table 12. Both the 9-oxononanoic acid and heptanal parameters are based on the same number of heavy atoms per bead. For both molecules, the same bead-to-bead distance and force constant will be used between the headgroup bead and first bead of the chain in the coarse-grained representation of the molecules.

Molecule	Fitted Bead-to-Bead Distance (nm)	Fitted Force Constant (kJ mol^{-1} nm^{-2})	Force Constant Used (kJ mol^{-1} nm^{-2})
nonanal	0.38	1224	1200
9-oxononanoic acid	0.43	972	1000
heptanal	0.43	1001	1000

Table 12: Bead-to-bead distances between the aldehyde bead and adjacent chain bead for nonanal and 9-oxononanoic acid determined from fitting to CHARMM all-atom simulations.

4.4 Method for Coarse-Grained Simulations

4.4.1 Pressure-Area Isotherm of Palmitoleic Acid

In accordance with previous pressure-area isotherm simulations, the system of palmitoleic acid was set up in a box of size 18 nm × 18 nm × 42 nm, containing 882 palmitoleic acids (441 in each monolayer), 12852 water beads and 1300 antifreeze beads. This initial structure was compressed in the lateral dimension, without altering the box length in the normal direction. The number of beads, pressure and temperature were kept constant in the box (NPT ensemble). Semi-isotropic pressure coupling was applied to the system, with pressure controlled by a Berendsen barostat. A coupling time constant of 4 ps with a compressibility of 5×10^{-5} bar^{-1} in the x/y dimensions of the box was used. A lateral pressure of +60 bar was applied, causing a decrease in water surface area available per molecule. Snapshots were taken at several points during the compression. Each of these snapshots was run in the NVT ensemble for 1000 ns (200 ns equilibration time and 800 ns production time). Only the production time was used for analysis.

4.4.2 Ozonolysis Products of Palmitoleic Acid and Oleic Acid

Coarse-grained simulations were performed for the oleic acid and palmitoleic acid ozonolysis products using the newly derived parameters from the CHARMM simulations described in sections 4.3.9 and 4.3.10. Each molecule was set up in the same way as for oleic acid described previously in Chapter 2, generating starting structures with two monolayers at the vacuum-water interface, as shown in Figure 77. Each starting configuration was run in the NVT ensemble for 1000 ns.

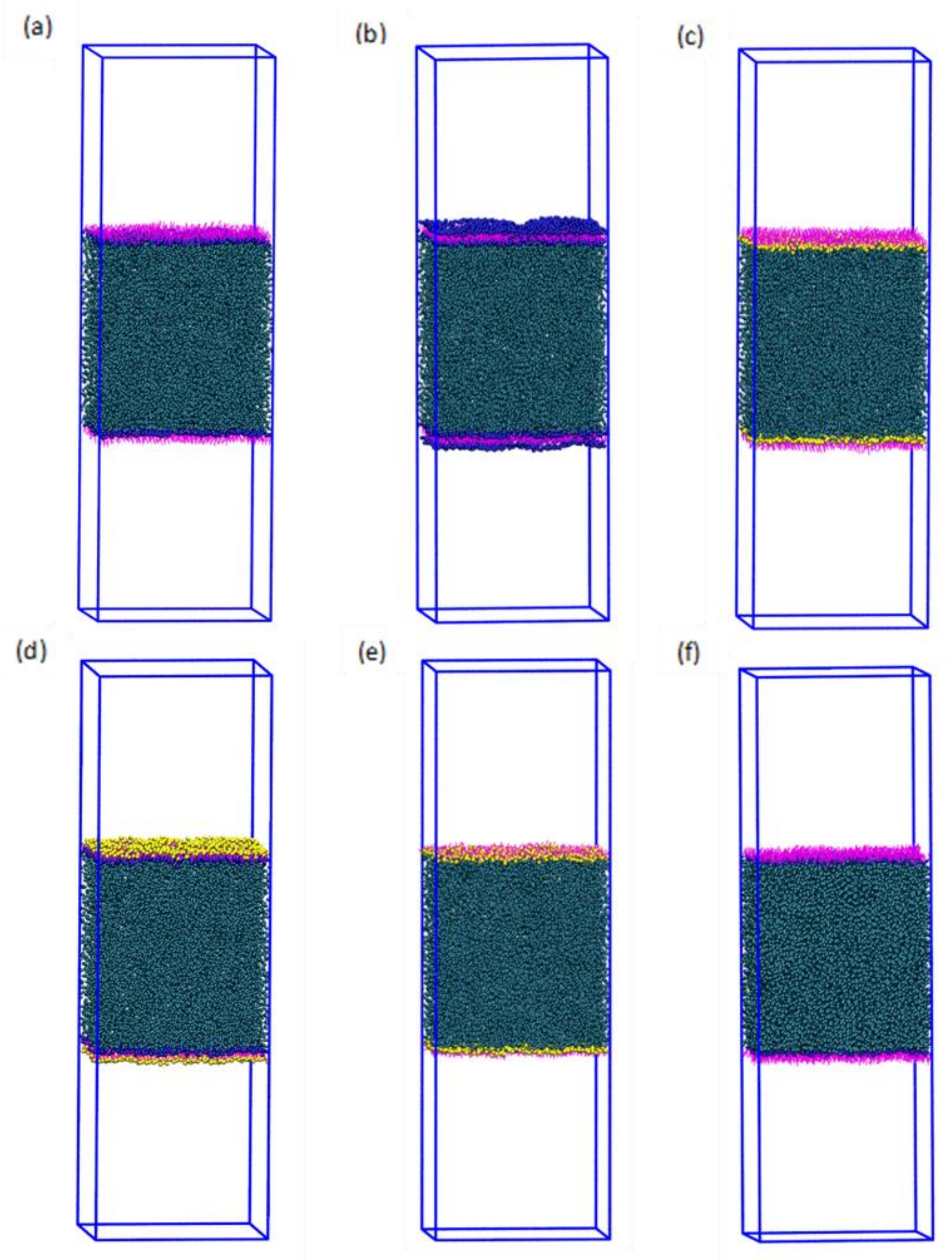

Figure 77: Starting structures for (a) nonanoic acid (b) azelaic acid (c) nonanal and (d) 9-oxononanoic acid (e) heptanal (f) heptanoic acid. Water = teal, carbon chain-magenta, headgroup beads: P3-blue, Na-yellow.

4.5 Results and Discussion of Coarse-Grained Simulations

4.5.1 Pressure-Area Isotherm of Palmitoleic Acid

The pressure-area isotherm for palmitoleic acid produced from simulations is shown in Figure 78. Three simulations were run for each point on the isotherm allowing the determination of the mean surface pressure at each area per molecule and the 95 % confidence interval.

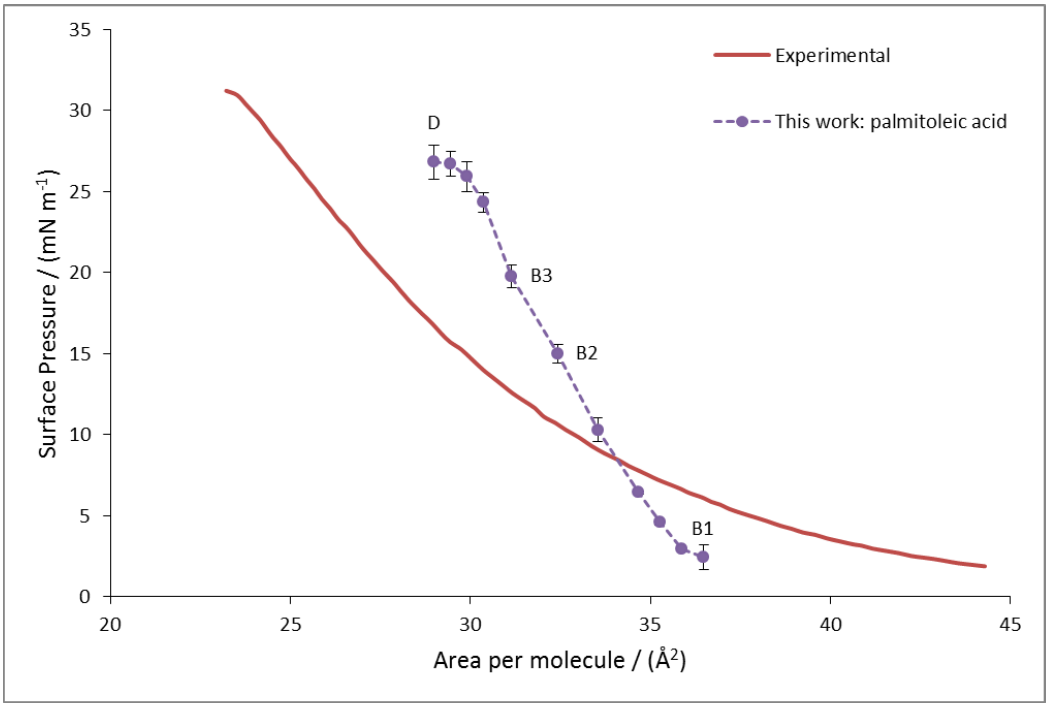

Figure 78: Simulated pressure-area Isotherm for palmitoleic acid at the air-water interface compared to the experimental isotherm by Sebastiani.[10] Isotherms produced in this work: Mean surface pressures, with 95 % confidence intervals shown. Phase behaviour of simulated isotherm indicated: (B1, B2 and B3) liquid-expanded region and (D) equilibrium spreading pressure.

Equilibrium spreading pressures for both oleic acid and palmitoleic acid are similar in experiments, reaching 32 mN m^{-1}.[10] To our knowledge the only pressure-area isotherm reported in the literature for palmitoleic acid is by Sebastiani as shown in Figure 78; hence it is not possible to get a consensus of the actual equilibrium spreading pressure and an estimate of the potential spread. The equilibrium spreading pressure determined in this work from simulations for palmitoleic acid is 26.80 ± 1.06 mN m^{-1}.

In comparison to the isotherm of oleic acid, the isotherm of palmitoleic acid is shifted to the left, hence to lower areas per molecules, meaning that the shorter chain length of palmitoleic acid allows the molecules to pack more closely. Like oleic acid, palmitoleic acid chains remain disordered under compression, as shown in Figure 79 and Figure 80. This agrees well with the pressure-area isotherms for oleic acid and palmitoleic acid at the air-water interface produced with a Langmuir trough by Sebastiani, where it is concluded that films of both molecules remain in a disordered liquid-expanded phase until film collapse.[10] This was verified in experiments by BAM images of the films at low surface pressures which showed featureless, isotropic surfaces.[10]

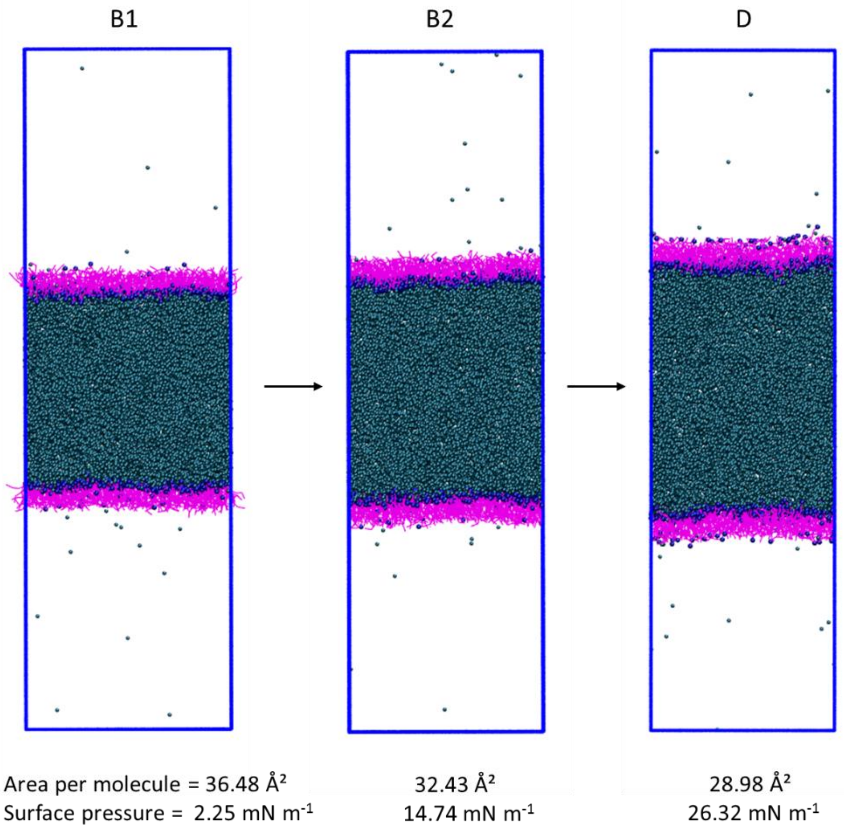

Figure 79: Comparison of palmitoleic acid monolayers from low to high surface pressures (B1, B2, D—points indicated on isotherm in Figure 78). Under compression more palmitoleic acid molecules squeeze out of the layer, indicating a collapse of the system. Palmitoleic acid headgroup: purple, palmitoleic acid chain: magenta, water: teal.

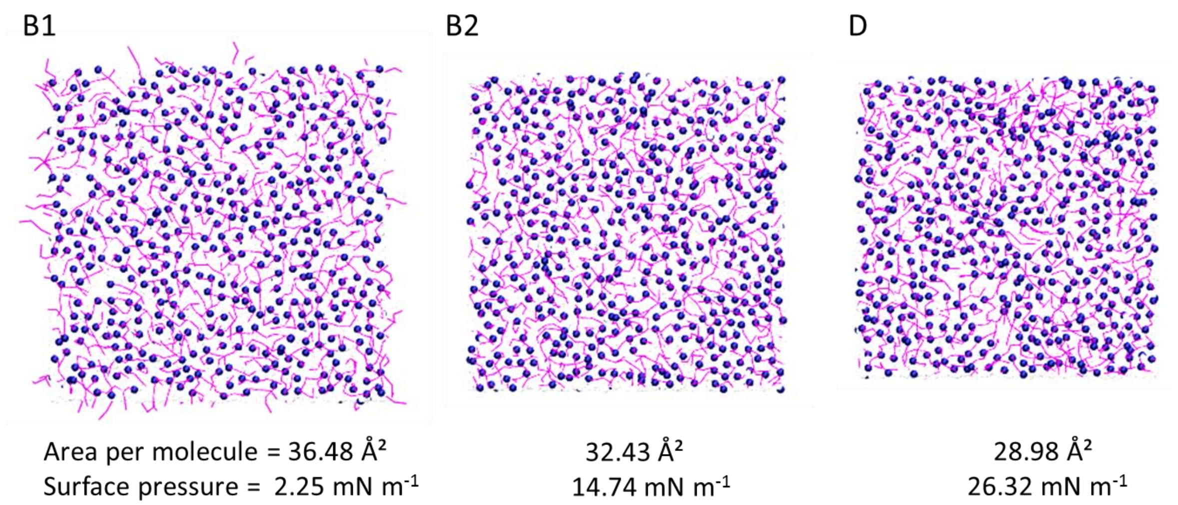

Figure 80: Top view of the upper palmitoleic acid monolayer at several points along the pressure-area isotherm (B1, B2, D—points indicated on isotherm in Figure 78). Palmitoleic acids chains stay disordered under compression. Palmitoleic acid headgroup: purple, palmitoleic acid chain: magenta.

As previously described for oleic acid, the internal angles (α) and (θ) of palmitoleic acid, represented in Figure 81, were determined from simulations. Analysis was performed at three different points along the isotherm: at the lowest surface pressure at 2.25 mN m^{-1}, one in the middle of the isotherm at a surface pressure of 14.47 mN m^{-1} and one at the highest point of the isotherm at a surface pressure of 26.32 mN m^{-1}.

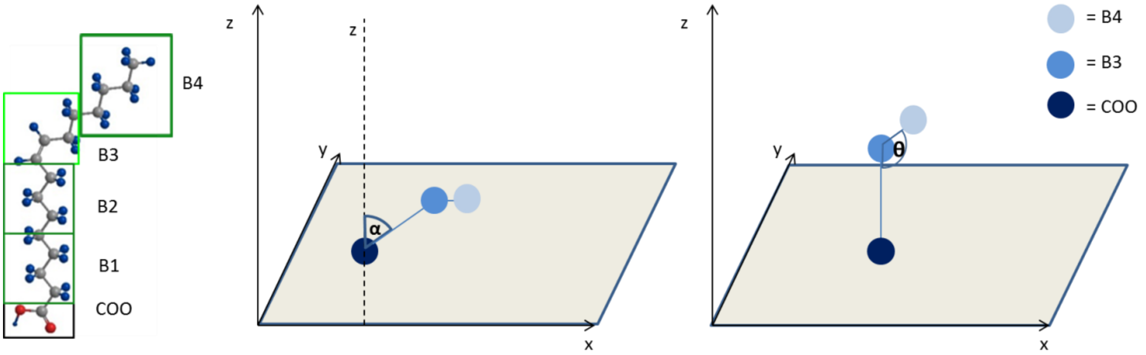

Figure 81: Representation of angles (α) and (θ) of a palmitoleic acid molecule.

As shown in Figure 82, angle (θ) increases with increasing surface pressure. At a low surface pressure and a high area per molecule, the peak of the angle distribution lies at 122°, close to the equilibrium angle of 120°. Under compression, this angle increases slightly: at a surface pressure of 14.47 mN m^{-1} the peak of the angle distribution is at 125°, and at a surface pressure of 26.32 mN m^{-1} the peak lies at 127°. This trend matches the results obtained for oleic acid, where a decrease in surface area per molecules causes the molecules to orient in a way so as to increase their packing ability.

Angle (α), which represents the tilt of the molecules with respect to the monolayer normal, decreases with increasing surface pressures. At a low surface pressure, molecules lie at an angle of 27°; under compression, the tilt of the molecules decreases to 22° at a surface pressure of 14.47 mN m^{-1}, and remains at this angle until the monolayer collapses. At the highest surface pressure, an increase in molecules with a higher angle (α) can be seen (>90°), meaning molecules lie horizontal with respect to the monolayer normal or are turned upside down. This is most likely due to an increase in molecules that move out of the layer, indicating the collapse of the monolayer—to verify this, contour plots of angle (α) with respect to the *z*-coordinate of the headgroup bead were produced.

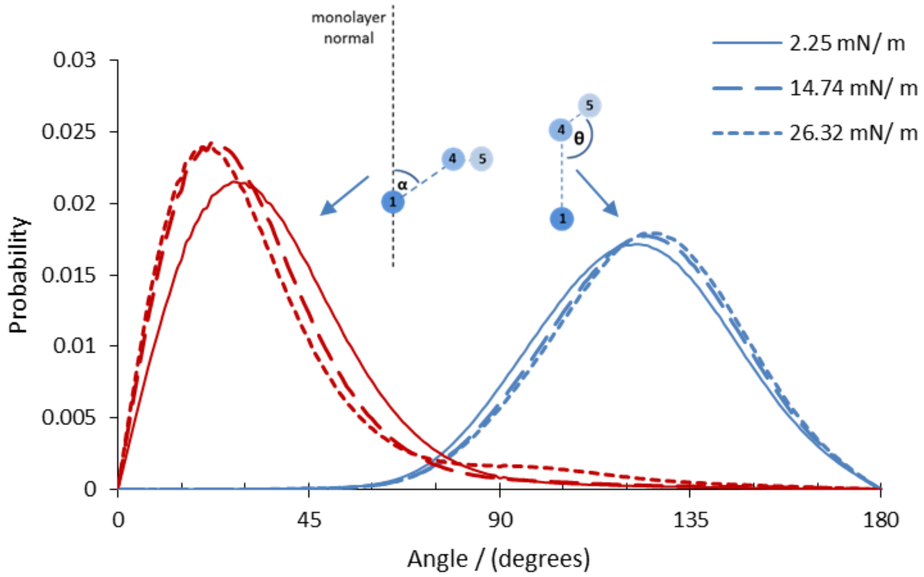

Figure 82: Angle Distributions of angle (α) and (θ) for 3 monolayers of palmitoleic acid with varying surface pressures.

Figure 83 shows contour plots of the molecules' tilt with respect to the *z*-axis against the *z*-coordinate of the respective molecules over the 800 ns production time. The contour plots show both the top monolayer and the bottom monolayer. In the plots, each monolayer shows two distinct regions—the highest density regions indicating the molecules within the layer and the second regions at higher angles indicating the molecules that have moved out of the layer. It is shown that, under compression, more molecules move out of the layer.

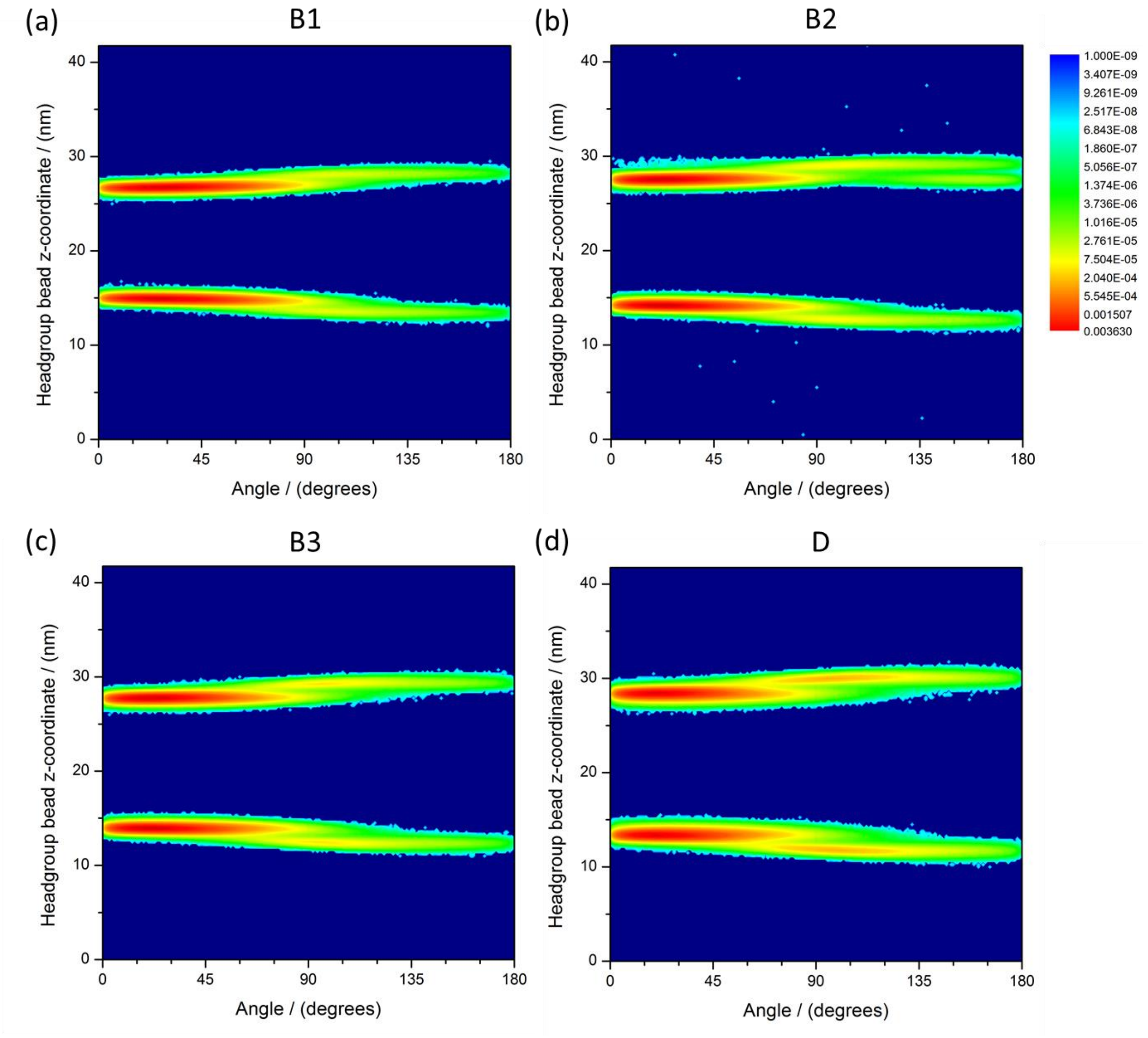

Figure 83: Contour plots showing the probability of finding the headgroup of a molecule at a certain *z*-coordinate with respect to the molecules angle (α) for two systems where monolayers in (a) (B1) have an area per molecule of 36.48 Å^2 and a surface pressure of 2.25 mN m^{-1}, monolayers in (b) (B2) have an area per molecule of 32.43 Å^2 and a surface pressure of 14.74 mN m^{-1}, monolayers in (c) (B3) have an area per molecule of 31.14 Å^2 and a surface pressure of 19.46 mN m^{-1}, and monolayers in (d) (D) have an area per molecule of 28.98 Å^2 and a surface pressure of 26.32 mN m^{-1}. Points B1, B2, B3 and D are indicated on pressure-area isotherm in Figure 78.

Determining the lowest density regions in the contour plots between the two regions in each monolayer allowed the approximation of the percentage of molecules that are not in the typical monolayer configuration during the production time, as shown in Figure 84. The general trend shows that the lower the area per molecule and the higher the surface pressure, the more molecules move out of the layer. At the equilibrium spreading pressure, approximately 8.3 % of the molecules get squeezed out of the layer. The only exception is the monolayer at an area per molecule of 32.43 Å^2 and a surface pressure of 14.74 mN m^{-1}, which shows a higher percentage of molecules that have turned out of the layer than expected. As shown in the contour plot of the respective monolayers in Figure 83, this is likely due to molecules being lost from the surface to the vacuum, which is not observed for the other monolayers.

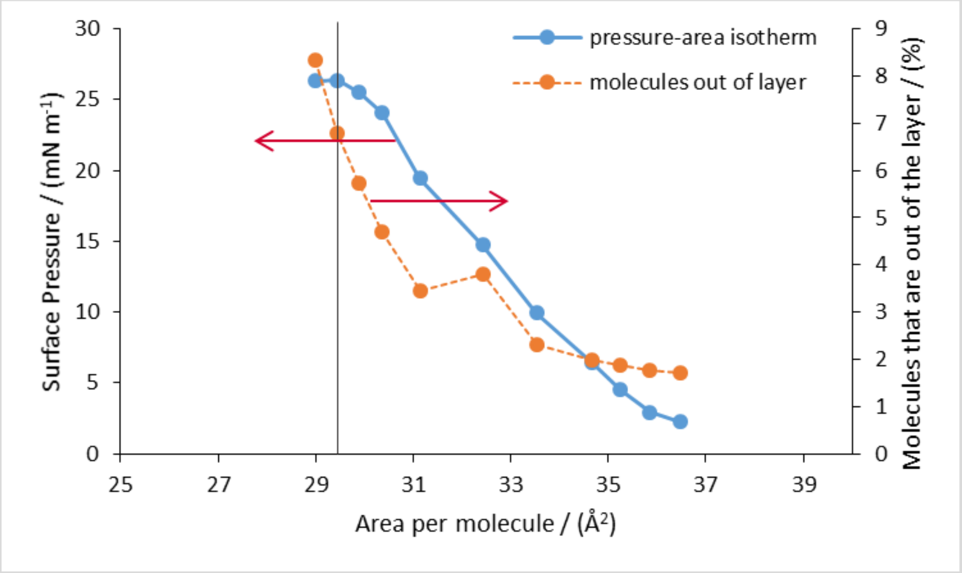

Figure 84: Pressure-area isotherm and percentage of palmitoleic acid molecules that are out of the layer during the production time, based on calculations from the contour plots, against the area per molecule. Vertical line indicates the percentage of molecules that move out of the layer at the equilibrium spreading pressure (area per molecule = 28.98 Å^2, surface pressure = 26.32 mN m^{-1}). Arrows indicate relevant axes.

4.5.2 Phase Behaviour of Ozonolysis Products from Coarse-Grained Simulations

4.5.2.1 Nonanoic Acid

As shown in Figure 85, nonanoic acid stays at the water surface throughout the simulation, with some nonanoic acid molecules changing orientation. Nonanoic acid has a much shorter chain length compared to the previously investigated C-16 and C-18 carbon acids. With the chain-chain interactions within nonanoic acid being less strong, we expect the film to be less stable under compression. However, as nonanoic acid remains at the interface it is interesting to study its behaviour further in mixed monolayers, giving a more realistic proxy for aged atmospheric aerosol surface film.

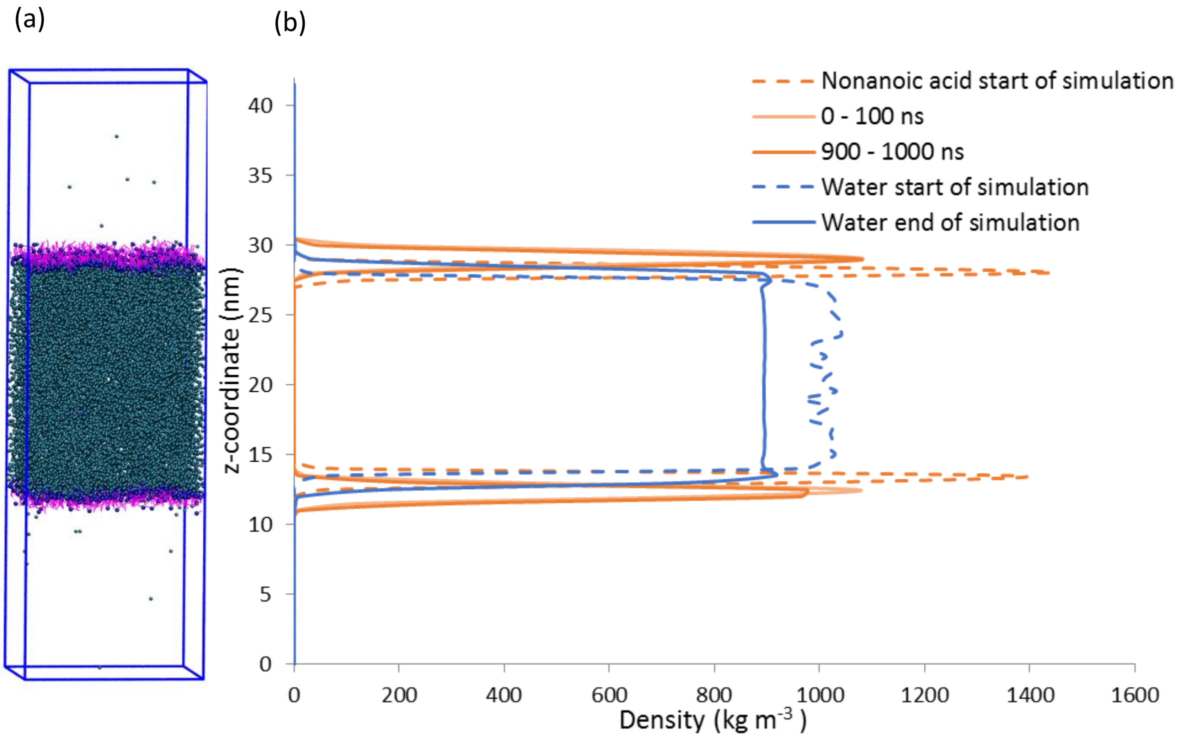

Figure 85: (a) Image of nonanoic acid at the vacuum-water interface after 1000 ns simulation time (water = teal, nonanoic acid = P3 headgroup blue, chain magenta). (b) Average density profiles of water (start and end of simulation) and nonanoic acid (start of simulation, 0–100 ns and 900–1000 ns). Orange lines describe the species of interest's time evolution.

4.5.2.2 Azelaic Acid

The aqueous solubility of azelaic acid is 2.4 g L^{-1}, an order of magnitude larger than that of nonanoic acid, which lies at 0.28 g L^{-1}.[11-13] Simulations show that azelaic acid, starting off as a layer at the vacuum-water interface, diffuses into the water where it rapidly equilibrates. As shown with the density profiles in Figure 86, after 100 ns of simulation time, the molecules agglomerate, the resulting structure then moves freely through the water within the simulation box.

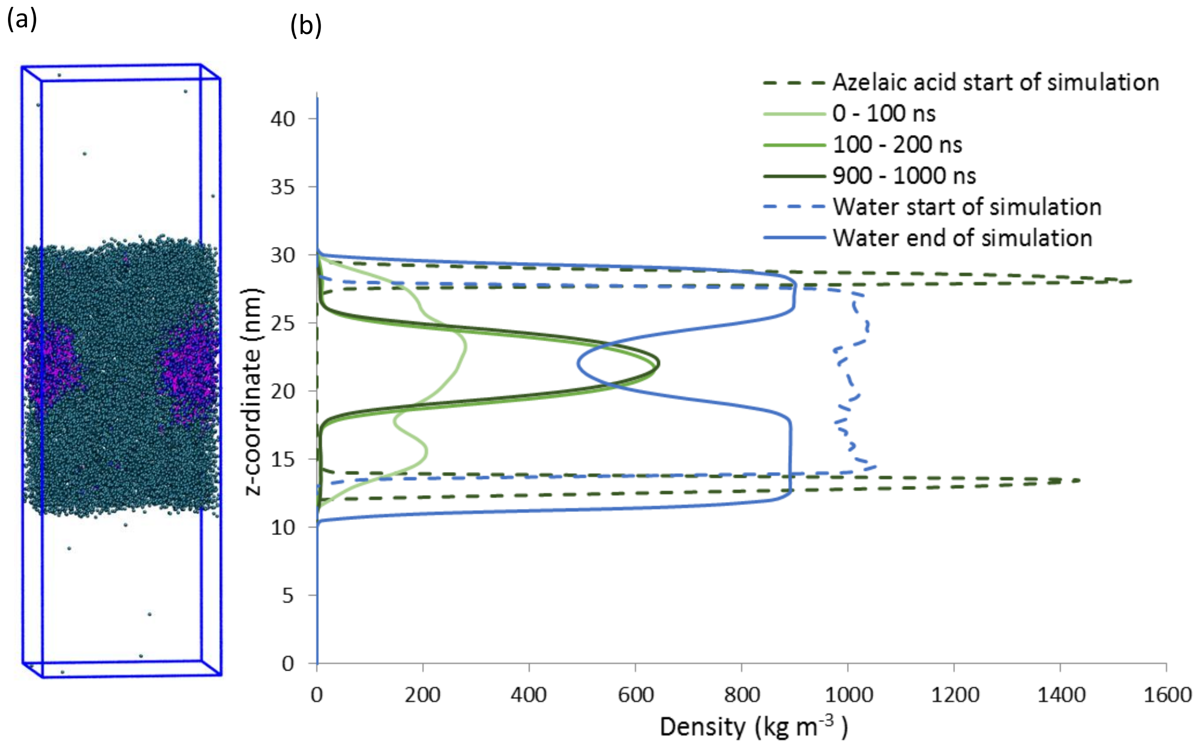

Figure 86: (a) Image of azelaic acid in water after 1000 ns simulation time (water = teal, azelaic acid = P3 headgroup blue, carbon chain magenta). (b) Average density profiles of water (start and end of simulation) and azelaic acid (start of simulation, 0–100 ns, 100–200 ns and 900–1000 ns)

4.5.2.3 Nonanal

Nonanal is a volatile compound and hence is expected to evaporate from the droplet's surface, as observed in experimental studies.[2, 3] Due to the closed nature of the simulation system, the number of particles in the box stays constant throughout the simulation. Molecules that leave the surface of the monolayer and leave the simulation box at the top will reappear at the bottom of the simulation box. Simulations show that it is more favourable for the molecules in the simulation box to join the opposite monolayer and group together than to remain in the vacuum. This shows a clear limitation of the model which approximates air as a vacuum in a closed simulation box. The image in Figure 87 shows that nonanal molecules aggregate to minimise the contact with the surface of the water. The system equilibrates within the first 100 ns. The hydrophobic chains point to the centre of the cylinder-like structure. Both top and bottom layers show the same behaviour, with the bottom layer cylinder being rotated by 90°.

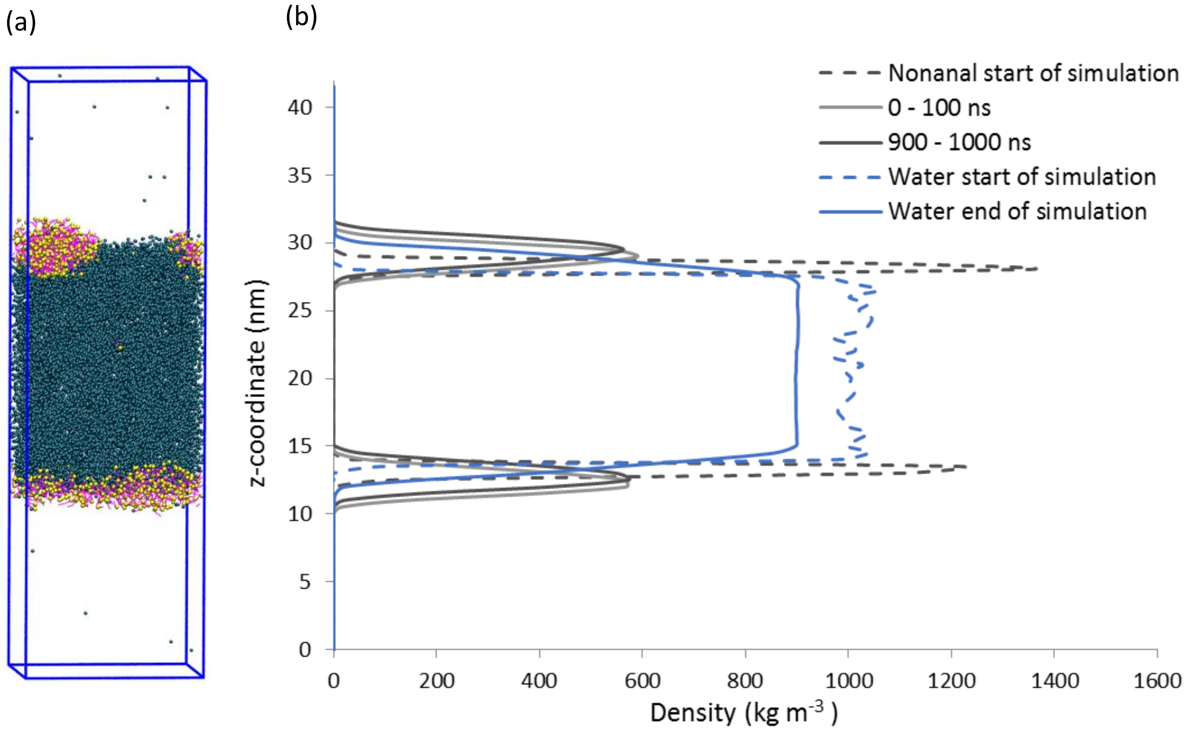

Figure 87: (a) Image of nonanal at the vacuum-water interface after 1000 ns simulation time (water = teal, nonanal = headgroup yellow, chain pink). (b) Average density profiles along the *z*-axis of the box for water (start and end of simulation) and nonanal (start of simulation, 0–100 ns, and 900–1000 ns)

4.5.2.4 9-Oxononanoic Acid

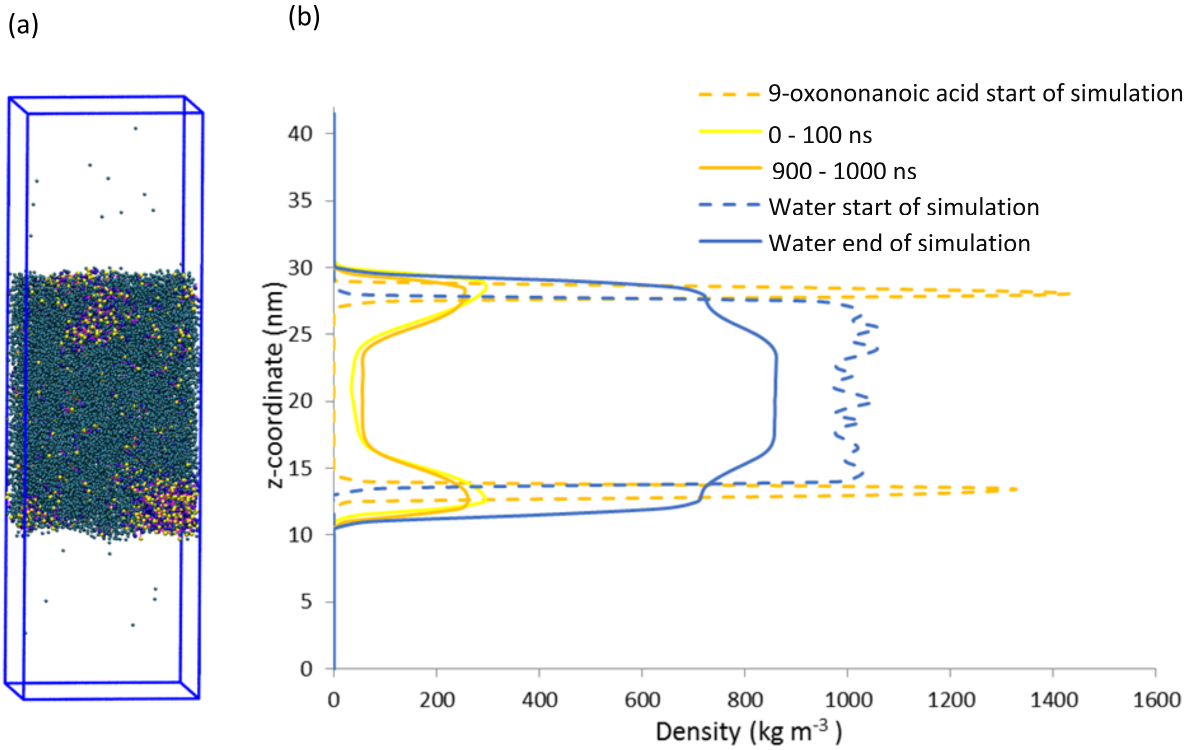

Figure 88: (a) Image of 9-oxononanoic acid in water after 1000 ns simulation time (water = teal, 9-oxononanoic acid = Na group yellow, P3 group blue, carbon chain bead magenta). (b) Average density profiles along the *z*-axis of the box for water (start and end of simulation) and 9-oxononanoic acid (start of simulation, 0–100 ns, and 900–1000 ns).

King *et al.* state that the solubility of 9-oxononanoic acid lies between that of nonanoic acid and azelaic acid.[12] Simulations show that 9-oxononanoic acid rapidly diffuses into the water, with a higher proportion of molecules just below the water surface. Some of the molecules cluster together. This is a particularly interesting observation due to the acid not being readily commercially available; to our knowledge, no experimental studies have been performed on the pure compound.

4.5.2.5 Heptanal

The top layer of heptanal rapidly loses material which, due to the closed nature of the system, accumulates on the surface of the water on the opposite side of the box. This shows the volatility of the compound. Just as for nonanal, we would expect heptanal to rapidly evaporate from the surface of the droplet once formed.

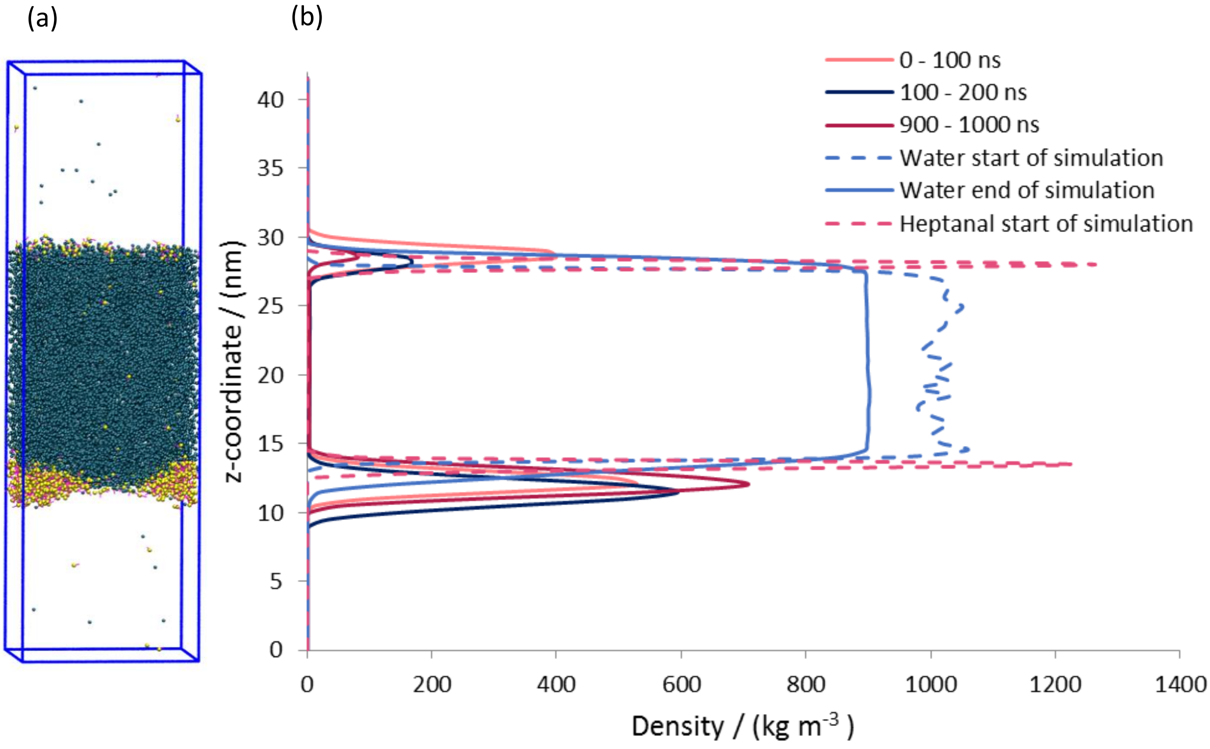

Figure 89: (a) Image of heptanal in water after 1000 ns simulation time (water = teal, heptanal = Na group yellow, carbon chain bead magenta). (b) Average density profiles along the *z*-axis of the box for water (start and end of simulation) and heptanal (start of simulation, 0–100 ns, 100–200 ns and 900–1000 ns).

4.5.2.6 Heptanoic Acid

Similar to nonanoic acid, the two carbon shorter compound, heptanoic acid, stays as a layer at the surface of the water, as shown in Figure 90, throughout the simulation time. It will therefore be interesting to simulate mixed layers containing heptanoic acid in future simulations as a more realistic proxy of the atmospheric aerosol surface film composition after the ozonolysis of palmitoleic acid.

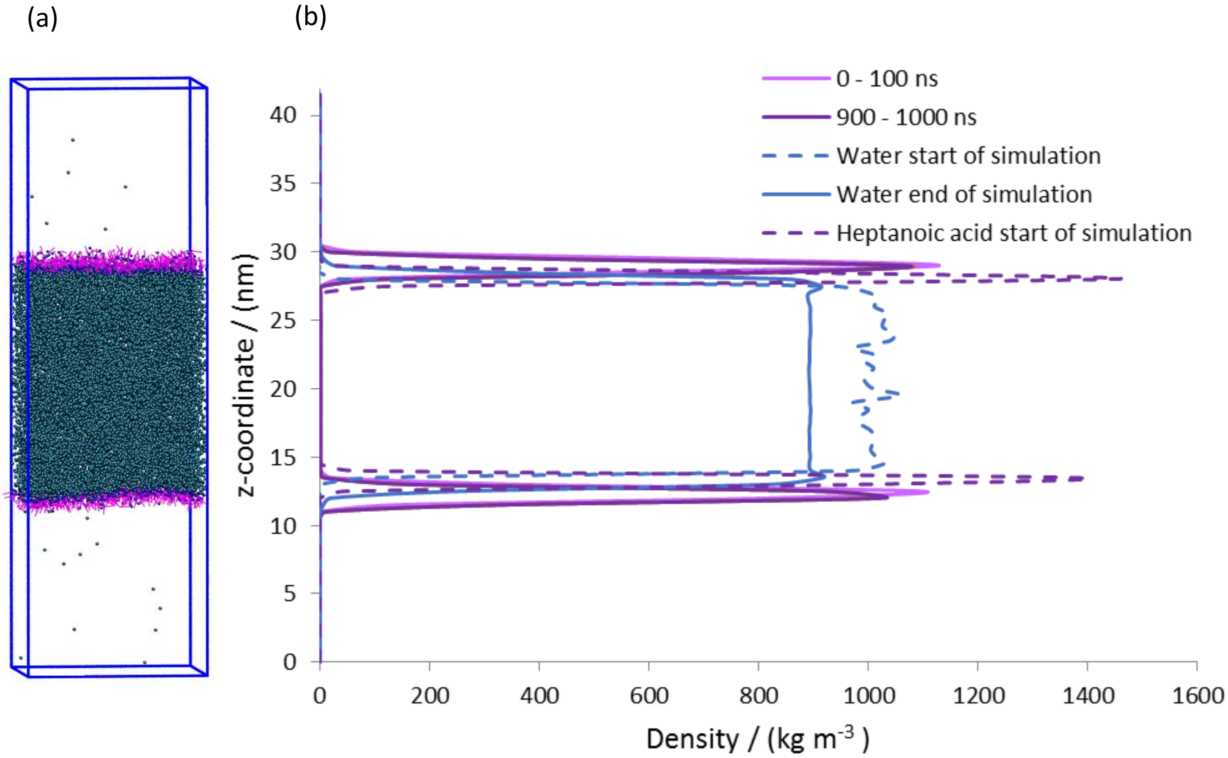

Figure 90: (a) Image of heptanoic acid at the water surface after 1000 ns simulation time (water = teal, heptanoic acid = carboxyl group blue, carbon chain beads magenta). (b) Average density profiles along the *z*-axis of the box for water (start and end of simulation) and heptanoic acid (start of simulation, 0–100 ns, and 900–1000 ns).

4.6 Conclusions

In this chapter, a pressure-area isotherm for palmitoleic acid was produced from simulations, which showed that palmitoleic acid, like oleic acid, stays as a disordered layer under compression until the monolayer collapses. It was shown that the number of molecules that squeeze out of the layer increases with increasing surface pressure.

The phase behaviour of the ozonolysis products of oleic acid and palmitoleic acid were determined in this chapter from simulations. Simulations show that both nonanal and heptanal group together at the vacuum-water interface with some molecules moving into the vacuum. The closed nature of the simulation system does not allow molecules to be lost from the system, however, in the atmosphere, we would expect both compounds to evaporate from the droplet surface. Both heptanoic acid and nonanoic acid remain as monolayers at the surface of the water over the timescale of our simulations. Simulations of azelaic acid show that this compound diffuses into the bulk water, and agglomerates. Simulations of 9-oxononanoic acid show that the compound diffuses into the bulk water, groups, and stays just below the surface of the water over the timescale of the simulations.

Out of the simulated reaction products, the only ones remaining at the surface of the aerosol are nonanoic acid, formed from the ozonolysis of oleic acid, and heptanoic acid, formed from the ozonolysis of palmitoleic acid. They will be modelled in mixed surface films in the next chapter in order to get a better proxy of the surface composition of the aged aerosol after ozonolysis.

4.7 References

1. C. Pfrang, F. Sebastiani, C. O. M. Lucas, M. D. King, I. D. Hoare, D. Chang and R. A. Campbell, *Phys. Chem. Chem. Phys.*, 2014, **16**, 13220-13228.
2. L. F. Voss, M. F. Bazerbashi, C. P. Beekman, C. M. Hadad and H. C. Allen, *J. Geophys. Res.*, 2007, **112**.
3. J. Zahardis and G. A. Petrucci, *Atmos. Chem. Phys.*, 2007, **7**, 1237-1274.
4. C. Pfrang, M. Shiraiwa and U. Pöschl, *Atmos. Chem. Phys.*, 2011, **11**, 7343-7354.
5. O. Vesna, S. Sjogren, E. Weingartner, V. Samburova, M. Kalberer, H. W. Gäggeler and M. Ammann, *Atmos. Chem. Phys.*, 2008, **8**, 4683-4690.
6. W. F. Rogge, M. A. Mazurek, L. M. Hildemann, G. R. Cass and B. R. T. Simoneit, *Atmos. Environ. A-Gen.*, 1993, **27**, 1309-1330.
7. S. J. Marrink, H. J. Risselada, S. Yefimov, D. P. Tieleman and A. H. de Vries, *J. Phys. Chem. B*, 2007, **111**, 7812-7824.
8. L. Monticelli, S. K. Kandasamy, X. Periole, R. G. Larson, D. P. Tieleman and S.-J. Marrink, *J. Chem. Theory Comp.*, 2008, **4**, 819-834.
9. S. J. Marrink, H. J. Risselada, S. Yefimov, D. P. Tieleman and A. H. d. Vries,(2007), *The MARTINI forcefield: coarse grained model for biomolecular simulations*, http://md.chem.rug.nl/cgmartini/images/parameters/ITP/martini_v2.0.itp, [August 2014]
10. F. Sebastiani, *Neutron Reflectometry and Ellipsometry Applied to Atmospheric Night-time Oxidation*, University of Reading Ph.D., 2014.
11. J. B. Gilman, T. L. Eliason, A. Fast and V. Vaida, *J. Colloid Interf. Sci.*, 2004, **280**, 234-243.
12. M. D. King, A. R. Rennie, K. C. Thompson, F. N. Fisher, C. C. Dong, R. K. Thomas, C. Pfrang and A. V. Hughes, *Phys. Chem. Chem. Phys.*, 2009, **11**, 7699-7707.
13. R. Tuckermann, *Atmos. Environ.*, 2007, **41**, 6265-6275.

Chapter 5

Mixed Component Surface Films

5.1 Mixed Organic Aerosols

Atmospheric aerosols are made up of a variety of compounds. To provide a more representative model of the surface composition of an atmospheric aerosol, this chapter focuses on mixed component films. In the literature, several studies have reported on mixed component films as a proxy for surface films on atmospheric aerosols.[1-4] Molecular dynamics simulations of such systems are still scarce;[1] however, they provide useful insight on a molecular level into the structure and dynamics of surface films.
Low solubility in the subphase and low volatility cause a molecule to stay at the interface. The more hydrophobic an acid, meaning the longer the carbon chain, the more likely it is to remain at the interface.[2] In this work, mixed component films will be compared to their single component counterparts in order to establish film selectivity and structural stability.

Mixed films of oleic acid (OA) and its saturated analogue, stearic acid (SA), will be investigated in this chapter at the following compositions: 50:50, 33:67 and 22:78. These compositions were chosen based on upcoming experimental work in the research group.

A further mixture of 10:90 OA:SA will be modelled, as recent experimental studies on surface-active insoluble material from real aerosols suggest that a higher proportion of the saturated compound than the unsaturated compound is present on the surface of the atmospheric aerosol.[5] This suggests that the mixtures with a low percentage of OA present will be the most atmospherically relevant.

Unsaturated compounds are susceptible to ozonolysis in the atmosphere. As was established in the previous chapter, the only compound expected to remain at the interface after the ozonolysis of OA is nonanoic acid (NA). Hence, to determine the maximum effect of NA on the ordering and structure of the surface film, a quarter of the OA molecules in the 33:67 OA:SA mixture, will be replaced by NA molecules.

Palmitoleic acid (POA) surface films on atmospheric aerosols have received little attention to date—to establish whether there is a difference in behaviour between POA and OA, mixtures of SA and POA were simulated. This was done in order to establish if the shorter chain length of POA, compared to OA, causes changes to the molecular packing at the interface, which would change the droplets interfacial properties and hence could have effects on its lifetime in the atmosphere, suggesting that it would be useful to get more experimental insight into this compound. Here, mixtures containing 10:90 and 22:78 POA:SA will be modelled. The only compound expected to remain at the interface after the ozonolysis of POA, as established in Chapter 4, is heptanoic acid (HA). Simulations of mixed component films containing HA will give a proxy of an aged POA film in the atmosphere.

5.2 Method

5.2.1 Composition and System Setup of Mixed Component Surface Films

5.2.1.1 Mixed Monolayers Containing Oleic Acid and Stearic Acid

Molecules in this chapter will be mapped, as established in previous chapters. OA is represented by a P3 bead followed by C2, C2, C3, C2, C2 beads, with parameters described in Chapter 2, section 2.3.2. SA is represented by a P3 bead, followed by four C1 beads. For detailed parameters, see Chapter 3, section 3.2.2. NA is mapped onto a P3 bead followed by two C1 beads, with the parameters used specified in Chapter 4, section 4.3.3.

Mixtures were set up in a grid at the vacuum-water interface. The molecules were set up in ordered arrays; however, a large initial area per molecule was chosen in order to allow enough space for the molecules to rearrange freely on the surface under compression. Each system contained 484 molecules in each monolayer. 4 different mixtures of OA and SA were set up at different ratios (50:50, 33:67, 22:78 and 10:90). The first three mixtures were chosen to match upcoming experiments in the research group. The mixture of 10 % OA and 90 % SA was chosen based on literature data, which suggested that the amount of unsaturated material on the surface of atmospheric aerosols is much lower than originally expected. The low quantity of OA in the sample makes it challenging to produce the mixture accurately in a laboratory, and to follow during ozonolysis, given the much reduced signal-to-noise ratios. However, out of the simulated systems, this is possibly the most relevant surface composition with regard to real atmospheric aerosol surface films.

The mixtures' compositions are listed in Table 13, with the monolayers set up shown in Figure 91.

Mixture (OA:SA)	50:50	33:67	22:78	10:90
Oleic acid molecules	242	162	106	48
Stearic acid molecules	242	322	378	436

Table 13: Mixtures of OA and SA. Number of molecules in each monolayer stated.

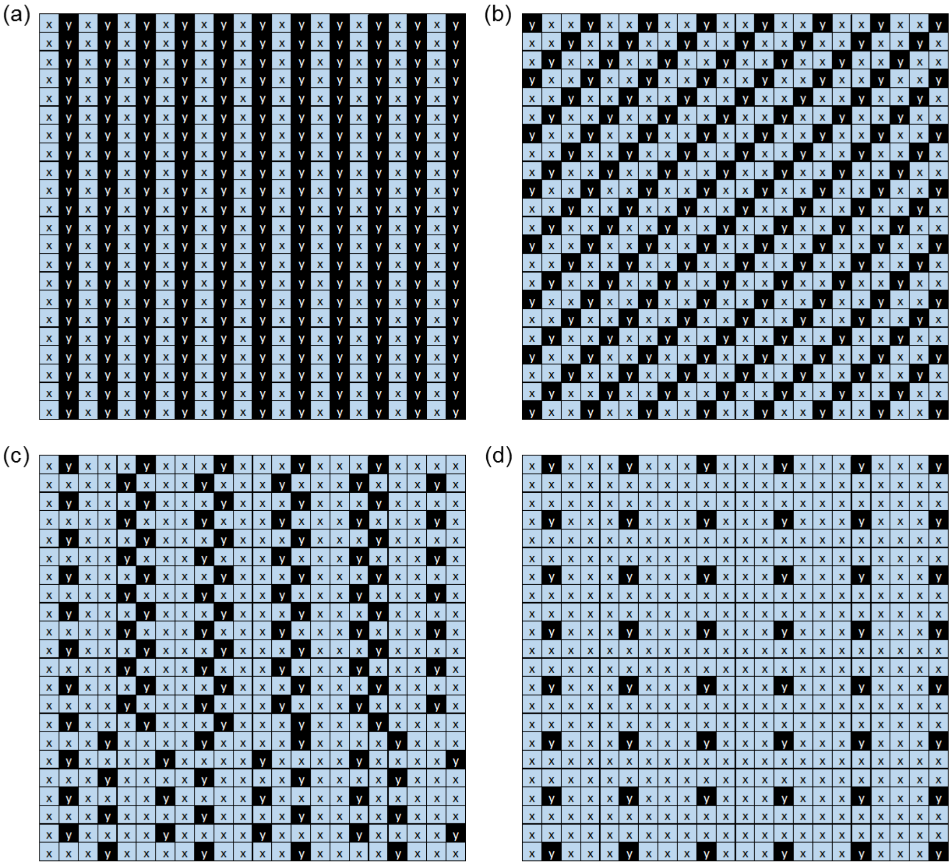

Figure 91: Initial configurations with compositions of y:x = (a) 50:50, (b) 33:67, (c) 22:78, and (d) 10:90, where y = OA and x = SA.

To represent the aging of a monolayer at the interface, a further system was set up, modifying the 33:67 OA:SA mixture by replacing a quarter of the OA molecules in the system with NA molecules. The final system composition contained 40 NA molecules, 122

OA molecules and 322 SA molecules in each monolayer, with the initial system setup shown in Figure 92.

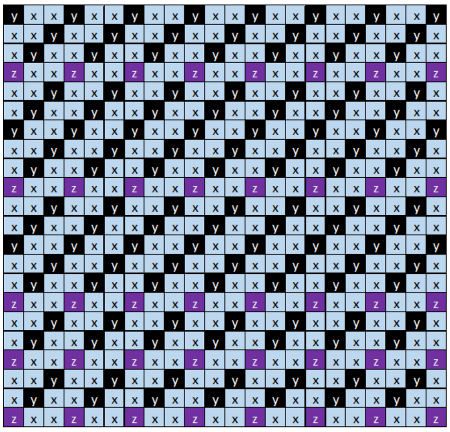

y	x	x	y	x	x	y	x	x	y	x	x	y	x	x	y	x	x	y	x	x	y
x	x	y	x	x	y	x	x	y	x	x	y	x	x	y	x	x	y	x	x	y	x
x	y	x	x	y	x	x	y	x	x	y	x	x	y	x	x	y	x	x	y	x	x
z	x	x	z	x	x	z	x	x	z	x	x	z	x	x	z	x	x	z	x	x	z
x	x	y	x	x	y	x	x	y	x	x	y	x	x	y	x	x	y	x	x	y	x
x	y	x	x	y	x	x	y	x	x	y	x	x	y	x	x	y	x	x	y	x	x
y	x	x	y	x	x	y	x	x	y	x	x	y	x	x	y	x	x	y	x	x	y
x	x	y	x	x	y	x	x	y	x	x	y	x	x	y	x	x	y	x	x	y	x
x	y	x	x	y	x	x	y	x	x	y	x	x	y	x	x	y	x	x	y	x	x
z	x	x	z	x	x	z	x	x	z	x	x	z	x	x	z	x	x	z	x	x	z
x	x	y	x	x	y	x	x	y	x	x	y	x	x	y	x	x	y	x	x	y	x
x	y	x	x	y	x	x	y	x	x	y	x	x	y	x	x	y	x	x	y	x	x
y	x	x	y	x	x	y	x	x	y	x	x	y	x	x	y	x	x	y	x	x	y
x	x	y	x	x	y	x	x	y	x	x	y	x	x	y	x	x	y	x	x	y	x
x	y	x	x	y	x	x	y	x	x	y	x	x	y	x	x	y	x	x	y	x	x
z	x	x	z	x	x	z	x	x	z	x	x	z	x	x	z	x	x	z	x	x	z
x	x	y	x	x	y	x	x	y	x	x	y	x	x	y	x	x	y	x	x	y	x
x	y	x	x	y	x	x	y	x	x	y	x	x	y	x	x	y	x	x	y	x	x
z	x	x	z	x	x	z	x	x	z	x	x	z	x	x	z	x	x	z	x	x	z
x	x	y	x	x	y	x	x	y	x	x	y	x	x	y	x	x	y	x	x	y	x
x	y	x	x	y	x	x	y	x	x	y	x	x	y	x	x	y	x	x	y	x	x
z	x	x	z	x	x	z	x	x	z	x	x	z	x	x	z	x	x	z	x	x	z

Figure 92: Initial configuration for monolayer with composition of z:y:x = 8:25:67, where z = NA, y = OA and x = SA.

5.2.1.2 Mixed Monolayers Containing Palmitoleic Acid

Mixtures were set up containing POA and SA, with the following compositions: 10:90 and 22:78 POA:SA. The setup used is the same as for the OA:SA mixtures previously described in section 5.2.1.1. Furthermore, by replacing a quarter of the POA molecules in the 22:78 POA:SA mixture, a further system was set up containing 26 HA molecules, 80 POA molecules and 378 SA molecules, with the initial system configuration shown in Figure 93.

POA is represented by a P3 bead followed by C1, C1, C3, C1 beads, with detailed parameters given in Chapter 4, section 4.3.2. HA is mapped onto a P3 bead followed by two C2 beads. Parameters for this compound can be found in Chapter 4, section 4.3.8.

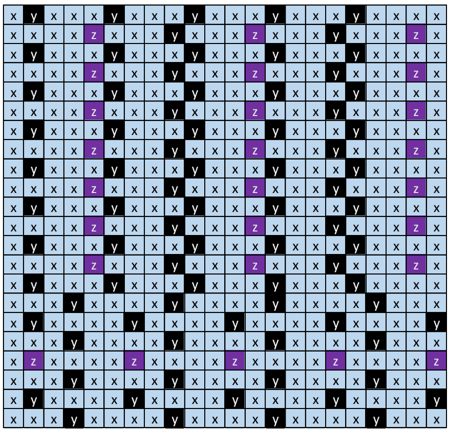

x	y	x	x	x	y	x	x	x	y	x	x	x	y	x	x	x	y	x	x	x	x
x	x	x	x	z	x	x	x	y	x	x	x	z	x	x	x	y	x	x	x	z	x
x	y	x	x	x	y	x	x	x	y	x	x	x	y	x	x	x	y	x	x	x	x
x	x	x	x	z	x	x	x	y	x	x	x	z	x	x	x	y	x	x	x	z	x
x	y	x	x	x	y	x	x	x	y	x	x	x	y	x	x	x	y	x	x	x	x
x	x	x	x	z	x	x	x	y	x	x	x	z	x	x	x	y	x	x	x	z	x
x	y	x	x	x	y	x	x	x	y	x	x	x	y	x	x	x	y	x	x	x	x
x	x	x	x	z	x	x	x	y	x	x	x	z	x	x	x	y	x	x	x	z	x
x	y	x	x	x	y	x	x	x	y	x	x	x	y	x	x	x	y	x	x	x	x
x	x	x	x	z	x	x	x	y	x	x	x	z	x	x	x	y	x	x	x	z	x
x	y	x	x	x	y	x	x	x	y	x	x	x	y	x	x	x	y	x	x	x	x
x	x	x	x	z	x	x	x	y	x	x	x	z	x	x	x	y	x	x	x	z	x
x	y	x	x	x	y	x	x	x	y	x	x	x	y	x	x	x	y	x	x	x	x
x	x	x	x	z	x	x	x	y	x	x	x	z	x	x	x	y	x	x	x	z	x
x	y	x	x	x	y	x	x	x	y	x	x	x	y	x	x	x	y	x	x	x	x
x	x	x	y	x	x	x	x	y	x	x	x	x	y	x	x	x	x	y	x	x	x
x	y	x	x	x	x	y	x	x	x	x	y	x	x	x	x	y	x	x	x	x	y
x	x	x	y	x	x	x	x	y	x	x	x	x	y	x	x	x	x	y	x	x	x
x	z	x	x	x	x	z	x	x	x	x	z	x	x	x	x	z	x	x	x	x	z
x	x	x	y	x	x	x	x	y	x	x	x	x	y	x	x	x	x	y	x	x	x
x	y	x	x	x	x	y	x	x	x	x	y	x	x	x	x	y	x	x	x	x	y
x	x	x	y	x	x	x	x	y	x	x	x	x	y	x	x	x	x	y	x	x	x

Figure 93: Initial configuration for monolayer with composition of z:y:x = 5:17:78, where z = HA, y = POA and x = SA.

5.2.2 Pressure-Area Isotherms of Mixed Component Surface Films

Pressure-area isotherms were produced from simulations of the mixed component systems. For details of the simulation parameters, please see Chapter 4, section 4.4.1. This work used the UK Research Data Facility (http://www.archer.ac.uk/documentation/rdf-guide).

5.3 Results and Discussion

5.3.1 Pressure-Area Isotherms of Mixed Monolayers Containing Oleic Acid

5.3.1.1 50 % Oleic Acid: 50 % Stearic Acid Mixture

The pressure-area isotherm for the 50:50 OA:SA mixture is shown in Figure 94.

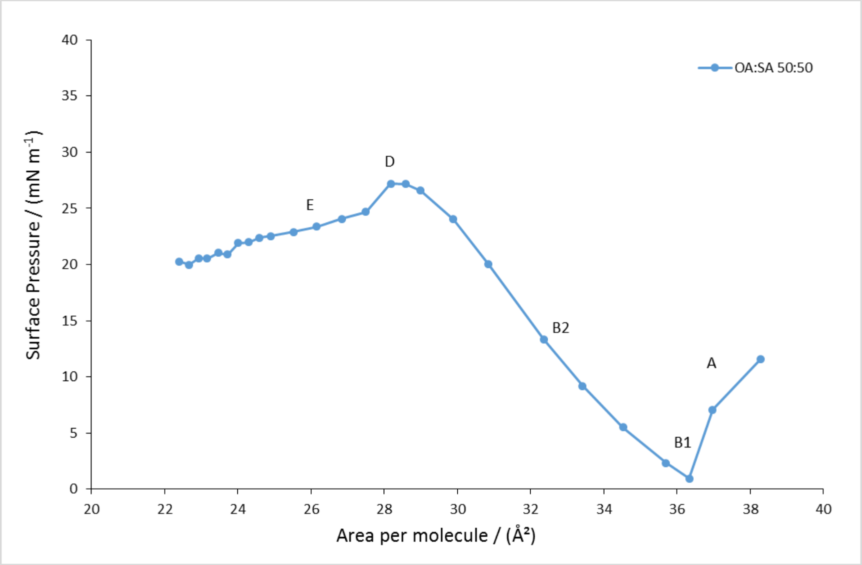

Figure 94: Pressure-area isotherm of a 50 % OA: 50 % SA mixture. Phase behaviour of simulated isotherm indicated: (A) gas-liquid coexisting region, (B1 and B2) liquid-expanded region, (D) equilibrium spreading pressure and (E) film collapse region.

During the simulation, molecules stay disordered, as shown in Figure 95. Once the equilibrium spreading pressure (D) is reached, at a surface pressure of 27 mN m^{-1}, further compression causes a breakdown of the monolayer (E). The number of molecules that move out of the layer increases, forming a bilayer-like structure, as shown in Figure 96 (E).

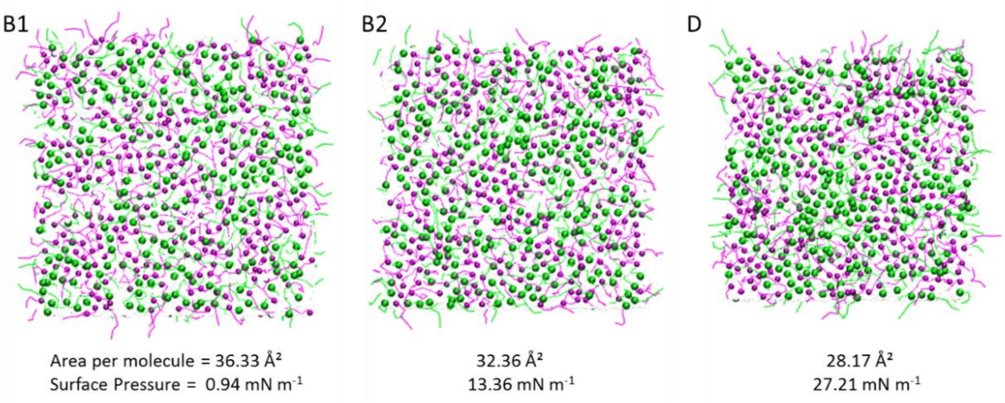

Figure 95: Snapshots of the top monolayer view from low to high surface pressures of the 50 % OA: 50 % SA mixture (B1, B2, D—points indicated on isotherm in Figure 94). OA = magenta, SA = green.

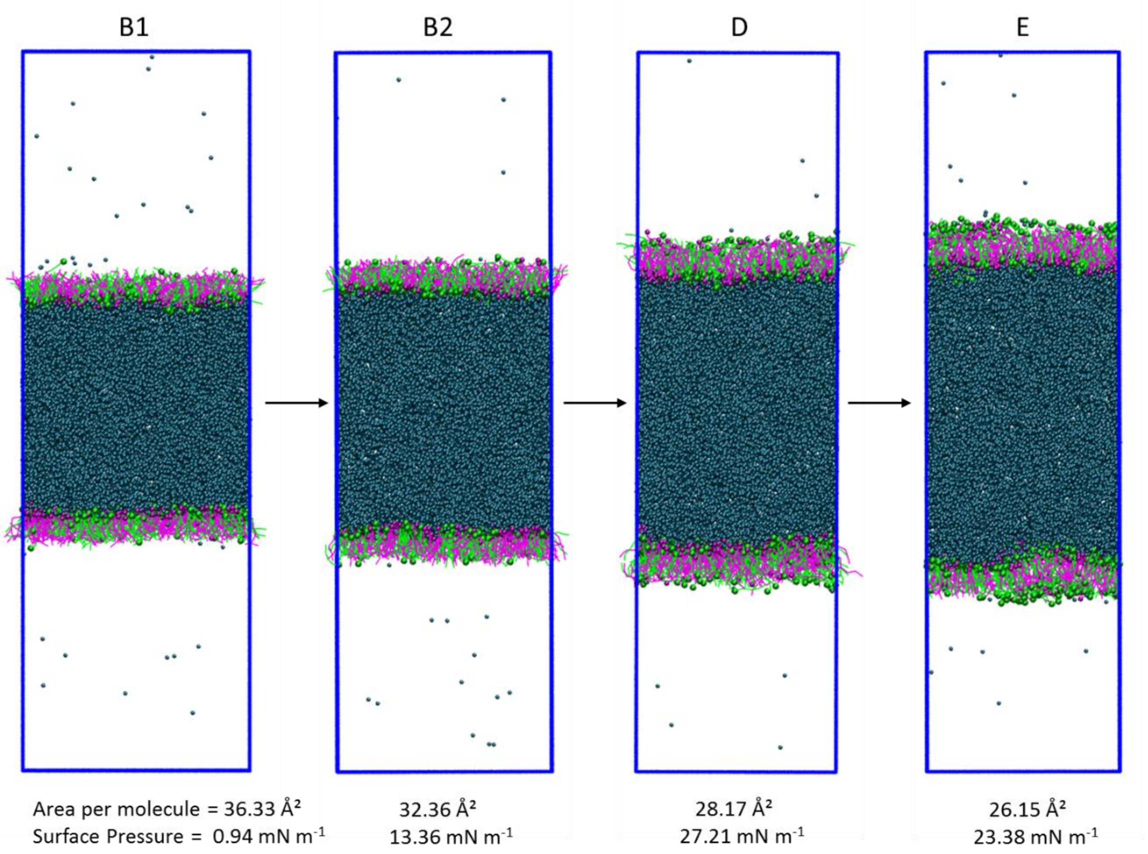

Figure 96: Snapshots of the side view of the simulation box from low to high surface pressures of the 50 % OA: 50 % SA mixture (B1, B2, D, E—points indicated on isotherm in Figure 94). OA = magenta, SA = green, water = teal.

In the literature there is one experimental pressure-area isotherm for a 50:50 OA:SA mixture produced by Sebastiani.[6] The experimental isotherm increases until a surface pressure of 32 mN m^{-1}, followed by a slight drop in surface pressure, after which pressures stay constant.[6] In experiments, the shape of the isotherm for the mixture is similar to that of a pure OA isotherm. This agrees well with the simulated isotherm, where both the simulated pressure-area isotherm for the mixture and for OA have a similar shape and reach similar equilibrium spreading pressures, as shown in Figure 97. Due to the linear carbon chain of SA, the molecules in the monolayers in the mixture can pack more closely, resulting in a shift of the isotherm to lower areas per molecule compared to the pure OA system.

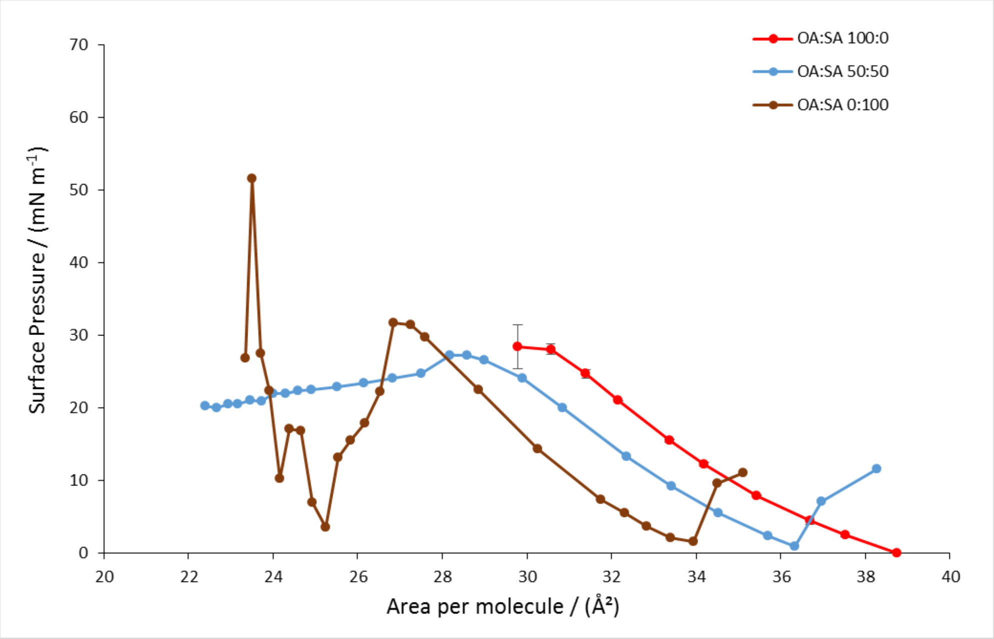

Figure 97: Pressure-area isotherm of the 50:50 mixture compared to the pressure-area isotherms of the pure compounds.

Monolayers were analysed by correlating the angle of the molecule with respect to the *z*-axis, angle(α), to the *z*-coordinate of the headgroup bead of the molecule. Resulting contour plots for both OA and SA are shown in Figure 98 and Figure 99. For a detailed description of the analysis method please see Chapter 2, section 2.3.3 for OA and Chapter 3, section 3.3.4 for SA.

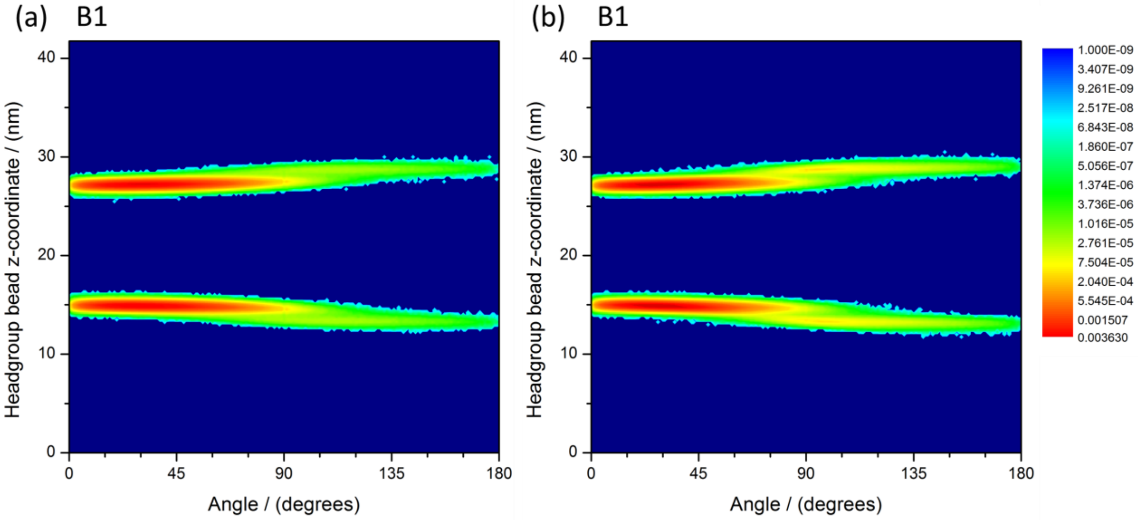

Figure 98: Contour plots showing the probability of finding the headgroup of a molecule at a certain *z*-coordinate with respect to the molecules angle(α) for the 50:50 OA:SA mixture, at an area per molecule of 36.33 Å^2 and a surface pressure of 0.94 mN m^{-1} (B1) , for OA (a) and SA (b).
Point B1 is indicated on the pressure-area isotherm in Figure 94.

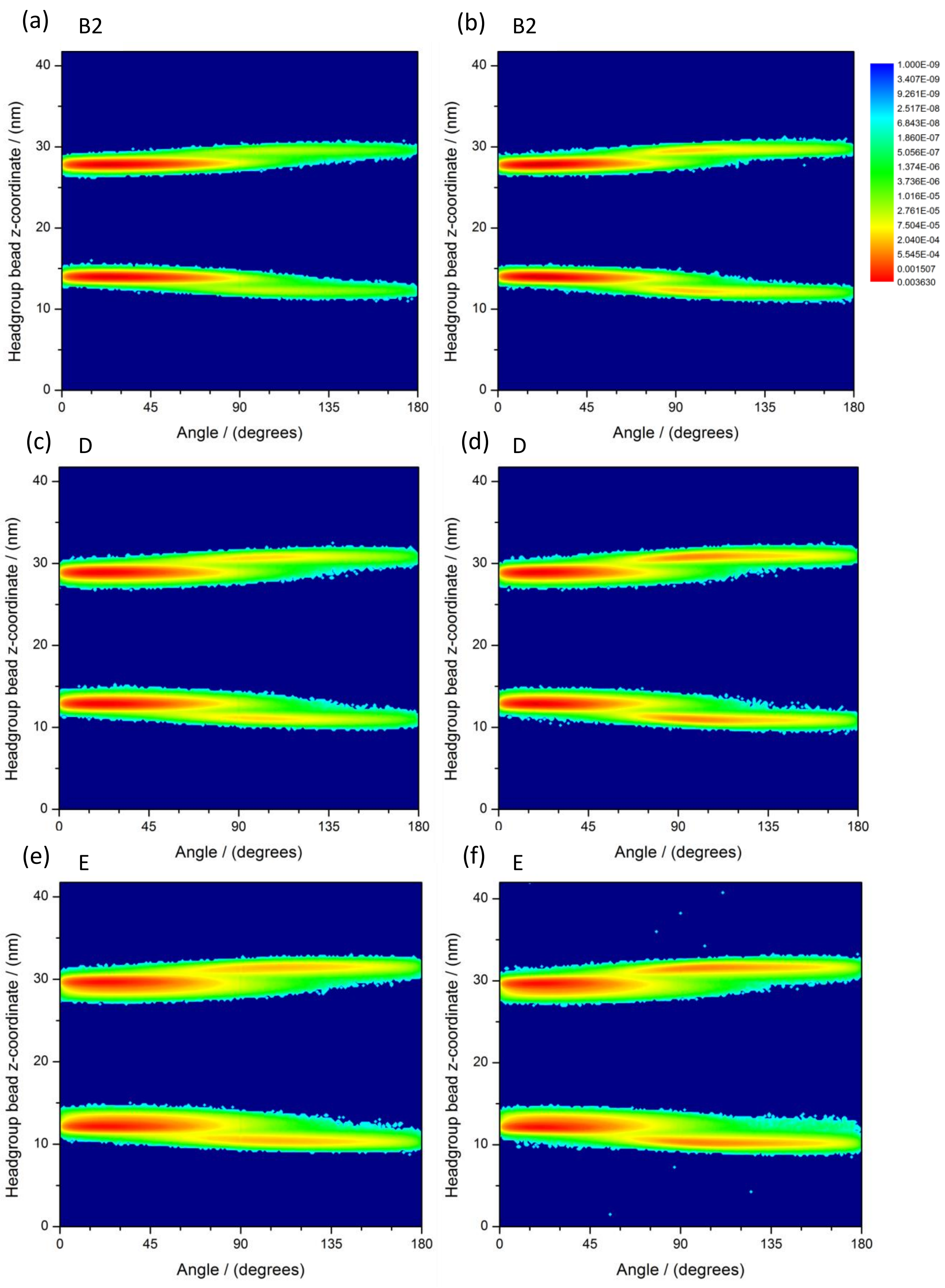

Figure 99: Contour plots showing the probability of finding the headgroup of a molecule at a certain *z*-coordinate with respect to angle(α) for the 50:50 mixture, (a) and (b) (B2) area per molecule = 32.36 Å^2 , surface pressure = 13.36 mN m^{-1}; (c) and (d) (D) area per molecule = 28.17 Å^2, surface pressure = 27.21 mN m^{-1}; (e) and (f) (E) area per molecule = 23.62 Å^2, surface pressure = 23.38 mN m^{-1}. Contour plots (a), (c), (e) = OA, contour plots (b), (d), (f) = SA. Points B2, D and E are indicated on the pressure-area isotherm in Figure 94.

Contour plots show that more SA molecules than OA molecules move away from the normal monolayer position. An overall increase in molecules that change orientation is observed as the area per molecule decreases. This was quantified by calculating the percentage of OA molecules and SA molecules that move out of the layer at each area per molecule, with results shown in Figure 100.

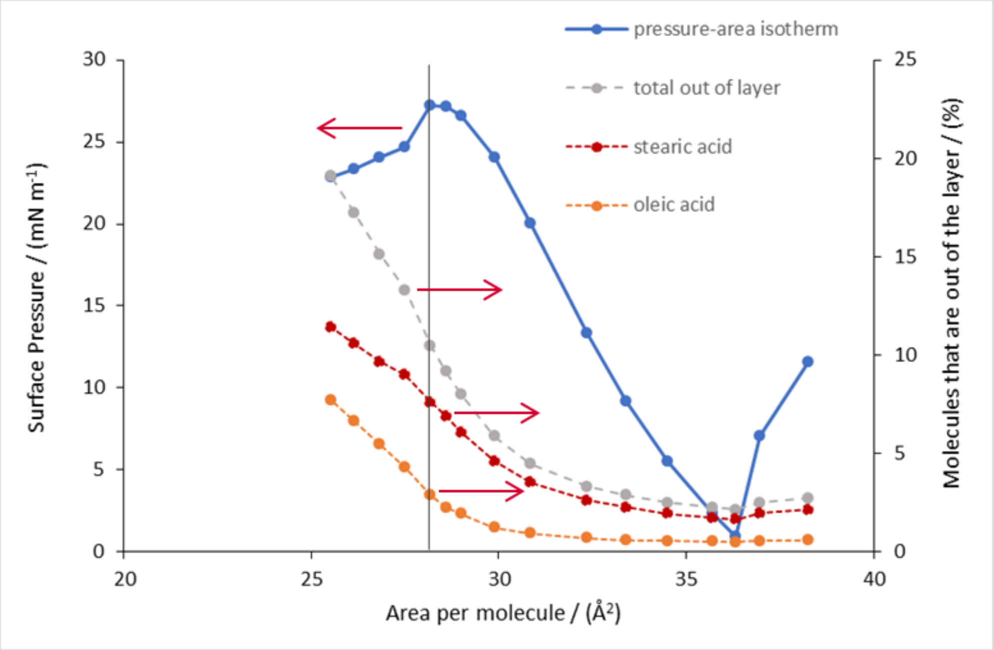

Figure 100: Total average percentage of molecules moving out of each monolayer over the production time of the simulation, with separate contributions of OA molecules and SA molecules shown, against the area per molecule, in comparison to the mixtures pressure-area isotherm.
Vertical line indicates the percentage of molecules that move out of the layer at the equilibrium spreading pressure (area per molecule = 28.17 Å^2, surface pressure = 27.21 mN m^{-1}). Arrows indicate relevant axes.

The percentage of molecules that change orientation stays more or less constant up to just before the equilibrium spreading pressure is reached. At the equilibrium spreading pressure, approximately 10.5 % of the molecules in each monolayer change orientation, of which 7.6 % are SA molecules and 2.9 % are OA molecules. This can be correlated to experimental results by Sebastiani, where BAM images show bright white spots at the equilibrium spreading pressure indicating the breakdown of the monolayer structure.[6]

In experiments reported by Sebastiani, circular domains can be clearly distinguished from the onset of the compression, suggesting a phase separation between the OA and SA molecules in the system.[6] Here, the white domains indicate an ordering of the molecules, giving rise to a difference in surface reflectivity, and hence can be correlated to the ordered phases formed by SA.[6] If the simulation system were to phase separate we would expect this to be visible in the 1 µs simulation time.

To test this, a monolayer at a low surface pressure was further analysed, counting the total number of neighbours for each SA molecule in the system, within a set radius of 1 nm around the reference molecule, as illustrated in Figure 101.

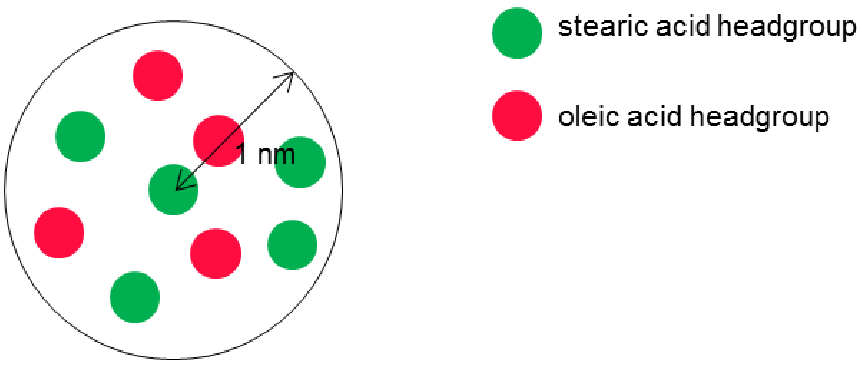

Figure 101: Molecules surrounding a reference SA molecule within a radius of 1 nm within the monolayer. SA headgroup = green, OA headgroup = magenta.

The average ratio of the SA molecules to the total fatty acid molecules surrounding each molecule was determined for every 20th frame, with results shown in Figure 102.

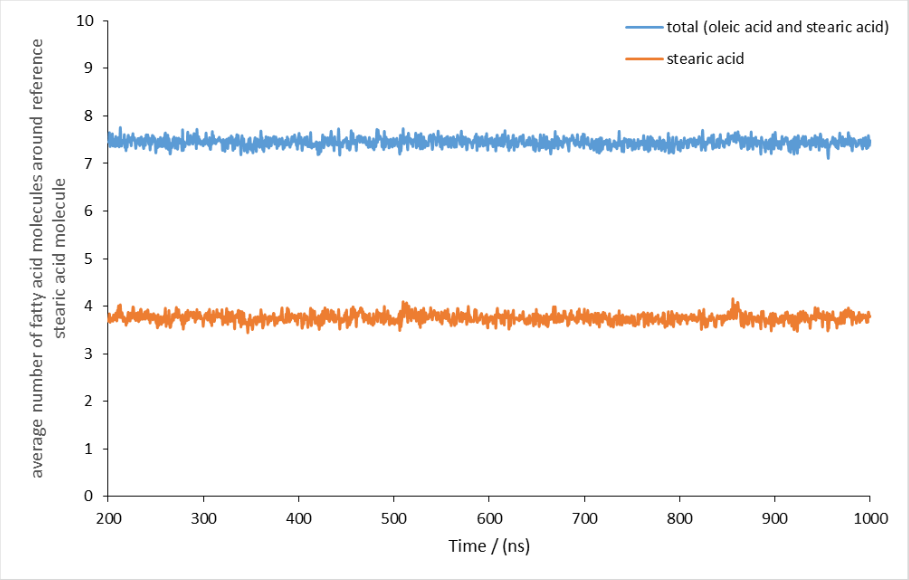

Figure 102: Average number of fatty acid molecules that surround each SA molecule as a function of time.

The flat line in Figure 102 shows no evidence of phase separation. This difference in behaviour between experiments and the simulation system might be due to the sample preparation and size scale used in experiments compared to simulations. We suggest that the mixture used in experiments was not fully mixed before being spread at the air-water interface, resulting in separate domains of SA and OA.

Molecules in a pure SA system, as previously shown in experiments and simulations in Chapter 3, have a tendency to group and order.[2, 7, 8] With the size of the spherical domains on the BAM images of the 50:50 OA:SA mixture ranging in diameters from 5 to 25 µm, the SA molecules in the centre of the domain will be completely unaffected by the surrounding disordered OA molecules, as if they were in a pure SA system. This is possible as the interfacial area is much larger in experiments (700 cm^2 to 80 cm^2), than the interfacial area used in simulations (equivalent to a droplet diameter < 2.5 µm). Hence, more material is needed to form a monolayer in experiments than is expected to be present at the surface of a droplet in the atmosphere. This means that in experiments, due to the amount of material present, SA molecules that group together, caused by insufficient mixing, can behave as if they were in a pure SA system and thus cause a phase separation. With much less material present on actual aerosols, the number of SA molecules in this case might be insufficient to form domains of SA which are unaffected by the disordered OA molecules. Hence, this phase separation might be unrealistic on a smaller size scale.

The experimental system might equilibrate into an evenly mixed phase if left at the interface for a sufficient amount of time. Even though the phase separation observed in experiments does not seem to influence the overall pressure profile of the mixture, which are similar in experiments and simulations, it is important to further investigate this in experiments, as this surface behaviour may have significant effects on other analysis methods, such as neutron reflectometry data, where islands drifting in and out of the beam could give rise to unrealistic results.

Mixtures in experiments might equilibrate over time and form a well-mixed layer, which would result in a better approximation of the surface of a real atmospheric aerosol. I suggest the following modifications to the experimental setup in order to minimise the formation of domains and hence reduce the time it takes for the system to equilibrate: Tests should be conducted with the Langmuir trough being compressed to the smallest possible area in order to minimise the amount of material that needs to be spread at the surface and therefore minimise the number of SA molecules that can form domains. Furthermore, as domains in experiments already appear for surface films with low surface pressures (liquid-expanded films), it is sufficient to spread only a little material on the surface. Taking BAM images over an extended time period, without altering the troughs interfacial area, will allow to monitor the structure of the surface film. Furthermore, altering the spreading method, e.g spreading OA on the surface first, so that an evenly disordered film is formed, and then spreading SA, might give rise to a better mixing of the two compounds.

5.3.1.2 33 % Oleic Acid: 67 % Stearic Acid Mixture

The pressure-area isotherm for the 33 % OA: 67 % SA mixture is shown in Figure 103, compared to the previously simulated 50:50 OA:SA mixture and the pure compounds. To our knowledge, there are no experimental pressure-area isotherms for this mixture. Similar to the 50:50 OA:SA mixture, molecules stay in a disordered liquid-expanded phase under compression, until the equilibirum spreading pressure is reached. The equilibrium spreading pressure is found to be 28 mN m^{-1}.

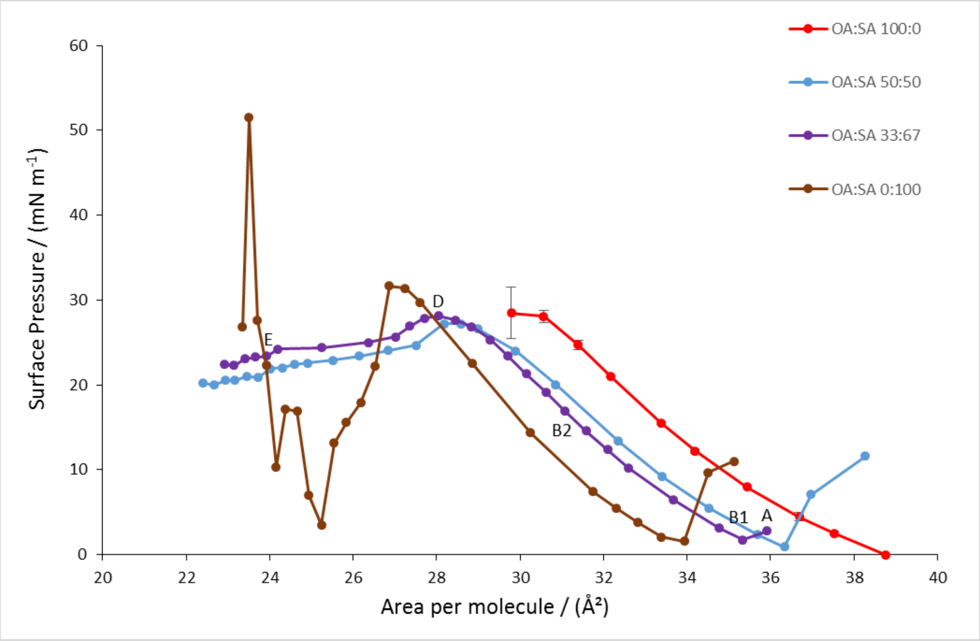

Figure 103: Pressure-area isotherm of the 33:67 OA:SA mixture compared to the pressure-area isotherms of the 50:50 OA:SA mixture and of the pure compounds. Phase behaviour of simulated 33:67 OA:SA mixture isotherm indicated: (A) gas-liquid coexisting region, (B1 and B2) liquid-expanded region, (D) equilibrium spreading pressure and (E) film collapse region.

The system resembles OA more closely than SA, meaning that the 33 % OA molecules in the system disrupt the monolayer, with their unsaturated carbon chain, to an extent where it is not possible for the system to form a liquid-condensed phase or solid state.

For a given aerosol, with a specific number of surfactant molecules, the following applies: in the atmosphere, an aerosol with a submicron diameter will have a low surface area per molecule. The more water this aerosol takes up the larger it becomes, increasing its surface area, and hence increasing the space available for each surface molecule, as illustrated in Figure 104. Regarding the growth process, we therefore have to consider the isotherm from low to high areas per molecule. Once the equilibrium spreading pressure is reached, resulting in the highest surface pressure in the system and ultimately the lowest possible surface tension, the growth of the aerosol leads to an increase in surface area. This means molecules move further apart from one another, resulting in a reduced surface pressure and an increase in surface tension. Once the molecules are in the two-dimensional gas phase there is no longer a surface pressure or surface tension effect from the molecules at the surface. Thus, the surface tension equals that of water. This growth process ultimately affects the ability of the aerosol to act as a cloud condensation nucleus. The larger the depression of surface tension and the lower the surface pressure, the more likely it is for the aerosol to act as a cloud condensation nucleus.

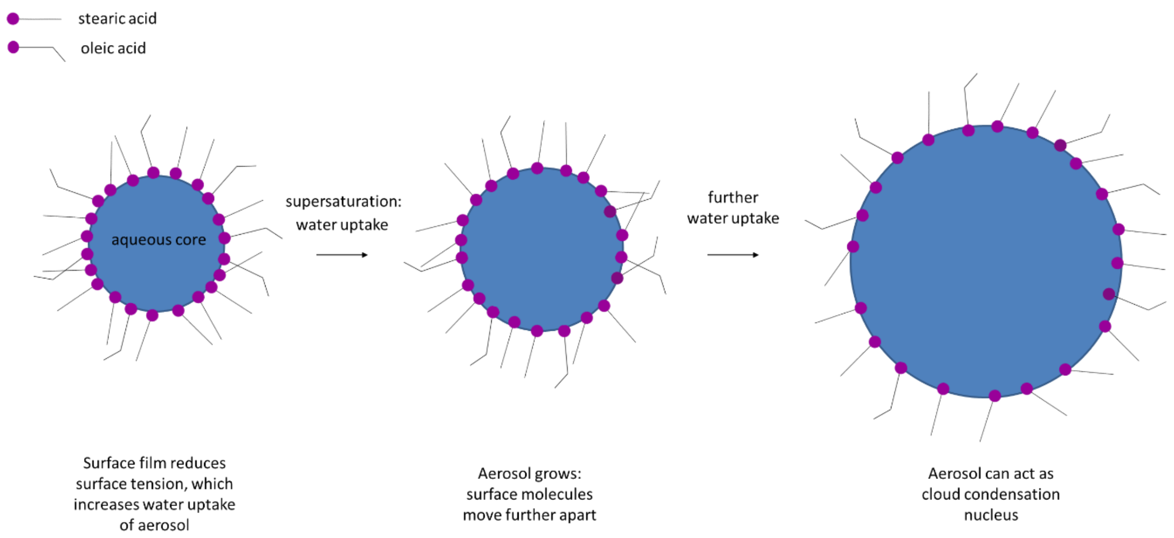

Figure 104: Illustration of the growth process of an atmospheric aerosol. The surface film causes a surface tension depression, which results in an increase in the aerosol's cloud nucleus activation potential. As the aerosol grows molecules move further apart from one another, causing an increase in surface tension. Once the critical supersaturation is reached, the aerosol can act as cloud condensation nucleus.

As shown in the graph in Figure 103, the 33:67 OA:SA isotherm is shifted to lower areas per molecule compared to the 50:50 OA:SA isotherm. Substituting OA with the less bulky SA results, for any given area per molecule in the liquid-expanded phase, in a lower surface pressure, which means the surface film is less effective in suppressing the surface tension of the aerosol. Simulations hence suggest that cloud condensation nuclei activation is favoured by a higher concentration of unsaturated material.

Snapshots of the disordered monolayers are shown in Figure 105 and Figure 106. With decreasing area per molecule, more molecules move away from the normal monolayer position. Resembling the behaviour of the 50:50 OA:SA mixture, the 33:76 OA:SA mixture forms a bilayer-like structure, Figure 106 (E), after the equilibrium spreading pressure (D) is reached and the monolayer collapses.

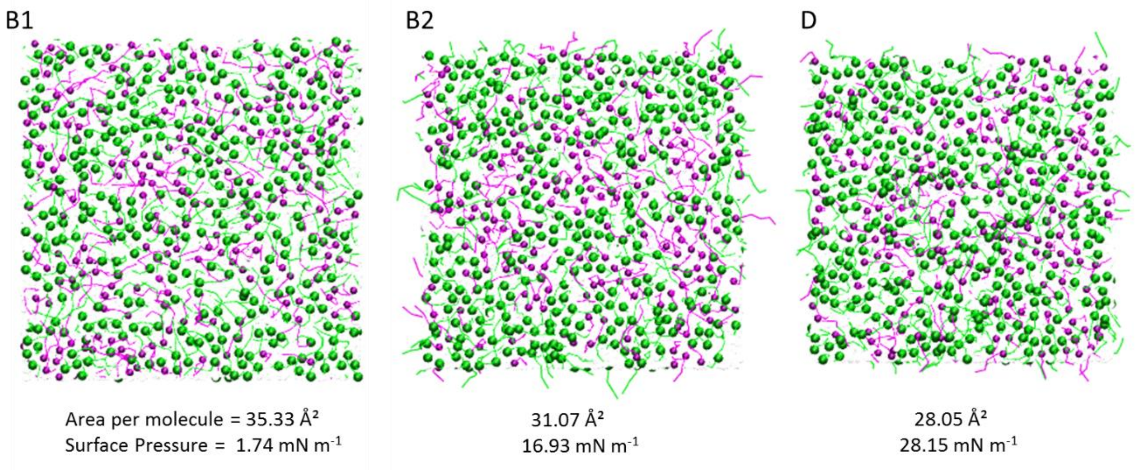

Figure 105: Snapshots of the top monolayer view from low to high surface pressures of the 33 % OA: 67 % SA mixture (B1, B2, D—points indicated on isotherm in Figure 103). OA = magenta, SA = green.

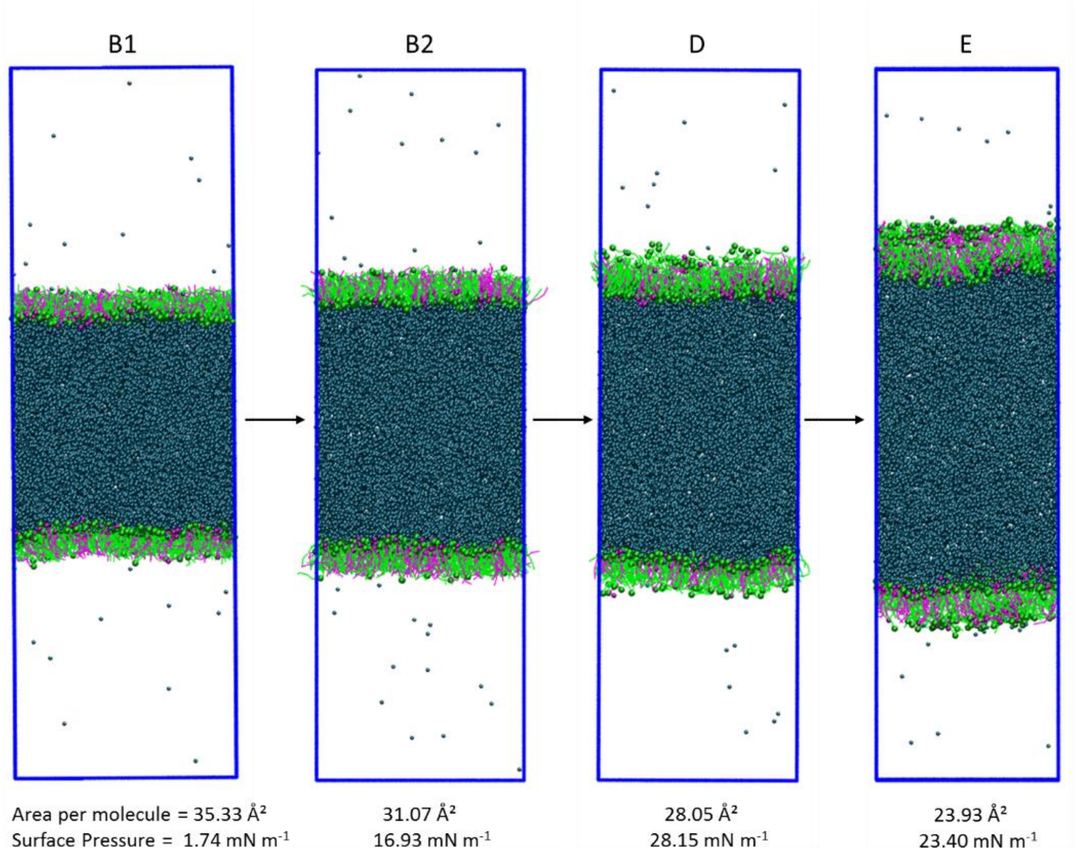

Figure 106: Snapshots showing the side view of the simulation box from low to high surface pressures of the 33 % OA: 67 % SA mixture (B1, B2, D—points indicated on isotherm in Figure 103).
OA = magenta, SA = green, water = teal.

Similar to the 50:50 mixture, more SA molecules than OA molecules move out of the layer. The corresponding contour plots are shown in Figure 107 and Figure 108. The contour plots display the general trend that for both OA and SA the molecules that change orientation increases with a decrease in the area per molecule.

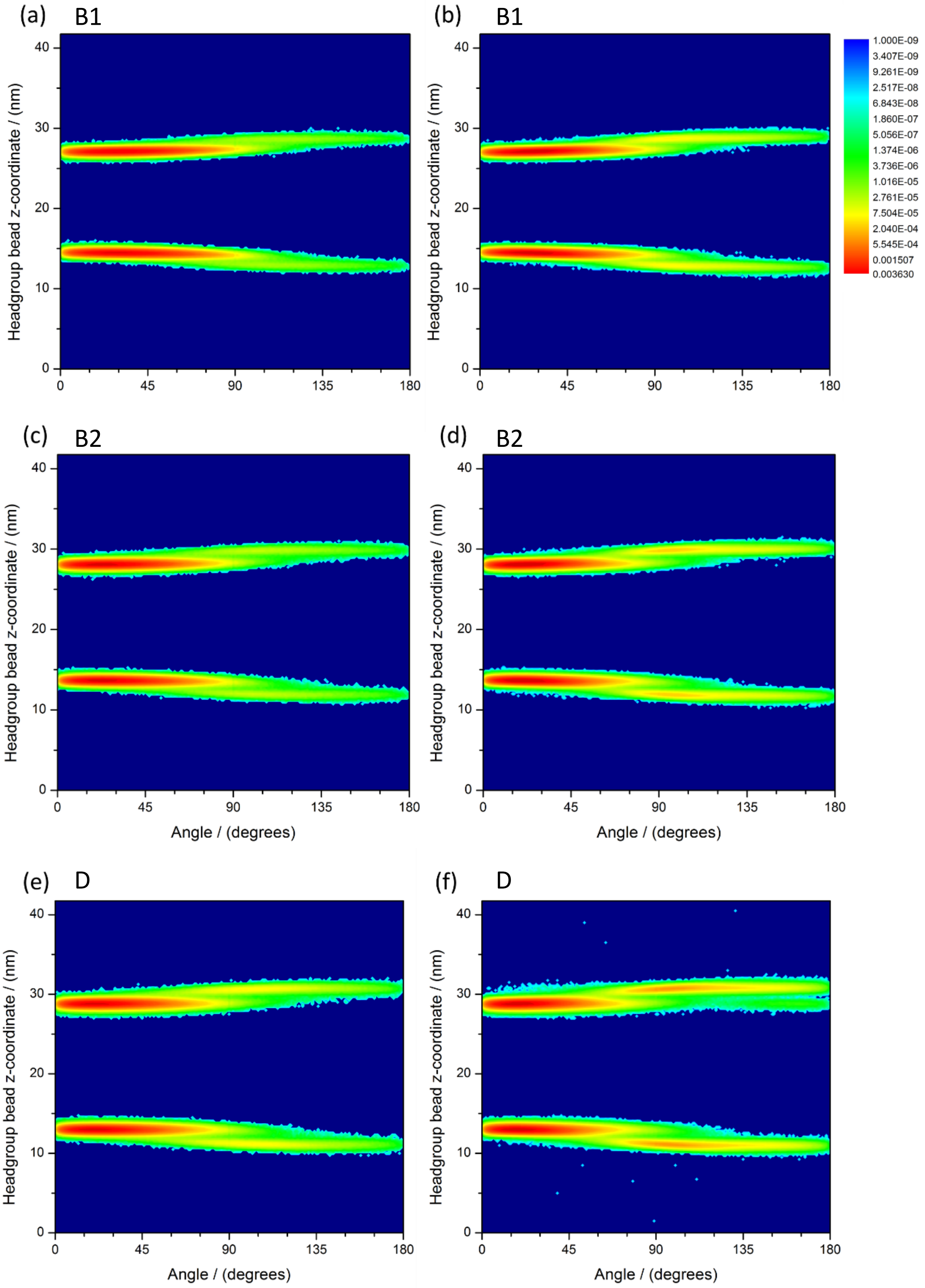

Figure 107: Contour plots showing the probability of finding the headgroup of a molecule at a certain *z*-coordinate with respect to angle(α) for the 33:67 mixture, (a) and (b) (B1) area per molecule = 35.33 Å^2, surface pressure = 1.74 mN m^{-1}, (c) and (d) (B2) area per molecule = 31.07 Å^2, surface pressure = 16.93 mN m^{-1}, (e) and (f) (D) area per molecule = 28.05 Å^2, surface pressure = 28.15 mN m^{-1}. Contour plots (a), (c), (e) = OA, contour plots (b), (d), (f) = SA. Points B1, B2 and D are indicated on the pressure-area isotherm in Figure 103.

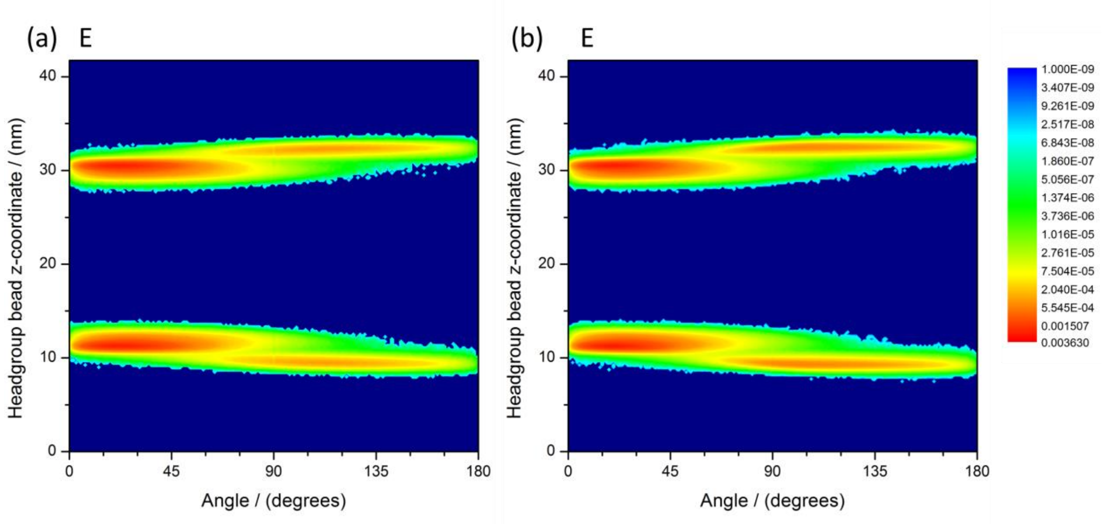

Figure 108: Contour plots showing the probability of finding the headgroup of a molecule at a certain *z*-coordinate with respect to angle(α) for the 33:67 mixture, (a) and (b) (E) area per molecule = 23.93 Å^2, surface pressure = 23.40 mN m^{-1}. Contour plot (a) = OA, contour plot (b) = SA. Point E is indicated on the pressure-area isotherm in Figure 103.

The percentage of OA molecules and SA molecules that move out of the layer at each area per molecule are shown in Figure 109. At the equilibrium spreading pressure, 9.1 % of molecules have moved out of the layer: 7.7 % are SA molecules and 1.4 % are OA molecules. This is a decrease of approximately 1.4 % of molecules at this point compared to the 50:50 OA:SA mixture.

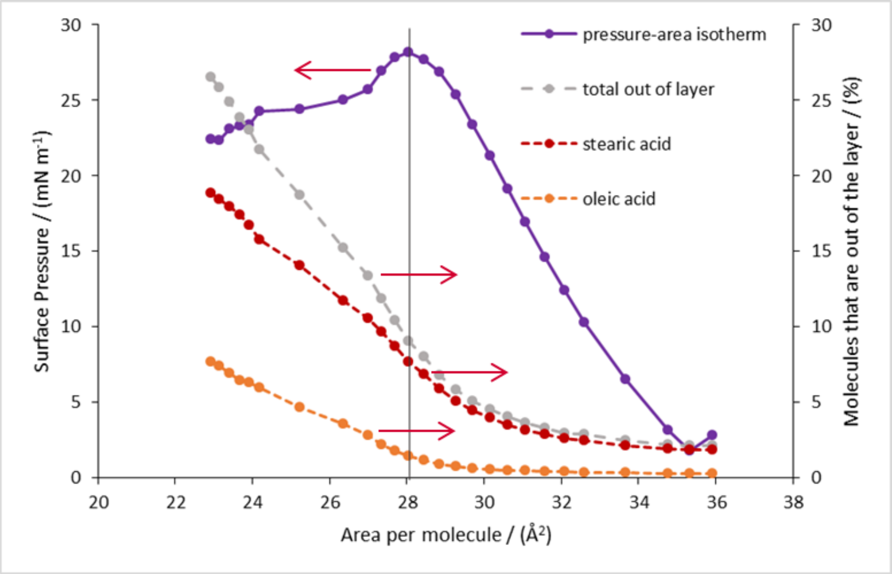

Figure 109: Total average percentage of molecules moving out of each monolayer over the production time of the simulation, with separate contributions of OA molecules and SA molecules shown, against the area per molecule, in comparison to the mixtures pressure-area isotherm.
Vertical line indicates the percentage of molecules that move out of the layer at the equilibrium spreading pressure (area per molecule = 28.05 Å^2, surface pressure = 28.15 mN m^{-1}). Arrows indicate relevant axes.

5.3.1.3 22 % Oleic Acid: 78 % Stearic Acid Mixture

The isotherm for the 22 % OA: 78 % SA mixture is shown in Figure 110.

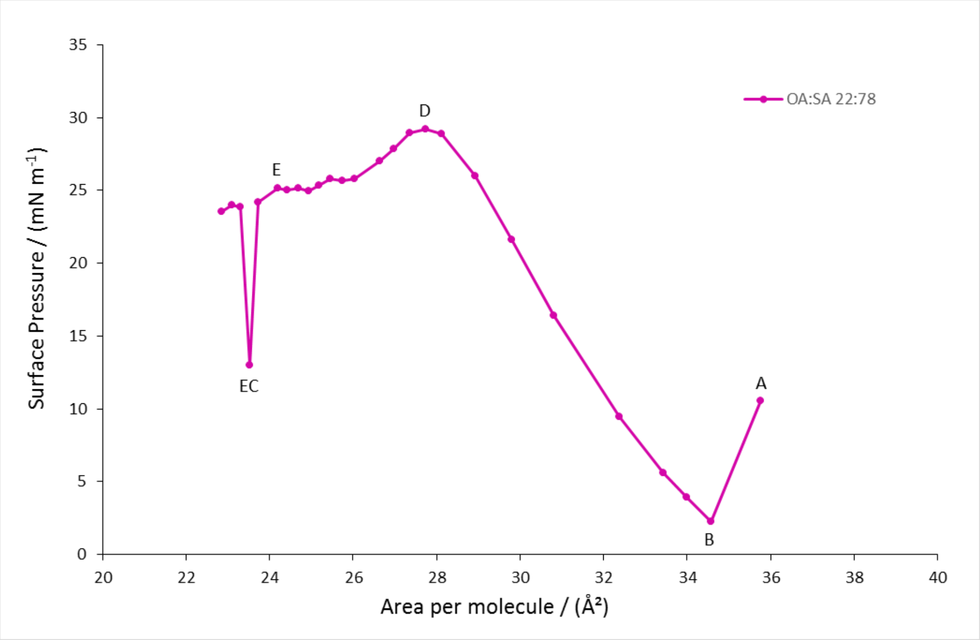

Figure 110: Pressure-area isotherm of a 22 % OA: 78 % SA mixture. Phase behaviour of simulated isotherm indicated: (A) gas-liquid coexisting region, (B) liquid-expanded region, (D) equilibrium spreading pressure (E) film collapse region and an anomalous point with one layer in the film collapse region and one layer in the liquid-condensed region (EC).

Similarly to the previously discussed mixtures, a liquid-expanded phase is formed, followed by a breakdown of the system into a bilayer-like structure, as shown in Figure 112 and Figure 113. There is one anomalous point (Figure 110 (EC)), where the surface pressure suddenly drops, which will be discussed in detail later on in the section.

To my knowledge there are no experimental pressure-area isotherms for a 22 % OA: 78 % SA mixture to date. The isotherm, in comparison to the previously simulated mixtures and isotherms of the pure compounds, is shown in Figure 111. The equilibrium spreading pressure was found to be at 29 mN m^{-1}. The pressure-area isotherm of the 22:78 OA:SA mixture is shifted to lower areas per molecule, compared to the previously simulated mixtures. A possible explanation for this is that, by replacing unsaturated molecules with saturated molecules, the steric hindrance of the system is reduced, hence allowing molecules to pack more closely.

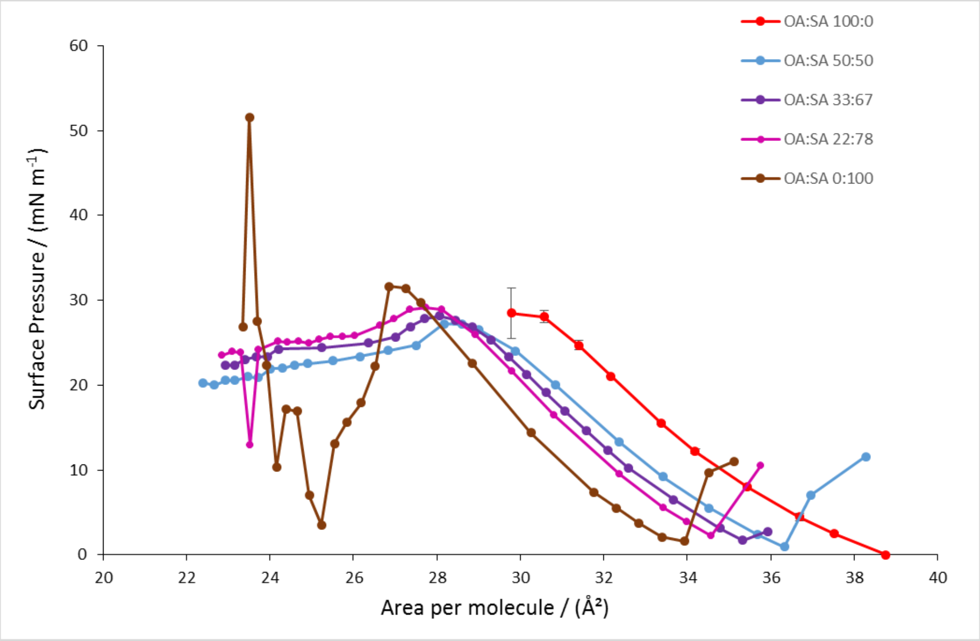

Figure 111: Pressure-area isotherm of the 22:78 OA:SA mixture compared to the pressure-area isotherms of the previously simulated mixtures and of the pure compounds.

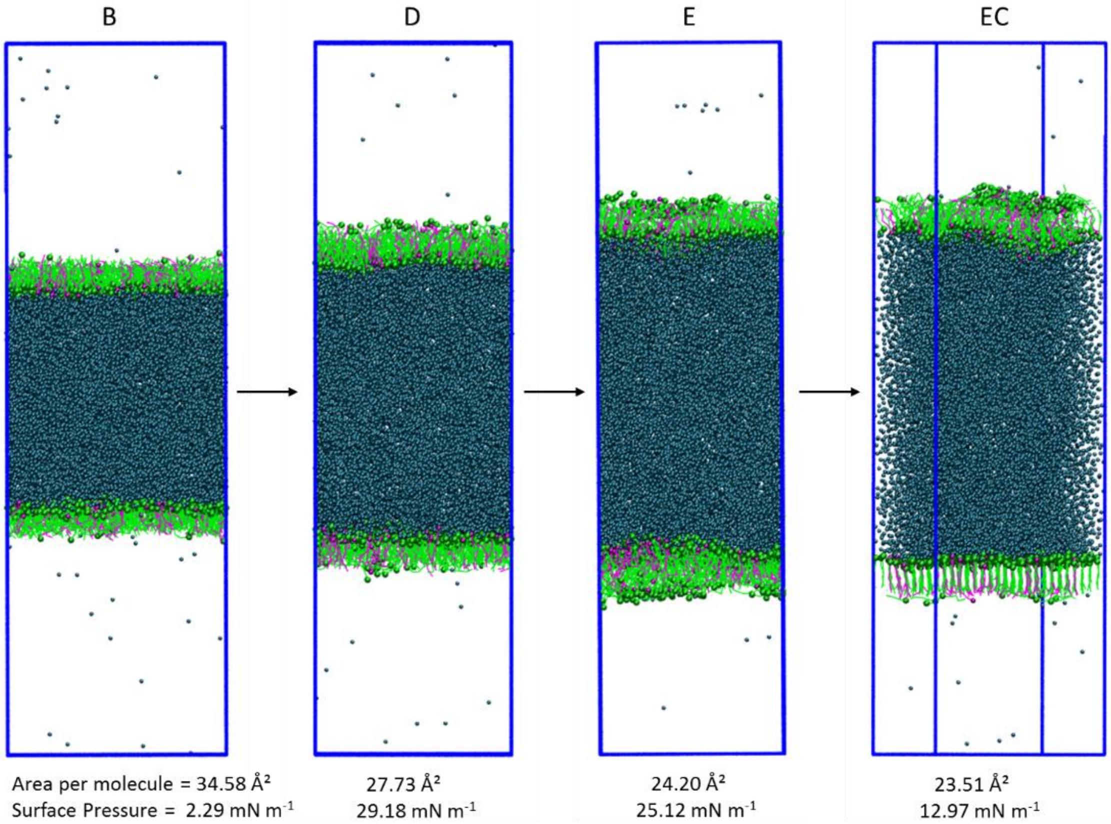

Figure 112: Snapshots of the side view of the simulation box from low to high surface pressures of the 22 % OA: 78 % SA mixture (B, D, E, EC—points indicated on isotherm in Figure 110). OA = magenta, SA = green, water = teal.

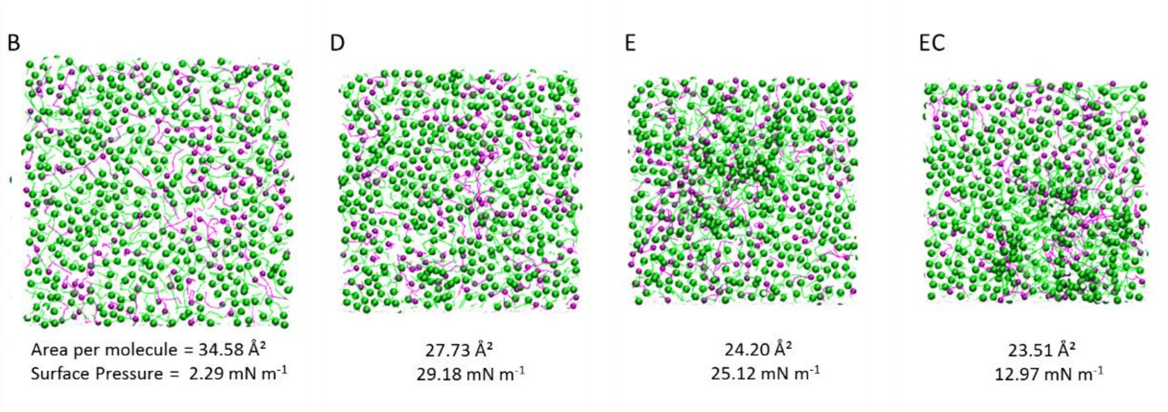

Figure 113: Snapshots of the top monolayer view from low to high surface pressures of the 22 % OA: 78 % SA mixture (B, D, E, EC—points indicated on isotherm in Figure 110). OA = magenta, SA = green.

The contour plots of the mixture, as shown in Figure 114 (a,b,c,d), resemble the ones of the 33:67 OA:SA mixture. As the surface pressure in the system increases, more molecules move out of the layer. More SA molecules than OA molecules move away from the normal monolayer position. Once the equilibrium spreading pressure is reached the number of molecules that leave the monolayer increases further, indicating the breakdown of the system.

At the point where the surface pressure suddenly drops in the pressure-area isotherm (Figure 110 (EC)), a different phase behaviour for the top and bottom layer is observed. One layer is broken down into a bilayer-like structure (Figure 114(e) and (f) top layer), similar to the adjacent points on the isotherm. The other monolayer is ordered, forming a liquid-condensed phase (Figure 114 (e) and (f) bottom layer). This suggests two phases are possible at this point. Similar behaviour was previously observed for simulations of pure SA monolayers, as described in Chapter 3, section 3.3.4. The phase that will be thermodynamically most stable will be observed in experiments. It can be concluded, that it is possible for the system to form an ordered liquid-condensed phase; however, experimental isotherms for this mixture would be useful to determine the thermodynamically most stable phase.

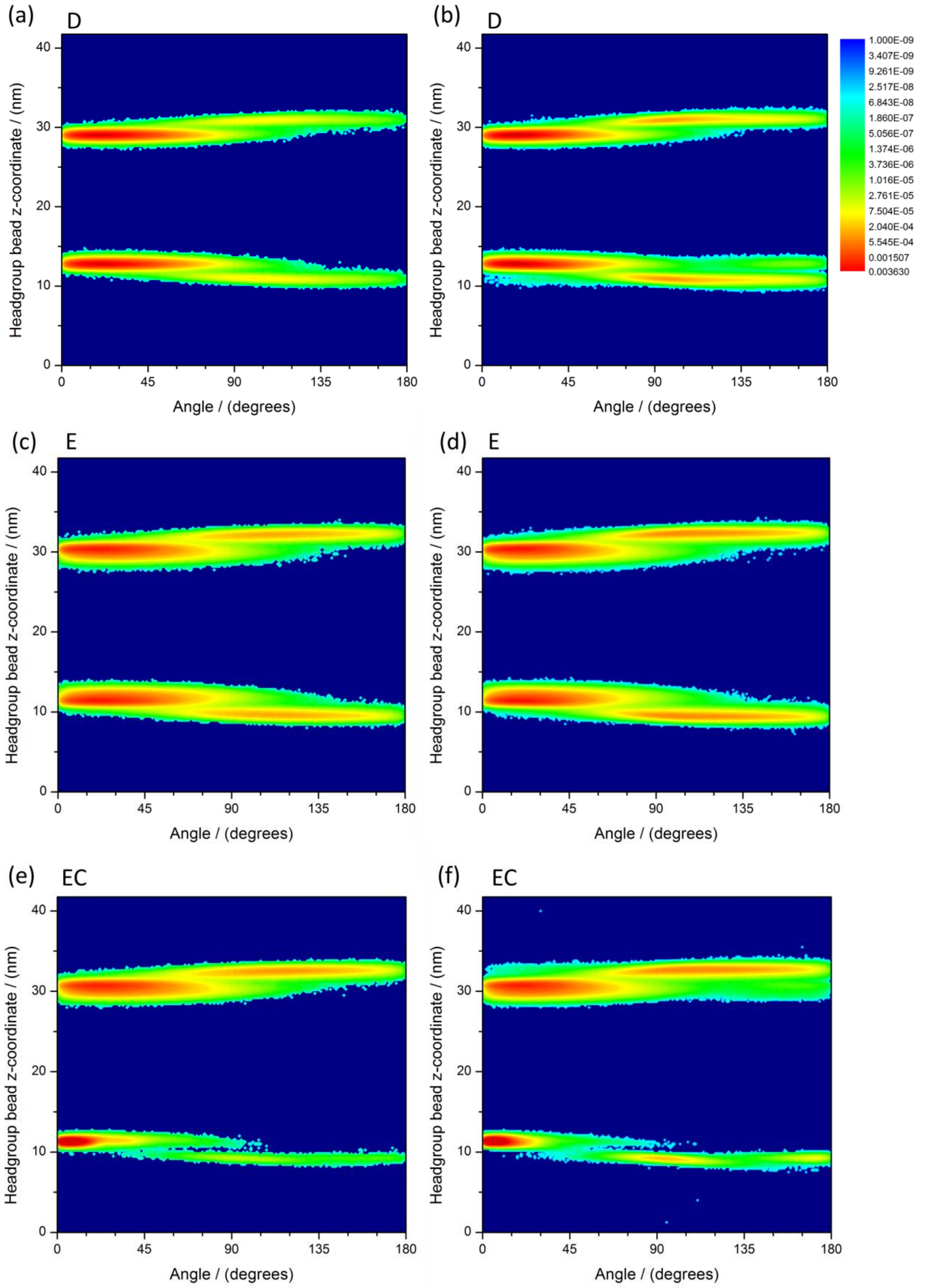

Figure 114: Contour plots showing the probability of finding the headgroup of a molecule at a certain *z*-coordinate with respect to angle(α) for the 22:78 mixture, (a) and (b) (D) area per molecule = 27.73 Å^2, surface pressure = 29.18 mN m^{-1}; (c) and (d) (E) area per molecule = 24.20 Å^2, surface pressure = 25.12 mN m^{-1} and (e) and (f) (EC) area per molecule = 23.51 Å^2, surface pressure = 12.97 mN m^{-1}. Contour plots (a), (c), (e) = oleic acid, contour plots (b), (d), (f) = stearic acid. Points D, E and EC are indicated on the pressure-area isotherm in Figure 110.

The percentage of molecules that change orientation at each area per molecule, in comparison to the mixture's pressure-area isotherm, is shown in Figure 115. At the equilibrium spreading pressure over the 800 ns production time, an average of 8.6 % of molecules change orientation in each monolayer: 7.8 % are SA molecules and 0.8 % are OA molecules.

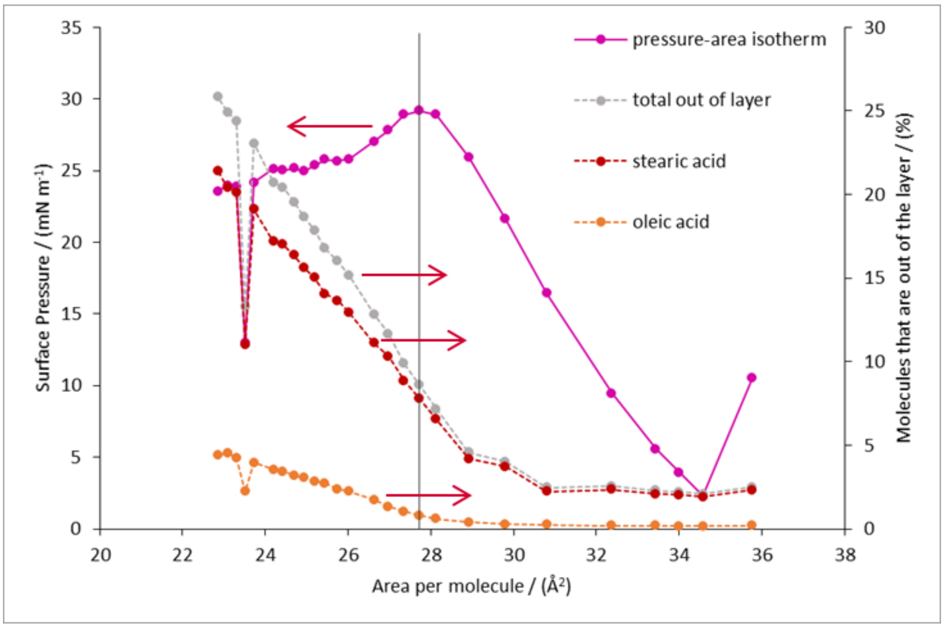

Figure 115: Total average percentage of molecules moving out of each monolayer over the production time of the simulation, with separate contributions of OA molecules and SA molecules shown, against the area per molecule, in comparison to the mixtures pressure-area isotherm.
Vertical line indicates the percentage of molecules that move out of the layer at the equilibrium spreading pressure (area per molecule = 27.73 Å^2, surface pressure = 29.18 mN m^{-1}). Arrows indicate relevant axes.

After this point, the percentage of molecules that move out of the layer increases. At the anomalous point, where the surface pressure suddenly drops, the percentage of molecules that turn out of the top layer is 23.8 %, compared to 2.8 % in the bottom layer, indicating a difference in phase between the two layers. This gives an average percentage of 13.3 % of molecules that move out of this system during the production run, causing a drop in surface pressure.

5.3.1.4 10 % Oleic Acid: 90 % Stearic Acid Mixture

The pressure-area isotherm for the 10:90 OA:SA mixture is shown in Figure 116. The isotherm shows a liquid-expanded phase (B), a liquid-condensed phase (C) and solid state (D). Here, molecules are ordered.

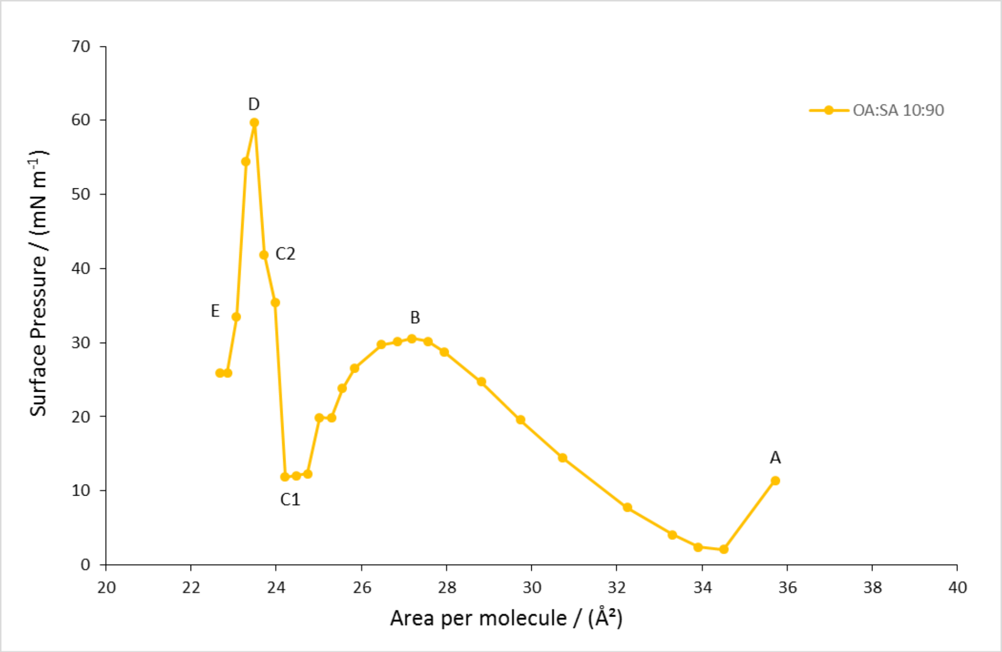

Figure 116: Pressure-area isotherm of a 10 % OA: 90 % SA mixture. Phase behaviour of simulated isotherm indicated: (A) gas-liquid coexisting region, (B) liquid-expanded region, (C1 and C2) liquid-condensed region, (D) equilibrium spreading pressure and (E) film collapse region.

This system is the most atmospherically relevant as we expect a much lower percentage of unsaturated material than saturated material to be present at the surface of the aerosol. This means that it is possible for the aerosol to form a surface layer in the solid state. Experimentally it is difficult to produce an isotherm with such a low percentage of unsaturated material—hence, being able to control the amount of material in the system is possibly the most useful feature of the simulation system, thus allowing insight into systems that resemble atmospheric aerosols more closely.

Figure 117 shows the pressure-area isotherm of the mixture containing 10 % OA and 90 % SA compared to the previously simulated isotherms. This system most resembles the pure SA system, forming a liquid-condensed phase and solid state. The equilibrium spreading pressure, at which the system is in a solid state is, with 60 mN m^{-1}, slightly higher than that of the pure SA system.

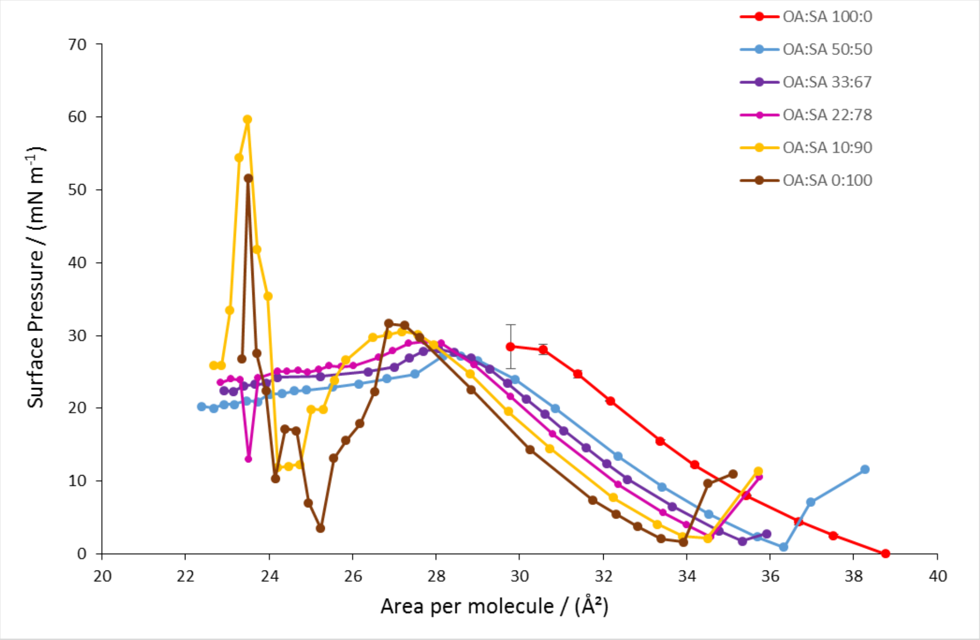

Figure 117: Pressure-area isotherm of the 10:90 OA: SA mixture compared to the pressure-area isotherms of the previously simulated mixtures and of the pure compounds.

Similarly to the pure SA system, the system forms a liquid-expanded phase (B) which then rearranges to form an ordered surface film (C and D), as shown in Figure 118 and Figure 119. The low number of unsaturated molecules in the system does not prevent the formation of a stable, ordered film, with few molecules moving away from the normal monolayer position.

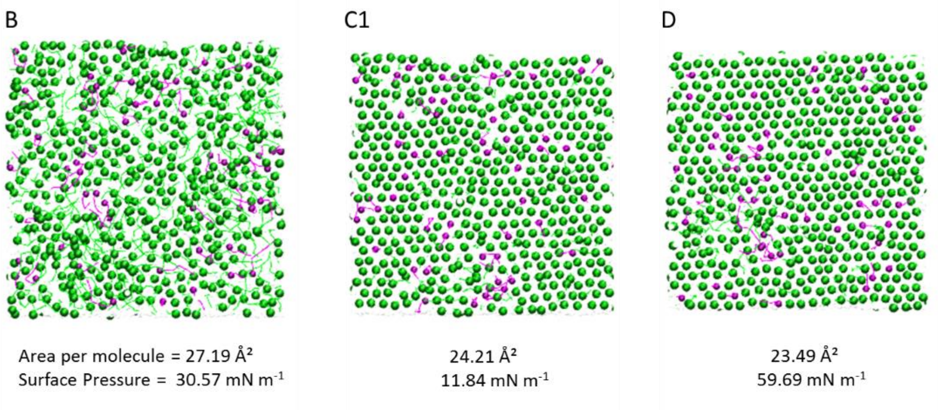

Figure 118: Snapshots of top monolayer view from high to low surface area per molecule of the 10 % OA: 90 % SA mixture (B, C1, D—points indicated on isotherm in Figure 116). From left to right: the system forms a liquid-expanded phase (B) which then breaks down to form a liquid-condensed phase (C1), with molecules ordering, and solid state (D).
OA = magenta, SA = green.

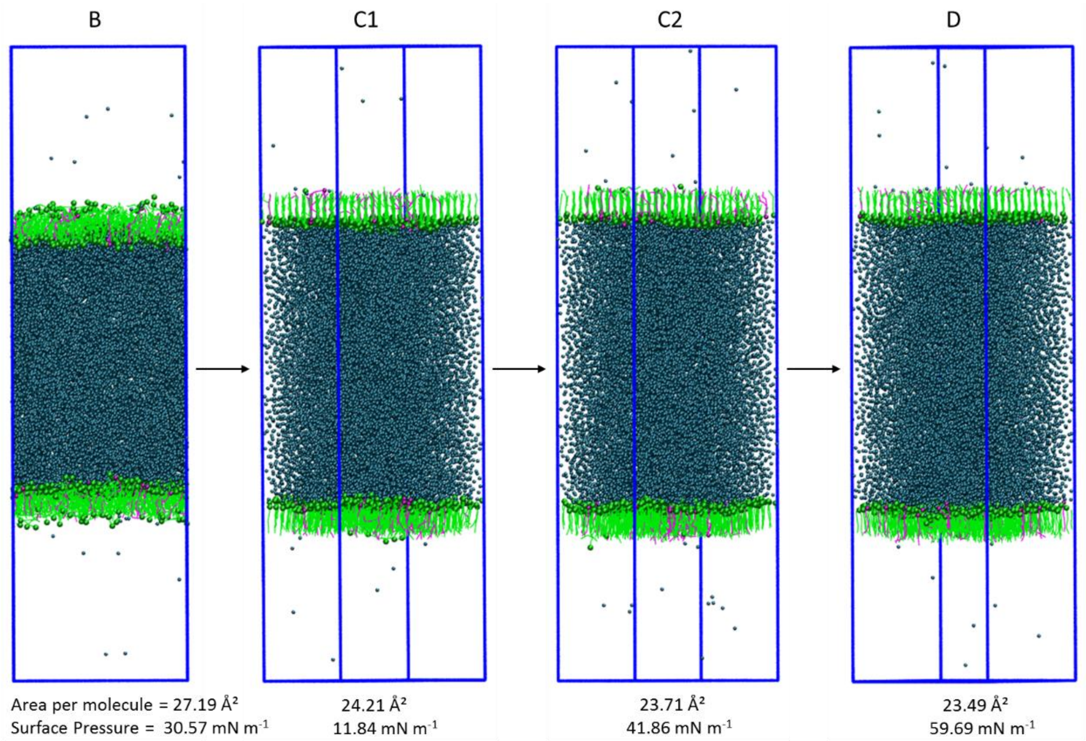

Figure 119: Snapshots of side view of the simulation box from high to low surface area per molecule of the 10 % OA: 90 % SA mixture, showing the rearrangement of the system from a disordered liquid-expanded phase (B1) to an order liquid-condensed phase (C1 and C2) and solid state (D). Points B, C1, C2 and D are indicated on isotherm in Figure 116. OA = magenta, SA = green, water = teal.

Contour plots showing the system in the liquid-expanded region (B), liquid-condensed region (C1 and C2) and at the equilibrium spreading pressure (D), are shown in Figure 120 and Figure 121.

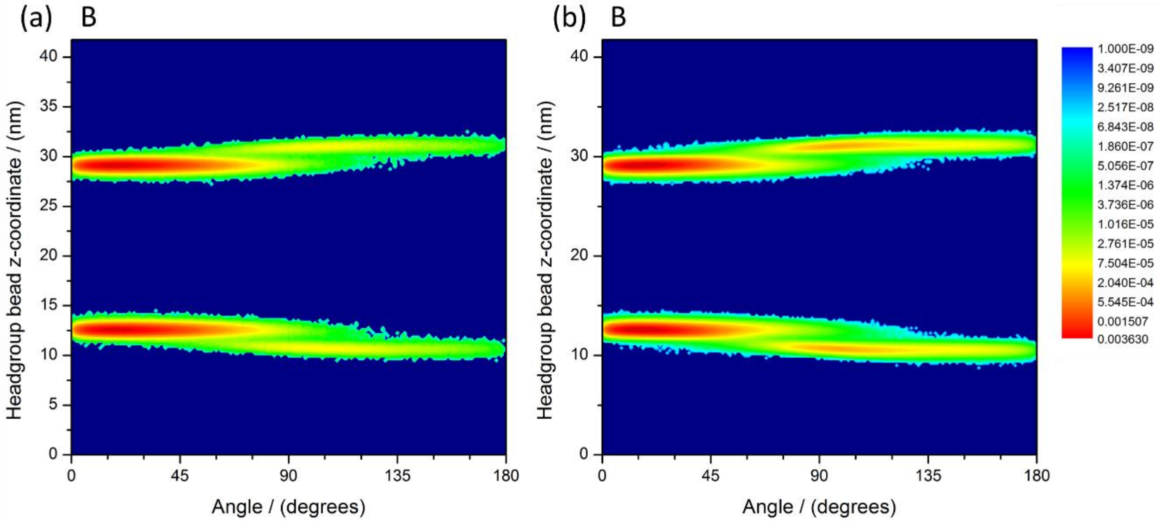

Figure 120: Contour plots showing the probability of finding the headgroup of a molecule at a certain *z*-coordinate with respect to angle(α) for the 10:90 mixture, (a) and (b) (B) area per molecule = 27.19 Å^2, surface pressure = 30.57 mN m^{-1}. Contour plot (a) = OA, contour plot (b) = SA. Point B is indicated on the pressure-area isotherm in Figure 116.

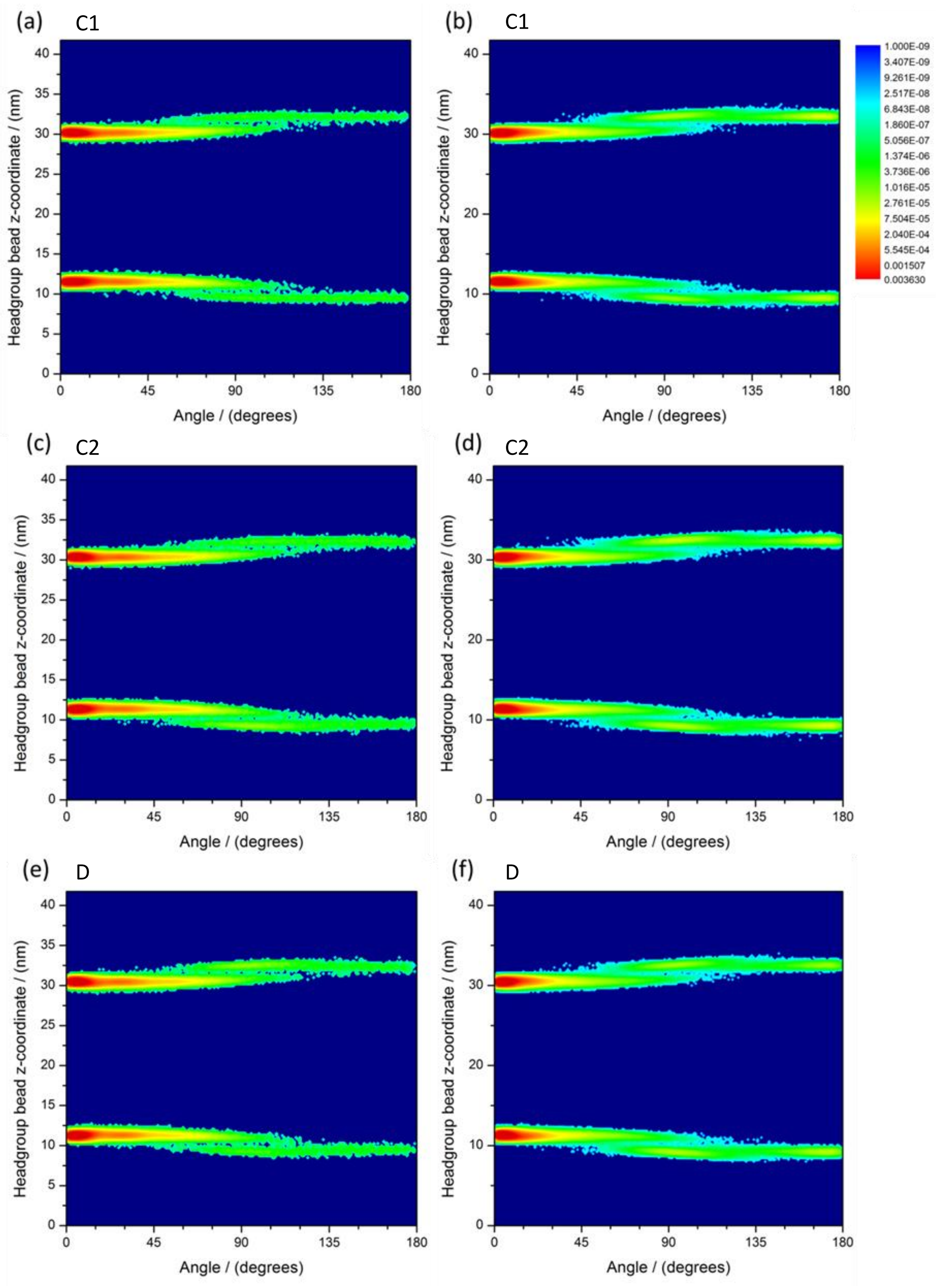

Figure 121: Contour plots showing the probability of finding the headgroup of a molecule at a certain *z*-coordinate with respect to angle(α) for the 10:90 mixture, (a) and (b) (C1) area per molecule = 24.21 Å^2, surface pressure = 11.84 mN m^{-1}; (c) and (d) (C2) area per molecule = 23.71 Å^2, surface pressure = 41.86 mN m^{-1}; (e) and (f) (D) area per molecule = 23.49 Å^2, surface pressure = 59.69 mN m^{-1}. Contour plots (a), (c), (e) = OA, contour plots (b), (d), (f) = SA. Points C1, C2 and D are indicated on the pressure-area isotherm in Figure 116.

The phase of the system changes from a liquid-expanded phase, Figure 120 (B), to a liquid-condensed phase, Figure 121 (C), indicated by a decrease in number of molecules that move out of the layer. Once in the liquid-condensed phase, Figure 121 (b) and (d), most SA molecules have a tilt of 30° or less with respect to the *z*-axis, forming structured films.

The percentage of molecules that change orientation at each area per molecule in the isotherm is shown in Figure 122. At the equilibrium spreading pressure, molecules are in the solid state; here, only 0.56 % of molecules change orientation: 0.53 % are SA molecules and 0.03 % are OA molecules.

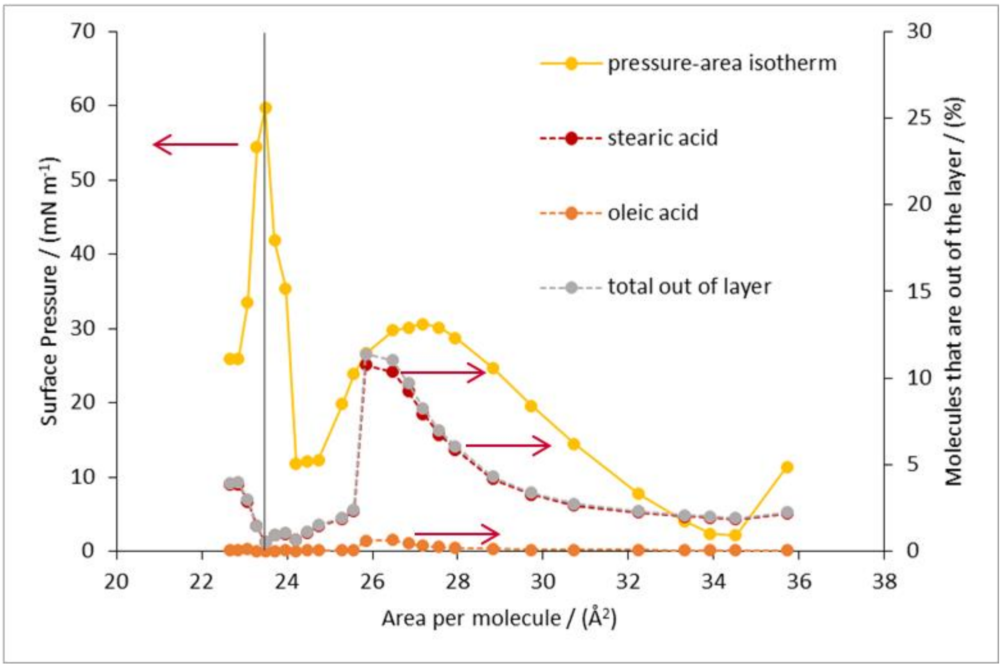

Figure 122: Total average percentage of molecules moving out of each monolayer over the production time of the simulation, with separate contributions of OA molecules and SA molecules shown, against the area per molecule, in comparison to the mixtures pressure-area isotherm.
Vertical line indicates the percentage of molecules that move out of the layer at the equilibrium spreading pressure (area per molecule = 23.49 Å^2, surface pressure = 59.69 mN m^{-1}). Arrows indicate relevant axes.

In the atmosphere, the formation of a well-ordered film on the surface of the aerosol may act as a transport barrier. In the literature, experimental studies showed that a pure SA layer on an ammonium sulfate core formed small droplets at or below the detection limit, which prevented water uptake.[9] The system simulated here with only 10 % unsaturated material behaves much like a pure SA surface film. The well-ordered chains may hence form a hydrophobic barrier preventing the uptake of water and other molecules, and therefore preventing the growth of the aerosol, thus affecting its size and lifetime in the atmosphere.

5.3.1.5 Comparison of the Simulated Mixtures

The percentage of molecules that change orientation for the simulated OA: SA mixtures is summarised in Figure 123. All systems show an initial increase in molecules that change orientation. Only the pure SA system and the system with 10 % OA show a metastable liquid-expanded phase, which then rearranges to form a liquid-condensed phase and solid state, indicated by a sharp drop in molecules that change orientation. In the remaining systems, the percentage of molecules that move out of the layer increases once the equilibrium spreading pressure is reached, causing a collapse of the system into bilayer-like structures. With an increase in SA molecules in the system, the percentage of fatty acid molecules that change orientation is lower for a given area per molecule, indicating the ability for the system to pack more closely due to a reduction in steric hindrance caused by a lower number of OA molecules present. This analysis method shows that, by determining the percentage of molecules that move out of the layer, the phase behaviour of the system can be clearly identified.

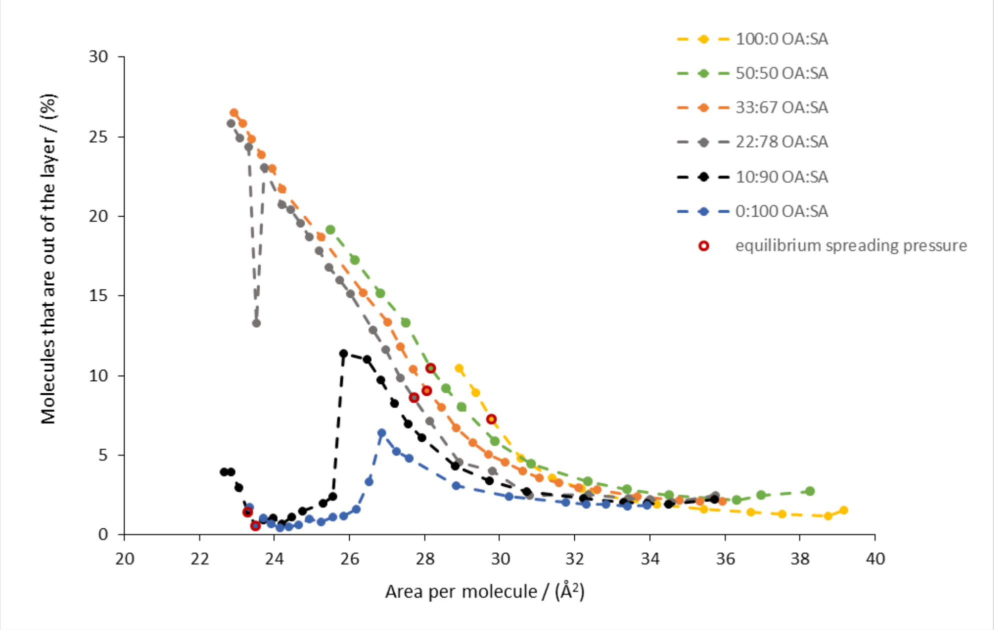

Figure 123: Comparison of the total average percentage of molecules moving out of each monolayer over the production time of the simulation for all simulated mixtures. Average percentage of molecules that move out of each monolayer at the equilibrium spreading pressure for each mixture indicated.

5.3.1.6 8 % Nonanoic Acid: 25 % Oleic Acid: 67 % Stearic Acid Mixture

To determine the effect of the only surface active molecule produced from the oxidative degradation of OA, NA—25 % of OA molecules were replaced by NA molecules in the 33:67 OA:SA mixture, resulting in a mixture of 8:25:67 NA:OA:SA. Here, a yield of 25 % of NA was chosen, to represent an upper limit of the possible production of NA from the ozonolysis of OA, in order to see the maximum effect the compound could have on the surface film. The pressure-area isotherm for this mixture is shown in Figure 124, in comparison to the pressure-area isotherm of the mixture containing 33:67 OA:SA.

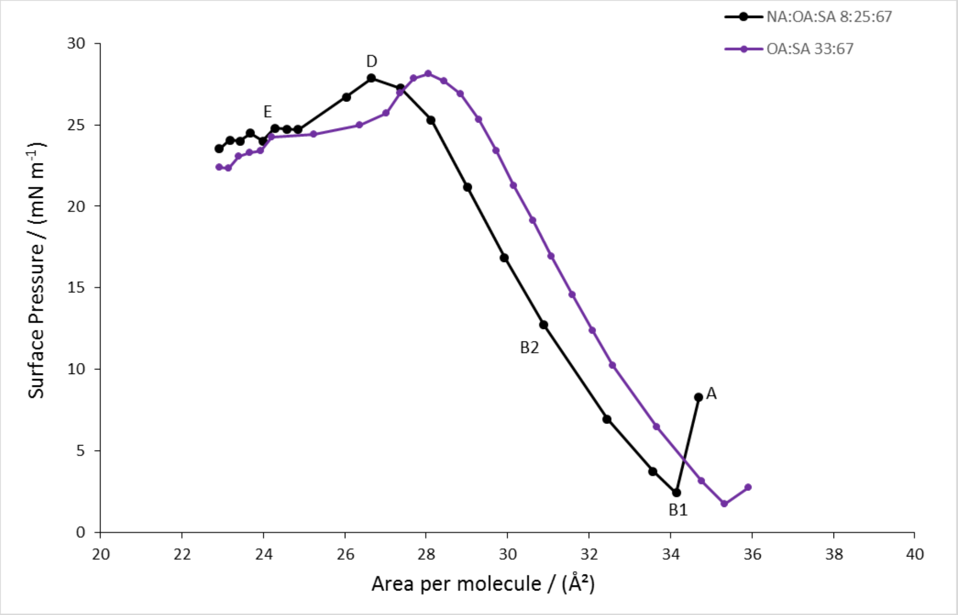

Figure 124: Pressure-area isotherm of the 8:25:67 mixture (NA:OA:SA) compared to the pressure-area isotherms of the 33:67 OA:SA mixture. Phase behaviour of simulated 8:25:67 NA:OA:SA mixture isotherm indicated: (A) gas-liquid coexisting region, (B1 and B2) liquid-expanded phase, (D) equilibrium spreading pressure and (E) film collapse region.

The equilibrium spreading pressure lies at 28 mN m^{-1} (Figure 124 (D)), which is similar to the equilibrium spreading pressure of the 33:76 OA:SA mixture. The isotherm is shifted to lower areas per molecule. This is most likely due to the replacement of unsaturated OA molecules by linear saturated NA molecules, resulting in a reduction in steric hindrance. As shown in Figure 125 and Figure 126, the mixture containing NA stays as a disordered layer under compression (B1 and B2) until the equilibrium spreading pressure (D) is reached and the monolayer breaks down (E).

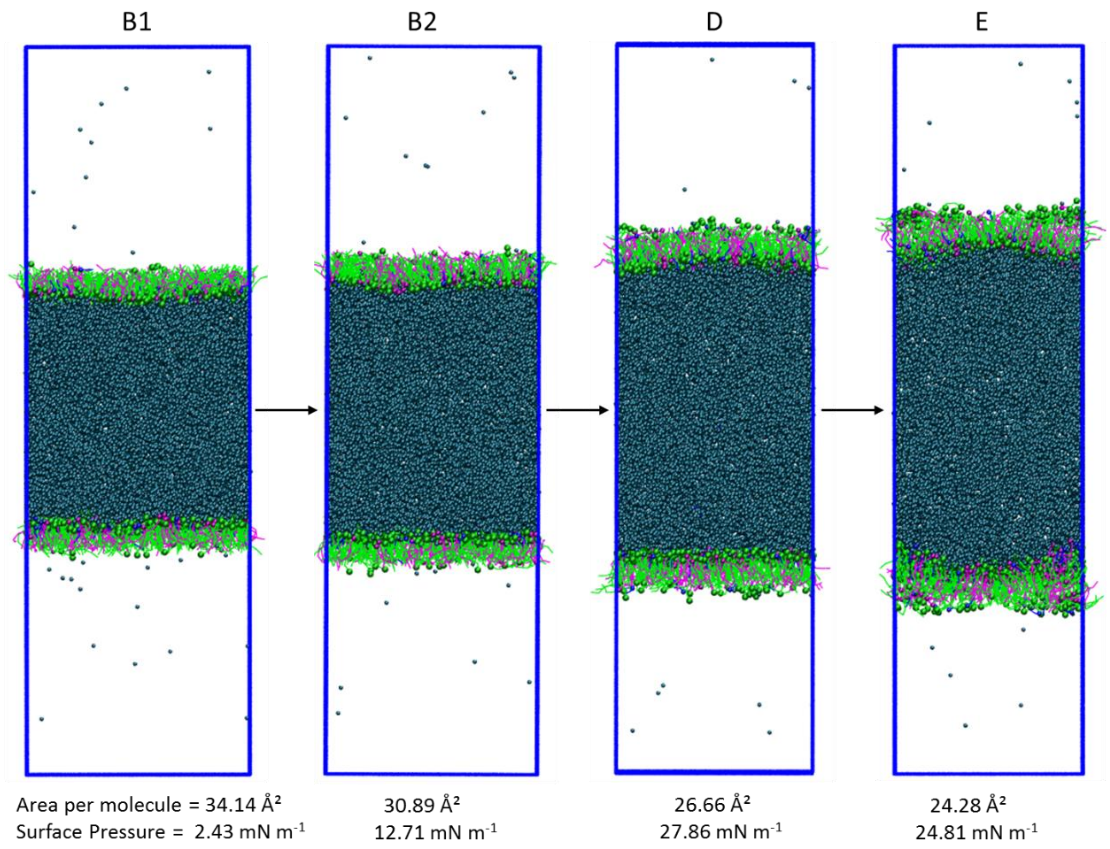

Figure 125: Snapshots of side view of the simulation box from high to low surface area per molecule of the 8:25:67 NA:OA:SA mixture isotherm (B1, B2, D, E—points indicated on isotherm in Figure 124). OA = magenta, SA = green, NA = purple, water = teal.

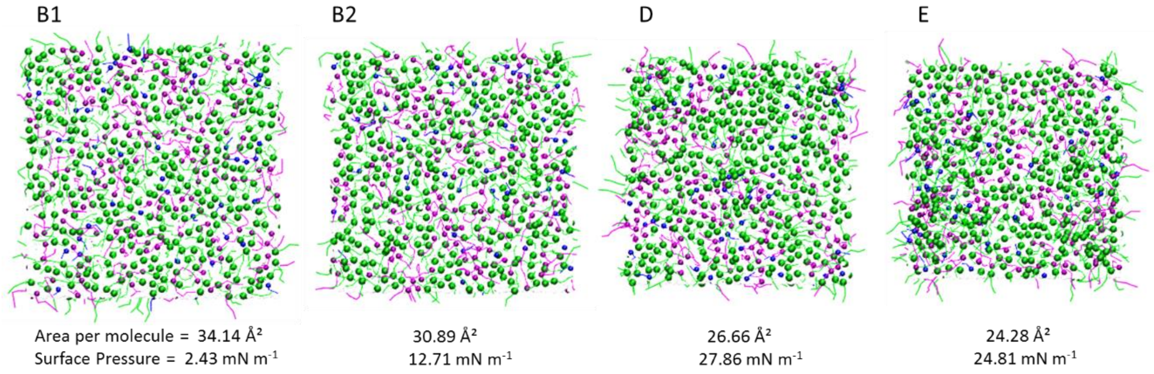

Figure 126: Snapshots of top monolayer view from high to low surface area per molecule of the 8:25:67 NA:OA:SA mixture (B1, B2, D, E—points indicated on isotherm in Figure 124). OA = magenta, SA = green, NA = purple.

On the aerosol, the oxidised surface film would result, for any given area per molecule of a surface film in the liquid-expanded phase, in a lower surface pressure. Thus, the film would be less effective in reducing the surface tension of the system after ozonolysis, meaning the aerosol would have a lower cloud activation potential.

5.3.2 Pressure-Area Isotherms of Mixed Monolayers Containing Palmitoleic Acid

In the following sections, mixtures containing POA and SA are simulated. The aim was to determine how the use of a shorter chain fatty acid compares to the previously simulated OA mixtures and to determine if the shorter chain length of POA enables the formation of a structured surface film. Therefore, the focus in this section is on the 10:90 and 22:78 POA:SA mixtures, which are the most atmospherically relevant, and which showed differences in their phase behaviour for the OA mixtures.

5.3.2.1 10 % Palmitoleic Acid: 90 % Stearic Acid Mixture

The pressure-area isotherm of the 10 % POA: 90 % SA mixture is shown in Figure 127.

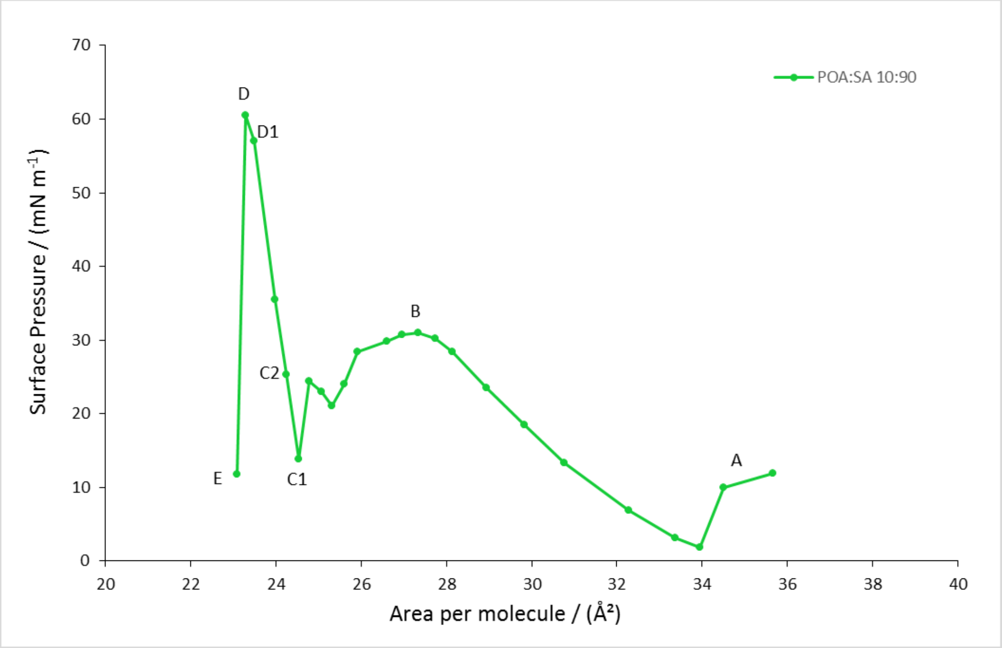

Figure 127: Pressure-area isotherm of a 10 % POA: 90 % SA mixture. Phase behaviour of simulated isotherm indicated: (A) gas-liquid coexisting region, (B) liquid-expanded region, (C1 and C2) liquid-condensed region, (D1) solid state, (D) equilibrium spreading pressure and (E) film collapse region.

The phase behaviour for this mixture is the same as for the 10:90 mixture containing OA. A liquid-expanded phase is formed (Figure 127 (D)), which then rearranges to form an ordered liquid-condensed phase (C) and a solid state (D). This is as expected, as the shorter chain length of POA should disrupt the layer less than OA does, and hence an ordered film is formed. The equilibrium spreading pressure is 61 mN m^{-1}, similar to that of the OA mixture, as shown in Figure 128.

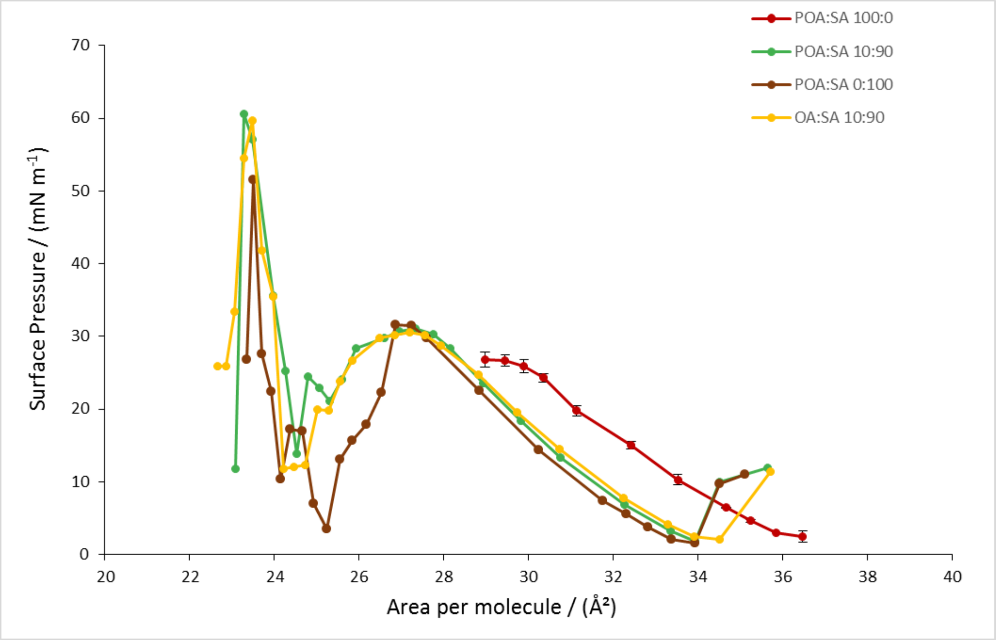

Figure 128: Pressure-area isotherm of the 10:90 POA:SA mixture compared to the pressure-area isotherms of the pure compounds and of the previously simulated 10:90 OA:SA mixture.

Due to the low percentage of POA, the behaviour of the system resembles the pure SA system much more closely. The rearrangement from a disordered liquid-expanded phase (B) to form an ordered film (C1, C2 and D1) is shown in Figure 129 and Figure 130.

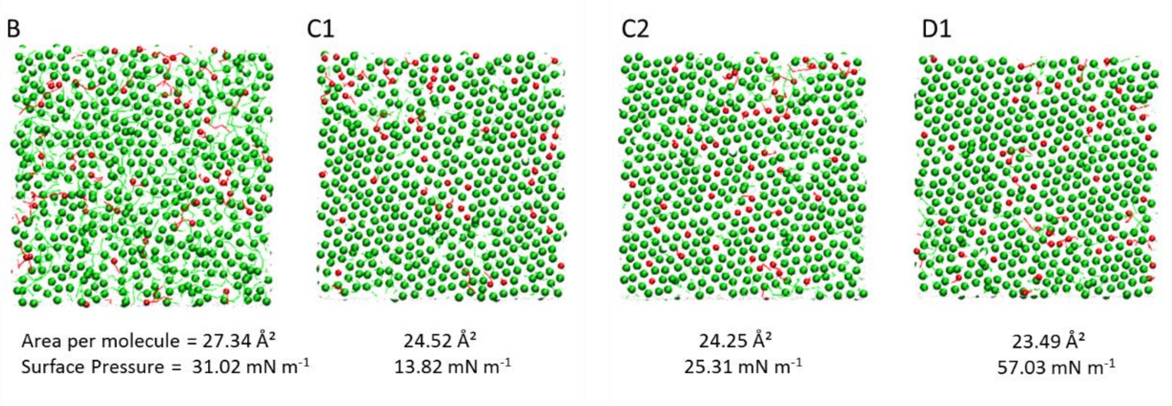

Figure 129: Snapshots of top monolayer view from high to low surface area per molecule of the 10 % POA: 90 % SA mixture (B, C1, C2, D1—points indicated on isotherm in Figure 127). From left to right: the system forms a liquid-expanded phase (B) which then breaks down to form a liquid-condensed phase (C1 and C2), with molecules ordering, and solid state (D1).
POA = red, SA = green.

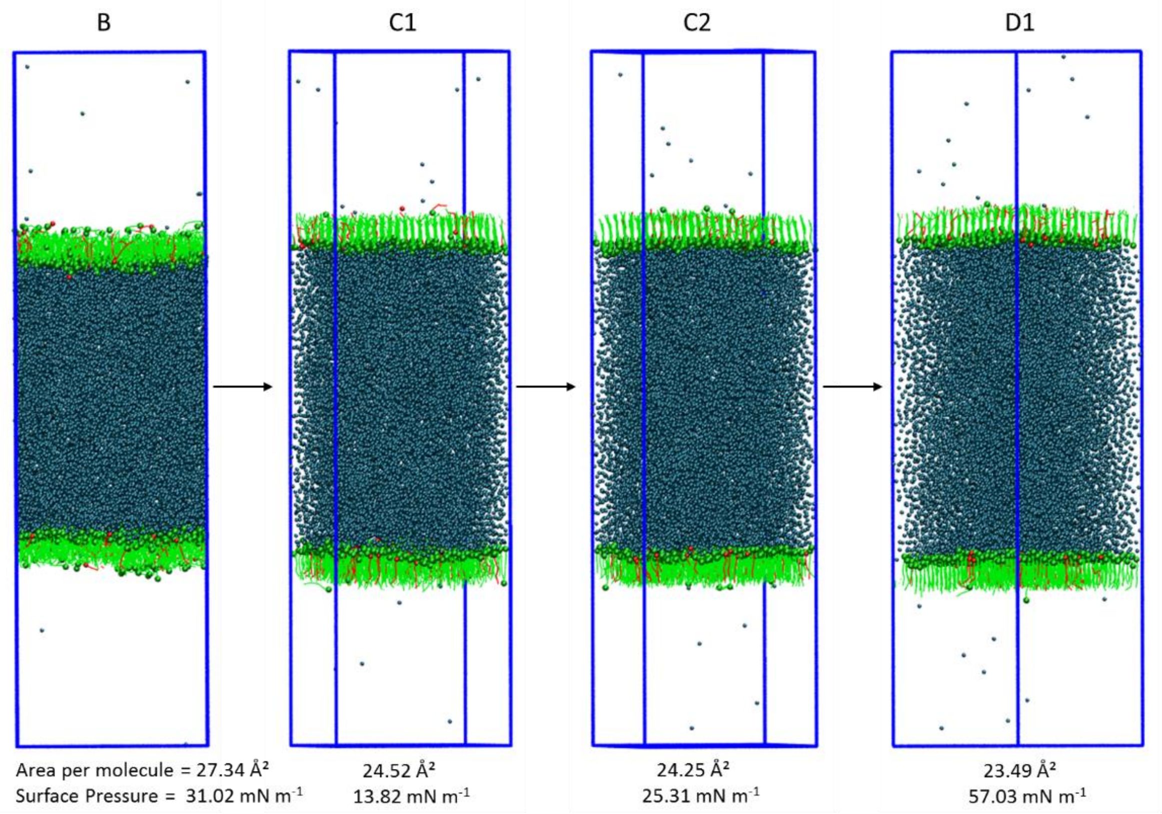

Figure 130: Snapshots of side view of the simulation box from high to low surface areas per molecule of the 10 % POA: 90 % SA mixture (B, C1, C2, D1—points indicated on isotherm in Figure 127). POA = red, SA = green, water = teal.

Contour plots for the mixture are shown in Figure 131. When looking at the contour plots on the right hand side, in Figure 131, representing the SA molecules in the system, the change in phase is indicated by the molecules in the normal monolayer positions ordering. The angle distributions become narrower, shifting towards lower angles of the molecules with respect to the *z*-axis. This means that the molecules order under compression.

Figure 132 shows, that once the system is in the liquid-condensed phase (C1) the number of molecules changing orientation decreases with decreasing area per molecule. An ordered film is obtained. Here, a decrease in the tilting of the molecules indicates a shift from the liquid-condensed phase (Figure 131 (d)) to solid state (Figure 131 (f)).

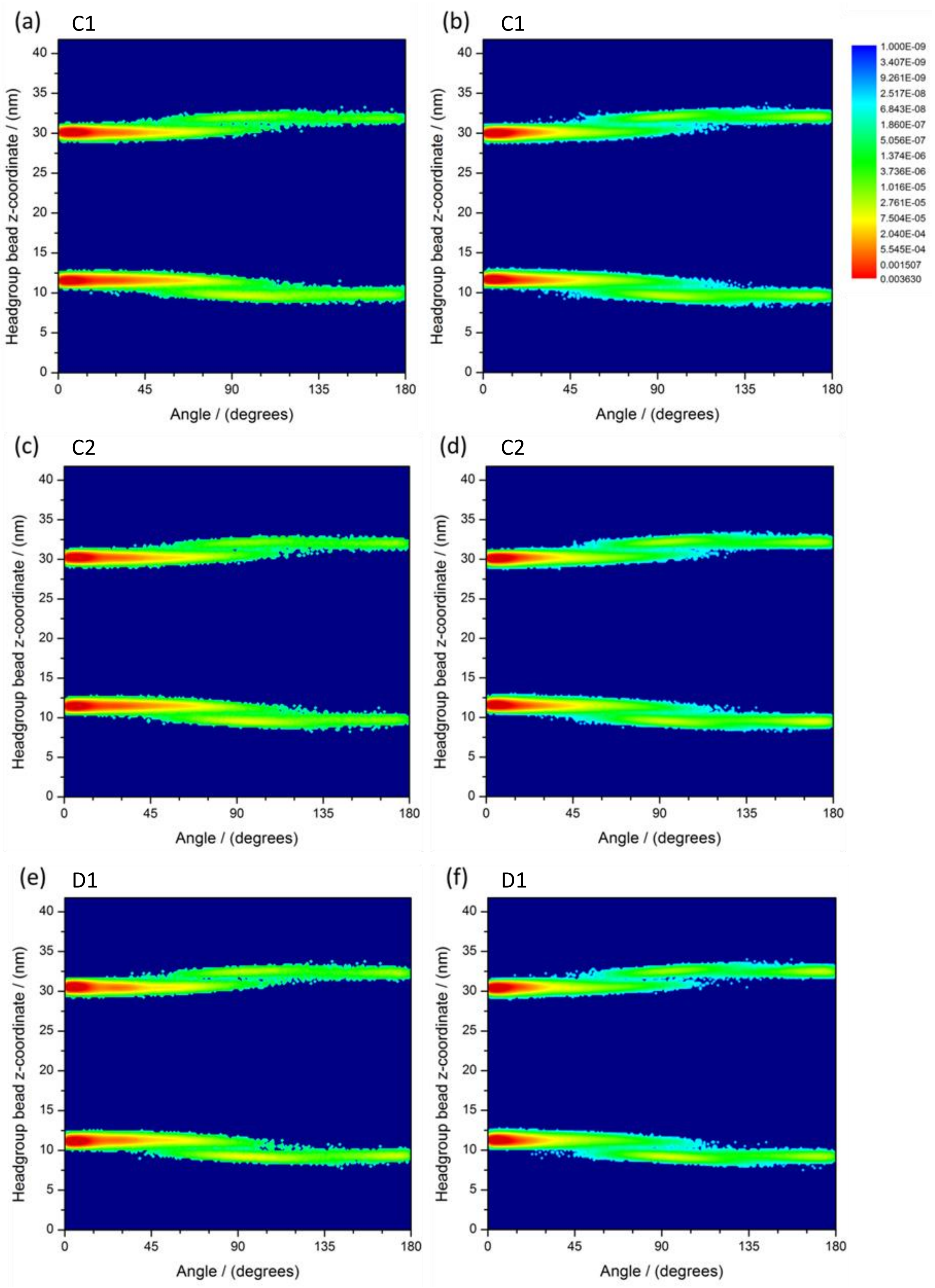

Figure 131: Contour plots showing the probability of finding the headgroup of a molecule at a certain *z*-coordinate with respect to angle(α) for the 10:90 POA:SA mixture, (a) and (b) (C1) area per molecule = 24.52 Å^2 , surface pressure = 13.82 mN m^{-1}; (c) and (d) (C2) area per molecule = 24.25 Å^2, surface pressure = 25.31 mN m^{-1}; (e) and (f) (D1) area per molecule = 23.49 Å^2, surface pressure = 57.03 mN m^{-1}. Contour plots (a), (c), (e) = POA, contour plots (b), (d), (f) = SA. Points C1, C2 and D1 are indicated on the pressure-area isotherm in Figure 127.

As shown in Figure 132, at the equilibrium spreading pressure (vertical line) the percentage of molecules that change orientation is low. After this point the percentage of molecules that change orientation rapidly increases indicating the collapse of the system, which is reflected by a drop in the surface pressure.

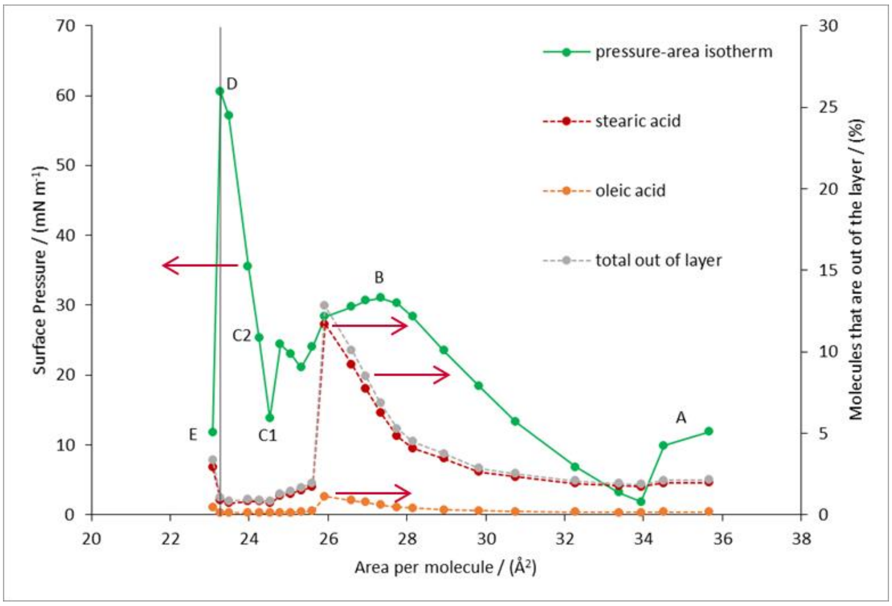

Figure 132: Total average percentage of molecules moving out of each monolayer over the production time of the simulation, with separate contributions of OA molecules and SA molecules shown, against the area per molecule, in comparison to the mixtures pressure-area isotherm. Vertical line indicates the percentage of molecules that move out of the layer at the equilibrium spreading pressure (area per molecule = 23.28 Å^2, surface pressure = 60.54 mN m^{-1}). Arrows indicate relevant axes. Phase behaviour of simulated isotherm indicated: (A) gas-liquid coexisting region, (B) liquid-expanded region, (C1 and C2) liquid-condensed region, (D) equilibrium spreading pressure and (E) film collapse region.

In the atmosphere, depending on the overall number of fatty acid molecules present on a particular aerosol, several scenarios are feasible. The fatty acid molecules might have to compete for space at the surface of the aerosol.[2] Hence, molecules will have a low surface area available resulting in a high surface pressure. Results obtained here show, that with a low percentage of unsaturated compound present in the monolayer, the molecules order and orient. Such a surface film on an atmospheric aerosol could act as a transport barrier, ultimately affecting the growth potential and lifetime of the aerosol.

If there are more surface sites than surface-active fatty acid molecules present, there might not be enough molecules to form an ordered film; this would lead to a less efficient transport barrier which could allow the evaporation of the aqueous sub-phase of the aerosol, causing a reduction in the size of the aerosol until an ordered film is reached.[10] If, however, there are more surface active fatty acid molecules than available surface sites, all surface sites will be occupied, and hence a solid state film can form (Figure 132 (D)). Here, further movement of species from the bulk to the surface may result in the collapse of the film (Figure 132 (E)). Donaldson *et al.* showed that it is thermodynamically feasible that if a surfactant film is compressed to the point of collapse, a spontaneous division of the aerosol into two particles, one larger and one smaller, can occur, leading to an increase in the number of smaller aerosols in the atmosphere.[11]

5.3.2.2 22 % Palmitoleic Acid: 78 % Stearic Acid Mixture

The pressure-area isotherm for the mixture of 22 % POA: 78 % SA is shown in Figure 133.

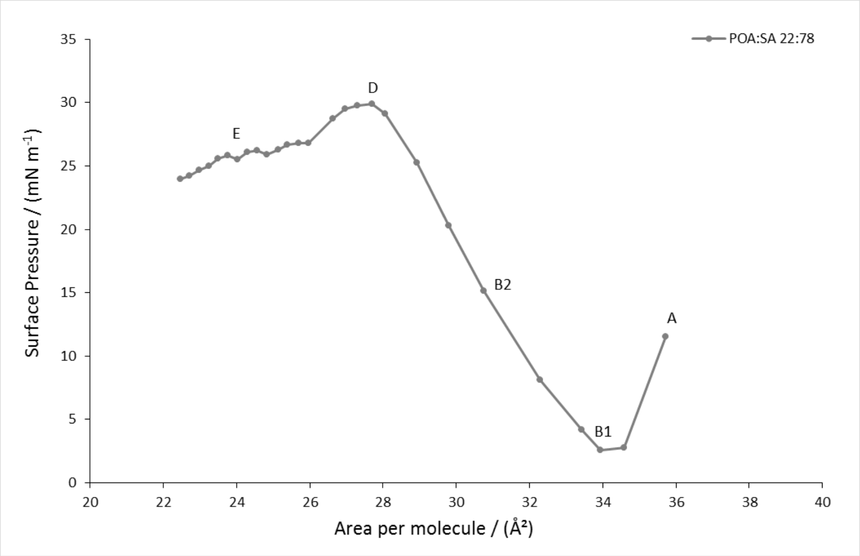

Figure 133: Pressure-area isotherm of a 22 % POA: 78 % SA mixture. Phase behaviour of simulated isotherm indicated: (A) gas-liquid coexisting region, (B1 and B2) liquid-expanded region, (D) equilibrium spreading pressure and (E) film collapse region.

The monolayer stays as a disordered surface film in the liquid-expanded phase under compression, until the equilibrium spreading pressure is reached (D), which lies at 30 mN m^{-1}. After this point, the monolayer collapses, with more molecules changing orientation (Figure 135 (E)). Unlike the 10:90 POA:SA system, the system containing 22 % POA does not form an ordered film, as shown in Figure 134 and Figure 135.

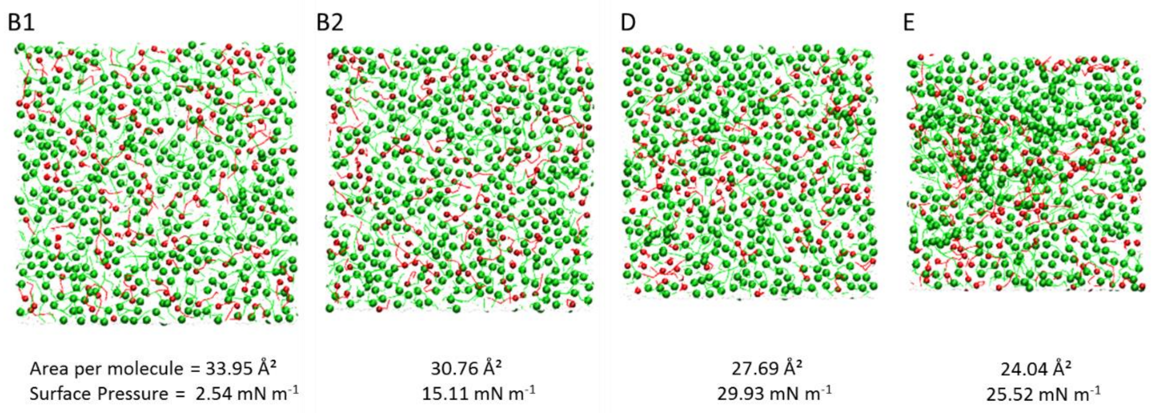

Figure 134: Snapshots of top monolayer view from low to high surface pressures of the 22 % POA: 78 % SA mixture (B1, B2, D, E—points indicated on isotherm in Figure 133). POA = red, SA = green.

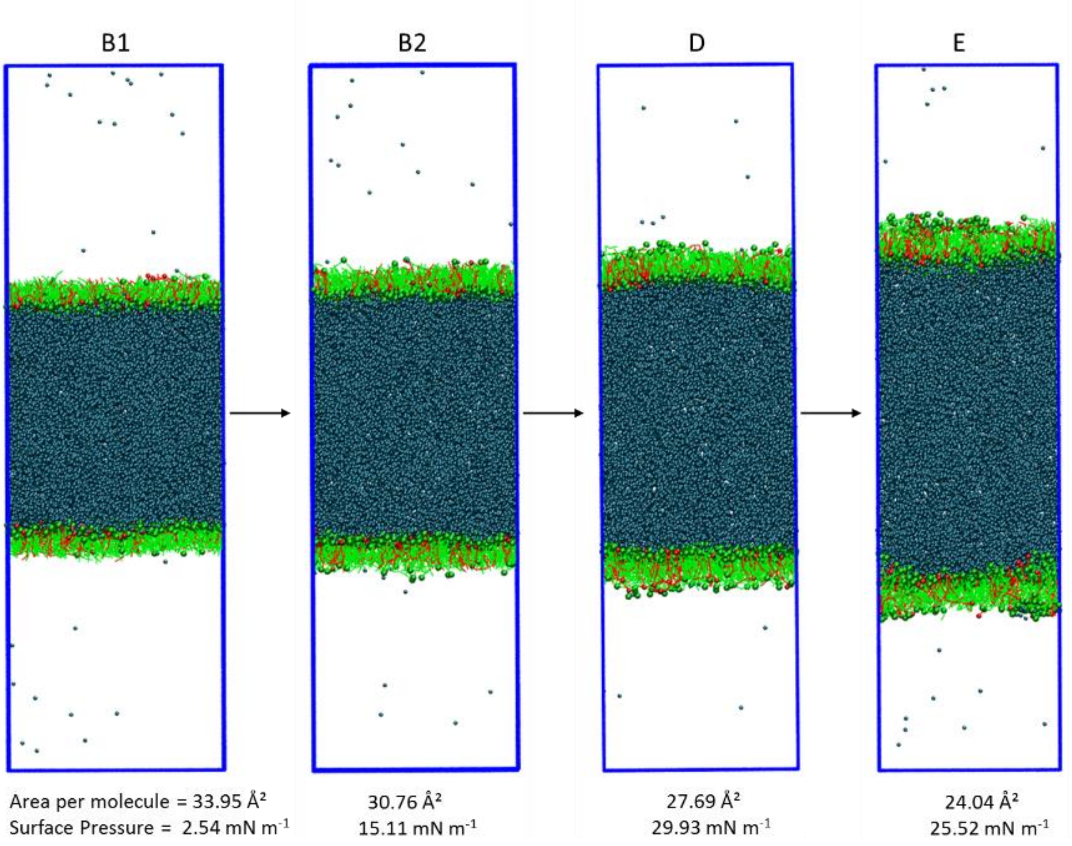

Figure 135: Snapshots of side view of the simulation box from low to high surface pressures of the 22 % POA: 78 % SA mixture (B1, B2, D, E—points indicated on isotherm in Figure 133). POA = red, SA = green, water = teal.

The isotherm, in comparison to the mixture containing 22:78 OA:SA, as shown in Figure 136, is shifted to slightly lower areas per molecule. This is most likely due to the shorter chain length of POA, resulting in a reduction in steric hindrance, allowing molecules to pack more closely.

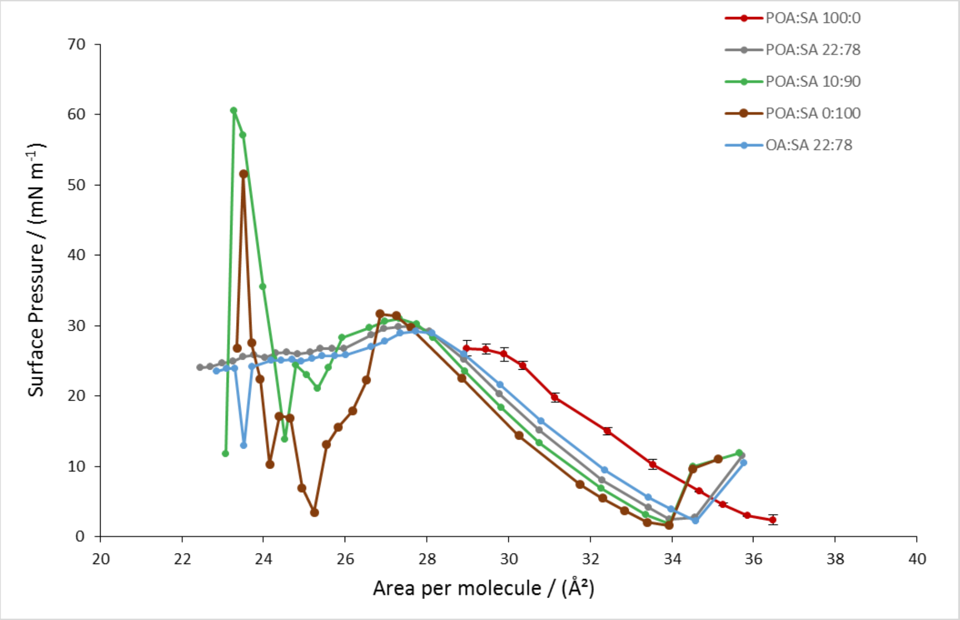

Figure 136: Pressure-area isotherm of the 22:78 POA:SA mixture compared to the pressure-area isotherms of the pure compounds and of the previously simulated mixtures: 10:90 POA:SA and 22:78 OA:SA.

The contour plots for the mixture, as shown in Figure 137, are similar to the ones obtained for the 50:50 (Figure 99), 33:67 (Figure 107) and 22:78 (Figure 114) OA:SA mixtures, featuring disordered, expanded films. The contour plots in Figure 137 show the system in the liquid-expanded phase (B), at the equilibrium spreading pressure (D) and in the film-collapse region (E). The contour plots illustrate, that as the monolayers are compressed, the overall number of molecules that change orientation increases. To quantify this, the percentage of POA and SA molecules that move out of the layer at each area per molecule was calculated (Figure 138). As shown in Figure 138, at the equilibrium spreading pressure, an average of 6.13 % of molecules moves out of each monolayer: 4.79 % are SA molecules and 1.34 % are POA molecules. Compared to the 22:78 OA:SA mixture this is a decrease of 2.47 % of molecules that change orientation at this point. This might be due to the shorter chain length of POA compared to OA, causing a reduction in the steric hindrance of the system, which subsequently reduces the number of molecules that move away from the normal monolayer position.

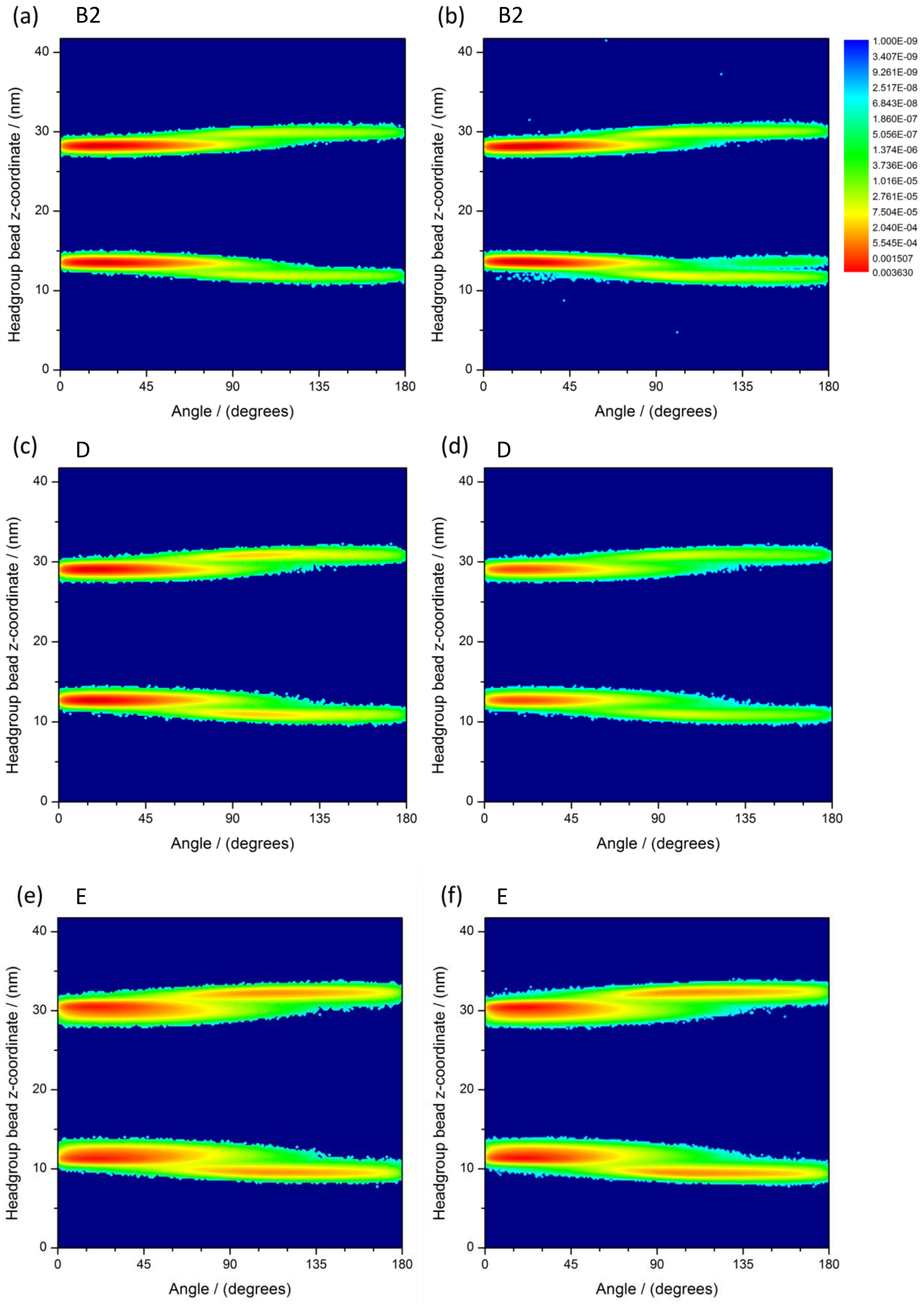

Figure 137: Contour plots showing the probability of finding the headgroup of a molecule at a certain *z*-coordinate with respect to angle(α) for the 22:78 POA:SA mixture, (a) and (b) (B2) area per molecule = 30.76 Å^2, surface pressure = 15.11 mN m^{-1}; (c) and (d) (D) area per molecule = 27.69 Å^2, surface pressure = 29.93 mN m^{-1}; (e) and (f) (E) area per molecule = 24.04 Å^2, surface pressure = 25.52 mN m^{-1}. Contour plots (a), (c), (e) = POA, contour plots (b), (d), (f) = SA. Points B2, D and E are indicated on the pressure-area isotherm in Figure 133.

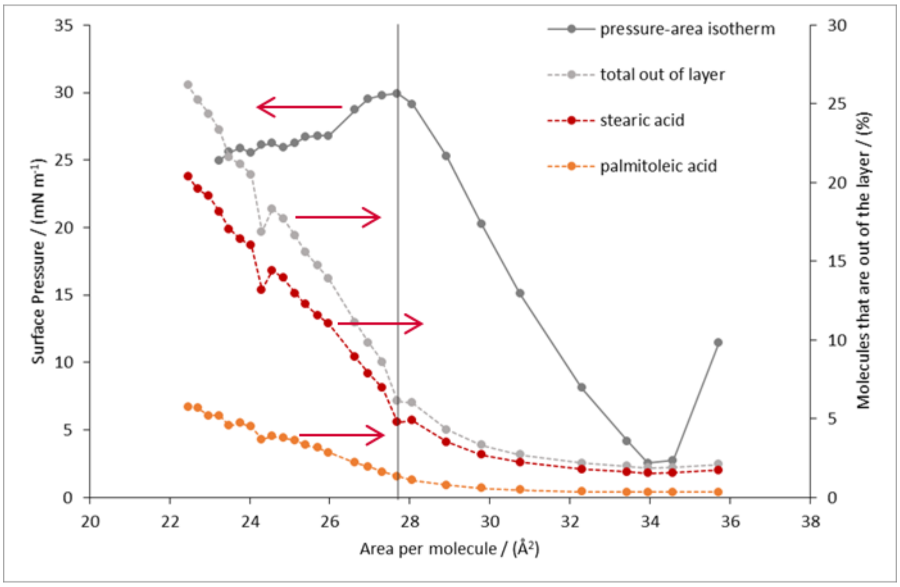

Figure 138: Total average percentage of molecules moving out of each monolayer over the production time of the simulation, with separate contributions of OA molecules and SA molecules shown, against the area per molecule, in comparison to the mixtures pressure-area isotherm.
Vertical line indicates the percentage of molecules that move out of the layer at the equilibrium spreading pressure (area per molecule = 27.69 Å^2, surface pressure = 29.93 mN m^{-1}). Arrows indicate relevant axes.

The higher the surface pressure, the lower the surface tension. This section showed that, when comparing the 22:78 POA:SA to the 22:78 OA:SA mixture, for any area per molecule in the liquid-expanded phase, the POA mixture has a lower surface pressure than the OA mixture. This means that, ultimately, the shorter chain POA molecules are less effective in suppressing the surface tension of the droplet, which will affect the potential of the droplet to act as cloud condensation nucleus.

5.3.2.3 5 % Heptanoic Acid: 17 % Palmitoleic Acid: 78 % Stearic Acid Mixture

The previously modelled mixture containing 22 % POA and 78 % SA formed disordered surface layers. Simulations in Chapter 4 showed that HA, which is an ozonolysis product of POA, remains at the surface of the water. To model the maximum impact HA could have on the surface film, using the 22:78 POA:SA mixture as a basis, 25 % of the POA molecules were replaced by HA molecules, resulting in a 5:17:78 HA:POA:SA mixture. The resulting pressure-area isotherm is shown in Figure 139 compared to the mixture containing 22:78 POA:SA.

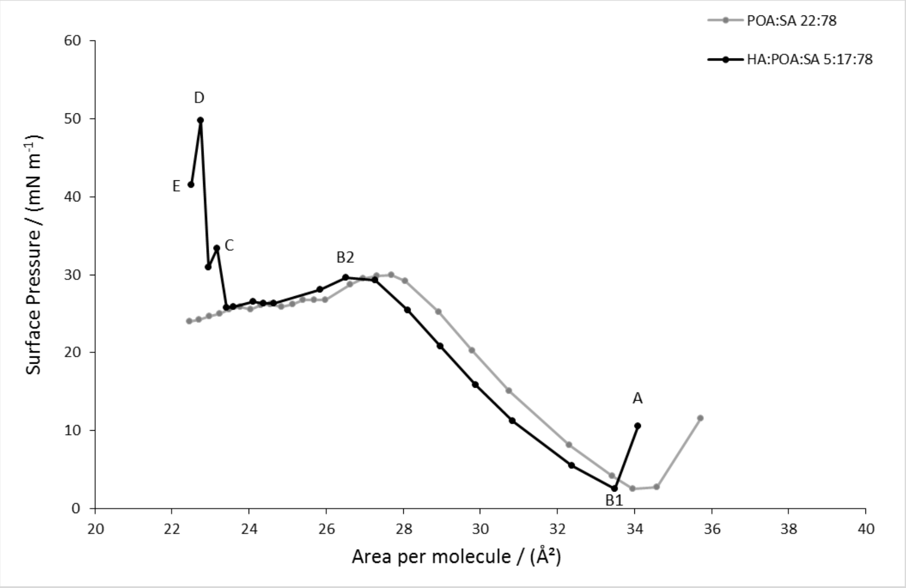

Figure 139: Pressure-area isotherm of the 5:17:78 mixture (HA:POA:SA) compared to the pressure-area isotherms of the 22:78 POA:SA mixture. Phase behaviour of simulated isotherm indicated: (A) gas-liquid coexisting region, (B1 and B2) liquid-expanded region, (C) liquid-condensed phase, (D) equilibrium spreading pressure and (E) film collapse region.

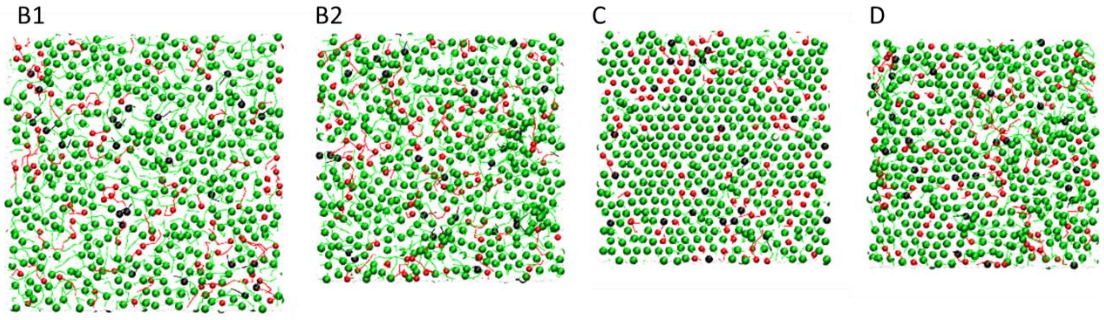

Area per molecule = 33.50 Å^2
Surface Pressure = 2.54 mN m^{-1}

26.53 Å^2
29.60 mN m^{-1}

23.18 Å^2
33.34 mN m^{-1}

22.74 Å^2
49.75 mN m^{-1}

Figure 140: Snapshots of top monolayer view from low to high surface pressures of the the 5:17:78 HA:POA:SA mixture (B1, B2, C, D—points indicated on isotherm in Figure 139). POA = red, SA = green, HA = black.

The results show that replacing some of the POA by the shorter linear carbon chain HA allows the system to form a liquid-condensed phase (Figure 139 (C)), with molecules ordering under compression (Figure 140 and Figure 141 (B to D)). Here, replacing the unsaturated molecule by a saturated molecule results in a reduction in steric hindrance, allowing molecules to pack more closely.

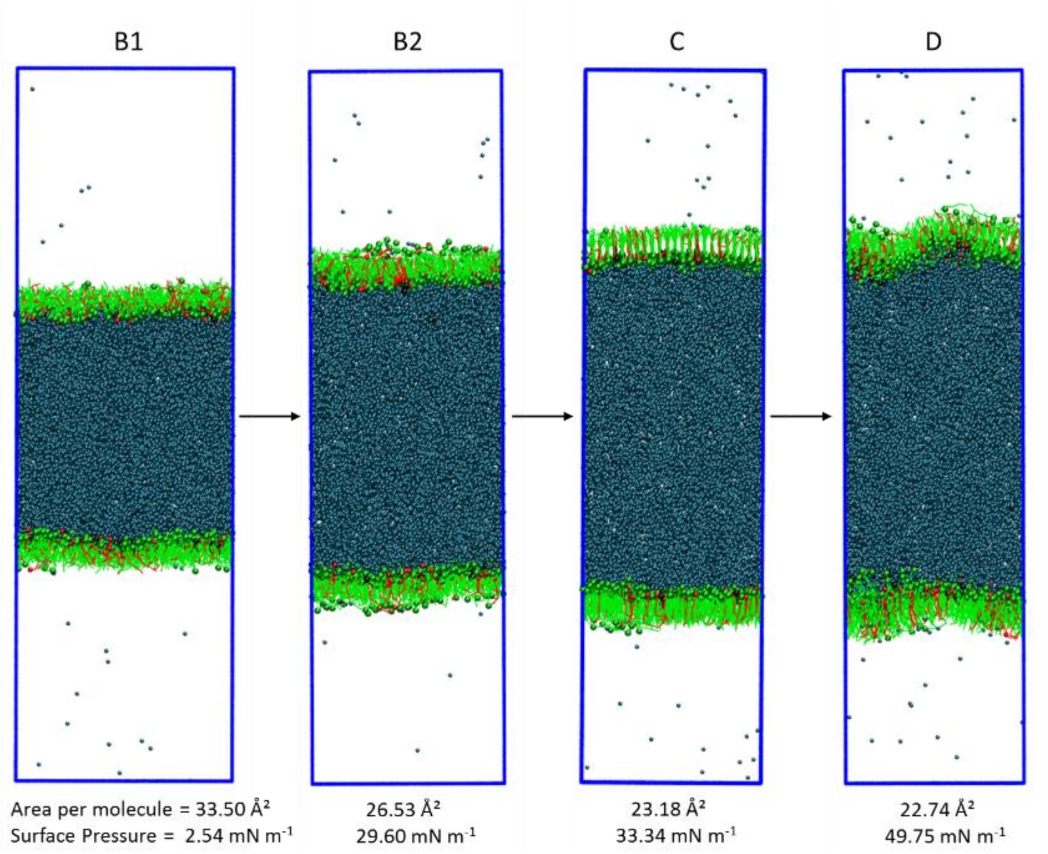

Figure 141: Snapshots of side view of the simulation box from low to high surface pressures of the the 5:17:78 HA:POA:SA mixture (B1, B2, C, D—points indicated on isotherm in Figure 139). POA = red, SA = green, HA = black, water = teal.

These results suggest that, at a low percentage of unsaturated material present at the surface, the ozonolysis of a surface film may change the phase behaviour of the system. The formation of an ordered surface film might prevent the growth of the aerosol by creating a hydrophobic barrier, hence preventing the uptake of other molecules. Thus, further research into the structure of surface films after ozonolysis might be an important factor in determining the aerosols' fate after ozonolysis.

5.4 Conclusions

Mixed monolayers of varying compositions were modelled in this chapter. For mixtures containing 33 % or more of the unsaturated component, disordered liquid-expanded films were formed. This suggests that the steric hindrance of the unsaturated molecules' double bond 'kink' in the aliphatic chain perturbs the packing ability of the film. In the atmosphere, there will be many more components present in the surface film. Here, the formation of a disordered surface film might be a less efficient transport barrier to the uptake of radicals and stable molecules.

Simulations allow insight into surface films with size scales and amount of material much more atmospherically realistic than those used in experiments on a Langmuir trough. Simulations with the 50:50 OA:SA mixture demonstrated that this can provide important additional information that can now be used to improve the setup for future experiments. From results obtained in this work, several modifications to experimental protocols were suggested. Allowing a longer equilibration time after spreading the material at the surface might help for the experimental system to form a homogenous surface film. Further improvements could include moving the barriers of the trough to the smallest possible surface area in order to reduce the amount of material needed to obtain a surface film (although this will still be orders of magnitude above atmospheric systems). Having a homogenous surface film will remove the experimental artefact of domains, and hence these modifications are an important factor to consider in future experiments.

A further strength of the simulation system is the ability to control the amount of material in the system at the molecular level, making it possible to obtain mixtures with very low concentrations of unsaturated material present, which are challenging to produce accurately in a laboratory. This enables a more realistic representation of the surface composition of an atmospheric aerosol—the simulated system containing only 10 % of unsaturated material is the most relevant of the simulated systems in this work. Out of the two component mixtures, only the mixtures containing 10 % unsaturated material formed surface films in a liquid-condensed phase and solid state, similar to a pure SA surface film. When the phase changes, it was shown that both the tilt of the molecule chains relative to the surface normal and the number of molecules that leave the normal monolayer position decrease. This results in a stable, ordered film. Further compression of the surface film causes a sharp decrease in surface pressures, with an increase in the proportion of molecules that change orientation. The formation of an ordered surface film on an atmospheric aerosol, resulting in a change of the surface from being hydrophilic to being hydrophobic, could act as an uptake barrier.

When modelling surface films containing reaction products from the ozonolysis of the unsaturated compound, it was shown that the phase behaviour of the system can change. Replacing unsaturated compounds by shorter chain linear fatty acids, the monolayer can change from a disordered layer to a well-ordered surface film. This means that reactions in the atmosphere can significantly affect the aerosol's structural properties and hence its growth potential. This highlights the need for further studies, determining the product yields from the ozonolysis of surfactants, to increase our understanding of changes to the aerosols' surface composition, which will ultimately change the aerosols' properties.

Surface pressure is directly linked to surface tension. The higher the surface pressure and the more compressed the film on the surface, the lower the surface tension of the aerosol. Two types of films were observed in this work—disordered liquid-expanded and ordered liquid-condensed films. Molecules in liquid-condensed films pack more closely, order and orient and hence reach higher surface pressures and are able to reduce the surface tension more efficiently, which should result in a more effective uptake of water. However, the ordered surface film is a more effective hydrophobic barrier on the surface of the aerosol, which may suppress the ability of the system to take up water at high relative humidity, and hence might suppress the ability of the aerosol to grow. Disordered molecules in the liquid-expanded phase on the other hand are a less efficient barrier. Hence, the surface tension depression here leads to an increase in water uptake of the molecule, which results in a lower critical supersaturation of the droplet and a larger droplet size at activation. Both ordered and disordered films will alter the growth process of the aerosol.

Molecular dynamics simulations have not yet been extensively used with regards to atmospheric chemistry. Work undertaken in this thesis highlights the benefits of being able to model interfacial films on fine aerosols using molecular dynamics simulations to gain insight into structural and dynamic properties. Here, the use of a coarse-grained simulation method allows insight beyond what can be feasibly modelled in all-atom simulations, with regards to system size and time scales.

5.5 References

1. A. Habartová, M. Roeselová and L. Cwiklik, *Langmuir*, 2015, **31**, 11508-11515.
2. J. B. Gilman, T. L. Eliason, A. Fast and V. Vaida, *J. Colloid Interf. Sci.*, 2004, **280**, 234-243.
3. J. B. Gilman, H. Tervahattu and V. Vaida, *Atmos. Environ.*, 2006, **40**, 6606-6614.
4. M. W. A. Skoda, B. Thomas, M. Hagreen, F. Sebastiani and C. Pfrang, *RSC Adv.*, 2017, **7**, 34208-34214.
5. S. H. Jones, M. D. King, A. D. Ward, A. R. Rennie, A. C. Jones and T. Arnold, *Atmos. Environ.*, 2017, **161**, 274-287.
6. F. Sebastiani, *Neutron Reflectometry and Ellipsometry Applied to Atmospheric Night-time Oxidation*, University of Reading Ph.D., 2014.
7. P. Wydro, B. Krajewska and K. Hąc-Wydro, *Biomacromolecules*, 2007, **8**, 2611-2617.
8. Y.-L. Lee, Y.-C. Yang and Y.-J. Shen, *J. Phys. Chem. B*, 2005, **109**, 4662-4667.
9. C. R. Ruehl and K. R. Wilson, *J. Phys. Chem. A*, 2014, **118**, 3952-3966.
10. L. F. Voss, M. F. Bazerbashi, C. P. Beekman, C. M. Hadad and H. C. Allen, *J. Geophys. Res.*, 2007, **112**.
11. D. J. Donaldson, A. F. Tuck and V. Vaida, *Phys. Chem. Chem. Phys.*, 2001, **3**, 5270-5273.

Chapter 6

6.1 Conclusions and Outlook

Work presented in this thesis focused on molecular dynamics simulations of fatty acid monolayers at the air-water interface to provide proxies for the complex organic surface films present on atmospheric aerosols. SA and the unsaturated fatty acids OA and POA together with their respective ozonolysis products, were successfully parameterised using the coarse-grained Martini force field.

Chapters 2 and 3 focused on the method development for the successful parameterisation of a fatty acid molecule. Several challenges based on the Martini force field approach were overcome—it was found that the building block approach of the Martini force field is not as easily transferable as originally assumed. Even though the basic parameters proved sufficient for the parameterisation of the carbon chain of the fatty acid molecules, the key parameters were found to be the equilibrium bead-to-bead distance and associated force constant of the headgroup bead to the chain. Without a sufficiently accurate description of these, it is not possible to obtain a good representation of the system that agrees well with experimental data. This is important to note for all future parameterisations within this force field.

Molecules in this work were hence parameterised using the all-atom CHARMM-36 force field. Structural data obtained from all-atom simulations allowed the calculation of the bead-to-bead distance and force constants needed for the coarse-grained simulations. Pressure-area isotherms were calculated for single component monolayers of OA and SA, which showed good agreement with regards to the expected range of surface pressures reported in experimental pressure-area isotherms, giving confidence in the approach used.

Chapter 4 focused on POA which, even though atmospherically relevant, has received little attention to date, with little knowledge on the compound’s phase behaviour and reactivity. Experimental studies on this compound would be useful to confirm ozonolysis products and determine product yields. POA was successfully parameterised in this work and a pressure-area isotherm was calculated from simulations. The phase behaviour of the three fatty acids showed that both POA and OA display a liquid-expanded phase and only the saturated linear carbon chain acid, SA, forms a liquid-condensed and solid phase surface film.

A key aspect of the work undertaken was to identify the behaviour for each of the ozonolysis products of both OA and POA. Simulations in this work suggest that azelaic acid and 9-oxononanoic acid diffuse into the water. Nonanal and heptanal, both volatile compounds, group on the surface of the water, showing their hydrophobic nature. In the atmosphere these two compounds are expected to evaporate from the aerosol's surface. HA and NA remain as monolayers at the surface of the water. The result obtained for 9-oxononanoic acid, which is not readily commercially available, is particularly interesting, as it should, in addition to azelaic acid and in addition to the reaction products remaining at the surface, be included in Köhler theory calculations to accurately predict the critical supersaturation of the droplet.

The successful parameterisation of the above mentioned compounds allowed the study of more complex systems, as presented in Chapter 5. Mixtures simulated in this work included mixing ratios of 10:90, 22:78, 33:67 and 50:50 of unsaturated to saturated compounds of which only the last has been studied experimentally. Studying a series of compositions provides complimentary information and additional insight that can be used to inform future experimental work.

Simulations of mixtures in this work showed that surface films with 33 % or more of the film consisting of the unsaturated component formed disordered liquid-expanded surface films. These surface films cause a reduction in the surface tension of the system. Hence, they have an effect on the Kelvin term in the Köhler equation. We would expect the lower surface tension to enhance water vapour uptake at supersaturation. This results in the molecules moving further apart, which causes a decrease in surface pressures and increase in the surface tension, until the surface tension matches the surface tension of pure water—here, the film would be in the two-dimensional gas phase. At this point, the droplets would be larger in size when activated compared to a droplet with no surfactant present. Oxidation of the unsaturated compound for a disordered surface film, as shown for the mixture containing 22 % POA: 78 % SA, could cause a phase change and lead to the formation of an ordered surface film—this ordered film could act as a hydrophobic barrier preventing the growth of the aerosol.

In simulations for the lowest concentration of unsaturated material to saturated material (10:90), a structured surface film with a liquid-condensed phase and solid state was formed. This was confirmed to be the case for surface films of mixtures containing OA and SA, and mixtures containing POA and SA. This is very interesting, as it suggests that, even with unsaturated compounds present, it is possible for the surface of the aerosols to be in a close-packed structure. This close-packed hydrophobic surface might hinder the ability of the aerosol to take up water, hence preventing the growth of the aerosol into cloud droplets.

These results have major implications for the fate of aerosols. If there is more surfactant present than available surface sites, such that the equilibrium surface pressure is reached, it is thermodynamically possible that the collapse of the system could lead to the spontaneous division of the aerosol into two particles—resulting in less surface active material in each particle.[1] This would lead to two aerosols with less compressed films. Here, two scenarios are feasible, depending on the supersaturation of the surrounding environment: if the supersaturation is higher, it could lead to the growth of the newly formed particles by the uptake of water vapour. If, however, the supersaturation is lower, it could lead to the evaporation of the sub-phase until an ordered film is formed, resulting in a greater number of smaller particles. This could be investigated in future work. A summary of results obtained in this thesis and the implications for the fate of atmospheric aerosols with varying surface composition are presented in Figure 142.

To date, few atmospheric studies utilise coarse-grained molecular dynamics simulations—this work shows that this is a useful tool in providing information on the order and structure of mixed component surface films on sub-micrometre particles and highlights the need for more research into the composition of organic surface films in order to further our understanding of their effects on particle growth and changes in cloud activation due to surface packing, which ultimately affects cloud formation and our climate.

A clear advantage of molecular dynamics simulations is the ability to follow the movement of each molecule over time. Even though we are still far from reaching experimental time scales, typical simulations are limited to the ns–μs timescale, computational power is fast improving, suggesting a bright future for this type of model description. In comparison to all-atom simulations, coarse-grained simulations allow a wider range of aerosol sizes to be studied, from the formation of clusters to particles in the Aitken mode, at timescales not yet accessible to all-atom simulations.

In this work, a cross-section through an aerosol was used as a basis for simulations, assuming a planar interface. This is a very useful assumption as it allows direct comparison to experimental pressure-area isotherms produced from planar interfaces, which is a good basis for the parametrisation of new molecules. As demonstrated in this work, molecular dynamics simulations provide a useful tool to gain insight into systems with a low proportion of unsaturated material (< 10 %) that cannot be easily produced in the laboratory. Now that the key stages in the parameterisation process of new molecules within the Martini force field have been identified, and a range of environmentally relevant fatty acids and reaction products have been parameterised, the simulation of spherical liquid-gas interfaces, with droplets in the submicron range up to the Aitken size mode becomes feasible.

This thesis focused on interfacial films on the surface of water. To get a more complete understanding of coated aerosols, future simulations could include changes to the sub-phase compositions, such as an aqueous sub-phase containing NaCl to mimic the core of sea salt aerosols. This would allow Köhler theory calculations from simulations, taking both the inorganic and organic fractions into account.

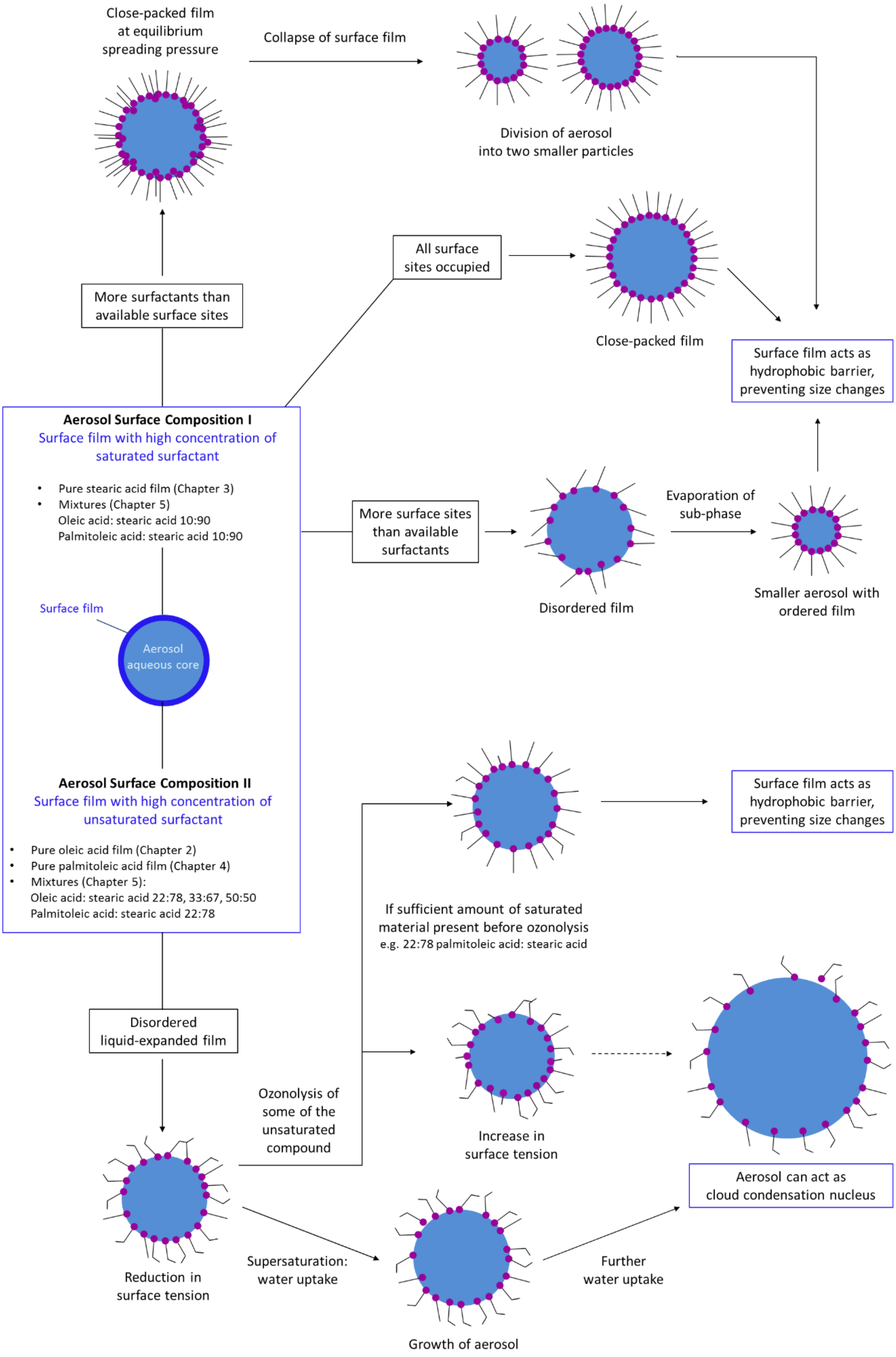

Figure 142: Summary of results obtained in this thesis for fatty acid surface films, highlighting the possible fates of fatty acid-coated aerosols in the atmosphere as suggested in the literature.[1, 2]

The incorporation of other atmospherically relevant fatty acids and fatty acid derivatives into the surface films will provide complementary information to experiments. Examples of such studies could include surface films containing methyl oleate, the methyl ester of OA, which is emitted both from cooking sources and biodiesels and palmitic acid, for which high emissions from cooking sources are reported.[3, 4] Furthermore, it would be interesting to study the effects of polyunsaturated fatty acids on surface films such as linoleic acid and linolenic acid, both unsaturated 18-carbon fatty acids emitted through meat cooking emissions, with two and three C=C bonds, respectively. The ozonolysis of these has been recently studied by He *et al.*, but no structural insight into such surface films was provided.[5]

Coarse-grained molecular dynamics simulations can hence be used as a complementary method to experiments, allowing insight into the phase behaviour of submicron particles, overcoming the spatial and timescale limitations of all-atom simulations. With the computational power available today, work carried out in this thesis paves the way for studies modelling surface films on aerosols up to the Aitken size mode, thus making it possible to model particles which are too small to be analysed by experimental techniques.

6.2 References

1. D. J. Donaldson, A. F. Tuck and V. Vaida, *Phys. Chem. Chem. Phys.*, 2001, **3**, 5270-5273.
2. L. F. Voss, M. F. Bazerbashi, C. P. Beekman, C. M. Hadad and H. C. Allen, *J. Geophys. Res.*, 2007, **112**.
3. C. Pfrang, F. Sebastiani, C. O. M. Lucas, M. D. King, I. D. Hoare, D. Chang and R. A. Campbell, *Phys. Chem. Chem. Phys.*, 2014, **16**, 13220-13228.
4. X. Zhao, Q. Hu, X. Wang, X. Ding, Q. He, Z. Zhang, R. Shen, S. Lü, T. Liu, X. Fu and L. Chen, *J. Atmos. Chem.*, 2015, **72**, 1-18.
5. X. He, C. Leng, S. Pang and Y. Zhang, *RSC Adv.*, 2017, **7**, 3204-3213.

Appendix

A.1 Internal Angles

This section provides information on the algorithm for calculating angle (θ), which represents the angle between the oleic acid headgroup bead, cis-double bond bead and last bead of the chain and angle (α), which represents the tilting of the molecules in the monolayer with respect to the *z*-axis.

The system is composed of two monolayers separated by water and antifreeze beads. The system contains oleic acid molecules numbered from 1 to n. The number of each oleic acid in the monolayers was divided by 2 and the oleic acid molecules were grouped according to the remainder. Hence two groups were formed, where those with remainder = 1 (odd numbers) make up the top monolayer and remainder = 0 (even numbers) are part of the bottom monolayer. The beads in the coordinate file are: COO = COO; B1 = C2; B3 = C3; B4 = C2 and B5 = C2. COO is the headgroup bead. The B3 bead describes the double bond in each oleic acid and B5 is the last bead in the oleic acid chain.

Calculating angle (θ):

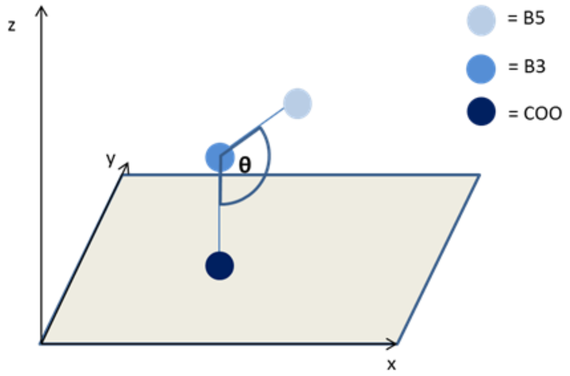

Figure 143: Representation of angle (θ) in an oleic acid molecule.

The vector $\mathbf{a}$ = B3 – COO and $\mathbf{b}$ = B3 – B5 intersect at point B3. The angle (θ), between **a** and **b** was calculated:

$$\cos(\theta) = \frac{\mathbf{a} \cdot \mathbf{b}}{|\mathbf{a}|\ |\mathbf{b}|} \tag{37}$$

Calculating angle (α):

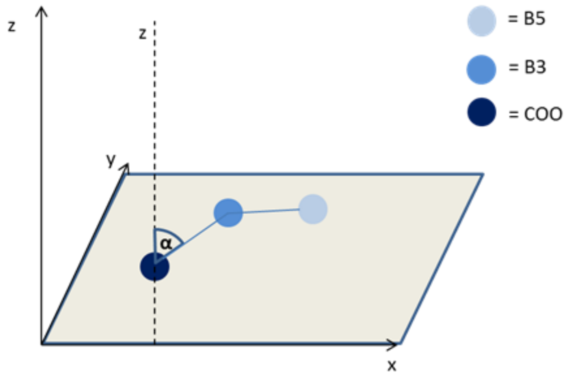

Figure 144: Representation of angle (α) in an oleic acid molecule.

For the top layer (group 1):

The angle (α) between the *z*-axis vector, **z** = (0,0,1) and vector **c** = COO – B3 was calculated as follows:

$$\cos(\alpha) = \frac{\mathbf{z} \cdot \mathbf{c}}{|\mathbf{z}|\ |\mathbf{c}|} \tag{38}$$

For the bottom layer (group 0):

The angle (α) between the *z*-axis vector, −**z** = (0,0,-1) and vector **c** = B3 – COO was calculated as follows:

$$\cos(\alpha) = \frac{(-\mathbf{z}) \cdot \mathbf{c}}{|(-\mathbf{z})|\ |\mathbf{c}|} \tag{39}$$

A.2 Determining the Lowest Density Regions in the Contour Plots

By changing the scale on the graph and changing the contours, it is possible to determine a straight line which divides the two density regions for each of the monolayers. From the obtained coordinates the equation of the lines can be determined, which allows the percentage of molecules that move out of layer to be determined calculated.

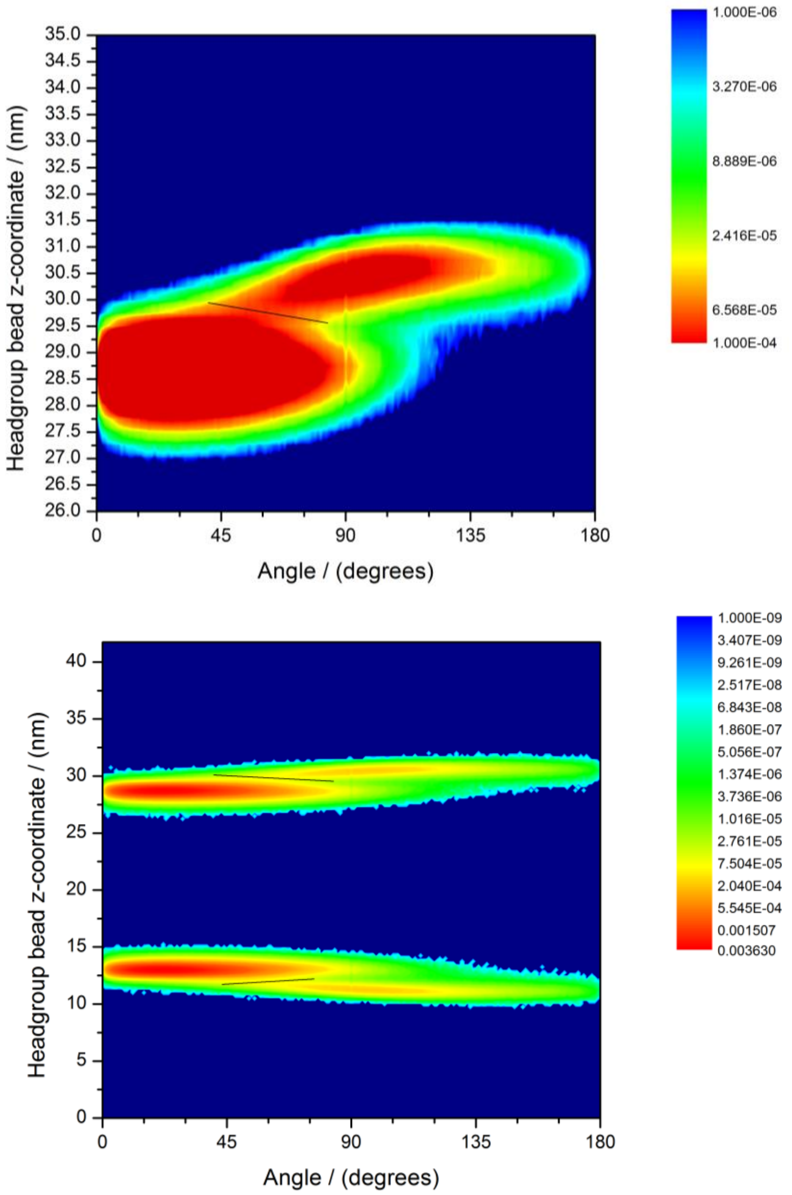

Figure 145: Fitting of lines between density regions in the monolayers to determine the percentage of molecules that move out each layer during the production run.

A.3 CHARMM Parameters for Molecules Simulated in this Work

The following sections give the topology files for all molecules simulated using the CHARMM-36 force field in this thesis. Structures have been adapted from previously parameterised lipid molecules, see http://mackerell.umaryland.edu/charmm_ff.shtml. The first line in the topology file states the residue (RESI) and residue name (e.g. STAP) and total charge of the molecule (e.g 0.00). The following lines state all the atoms in the residue. For each 'ATOM', the atom name, type and partial charge are given. The 'GROUP' section combines atoms; here the charge for each group equals zero. The topology file continues by giving a list defining the bonding between pairs of atoms. The final section of the topology file states the dihedral angles in the standard format. All other parameters used are stated elsewhere and are part of the standard force field parameters for use with GROMACS.

A.3.1 Stearic Acid

```
RESI STAP          0.00 ! stearic acid
!

GROUP                   !                  H1C
ATOM H1C   HOL      0.44 !                   |
ATOM O1    OHL     -0.61 !             O2    O1
ATOM C1    CL       0.75 !              \\  /
ATOM O2    OBL     -0.55 !               C1
ATOM C2    CTL2    -0.21 !                |
ATOM H2A   HAL2     0.09 !        H2A---C2---H2B
ATOM H2B   HAL2     0.09 !                |
GROUP                   !                |
ATOM C3    CTL2    -0.18 !                |
ATOM H3A   HAL2     0.09 !        H3A ---C3---H3B
ATOM H3B   HAL2     0.09 !                |
GROUP                   !                |
ATOM C4    CTL2    -0.18 !                |
ATOM H4A   HAL2     0.09 !        H4A ---C4---H4B
ATOM H4B   HAL2     0.09 !                |
GROUP                   !                |
ATOM C5    CTL2    -0.18 !                |
ATOM H5A   HAL2     0.09 !        H5A ---C5---H5B
ATOM H5B   HAL2     0.09 !                |
GROUP                   !                |
ATOM C6    CTL2    -0.18 !                |
ATOM H6A   HAL2     0.09 !        H6A ---C6---H6B
ATOM H6B   HAL2     0.09 !                |
GROUP                   !                |
ATOM C7    CTL2    -0.18 !                |
ATOM H7A   HAL2     0.09 !        H7A ---C7---H7B
ATOM H7B   HAL2     0.09 !                |
GROUP                   !                |
ATOM C8    CTL2    -0.18 !                |
```

```
ATOM H8A  HAL2    0.09 !        H8A ---C8---H8B
ATOM H8B  HAL2    0.09 !               |
GROUP                  !               |
ATOM C9   CTL2   -0.18 !               |
ATOM H9A  HAL2    0.09 !        H9A ---C9---H9B
ATOM H9B  HAL2    0.09 !               |
GROUP                  !               |
ATOM C10  CTL2   -0.18 !               |
ATOM H10A HAL2    0.09 !        H10A---C10--H10B
ATOM H10B HAL2    0.09 !               |
GROUP                  !               |
ATOM C11  CTL2   -0.18 !               |
ATOM H11A HAL2    0.09 !        H11A---C11--H11B
ATOM H11B HAL2    0.09 !               |
GROUP                  !               |
ATOM C12  CTL2   -0.18 !               |
ATOM H12A HAL2    0.09 !        H12A---C12--H12B
ATOM H12B HAL2    0.09 !               |
GROUP                  !               |
ATOM C13  CTL2   -0.18 !               |
ATOM H13A HAL2    0.09 !        H13A---C13--H13B
ATOM H13B HAL2    0.09 !               |
GROUP                  !               |
ATOM C14  CTL2   -0.18 !               |
ATOM H14A HAL2    0.09 !        H14A---C14--H14B
ATOM H14B HAL2    0.09 !               |
GROUP                  !               |
ATOM C15  CTL2   -0.18 !               |
ATOM H15A HAL2    0.09 !        H15A---C15--H15B
ATOM H15B HAL2    0.09 !               |
GROUP                  !               |
ATOM C16  CTL2   -0.18 !               |
ATOM H16A HAL2    0.09 !        H16A---C16--H16B
ATOM H16B HAL2    0.09 !               |
GROUP                  !               |
ATOM C17  CTL2   -0.18 !               |
ATOM H17A HAL2    0.09 !        H17A---C17--H17B
ATOM H17B HAL2    0.09 !               |
GROUP                  !               |
ATOM C18  CTL3   -0.27 !               |
ATOM H18A HAL3    0.09 !        H18A---C18--H18B
ATOM H18B HAL3    0.09 !               |
ATOM H18C HAL3    0.09 !              H18C

! bonding
BOND  H1C  O1
BOND  O1   C1
DOUBLE  C1  O2
BOND  C1   C2
BOND  C2   H2A       C2   H2B       C2   C3
BOND  C3   H3A       C3   H3B       C3   C4
BOND  C4   H4A       C4   H4B       C4   C5
BOND  C5   H5A       C5   H5B       C5   C6
BOND  C6   H6A       C6   H6B       C6   C7
BOND  C7   H7A       C7   H7B       C7   C8
BOND  C8   H8A       C8   H8B       C8   C9
BOND  C9   H9A       C9   H9B       C9   C10
BOND  C10  H10A      C10  H10B      C10  C11
```

```
BOND  C11  H11A      C11  H11B      C11  C12
BOND  C12  H12A      C12  H12B      C12  C13
BOND  C13  H13A      C13  H13B      C13  C14
BOND  C14  H14A      C14  H14B      C14  C15
BOND  C15  H15A      C15  H15B      C15  C16
BOND  C16  H16A      C16  H16B      C16  C17
BOND  C17  H17A      C17  H17B      C17  C18
BOND  C18  H18A      C18  H18B      C18  H18C

IMPR C1 O1 C2 O2

IC H1C    O1     C1     C2    0.0000  0.0000  180.00  0.0000   0.0000
IC C2     O1     *C1    O2    0.0000  0.0000  0.0000  0.0000   0.0000
IC O1     C1     C2     C3    0.0000  0.0000  180.00  0.0000   0.0000
IC C3     C1     *C2    H2A   0.0000  0.0000  120.00  0.0000   0.0000
IC C3     C1     *C2    H2B   0.0000  0.0000 -120.00  0.0000   0.0000
IC C1     C2     C3     C4    0.0000  0.0000  180.00  0.0000   0.0000
IC C4     C2     *C3    H3A   0.0000  0.0000  120.00  0.0000   0.0000
IC C4     C2     *C3    H3B   0.0000  0.0000 -120.00  0.0000   0.0000
IC C2     C3     C4     C5    0.0000  0.0000  180.00  0.0000   0.0000
IC C5     C3     *C4    H4A   0.0000  0.0000  120.00  0.0000   0.0000
IC C5     C3     *C4    H4B   0.0000  0.0000 -120.00  0.0000   0.0000
IC C3     C4      C5    C6    0.0000  0.0000  180.00  0.0000   0.0000
IC C6     C4     *C5    H5A   0.0000  0.0000  120.00  0.0000   0.0000
IC C6     C4     *C5    H5B   0.0000  0.0000 -120.00  0.0000   0.0000
IC C4     C5     C6     C7    0.0000  0.0000  180.00  0.0000   0.0000
IC C7     C5     *C6    H6A   0.0000  0.0000  120.00  0.0000   0.0000
IC C7     C5     *C6    H6B   0.0000  0.0000 -120.00  0.0000   0.0000
IC C5     C6     C7     C8    0.0000  0.0000  180.00  0.0000   0.0000
IC C8     C6     *C7    H7A   0.0000  0.0000  120.00  0.0000   0.0000
IC C8     C6     *C7    H7B   0.0000  0.0000 -120.00  0.0000   0.0000
IC C6     C7     C8     C9    0.0000  0.0000  180.00  0.0000   0.0000
IC C9     C7     *C8    H8A   0.0000  0.0000  120.00  0.0000   0.0000
IC C9     C7     *C8    H8B   0.0000  0.0000 -120.00  0.0000   0.0000
IC C7     C8     C9     C10   0.0000  0.0000  180.00  0.0000   0.0000
IC C10    C8     *C9    H9A   0.0000  0.0000  120.00  0.0000   0.0000
IC C10    C8     *C9    H9B   0.0000  0.0000 -120.00  0.0000   0.0000
IC C8     C9     C10    C11   0.0000  0.0000  180.00  0.0000   0.0000
IC C11    C9     *C10   H10A  0.0000  0.0000  120.00  0.0000   0.0000
IC C11    C9     *C10   H10B  0.0000  0.0000 -120.00  0.0000   0.0000
IC C9     C10    C11    C12   0.0000  0.0000  180.00  0.0000   0.0000
IC C12    C10    *C11   H11A  0.0000  0.0000  120.00  0.0000   0.0000
IC C12    C10    *C11   H11B  0.0000  0.0000 -120.00  0.0000   0.0000
IC C10    C11    C12    C13   0.0000  0.0000  180.00  0.0000   0.0000
IC C13    C11    *C12   H12A  0.0000  0.0000  120.00  0.0000   0.0000
IC C13    C11    *C12   H12B  0.0000  0.0000 -120.00  0.0000   0.0000
IC C11    C12    C13    C14   0.0000  0.0000  180.00  0.0000   0.0000
IC C14    C12    *C13   H13A  0.0000  0.0000  120.00  0.0000   0.0000
IC C14    C12    *C13   H13B  0.0000  0.0000 -120.00  0.0000   0.0000
IC C12    C13    C14    C15   0.0000  0.0000  180.00  0.0000   0.0000
IC C15    C13    *C14   H14A  0.0000  0.0000  120.00  0.0000   0.0000
IC C15    C13    *C14   H14B  0.0000  0.0000 -120.00  0.0000   0.0000
IC C13    C14    C15    C16   0.0000  0.0000  180.00  0.0000   0.0000
IC C16    C14    *C15   H15A  0.0000  0.0000  120.00  0.0000   0.0000
IC C16    C14    *C15   H15B  0.0000  0.0000 -120.00  0.0000   0.0000
IC C14    C15    C16    C17   0.0000  0.0000  180.00  0.0000   0.0000
IC C17    C15    *C16   H16A  0.0000  0.0000  120.00  0.0000   0.0000
IC C17    C15    *C16   H16B  0.0000  0.0000 -120.00  0.0000   0.0000
```

```
IC C15    C16    C17    C18   0.0000  0.0000  180.00  0.0000   0.0000
IC C18    C16    *C17   H17A  0.0000  0.0000  120.00  0.0000   0.0000
IC C18    C16    *C17   H17B  0.0000  0.0000 -120.00  0.0000   0.0000
IC C16    C17    C18    H18A  0.0000  0.0000  180.00  0.0000   0.0000
IC H18A   C17    *C18   H18B  0.0000  0.0000  120.00  0.0000   0.0000
IC H18A   C17    *C18   H18C  0.0000  0.0000 -120.00  0.0000   0.0000
```

A.3.2 Azelaic Acid

```
RESI AAP          0.00 ! azelaic acid
!

GROUP                                     H1C
ATOM H1C  HOL      0.44 !                   |
ATOM O1   OHL     -0.61 !             O2   O1
ATOM C1   CL       0.75 !              \\ /
ATOM O2   OBL     -0.55 !               C1
ATOM C2   CTL2    -0.21 !               |
ATOM H2A  HAL2     0.09 !         H2A---C2---H2B
ATOM H2B  HAL2     0.09 !               |
GROUP                   !               |
ATOM C3   CTL2    -0.18 !               |
ATOM H3A  HAL2     0.09 !        H3A ---C3---H3B
ATOM H3B  HAL2     0.09 !               |
GROUP                   !               |
ATOM C4   CTL2    -0.18 !               |
ATOM H4A  HAL2     0.09 !        H4A ---C4---H4B
ATOM H4B  HAL2     0.09 !               |
GROUP                   !               |
ATOM C5   CTL2    -0.18 !               |
ATOM H5A  HAL2     0.09 !        H5A ---C5---H5B
ATOM H5B  HAL2     0.09 !               |
GROUP                   !               |
ATOM C6   CTL2    -0.18 !               |
ATOM H6A  HAL2     0.09 !        H6A ---C6---H6B
ATOM H6B  HAL2     0.09 !               |
GROUP                   !               |
ATOM C7   CTL2    -0.18 !               |
ATOM H7A  HAL2     0.09 !        H7A ---C7---H7B
ATOM H7B  HAL2     0.09 !               |
GROUP                   !               |
ATOM C8   CTL2    -0.21 !               |
ATOM H8A  HAL2     0.09 !        H8A ---C8---H8B
ATOM H8B  HAL2     0.09 !               |
ATOM C9   CL       0.75 !               |
ATOM O3   OBL     -0.55 !               C9
ATOM O4   OHL     -0.61 !              /  \\
ATOM H9C  HOL      0.44 !            O4     O3
                                     |
                                    H9C
! bonding
BOND  H1C  O1
BOND  O1   C1
DOUBLE  C1  O2
BOND  C1   C2
BOND  C2   H2A       C2   H2B       C2   C3
```

```
BOND  C3   H3A       C3   H3B       C3   C4
BOND  C4   H4A       C4   H4B       C4   C5
BOND  C5   H5A       C5   H5B       C5   C6
BOND  C6   H6A       C6   H6B       C6   C7
BOND  C7   H7A       C7   H7B       C7   C8
BOND  C8   H8A       C8   H8B       C8   C9
DOUBLE  C9   O3
BOND  C9   O4
BOND  O4   H9C

IMPR C1 O1 C2 O2
IMPR C9 O4 C8 O3

IC H1C    O1     C1     C2    0.0000  0.0000  180.00  0.0000   0.0000
IC C2     O1     *C1    O2    0.0000  0.0000  0.0000  0.0000   0.0000
IC O1     C1     C2     C3    0.0000  0.0000  180.00  0.0000   0.0000
IC C3     C1     *C2    H2A   0.0000  0.0000  120.00  0.0000   0.0000
IC C3     C1     *C2    H2B   0.0000  0.0000 -120.00  0.0000   0.0000
IC C1     C2     C3     C4    0.0000  0.0000  180.00  0.0000   0.0000
IC C4     C2     *C3    H3A   0.0000  0.0000  120.00  0.0000   0.0000
IC C4     C2     *C3    H3B   0.0000  0.0000 -120.00  0.0000   0.0000
IC C2     C3     C4     C5    0.0000  0.0000  180.00  0.0000   0.0000
IC C5     C3     *C4    H4A   0.0000  0.0000  120.00  0.0000   0.0000
IC C5     C3     *C4    H4B   0.0000  0.0000 -120.00  0.0000   0.0000
IC C3     C4      C5    C6    0.0000  0.0000  180.00  0.0000   0.0000
IC C6     C4     *C5    H5A   0.0000  0.0000  120.00  0.0000   0.0000
IC C6     C4     *C5    H5B   0.0000  0.0000 -120.00  0.0000   0.0000
IC C4     C5     C6     C7    0.0000  0.0000  180.00  0.0000   0.0000
IC C7     C5     *C6    H6A   0.0000  0.0000  120.00  0.0000   0.0000
IC C7     C5     *C6    H6B   0.0000  0.0000 -120.00  0.0000   0.0000
IC C5     C6     C7     C8    0.0000  0.0000  180.00  0.0000   0.0000
IC C8     C6     *C7    H7A   0.0000  0.0000  120.00  0.0000   0.0000
IC C8     C6     *C7    H7B   0.0000  0.0000 -120.00  0.0000   0.0000
IC C6     C7     C8     C9    0.0000  0.0000  180.00  0.0000   0.0000
IC C9     C7     *C8    H8A   0.0000  0.0000  120.00  0.0000   0.0000
IC C9     C7     *C8    H8B   0.0000  0.0000 -120.00  0.0000   0.0000
IC O4     C9     C8     C7    0.0000  0.0000  180.00  0.0000   0.0000
IC C8     O4     *C9    O3    0.0000  0.0000  0.0000  0.0000   0.0000
IC H9C    O4     C9     C8    0.0000  0.0000  180.00  0.0000   0.0000
```

A.3.3 Heptanal

```
RESI HEP            0.00 ! Heptanal
!

GROUP                        H1C
ATOM C1  CG2O4      0.20 !    |
ATOM H1C HGR52      0.09 ! O1=C1
ATOM O1  OG2D1     -0.40 !    |
ATOM C2  CG321     -0.07 !H2A-C2-H2B
ATOM H2A HGA2       0.09 !    |
ATOM H2B HGA2       0.09 !    |
GROUP                    !    |
ATOM C3  CG321     -0.18 !H3A-C3-H3B
ATOM H3A HGA2       0.09 !    |
ATOM H3B HGA2       0.09 !    |
```

```
GROUP                   !    |
ATOM C4  CG321    -0.18 !H4A-C4-H4B
ATOM H4A HGA2      0.09 !    |
ATOM H4B HGA2      0.09 !    |
GROUP                   !    |
ATOM C5  CG321    -0.18 !H5A-C5-H5B
ATOM H5A HGA2      0.09 !    |
ATOM H5B HGA2      0.09 !    |
GROUP                   !    |
ATOM C6  CG321    -0.18 !H6A-C6-H6B
ATOM H6A HGA2      0.09 !    |
ATOM H6B HGA2      0.09 !    |
GROUP                   !    |
ATOM C7  CG331    -0.27 !H7A-C7-H7B
ATOM H7A HGA3      0.09 !    |
ATOM H7B HGA3      0.09 !    H7C
ATOM H7C HGA3      0.09 !

! bonding
BOND H1C   C1
DOUBLE C1   O1
BOND  C1   C2
BOND  C2   H2A       C2   H2B       C2   C3
BOND  C3   H3A       C3   H3B       C3   C4
BOND  C4   H4A       C4   H4B       C4   C5
BOND  C5   H5A       C5   H5B       C5   C6
BOND  C6   H6A       C6   H6B       C6   C7
BOND  C7   H7A       C7   H7B       C7   H7C

IMPR C1 C2 O1 H1C

IC O1     C1      C2    C3    0.0000  0.0000  180.00  0.0000   0.0000
IC C3     C2      C1    H1C   0.0000  0.0000  0.0000  0.0000   0.0000
IC H2A    C2      C1    O1    0.0000  0.0000  120.00  0.0000   0.0000
IC H2B    C2      C1    O1    0.0000  0.0000 -120.00  0.0000   0.0000
IC C3     C1     *C2    H2A   0.0000  0.0000  120.00  0.0000   0.0000
IC C3     C1     *C2    H2B   0.0000  0.0000 -120.00  0.0000   0.0000
IC C1     C2     C3     C4    0.0000  0.0000  180.00  0.0000   0.0000
IC C4     C2     *C3    H3A   0.0000  0.0000  120.00  0.0000   0.0000
IC C4     C2     *C3    H3B   0.0000  0.0000 -120.00  0.0000   0.0000
IC C2     C3     C4     C5    0.0000  0.0000  180.00  0.0000   0.0000
IC C5     C3     *C4    H4A   0.0000  0.0000  120.00  0.0000   0.0000
IC C5     C3     *C4    H4B   0.0000  0.0000 -120.00  0.0000   0.0000
IC C3     C4      C5    C6    0.0000  0.0000  180.00  0.0000   0.0000
IC C6     C4     *C5    H5A   0.0000  0.0000  120.00  0.0000   0.0000
IC C6     C4     *C5    H5B   0.0000  0.0000 -120.00  0.0000   0.0000
IC C4     C5     C6     C7    0.0000  0.0000  180.00  0.0000   0.0000
IC C7     C5     *C6    H6A   0.0000  0.0000  120.00  0.0000   0.0000
IC C7     C5     *C6    H6B   0.0000  0.0000 -120.00  0.0000   0.0000
IC C5     C6     C7     H7C   0.0000  0.0000  180.00  0.0000   0.0000
IC H7C    C6     *C7    H7A   0.0000  0.0000  120.00  0.0000   0.0000
IC H7C    C6     *C7    H7B   0.0000  0.0000 -120.00  0.0000   0.0000
```

A.3.4 Heptanoic Acid

```
RESI HPA          0.00 ! heptanoic acid
!

GROUP                                     H1C
ATOM H1C  HOL     0.44 !                   |
ATOM O1   OHL    -0.61 !             O2    O1
ATOM C1   CL      0.75 !              \\ /
ATOM O2   OBL    -0.55 !               C1
ATOM C2   CTL2   -0.21 !               |
ATOM H2A  HAL2    0.09 !         H2A---C2---H2B
ATOM H2B  HAL2    0.09 !               |
GROUP                  !               |
ATOM C3   CTL2   -0.18 !               |
ATOM H3A  HAL2    0.09 !        H3A ---C3---H3B
ATOM H3B  HAL2    0.09 !               |
GROUP                  !               |
ATOM C4   CTL2   -0.18 !               |
ATOM H4A  HAL2    0.09 !        H4A ---C4---H4B
ATOM H4B  HAL2    0.09 !               |
GROUP                  !               |
ATOM C5   CTL2   -0.18 !               |
ATOM H5A  HAL2    0.09 !        H5A ---C5---H5B
ATOM H5B  HAL2    0.09 !               |
GROUP                  !               |
ATOM C6   CTL2   -0.18 !               |
ATOM H6A  HAL2    0.09 !        H6A ---C6---H6B
ATOM H6B  HAL2    0.09 !               |
GROUP                  !               |
ATOM C7   CTL3   -0.27 !               |
ATOM H7A  HAL3    0.09 !        H7A ---C7---H7B
ATOM H7B  HAL3    0.09 !               |
ATOM H7C  HAL3    0.09 !              H7C

! bonding
BOND  H1C  O1
BOND  O1   C1
DOUBLE  C1  O2
BOND  C1   C2
BOND  C2   H2A       C2   H2B       C2   C3
BOND  C3   H3A       C3   H3B       C3   C4
BOND  C4   H4A       C4   H4B       C4   C5
BOND  C5   H5A       C5   H5B       C5   C6
BOND  C6   H6A       C6   H6B       C6   C7
BOND  C7   H7A       C7   H7B       C7   H7C

IMPR C1 O1 C2 O2

IC H1C    O1     C1     C2     0.0000  0.0000  180.00  0.0000   0.0000
IC C2     O1     *C1    O2     0.0000  0.0000  0.0000  0.0000   0.0000
IC O1     C1     C2     C3     0.0000  0.0000  180.00  0.0000   0.0000
IC C3     C1     *C2    H2A    0.0000  0.0000  120.00  0.0000   0.0000
IC C3     C1     *C2    H2B    0.0000  0.0000 -120.00  0.0000   0.0000
IC C1     C2     C3     C4     0.0000  0.0000  180.00  0.0000   0.0000
IC C4     C2     *C3    H3A    0.0000  0.0000  120.00  0.0000   0.0000
IC C4     C2     *C3    H3B    0.0000  0.0000 -120.00  0.0000   0.0000
IC C2     C3     C4     C5     0.0000  0.0000  180.00  0.0000   0.0000
IC C5     C3     *C4    H4A    0.0000  0.0000  120.00  0.0000   0.0000
```

```
IC C5     C3     *C4    H4B   0.0000  0.0000 -120.00  0.0000   0.0000
IC C3     C4      C5    C6    0.0000  0.0000  180.00  0.0000   0.0000
IC C6     C4     *C5    H5A   0.0000  0.0000  120.00  0.0000   0.0000
IC C6     C4     *C5    H5B   0.0000  0.0000 -120.00  0.0000   0.0000
IC C4     C5     C6     C7    0.0000  0.0000  180.00  0.0000   0.0000
IC C7     C5     *C6    H6A   0.0000  0.0000  120.00  0.0000   0.0000
IC C7     C5     *C6    H6B   0.0000  0.0000 -120.00  0.0000   0.0000
IC C5     C6     C7     H7C   0.0000  0.0000  180.00  0.0000   0.0000
IC H7C    C6     *C7    H7A   0.0000  0.0000  120.00  0.0000   0.0000
IC H7C    C6     *C7    H7B   0.0000  0.0000 -120.00  0.0000   0.0000
```

A.3.5 Nonanal

```
RESI NN            0.00 ! Nonanal
!

GROUP                        H1C
ATOM C1  CG2O4     0.20 !     |
ATOM H1C HGR52     0.09 !  O1=C1
ATOM O1  OG2D1    -0.40 !     |
ATOM C2  CG321    -0.07 !H2A-C2-H2B
ATOM H2A HGA2      0.09 !     |
ATOM H2B HGA2      0.09 !     |
GROUP                   !     |
ATOM C3  CG321    -0.18 !H3A-C3-H3B
ATOM H3A HGA2      0.09 !     |
ATOM H3B HGA2      0.09 !     |
GROUP                   !     |
ATOM C4  CG321    -0.18 !H4A-C4-H4B
ATOM H4A HGA2      0.09 !     |
ATOM H4B HGA2      0.09 !     |
GROUP                   !     |
ATOM C5  CG321    -0.18 !H5A-C5-H5B
ATOM H5A HGA2      0.09 !     |
ATOM H5B HGA2      0.09 !     |
GROUP                   !     |
ATOM C6  CG321    -0.18 !H6A-C6-H6B
ATOM H6A HGA2      0.09 !     |
ATOM H6B HGA2      0.09 !     |
GROUP                   !     |
ATOM C7  CG321    -0.18 !H7A-C7-H7B
ATOM H7A HGA2      0.09 !     |
ATOM H7B HGA2      0.09 !     |
GROUP                   !     |
ATOM C8  CG321    -0.18 !H8A-C8-H8B
ATOM H8A HGA2      0.09 !     |
ATOM H8B HGA2      0.09 !     |
GROUP                   !     |
ATOM C9  CG331    -0.27 !H9A-C9-H9B
ATOM H9A HGA3      0.09 !     |
ATOM H9B HGA3      0.09 !    H9C
ATOM H9C HGA3      0.09 !

! bonding
BOND H1C   C1
DOUBLE C1   O1
BOND  C1   C2
```

```
BOND  C2   H2A       C2   H2B       C2   C3
BOND  C3   H3A       C3   H3B       C3   C4
BOND  C4   H4A       C4   H4B       C4   C5
BOND  C5   H5A       C5   H5B       C5   C6
BOND  C6   H6A       C6   H6B       C6   C7
BOND  C7   H7A       C7   H7B       C7   C8
BOND  C8   H8A       C8   H8B       C8   C9
BOND  C9   H9A       C9   H9B       C9   H9C



IMPR C1 C2 O1 H1C

IC O1     C1      C2    C3    0.0000  0.0000  180.00  0.0000   0.0000
IC C3     C2      C1    H1C   0.0000  0.0000  0.0000  0.0000   0.0000
IC H2A    C2      C1    O1    0.0000  0.0000  120.00  0.0000   0.0000
IC H2B    C2      C1    O1    0.0000  0.0000 -120.00  0.0000   0.0000
IC C3     C1     *C2    H2A   0.0000  0.0000  120.00  0.0000   0.0000
IC C3     C1     *C2    H2B   0.0000  0.0000 -120.00  0.0000   0.0000
IC C1     C2     C3     C4    0.0000  0.0000  180.00  0.0000   0.0000
IC C4     C2     *C3    H3A   0.0000  0.0000  120.00  0.0000   0.0000
IC C4     C2     *C3    H3B   0.0000  0.0000 -120.00  0.0000   0.0000
IC C2     C3     C4     C5    0.0000  0.0000  180.00  0.0000   0.0000
IC C5     C3     *C4    H4A   0.0000  0.0000  120.00  0.0000   0.0000
IC C5     C3     *C4    H4B   0.0000  0.0000 -120.00  0.0000   0.0000
IC C3     C4      C5    C6    0.0000  0.0000  180.00  0.0000   0.0000
IC C6     C4     *C5    H5A   0.0000  0.0000  120.00  0.0000   0.0000
IC C6     C4     *C5    H5B   0.0000  0.0000 -120.00  0.0000   0.0000
IC C4     C5     C6     C7    0.0000  0.0000  180.00  0.0000   0.0000
IC C7     C5     *C6    H6A   0.0000  0.0000  120.00  0.0000   0.0000
IC C7     C5     *C6    H6B   0.0000  0.0000 -120.00  0.0000   0.0000
IC C5     C6     C7     C8    0.0000  0.0000  180.00  0.0000   0.0000
IC C8     C6     *C7    H7A   0.0000  0.0000  120.00  0.0000   0.0000
IC C8     C6     *C7    H7B   0.0000  0.0000 -120.00  0.0000   0.0000
IC C6     C7     C8     C9    0.0000  0.0000  180.00  0.0000   0.0000
IC C9     C7     *C8    H8A   0.0000  0.0000  120.00  0.0000   0.0000
IC C9     C7     *C8    H8B   0.0000  0.0000 -120.00  0.0000   0.0000
IC C7     C8     C9     H9C   0.0000  0.0000  180.00  0.0000   0.0000
IC H9C    C8     *C9    H9A   0.0000  0.0000  120.00  0.0000   0.0000
IC H9C    C8     *C9    H9B   0.0000  0.0000 -120.00  0.0000   0.0000
```

A.3.6 9-Oxononanoic Acid

```
RESI ON            0.00 ! 9-oxononanoic acid
!

GROUP                   !        H1C
ATOM H1C HGP1      0.44 !        |
ATOM O1  OG311    -0.61 !  O2   O1
ATOM C1  CG2O2     0.75 !   \\ /
ATOM O2  OG2D1    -0.55 !    C1
ATOM C2  CG321    -0.21 !    |
ATOM H2A HGA2      0.09 !    |
ATOM H2B HGA2      0.09 !H2A-C2-H2B
GROUP                   !    |
ATOM C3  CG321    -0.18 !    |
ATOM H3A HGA2      0.09 !    |
```

```
ATOM H3B HGA2       0.09 !H3A-C3-H3B
GROUP                    !     |
ATOM C4  CG321     -0.18 !     |
ATOM H4A HGA2       0.09 !     |
ATOM H4B HGA2       0.09 !H4A-C4-H4B
GROUP                    !     |
ATOM C5  CG321     -0.18 !     |
ATOM H5A HGA2       0.09 !     |
ATOM H5B HGA2       0.09 !H5A-C5-H5B
GROUP                    !     |
ATOM C6  CG321     -0.18 !     |
ATOM H6A HGA2       0.09 !     |
ATOM H6B HGA2       0.09 !H6A-C6-H6B
GROUP                    !     |
ATOM C7  CG321     -0.18 !     |
ATOM H7A HGA2       0.09 !     |
ATOM H7B HGA2       0.09 !H7A-C7-H7B
GROUP                    !     |
ATOM C8  CG321     -0.07 !     |
ATOM H8A HGA2       0.09 !     |
ATOM H8B HGA2       0.09 !H8A-C8-H8B
ATOM C9  CG2O4      0.20 !     |
ATOM H9C HGR52      0.09 ! O3=C9
ATOM O3  OG2D1     -0.40 !     |
                         !    H9C


BOND  H1C  O1
BOND  O1   C1
DOUBLE  C1  O2
BOND  C1   C2
BOND  C2   H2A       C2   H2B       C2   C3
BOND  C3   H3A       C3   H3B       C3   C4
BOND  C4   H4A       C4   H4B       C4   C5
BOND  C5   H5A       C5   H5B       C5   C6
BOND  C6   H6A       C6   H6B       C6   C7
BOND  C7   H7A       C7   H7B       C7   C8
BOND  C8   H8A       C8   H8B       C8   C9
DOUBLE  C9   O3
BOND  C9   H9C

IMPR C1 O1 C2 O2
IMPR C9 C8 O3 H9C

IC H1C    O1     C1     C2    0.0000  0.0000  180.00  0.0000   0.0000
IC C2     O1     *C1    O2    0.0000  0.0000  0.0000  0.0000   0.0000
IC O1     C1     C2     H2A   0.0000  0.0000  120.00  0.0000   0.0000
IC O2     C1     C2     C3    0.0000  0.0000  0.0000  0.0000   0.0000
IC C3     C1     *C2    H2A   0.0000  0.0000  120.00  0.0000   0.0000
IC C3     C1     *C2    H2B   0.0000  0.0000 -120.00  0.0000   0.0000
IC C1     C2     C3     C4    0.0000  0.0000  180.00  0.0000   0.0000
IC C4     C2     *C3    H3A   0.0000  0.0000  120.00  0.0000   0.0000
IC C4     C2     *C3    H3B   0.0000  0.0000 -120.00  0.0000   0.0000
IC C2     C3     C4     C5    0.0000  0.0000  180.00  0.0000   0.0000
IC C5     C3     *C4    H4A   0.0000  0.0000  120.00  0.0000   0.0000
IC C5     C3     *C4    H4B   0.0000  0.0000 -120.00  0.0000   0.0000
IC C3     C4      C5    C6    0.0000  0.0000  180.00  0.0000   0.0000
IC C6     C4     *C5    H5A   0.0000  0.0000  120.00  0.0000   0.0000
```

```
IC C6     C4     *C5    H5B   0.0000  0.0000 -120.00  0.0000   0.0000
IC C4     C5     C6     C7    0.0000  0.0000  180.00  0.0000   0.0000
IC C7     C5     *C6    H6A   0.0000  0.0000  120.00  0.0000   0.0000
IC C7     C5     *C6    H6B   0.0000  0.0000 -120.00  0.0000   0.0000
IC C5     C6     C7     C8    0.0000  0.0000  180.00  0.0000   0.0000
IC C8     C6     *C7    H7A   0.0000  0.0000  120.00  0.0000   0.0000
IC C8     C6     *C7    H7B   0.0000  0.0000 -120.00  0.0000   0.0000
IC C6     C7     C8     C9    0.0000  0.0000  180.00  0.0000   0.0000
IC C9     C7     *C8    H8A   0.0000  0.0000  120.00  0.0000   0.0000
IC C9     C7     *C8    H8B   0.0000  0.0000 -120.00  0.0000   0.0000
IC C7     C8     C9     O3    0.0000  0.0000  180.00  0.0000   0.0000
IC C7     C8     C9     H9C   0.0000  0.0000  0.0000  0.0000   0.0000
IC C8     O3     *C9    H9C   0.0000  0.0000  0.0000  0.0000   0.0000
```

A.3.7 Palmitoleic Acid

```
RESI PAO          0.00 ! palmitoleic acid
!

GROUP                  !                 H1C
ATOM H1C  HOL      0.44 !                  |
ATOM O1   OHL     -0.61 !            O2   O1
ATOM C1   CL       0.75 !             \\ /
ATOM O2   OBL     -0.55 !              C1
ATOM C2   CTL2    -0.21 !               |
ATOM H2A  HAL2     0.09 !        H2A---C2---H2B
ATOM H2B  HAL2     0.09 !               |
GROUP                  !               |
ATOM C3   CTL2    -0.18 !               |
ATOM H3A  HAL2     0.09 !        H3A ---C3---H3B
ATOM H3B  HAL2     0.09 !               |
GROUP                  !               |
ATOM C4   CTL2    -0.18 !               |
ATOM H4A  HAL2     0.09 !        H4A ---C4---H4B
ATOM H4B  HAL2     0.09 !               |
GROUP                  !               |
ATOM C5   CTL2    -0.18 !               |
ATOM H5A  HAL2     0.09 !        H5A ---C5---H5B
ATOM H5B  HAL2     0.09 !               |
GROUP                  !               |
ATOM C6   CTL2    -0.18 !               |
ATOM H6A  HAL2     0.09 !        H6A ---C6---H6B
ATOM H6B  HAL2     0.09 !               |
GROUP                  !               |
ATOM C7   CTL2    -0.18 !               |
ATOM H7A  HAL2     0.09 !        H7A ---C7---H7B
ATOM H7B  HAL2     0.09 !               |
GROUP                  !               |
ATOM C8   CTL2    -0.18 !               |
ATOM H8A  HAL2     0.09 !        H8A ---C8---H8B
ATOM H8B  HAL2     0.09 !               |
GROUP                  !               |
ATOM C9   CEL1    -0.15 !               |
ATOM H9A  HEL1     0.15 !        H9A ---C9
GROUP                  !               ||
ATOM C10  CEL1    -0.15 !               ||
ATOM H10A HEL1     0.15 !        H10A---C10
GROUP                  !               |
```

```
ATOM C11  CTL2   -0.18 !              |
ATOM H11A HAL2    0.09 !       H11A---C11--H11B
ATOM H11B HAL2    0.09 !              |
GROUP                  !              |
ATOM C12  CTL2   -0.18 !              |
ATOM H12A HAL2    0.09 !       H12A---C12--H12B
ATOM H12B HAL2    0.09 !              |
GROUP                  !              |
ATOM C13  CTL2   -0.18 !              |
ATOM H13A HAL2    0.09 !       H13A---C13--H13B
ATOM H13B HAL2    0.09 !              |
GROUP                  !              |
ATOM C14  CTL2   -0.18 !              |
ATOM H14A HAL2    0.09 !       H14A---C14--H14B
ATOM H14B HAL2    0.09 !              |
GROUP                  !              |
ATOM C15  CTL2   -0.18 !              |
ATOM H15A HAL2    0.09 !       H15A---C15--H15B
ATOM H15B HAL2    0.09 !              |
GROUP                  !              |
ATOM C16  CTL3   -0.27 !              |
ATOM H16A HAL3    0.09 !       H16A---C16--H16B
ATOM H16B HAL3    0.09 !              |
ATOM H16C HAL3    0.09 !             H16C

! bonding
BOND  H1C  O1
BOND  O1   C1
DOUBLE  C1  O2
BOND  C1   C2
BOND  C2   H2A       C2   H2B       C2   C3
BOND  C3   H3A       C3   H3B       C3   C4
BOND  C4   H4A       C4   H4B       C4   C5
BOND  C5   H5A       C5   H5B       C5   C6
BOND  C6   H6A       C6   H6B       C6   C7
BOND  C7   H7A       C7   H7B       C7   C8
BOND  C8   H8A       C8   H8B       C8   C9
BOND  C9   H9A
DOUBLE  C9 C10
BOND  C10  H10A      C10  C11
BOND  C11  H11A      C11  H11B      C11  C12
BOND  C12  H12A      C12  H12B      C12  C13
BOND  C13  H13A      C13  H13B      C13  C14
BOND  C14  H14A      C14  H14B      C14  C15
BOND  C15  H15A      C15  H15B      C15  C16
BOND  C16  H16A      C16  H16B      C16  H16C

IMPR C1 O1 C2 O2

IC H1C    O1     C1     C2    0.0000  0.0000  180.00  0.0000   0.0000
IC C2     O1     *C1    O2    0.0000  0.0000  0.0000  0.0000   0.0000
IC O1     C1     C2     C3    0.0000  0.0000  180.00  0.0000   0.0000
IC C3     C1     *C2    H2A   0.0000  0.0000  120.00  0.0000   0.0000
IC C3     C1     *C2    H2B   0.0000  0.0000 -120.00  0.0000   0.0000
IC C1     C2     C3     C4    0.0000  0.0000  180.00  0.0000   0.0000
IC C4     C2     *C3    H3A   0.0000  0.0000  120.00  0.0000   0.0000
IC C4     C2     *C3    H3B   0.0000  0.0000 -120.00  0.0000   0.0000
IC C2     C3     C4     C5    0.0000  0.0000  180.00  0.0000   0.0000
```

```
IC C5     C3     *C4    H4A   0.0000  0.0000  120.00  0.0000   0.0000
IC C5     C3     *C4    H4B   0.0000  0.0000 -120.00  0.0000   0.0000
IC C3     C4      C5    C6    0.0000  0.0000  180.00  0.0000   0.0000
IC C6     C4     *C5    H5A   0.0000  0.0000  120.00  0.0000   0.0000
IC C6     C4     *C5    H5B   0.0000  0.0000 -120.00  0.0000   0.0000
IC C4     C5     C6     C7    0.0000  0.0000  180.00  0.0000   0.0000
IC C7     C5     *C6    H6A   0.0000  0.0000  120.00  0.0000   0.0000
IC C7     C5     *C6    H6B   0.0000  0.0000 -120.00  0.0000   0.0000
IC C5     C6     C7     C8    0.0000  0.0000  180.00  0.0000   0.0000
IC C8     C6     *C7    H7A   0.0000  0.0000  120.00  0.0000   0.0000
IC C8     C6     *C7    H7B   0.0000  0.0000 -120.00  0.0000   0.0000
IC C6     C7     C8     C9    0.0000  0.0000  180.00  0.0000   0.0000
IC C9     C7     *C8    H8A   0.0000  0.0000  120.00  0.0000   0.0000
IC C9     C7     *C8    H8B   0.0000  0.0000 -120.00  0.0000   0.0000
IC C7     C8     C9     C10   0.0000  0.0000  180.00  0.0000   0.0000
IC C10    C8     *C9    H9A   0.0000  0.0000  180.00  0.0000   0.0000
IC C8     C9     C10    C11   0.0000  0.0000  0.0000  0.0000   0.0000
IC C11    C9     *C10   H10A  0.0000  0.0000  180.00  0.0000   0.0000
IC C9     C10    C11    C12   0.0000  0.0000  180.00  0.0000   0.0000
IC C12    C10    *C11   H11A  0.0000  0.0000  120.00  0.0000   0.0000
IC C12    C10    *C11   H11B  0.0000  0.0000 -120.00  0.0000   0.0000
IC C10    C11    C12    C13   0.0000  0.0000  180.00  0.0000   0.0000
IC C13    C11    *C12   H12A  0.0000  0.0000  120.00  0.0000   0.0000
IC C13    C11    *C12   H12B  0.0000  0.0000 -120.00  0.0000   0.0000
IC C11    C12    C13    C14   0.0000  0.0000  180.00  0.0000   0.0000
IC C14    C12    *C13   H13A  0.0000  0.0000  120.00  0.0000   0.0000
IC C14    C12    *C13   H13B  0.0000  0.0000 -120.00  0.0000   0.0000
IC C12    C13    C14    C15   0.0000  0.0000  180.00  0.0000   0.0000
IC C15    C13    *C14   H14A  0.0000  0.0000  120.00  0.0000   0.0000
IC C15    C13    *C14   H14B  0.0000  0.0000 -120.00  0.0000   0.0000
IC C13    C14    C15    C16   0.0000  0.0000  180.00  0.0000   0.0000
IC C16    C14    *C15   H15A  0.0000  0.0000  120.00  0.0000   0.0000
IC C16    C14    *C15   H15B  0.0000  0.0000 -120.00  0.0000   0.0000
IC C14    C15    C16    H16A  0.0000  0.0000  180.00  0.0000   0.0000
IC H16A   C15    *C16   H16B  0.0000  0.0000  120.00  0.0000   0.0000
IC H16A   C15    *C16   H16C  0.0000  0.0000 -120.00  0.0000   0.0000
```

A.3.8 Nonanoic Acid

```
RESI NAP          0.00 ! nonanoic acid
!

GROUP                                     H1C
ATOM H1C  HOL      0.44 !                   |
ATOM O1   OHL     -0.61 !             O2   O1
ATOM C1   CL       0.75 !              \\ /
ATOM O2   OBL     -0.55 !               C1
ATOM C2   CTL2    -0.21 !               |
ATOM H2A  HAL2     0.09 !         H2A---C2---H2B
ATOM H2B  HAL2     0.09 !               |
GROUP                   !               |
ATOM C3   CTL2    -0.18 !               |
ATOM H3A  HAL2     0.09 !        H3A ---C3---H3B
ATOM H3B  HAL2     0.09 !               |
GROUP                   !               |
ATOM C4   CTL2    -0.18 !               |
ATOM H4A  HAL2     0.09 !        H4A ---C4---H4B
ATOM H4B  HAL2     0.09 !               |
```

```
GROUP                  !             |
ATOM C5   CTL2   -0.18 !             |
ATOM H5A  HAL2    0.09 !        H5A ---C5---H5B
ATOM H5B  HAL2    0.09 !             |
GROUP                  !             |
ATOM C6   CTL2   -0.18 !             |
ATOM H6A  HAL2    0.09 !        H6A ---C6---H6B
ATOM H6B  HAL2    0.09 !             |
GROUP                  !             |
ATOM C7   CTL2   -0.18 !             |
ATOM H7A  HAL2    0.09 !        H7A ---C7---H7B
ATOM H7B  HAL2    0.09 !             |
GROUP                  !             |
ATOM C8   CTL2   -0.18 !             |
ATOM H8A  HAL2    0.09 !        H8A ---C8---H8B
ATOM H8B  HAL2    0.09 !             |
GROUP                  !             |
ATOM C9   CTL3   -0.27 !             |
ATOM H9A  HAL3    0.09 !        H9A ---C9---H9B
ATOM H9B  HAL3    0.09 !             |
ATOM H9C  HAL3    0.09 !            H9C

! bonding
BOND  H1C  O1
BOND  O1   C1
DOUBLE  C1  O2
BOND  C1   C2
BOND  C2   H2A       C2   H2B       C2   C3
BOND  C3   H3A       C3   H3B       C3   C4
BOND  C4   H4A       C4   H4B       C4   C5
BOND  C5   H5A       C5   H5B       C5   C6
BOND  C6   H6A       C6   H6B       C6   C7
BOND  C7   H7A       C7   H7B       C7   C8
BOND  C8   H8A       C8   H8B       C8   C9
BOND  C9   H9A       C9   H9B       C9   H9C



IMPR C1 O1 C2 O2

IC H1C    O1     C1     C2    0.0000  0.0000  180.00  0.0000   0.0000
IC C2     O1     *C1    O2    0.0000  0.0000  0.0000  0.0000   0.0000
IC O1     C1     C2     C3    0.0000  0.0000  180.00  0.0000   0.0000
IC C3     C1     *C2    H2A   0.0000  0.0000  120.00  0.0000   0.0000
IC C3     C1     *C2    H2B   0.0000  0.0000 -120.00  0.0000   0.0000
IC C1     C2     C3     C4    0.0000  0.0000  180.00  0.0000   0.0000
IC C4     C2     *C3    H3A   0.0000  0.0000  120.00  0.0000   0.0000
IC C4     C2     *C3    H3B   0.0000  0.0000 -120.00  0.0000   0.0000
IC C2     C3     C4     C5    0.0000  0.0000  180.00  0.0000   0.0000
IC C5     C3     *C4    H4A   0.0000  0.0000  120.00  0.0000   0.0000
IC C5     C3     *C4    H4B   0.0000  0.0000 -120.00  0.0000   0.0000
IC C3     C4      C5    C6    0.0000  0.0000  180.00  0.0000   0.0000
IC C6     C4     *C5    H5A   0.0000  0.0000  120.00  0.0000   0.0000
IC C6     C4     *C5    H5B   0.0000  0.0000 -120.00  0.0000   0.0000
IC C4     C5     C6     C7    0.0000  0.0000  180.00  0.0000   0.0000
IC C7     C5     *C6    H6A   0.0000  0.0000  120.00  0.0000   0.0000
IC C7     C5     *C6    H6B   0.0000  0.0000 -120.00  0.0000   0.0000
IC C5     C6     C7     C8    0.0000  0.0000  180.00  0.0000   0.0000
```

```
IC C8      C6      *C7     H7A    0.0000  0.0000  120.00  0.0000   0.0000
IC C8      C6      *C7     H7B    0.0000  0.0000 -120.00  0.0000   0.0000
IC C6      C7      C8      C9     0.0000  0.0000  180.00  0.0000   0.0000
IC C9      C7      *C8     H8A    0.0000  0.0000  120.00  0.0000   0.0000
IC C9      C7      *C8     H8B    0.0000  0.0000 -120.00  0.0000   0.0000
IC C7      C8      C9      H9C    0.0000  0.0000  180.00  0.0000   0.0000
IC H9C     C8      *C9     H9A    0.0000  0.0000  120.00  0.0000   0.0000
IC H9C     C8      *C9     H9B    0.0000  0.0000 -120.00  0.0000   0.0000
```